Covalent Organic Frameworks

Form Follows Function

Laura Patricia Ascherl

2018

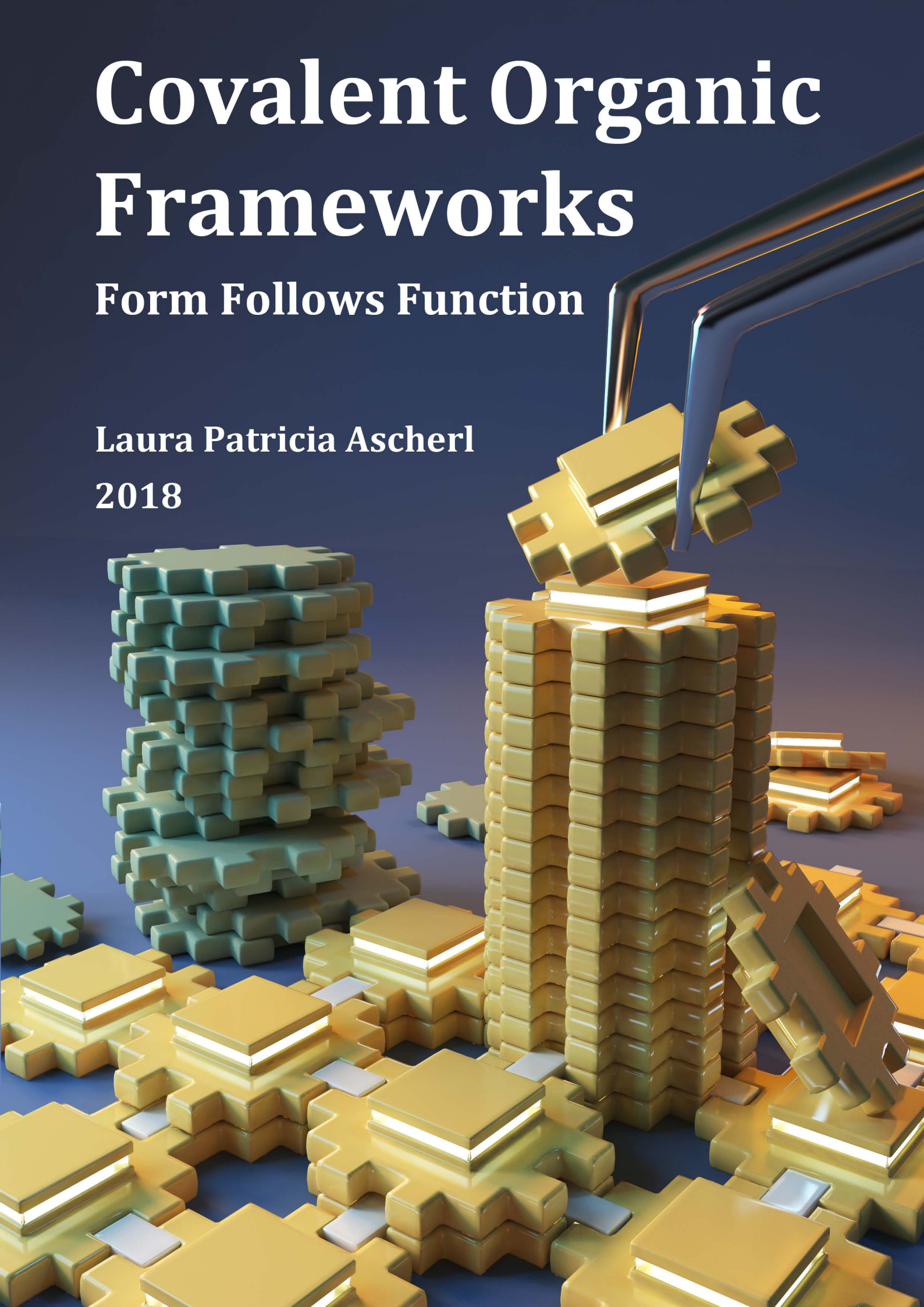

Dissertation zur Erlangung des Doktorgrades

der Fakultät für Chemie und Pharmazie

der Ludwig-Maximilians-Universität München

Covalent Organic Frameworks - Form Follows Function

Laura Patricia Ascherl

aus

München, Deutschland

2018

Erklärung

Diese Dissertation wurde im Sinne von § 7 der Promotionsordnung vom 28. November 2011 von Herrn Prof. Dr. Thomas Bein betreut.

Eidesstattliche Versicherung

Diese Dissertation wurde eigenständig und ohne unerlaubte Hilfe erarbeitet.

München, den 06.03.2018

……..

(Laura Ascherl)

Dissertation eingereicht am: 06.03.2018

1. Gutachter: Prof. Dr. Thomas Bein

2. Gutachter: Senior Lecturer Dr. Stefan Wuttke

Mündliche Prüfung am: 29.03.2018

Das menschliche Wissen gleicht einer Kugel, die sich ständig ausdehnt,
so dass ihr Inhalt immer größer, die Berührungspunkte mit dem
Ungewissen jedoch immer zahlreicher werden.

Blaise Pascal
(1623 – 1662)

für meine Familie

Danksagung

An dieser Stelle möchte ich zu allererst meinem Doktorvater Prof. Thomas Bein dafür danken, dass ich meinen Teil zu einem jungen, spannenden Forschungsthema beitragen durfte und mich dabei frei entfalten konnte, was meine Forschungsinteressen anging. Die Top-Ausstattung unserer Labore mit jeglichen Gerätschaften, die das Chemikerherz begehrt, hat das Arbeiten sehr angenehm gestaltet. Durch die Möglichkeit, unsere Arbeit auf vielen Konferenzen rund um den Globus vorzustellen, habe ich gelernt Vorträge auf großen Bühnen zu halten und konnte neben Kooperationen auch Freundschaften schließen. Vielen Dank dafür!

Ein großer Dank geht auch an meinen Zweitgutachter Senior Lecturer Dr. Stefan Wuttke, der für meine Prüfung extra seinen Flug anders gelegt hat.

Vielen Dank an meine vielen Kooperationspartner, ohne die unsere Paper nur halb so toll geworden wären: Unsere Rechenforce Tim Clark, Hannes Margraf und Matthias Hennemann in Erlangen, Karena Chapman und Saul Lapidus am Synchrotron in Argonne, Daniele Di Nuzzo und Sir Richard Friend in Cambridge und Simon Krause in Dresden. Nicht vergessen werden dürfen hier auch meine „in-house“-Kooperationspartner Derya Bessinger, Niklas Keller und Stephan Reuter für unsere erfolgreichen gemeinsamen Projekte, Konstantin Karaghiosoff und Christina Hettstedt für die Einkristallmessungen- und lösungen, Markus Döblinger für die TEM-Messungen, Tristan Harzer für die FIB-Lamellen, Alexander Hufnagel für die Konstruktion des Lösemittelsensors und Michael Beetz für das Video davon.

Für das geniale Coverbild geht mein Dank an den NIM-Criss!

Vielen Dank auch an Julia Nafe und Matthias Becker vom AK Knochel, die mir bei organischen Fragen jeglicher Art immer mit Rat und Tat zur Seite gestanden sind.

Meinen F-Praktikanten Sina(h), kleiner Flo und Tanja vielen Dank dafür, dass sie mich bei der Linkersynthese (und vor allem beim Säulen) so tatkräftig unterstützt haben.

Der MOF-COF-Subgroup vielen Dank für die vielen hilfreichen Diskussionen während unserer Subgroupmeetings.

An dieser Stelle möchte ich auch Tina Reuther, Regina Huber und Corinna Heidt danken, die dafür Sorge tragen, dass hier alles so reibungslos läuft.

Nicht fehlen dürfen hier auch die besten Benchmates Stephan und Derya, ohne die KOH-Bad-Ausräumen nur halb so viel Spaß gemacht hätte (und nur halb so häufig vorgekommen wäre).

Vielen Dank auch an Bianca für die gegenseitige Motivation beim Schreiben und vor allem Lernen und für unsere lustigen Mittagspausen!

Meinen Bürokollegen aus dem Ladiesoffice Dodo, Tina, Erika, Maria und Cindy und später Stephan, Michi und Niklas herzlichen Dank für die lustige Stimmung am Arbeitsplatz. Mein Dank gilt auch besonders meinem Schreibeoffice (Enrico, Alex, Erika und Maria) für die hilfreichen Diskussionen, die gegenseitige Motivation und die gute Atmosphäre in der heißen Schreibphase.

Nicht unerwähnt bleiben dürfen die extrem lustigen und nicht minder niveauvollen Mittagspausen mit meinem Lunchteam Michi, Joni, Derya und Stephan. Ich freue mich jeden Mittag wieder, wenn es endlich halb zwölf ist!

Für die Inspiration meiner Kapitelüberschriften herzlichen Dank an William Shakespeare (The Taming of the Shrew), The Police (Every Step you Take), E. L. James (50 Shades of Grey), Berlin (Take my Breath Away) und Daft Punk (Harder, Better, Faster, Stronger).

Vielen Dank meinen Mädls dafür, dass wir uns immer noch so gut verstehen und besonders für euer Verständnis, wenn ich mal wieder abends nicht mit von der Partie sein konnte, weil die Säule (ganz ausnahmsweise!) länger gedauert hat, als eigentlich geplant.

Ein besonders großes Dankeschön geht an Flo für seine persönliche und fachliche Unterstützung während der Doktorarbeit und dafür, dass ich mich immer auf ihn verlassen kann. Schön mit dir../!* Deine Begeisterungsfähigkeit, deine unendliche Geduld und Ausdauer bei noch so undankbaren Syntheseschritten, deine Motivation und deine Fähigkeit, immer über den Tellerrand hinauszublicken, haben nicht nur mir, sondern deiner ganzen Subgroup bei ihrer wissenschaftlichen Entwicklung enorm weitergeholfen.

Mein größter Dank gilt meinen Eltern, die mir die Faszination für Chemie irgendwie in die Wiege gelegt haben und ohne deren Unterstützung weder mein Studium noch meine Promotion möglich gewesen wären. Ich hab euch lieb! ♥

Abstract

Covalent organic frameworks (COFs) are a new and emerging class of porous and crystalline materials that are formed via the connection of organic subunits through covalent bonds. Their great structural flexibility allows for the realisation of COFs based on a modular principle, where the respective building blocks can be hand-picked and designed regarding features like pore size, pore geometry or specific functionalities of the resulting material. Potential for application has been demonstrated amongst others in gas storage, gas separation, sensing, drug delivery or (opto)electronics.

As COFs are polymers linked in two or three dimensions, the realisation of crystalline materials is challenging and only possible when the covalent bond formation mechanism is reversible, allowing the network to self-heal during synthesis. This healing mechanism, however, is only applicable to a limited number of attachment and detachment cycles until the building blocks get ultimately trapped in the growing network. This way, defects are inevitably incorporated in the resulting COF. Building blocks that are used in conventional 2D COF syntheses exhibit a combination of two properties potentially fraught with problems: (1) They prefer to stack with a lateral offset and (2) exhibit symmetry elements like rotational axes. Due to symmetry reasons, there is hence no preferred direction for the offset of adjacent COF layers. When growing islands on top of a perfect layer feature different offsets along symmetry-equivalent directions, they cannot merge into each other, resulting in lattice strain, defects and an overall compromised crystallinity.

Potential applications like optoelectronic devices would benefit to a great extent from highly crystalline, error-free domains for successful charge-transport, so the first part of this thesis is focused on the realisation of COFs with a very high degree of order. By applying tetraphenylethylene building blocks with a unique propeller-shaped three dimensional geometry, the individual COF sheets are locked in place as the molecules can stack perfectly eclipsed upon each other like puzzle pieces. Each building block can act as a docking site for newly attaching molecules during crystal growth, preventing stacking faults and dislocations. Studying a series of COFs comprising different linear linkers enabled us to observe that the molecular conformation of the bridge itself plays a crucial role in the realisation of error-free crystallites. To ensure that only the correct propeller enantiomer is incorporated within one

COF domain, bridges with *C*2 rotational axis synchronize adjacent core molecules by transmitting configurational information from one propeller to the other.

In the next part of this thesis, we extended our lock-and-key concept further and made it accessible to a broader range of bridging units. Switching from our initial building block that enforces strictly eclipsed packing to a tightly π-stacked central core unit that enables offset-stacking, we were able to realise conjugated COF single crystallites on the order of 0.5 μm. The armchair conformation of the tetraphenylpyrene core is synchronised via flat and rigid π-stacked bridges, which additionally allow for electronic communication between all subunits of the framework. Tuning the electron density of the bridging entitiy we were further able to modulate the optoelectronic properties of the respective COFs.

In the third part of this thesis we used our docking concept to realise highly crystalline and stable COF films that can change their electronic structure reversibly depending on the surrounding atmosphere. By combining electron-rich and -deficient building blocks, we synthesised the first solvatochromic COFs that show a strong charge-transfer induced colour change when exposed to humidity or solvent vapours. The extent of the colour change is dependent on the vapour concentration and the solvent polarity, allowing for contactless sensing of probe molecules. The growth of the COFs as oriented films guarantees highly accessible pores and thus ultrafast response times below 200 ms, outperforming even commercially available sensing devices. As a proof of concept, we constructed a humidity sensor with full reversibility and stability over at least 4000 cycles by applying a solvatochromic COF film as a light filter between a LED and a photoresistor.

Although many intriguing functionalities have been demonstrated with COFs, reversible structural flexibility has not been reported for 2D COFs yet. We surmised that a high degree of lateral displacement between individual COF layers combined with tightly interlocked π-stacks would enable the linear bridging units to move almost freely upon applying an external stimulus. Indeed, the design of multidentate COF linkers based on perylene-3,4,9,10-tetracarboxylic acid diimide allowed us to realise the first breathing 2D COFs that reversibly change their crystal and electronic structure when in contact with solvent molecules. During these “wine-rack” breathing transitions, the distance between the perylene-3,4,9,10-tetracarboxylic acid diimides can be tuned, allowing for switching on and off in-plane electronic coupling. Taking this concept further, we showed that slight modifications of the linear bridging unit can again inhibit the dynamic response due to steric effects.

The last part of this thesis was focused on structural requirements of building blocks for constructing large-pore COFs. We elaborated boundary conditions for linear bridging units as well as multidentate building blocks, taking into account multiple aspects like building block offset, alkyl chain packing and tilt angles. To achieve crystalline packing in such large-pore COF systems, we established that both building blocks have to be matched appropriately, allowing the COF to adapt one single, well-defined structure.

In conclusion, this thesis has been focused on exploring the fundamental relationships between linker design and resulting structural and functional characteristics of the respective covalent organic framework. The ability to realise highly crystalline networks with reversibly tuneable electronic, optical and geometric properties will help this young class of materials to evolve from a purely academic field of research and broaden the scope of possible applications.

Table of Contents

1 Introduction

1.1 Reticular chemistry – from molecules to networks

Humankind has ever since benefited from the unique properties of porous substances and we come across this class of materials constantly on a day-to-day basis. On the one hand, there are such rather obvious characteristics like the insulating capabilities of bricks due to encapsulated air or the sieving effect of a coffee filter that make our daily lives easier without us even noticing. On the other hand, we make use of and manipulate more subtle properties like the adsorption capabilities of activated carbon for purification purposes or ion exchange in zeolites for water softening. There are many more fields of research that would benefit from custom-made porous compounds, helping to promote progress on environmental, medical or scientific issues. It is therefore hardly surprising that great efforts are made to ultimately master the art of tailoring porous materials towards specifically defined applications.

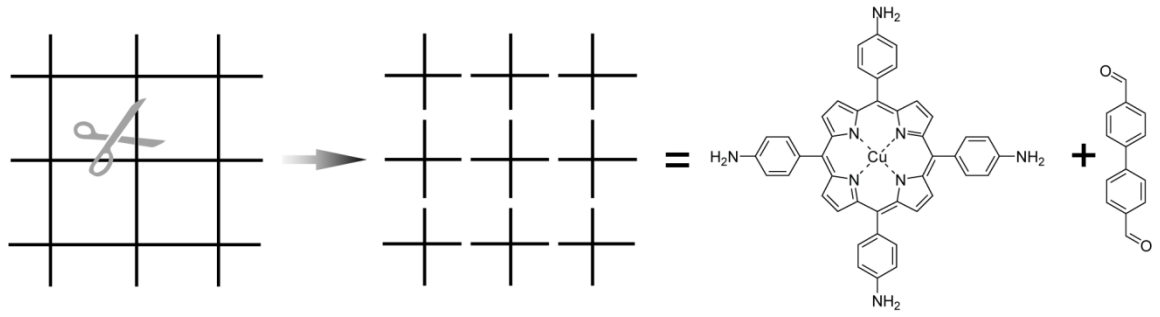

Figure 1.1 The basic principles of reticular chemistry. Cutting a desired target network into its geometric building blocks and finding molecular equivalents to these subunits allows for constructing a framework with predefined properties from scratch.

It was 2003 when the term ‘reticular synthesis’ was born, describing a new approach for the rational design of porous solid-state materials. The hitherto common way of synthesising new solid-state materials, referred to as “shake and bake’, ‘mix and wait’ and ‘heat and beat’”,[1] is depicted as a complex process where the resulting products have generally little in common with the bonding and connectivity of the reactants. As the structure of their constituents is typically altered during the reaction, the discovery of new materials is often described as serendipitous lucky finds. Reticular chemistry however opens up the opportunity to ultimately control the character of the desired material by applying subunits that maintain their rigid structure during synthesis, thus allowing to blueprint materials on a drafting table.

Conceptually, the construction of a new material follows easy steps (Figure 1.1), namely designing a target network with specific properties (pore size, pore shape, etc.) cutting it down into small subunits and finding respective molecular building blocks that can be joined together through sufficiently strong bonds.

1.2 From MOFs to COFs

The synthesis of the first metal organic framework (MOF) in 1999 marked a milestone in the history of porous materials.[2] With concepts borrowed from metal carboxylate chemistry, it had been possible for the very first time to achieve an open organic-inorganic-hybrid framework with a high surface area of 2900 m^2 g^{-1} and permanent porosity, which retained its crystallinity even when guest molecules had been completely removed. MOF-5 is composed of tetrahedral Zn_4O^{6+} clusters that are connected through benzene dicarboxylates (Figure 1.2) via coordinative bonds. The orientation of the linkers is hereby predefined by the bridged carboxylates, resulting in $Zn_4O(RCO_2)_6$ nodes that form the basis of the cubic 3D framework of MOF-5.

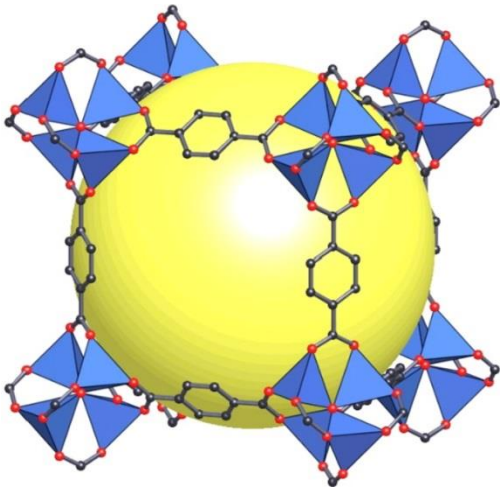

Figure 1.2 Structure of the first MOF.[3] MOF-5 consists of Zn_4O tetrahedra that are connected though benzene dicarboxylate linkers, yielding a cubic framework.

Modular design allows for the construction of frameworks with different pore sizes via adaptation of the linker length. This way, isoreticular MOFs (IRMOFs) following the same design principle with variable aperture can be synthesised.[4] Organic linkers are not restricted to be linear and to only bear two functional groups. Furthermore, the variety of metal clusters or multinuclear complexes thereof is huge. This immense diversity (indicated in Figure 1.3) opens up vast opportunities for realising new members of the MOF family with the added

benefit of reticular synthesis, the ability to predict or rather pre-design the topology of the resulting framework beforehand. This way, MOFs can be hand-tailored towards desired applications. Their tuneable pore size and high internal surface area of up to 7000 m^2 g^{-1}[5] make them ideal candidates for gas separation or gas storage. Even a pilot natural gas vehicle that is equipped with a MOF-based gas tank has recently been introduced by BASF.[6]

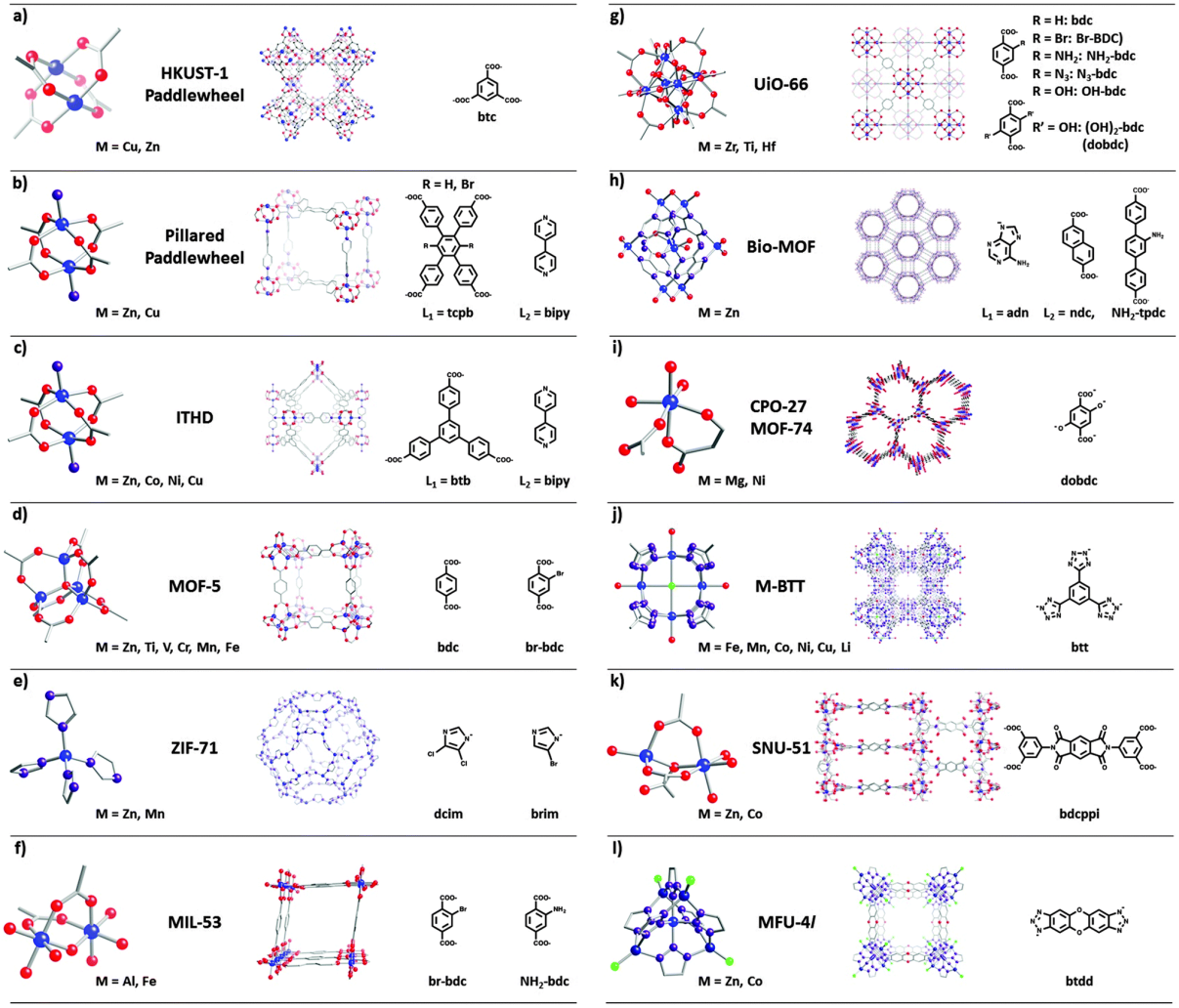

Figure 1.3 Geometric relationship in MOFs. A small selection of secondary building units (SBUs) and organic linkers that are used in MOF synthesis and their respective lattice structures.[7]

Their great structural diversity, tuneable pore functionality and small density open up additional potential applications including drug delivery, sensing, catalysis or solar energy conversion.

Even though these frameworks exhibit excellent thermal stability, the majority of them is prone to getting attacked by humidity, with water acting as a nucleophile[8] that destroys the

structure of the MOFs.[9] The moisture sensitivity of many MOFs can limit certain practical applications, as water or traces thereof are ubiquitous in industrial processes, and highlights the necessity for the development of porous materials with superior stability under ambient conditions.

In 2005 a new family of porous materials emerged, that is, the covalent organic frameworks (COFs), solely composed of organic subunits that are linked via covalent bonds.[10] This ultra-lightweight new class of materials disproved the serious issue of the "crystallisation problem" assuming that covalently linked organic molecules cannot be crystallised into a solid structure. The key to overcome this issue is to employ a reversible bond formation mechanism, allowing the network to self-heal (see Chapter 1.3 for other bond typed used in COF synthesis). The first two COFs were thus formed through the reversible condensation of aromatic building blocks: Benzenediboronic acid self-condenses to form boroxine-rings as linkage motifes (COF-1), whereas the co-condensation of benzenediboronic acid and hexahydroxytriphenylene (HHTP) yields a boronate ester linked COF (COF-5).

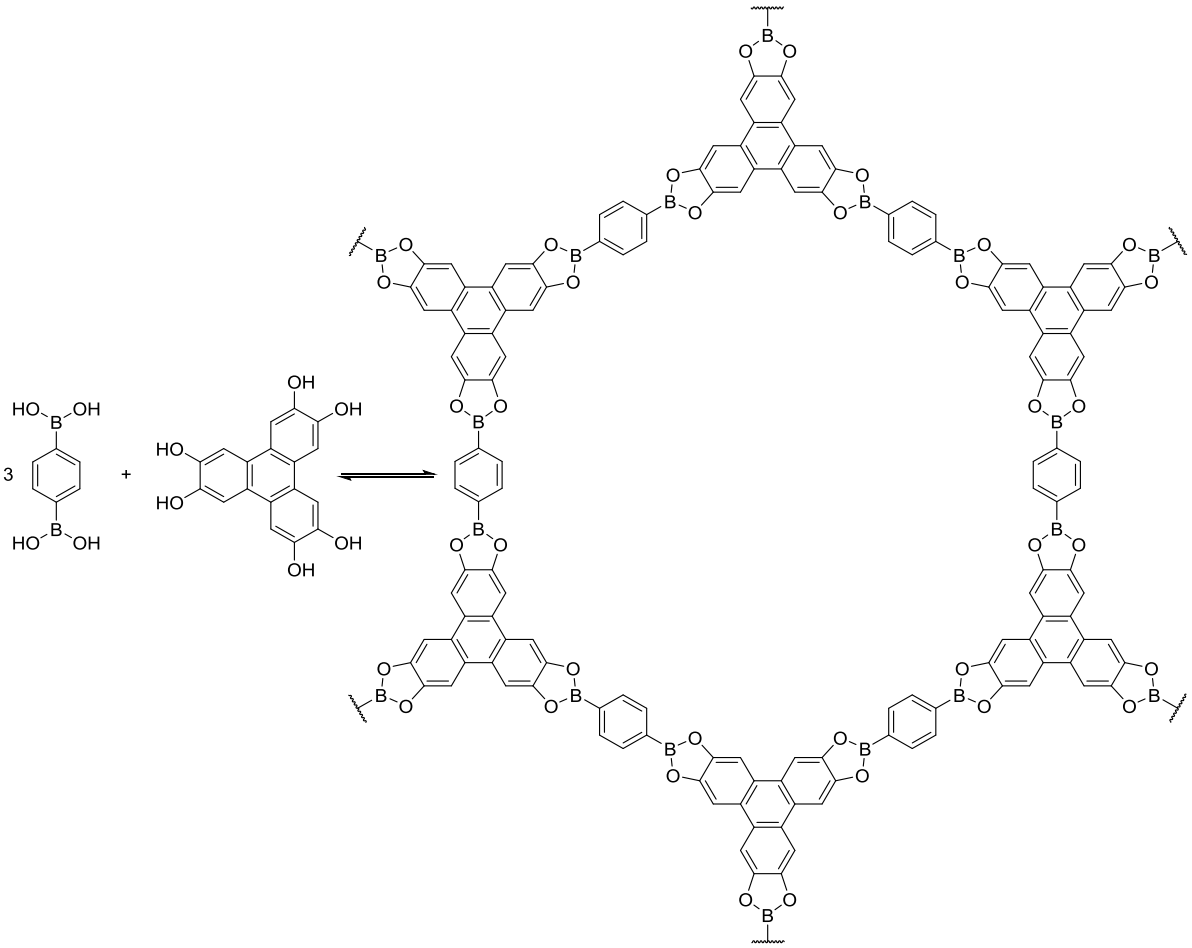

Figure 1.4 Reaction scheme for the formation of COF-5. Condensation of benzenediboronic acid and hexahydroxytriphenylene (HHTP) yields a hexagonal framework.

As organic synthesis offers a mine of possibilities regarding the design of new building blocks, the principles of reticular chemistry enable the realisation of a broad range of potential pore geometries and sizes, even allowing for the synthesis of dual-pore networks (Figure 1.5).

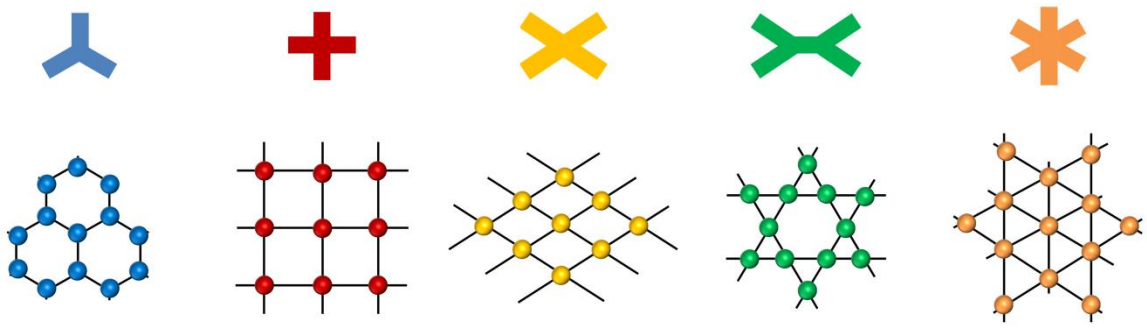

Figure 1.5 Different pore shapes of 2D COFs. The combination of multidentate building blocks together with linear bridging units results in the formation of various pore systems, for instance hexagonal (blue), quadratic (red), pseudo-quadratic/rhombic (yellow), dual-pore/star-shaped (green) or trigonal (orange).

In contrast to MOFs, the COFs mentioned above consist of two-dimensionally (2D) linked aromatic sheets that are not connected through bonds along the third dimension. Instead, they are rather loosely stacked on top of each other, yielding a porous channel system along the stacking direction (Figure 1.6).

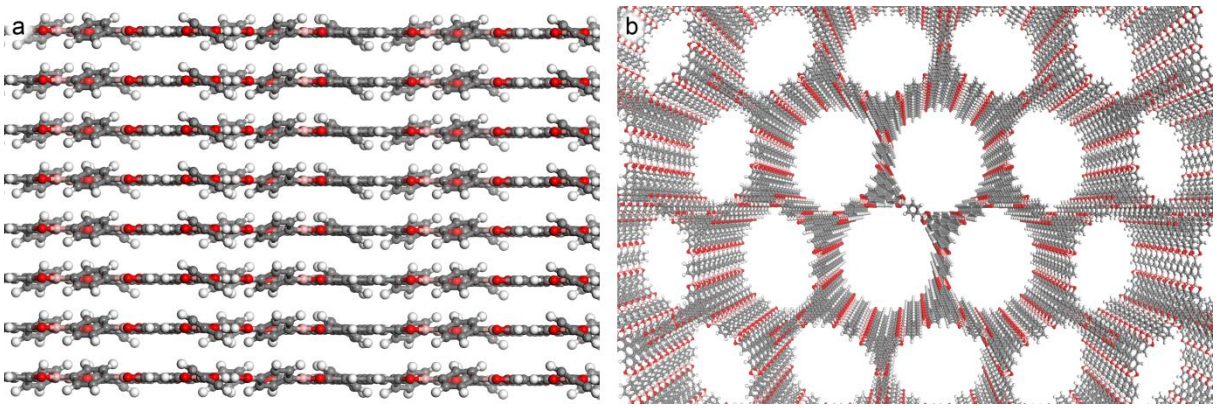

Figure 1.6 Schematic illustration of a 2D COF. Stacking individual COF sheets upon each other (**a**) results in the formation of a porous channel system along the stacking direction (**b**).

Noncovalent, attractive interactions between π-systems are considered to control phenomena such as base-base interactions in DNA,[11] folding of proteins[12] or the packing behaviour of large aromatic molecules.[13] Thus, "π-π interactions" are commonly understood to be responsible for the stacking of aromatic 2D COF sheets. However, the nature of these interactions is still discussed controversially in the community.

In the 1990ies, an electrostatic model for the origin of "π-π interactions" was proposed, emphasising the importance of quadrupole moments regarding the packing behaviour of aromatics systems.[14] However, newer results indicate that the stacking is mainly dominated by van-der-Waals interactions that can become significantly larger for π-systems compared to their saturated analogues. The flat shape of aromatic molecules allows them to get in closer contact to each other, maximising attractive dispersion components and indicating that the term "π-π interactions" might be a misnomer.[15] Nevertheless, it underlines the importance of aromaticity regarding the design and synthesis of new building blocks.

Apart from stacked 2D COFs, systems with a larger degree of similarity to MOFs can be realised by applying non-flat, three-dimensional (3D) molecular building blocks in COF synthesis.[16]

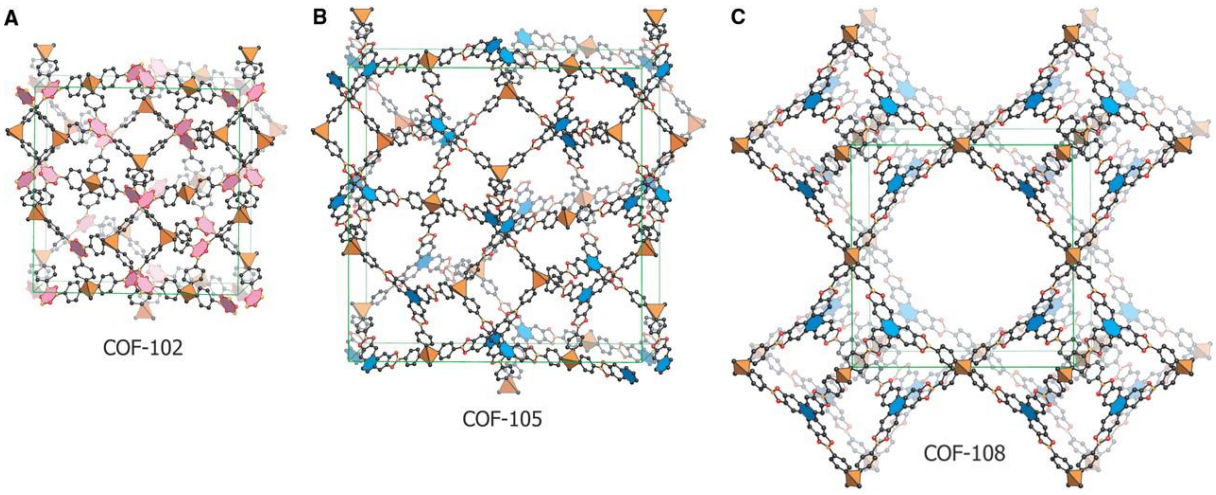

Figure 1.7 Simulated structures of selected 3D COFs. Structures of the boroxine-based COF-102, formed by the self-condensation of a tetrahedral tetraboronic acid and the boronate-ester connected COF-105 and COF-108, which are realised through the condensation of tetrahedral tetraboronic acids and HHTP.[16]

The resulting 3D COFs are connected covalently in all directions and exhibit a large surface area due to the full accessibility of all building blocks.

Their high surface areas of up to 2000 $m^2 g^{-1}$ for 2D COFs[17] and up to 4200 $m^2 g^{-1}$ for 3D COFs[16] together with tunable pore sizes ranging from 1.6 nm[18] (microporous) to 5.3 nm[19] (mesoporous) make COFs ideal candidates for gas storage, gas separation or catalysis. Additionally, fully open channel systems that allow for the easy ad- and desorption of guest molecules offer an ideal platform for sensing applications. Furthermore, the extended aromaticity of the 2D COF sheets and a very small interlayer distance enable charge-transport in-plane as well as along the stacks (see Chapter 1.4), making COFs attractive candidates for electronic applications.

1.3 Bond types in COF chemistry

Of key importance when aiming to synthesize such crystalline polymers is a reversible bond formation mechanism. By introducing – at least to some extent – an equilibrium between the attachment and detachment of the linkers within COF formation, building blocks incorporated at a "wrong" position can be detached again, allowing the network to self-heal.

Bond types that have been widely studied and established in the COF field (Figure 1.6) within the last years are boroxines,[10] [20] boronate esters,[21] [22] [23] [24] imines,[25] [26] [27] [28] [29] imides,[30] [31] triazines[32] [33] and hydrazones,[34] [35] whereas the degree of reversibility of the respective mechanism under synthesis conditions plays an important role regarding the stability and long-range order of the resulting network.

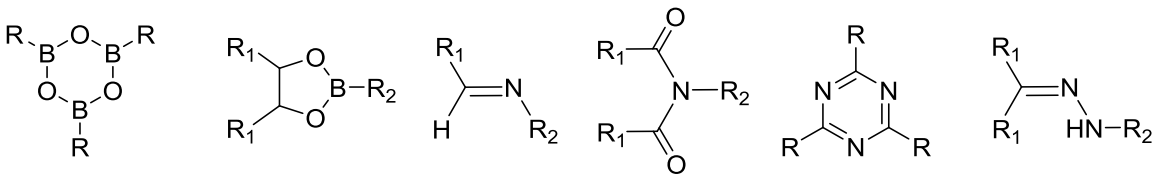

Figure 1.8 Selected bond types commonly used in COF synthesis.

While boronate esters can condense and hydrolyse easily at room temperature[36] – rendering the respective COFs prone to degradation already under ambient conditions![37] – , triazine-linked COFs need to be synthesized in $ZnCl_2$ melts at temperatures of around 400 °C[33]. These conditions can easily lead to the decomposition of more complex organic linkers and typically yield networks of limited crystallinity.[38] Stable bonds that are formed under moderate reaction conditions are thus very valuable for the COF field, making the multi-step imine condensation (Figure 1.9) the bond type of choice within this thesis.

The first step of the acid-catalysed imine formation is the protonation of the aldehyde, weakening the C=O bond and making the carbonyl carbon atom more electrophilic. This electrophilic carbon atom can now be attacked in the second step by a nucleophile, the amine nitrogen atom. This is however the rate-determining step, because primary amines are generally more basic than the carbonyl oxygen, resulting in a protonation of the amine itself and making it non-nucleophilic.[39] The following proton transfer generates the good leaving group H_2O^+ and frees the nitrogen lone pair. Elimination of H_2O results in the generation of the positively charged iminium, whereas the last deprotonation step releases the neutral imine.

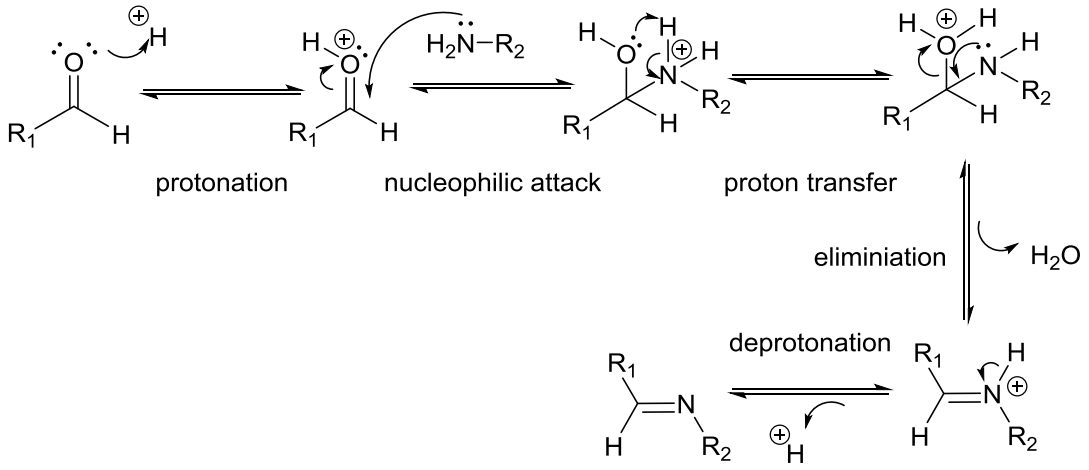

Figure 1.9 Acid-catalysed imine-formation.

The imine formation, which can also be performed under base-catalysed conditions, is fully reversible, allowing for the recovery of the initial starting materials aldehyde and amine, and is crucial for the synthesis of crystalline polymers such as COFs.

This healing mechanism applies only to a few attachment and detachment cycles in COF synthesis, before linkers and thus potential defects are ultimately trapped in the growing network. It is however possible to guide the building blocks to the right attachment sites by applying molecular puzzle pieces that can be stacked upon each other at one single, predefined position. Chapter 2 and 3 of this thesis focus on the elaboration of two concepts that help to maintain long-range order in COFs beyond the means of pure reversibility.

1.4 COFs as electroactive materials

The discovery that stacked, disc-like organic molecules are capable of anisotropically transporting photogenerated charge-carriers and optical excitations along the packing direction[40] led to a growing interest in this class of unique materials over the last 25 years, with potential applications ranging from 1D confined nanowires for miniaturized devices[41] through organic light emitting diodes[42] to photovoltaic devices.[43] These so-called discotic liquid crystals consist of self-assembling aromatic core units that are equipped with flexible alkyl chains, keeping the stacks separated and electrically insulated, thus guaranteeing an uniaxial pathway for the transport of charge carriers or optical excitations.

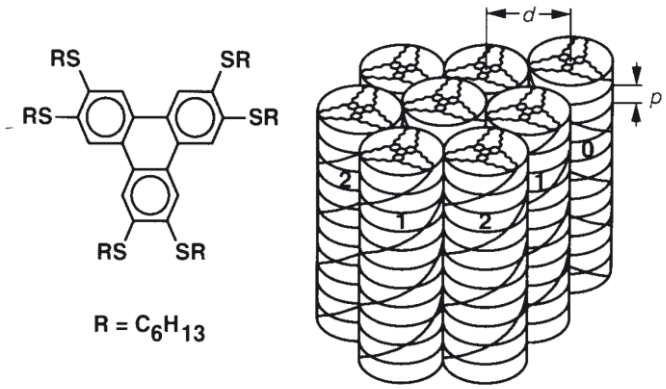

Figure 1.10 Discotic liquid crystal. Illustration of the packing behaviour of the first conductive discotic liquid crystal based on hexahexylthiotriphenylene (HHTT).[40]

For instance, triphenylene-fused triindole liquid crystals feature impressive hole mobilities of up to 2.8 $cm^2\ V^{-1}\ s^{-1}$ obtained from space charge limited current (SCLC) measurements,[44] thus surpassing amorphous silicon (approx. 1 $cm^2\ V^{-1}\ s^{-1}$) which is currently used in flat panel displays.[45] Other molecules that form these conductive, self-healing columnar mesophases are perylenes[42] and perylene-diimides,[43] [46] coronenes,[43] [47] and triphenylenes, [41, 42, 47-51] the latter being the most studied class of aromatic systems and not surprisingly blue-print or inspiration in COF design.

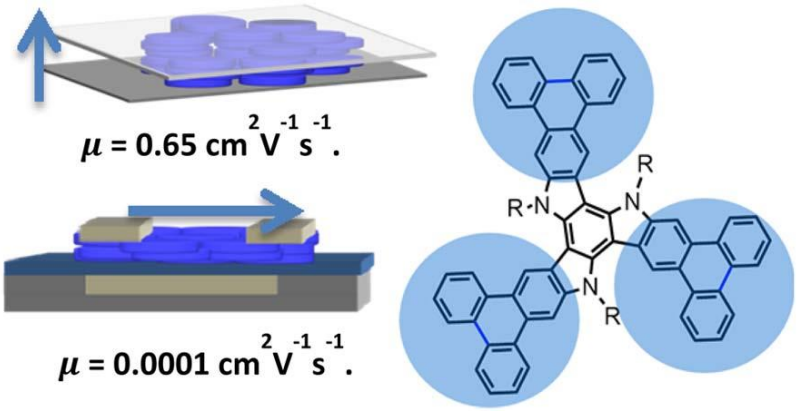

Figure 1.11 Illustration of the highly anisotropic mobilities of a triphenylene-fused triindole liquid crystal.[52]

The transport of charges along the other two remaining dimensions, parallel to the aromatic system, is already widely studied in organic photovoltaics (OPVs). Here, (hetero)aromatic building blocks such as alkyl-substituted thiophenes, benzodithiophenes, benzothiadiazoles or a combination thereof are polymerised to yield the active component of a solar cell (Figure 1.12). In principle, the conjugated character of these polymers offers two simple advantages: As the π-system is extended, the absorption capabilities are enhanced. Furthermore, electrons and holes can move along the polymer chain.

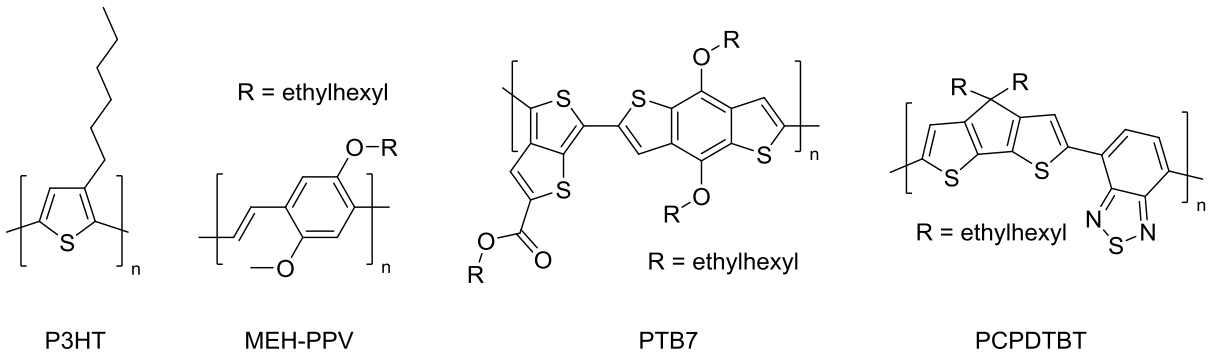

Figure 1.12 Structures of selected polymers used in organic photovoltaics.

However, organic solar cells consisting of only one single component typically exhibit low quantum yields and power conversion efficiencies. As organic molecules usually have low dielectric constants, the generation of free charge carriers is difficult because of strong Coulomb interaction between electrons and holes. The binding energy of the exciton cannot be easily overcome at room temperature and in order to facilitate the separation of the photogenerated charges, an additional electron acceptor molecule is needed.[53] Mixing the

conjugated polymer with fullerene acceptor molecules led to the first bulk-heterojunction organic solar cell, which exhibits a drastically increased photon-to-electron conversion efficiency.[54]

Another sophisticated approach towards higher efficiencies relies on maximising the degree of order of the polymer chains.[55] By combining the concepts mentioned above, bulk-heterojunctions consisting of fullerene acceptors with conjugated π-systems that are stacked in the third dimension could be realised (Figure 1.13). Their superior power conversion efficiencies of up to 8.7% are attributed to the closely packed, highly ordered and oriented structure of the active layer.[56]

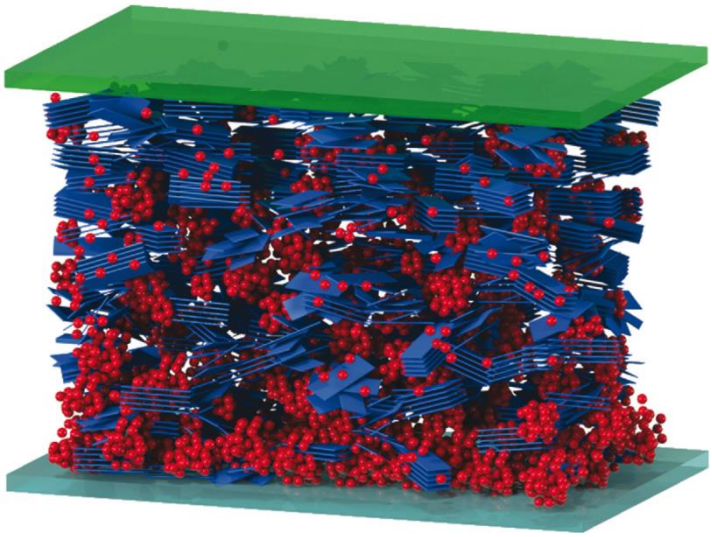

Figure 1.13 Schematic illustration of the ordered polymer (blue):fullerene (red) blend with enhanced power conversion efficiencies. The bulk heterojunctions consists of a blend of poly[N-(2-hexyldodecyl)-2,2′-bithiophene-3,3′-dicarboximide-*alt*-5,5-(2,5-bis(3-decylthiophen-2-yl)-thiophene)] (PBTI3T) and $PC_{71}BM$.[56]

Viewed from the structural perspective, 2D COFs are the ultimate combination of both stacked and conjugated π–systems, offering spatial control in all three dimensions and thus allowing for fine-tuning the electroactive properties. The porous structure of these crystalline framework materials enables the incorporation of acceptor molecules like fullerenes to form structured heterojunctions, thus facilitating the separation of generated charge carriers. Exploring this attractive paradigm, the first COF-based photovoltaic device could be realised by infiltrating a thienothiophene-HHTP boronic acid COF with PCBM, proving that light-induced charge-separation is possible with this class of materials.[57]

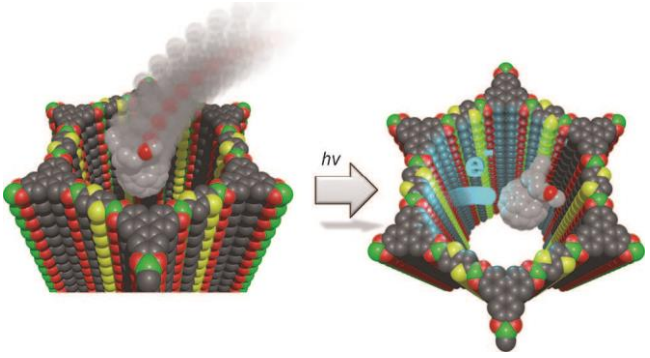

Figure 1.14 A COF:fullerene bulk heterojunctions. Infiltrating a thienothiophene-HHTP boronic acid COF with PCBM allows for the generation of light-induced charge carriers.[57]

Furthermore, the unique opportunity of building COFs based on a modular principle enables the incorporation of electron-donating and electron-accepting subunits within the same system, resulting in extremely well-ordered donor-acceptor-heterojunctions at the molecular level.[19] [23] This way, a first photovoltaic device realised by our group based on porphyrin and HHTP with matching HOMO and LUMO energy levels yielded promising external quantum efficiencies.[58] The convenience of assembling COFs from tailor-made linkers enables even fine tuning of the electronic properties by implementing only small changes in the linker design: Modifying the backbone of oligothiophene-bridged COFs with moieties that differ in their electron density, we were able to drastically influence the lifetimes of photogenerated charge carriers in these materials.[59]

Growing COFs as oriented thin films opens up new opportunities for studying the charge transport characteristics both along the stack as well as in-plane. For COF films based on boronate esters, the resulting mobilities are typically very anisotropic: Whereas charge transport along the column is possible and depends on the thickness of the respective thin film, the in-plane conductivity is expected to be low due to the insulating boronate ester bond.[60] When opting for conjugated bond types such as imines,[61] these limitations might be overcome, possibly enhancing the overall mobilities in COFs and opening up new opportunities for applications. For instance, we have developed an easy and straightforward method to grow imine-linked COFs as highly oriented thin films, which enabled us to realize the first COF-based, spectrally switchable photodetector.[62]

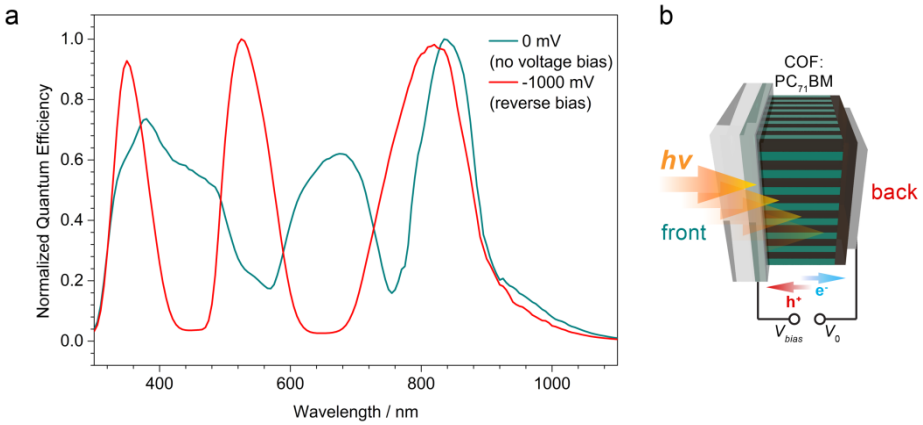

Figure 1.15 A spectrally switchable COF photodetector. (**a**) Comparing the quantum efficiencies at short circuit (green) and under reverse bias (red) reveals that the photodetector can be switched. (**b**) Illustration of the photodetector device.[62]

Future research could now focus on fine-tuning the charge transport properties along the stack by modifying packing distance and offset of the stacks, thus very likely influencing the degree of π-overlap and overall mobility. Regarding in-plane charge migration, the implementation of conjugated bond-types such as imines will possibly act as a game changer for realising new COF-based OPVs.

1.5 References

[1] O. M. Yaghi, M. O'Keeffe, N. W. Ockwig, H. K. Chae, M. Eddaoudi, J. Kim, *Nature* **2003**, *423*, 705.

[2] H. Li, M. Eddaoudi, M. O'Keeffe, O. M. Yaghi, *Nature* **1999**, *402*, 276.

[3] S. S. Kaye, A. Dailly, O. M. Yaghi, J. R. Long, *J. Am. Chem. Soc.* **2007**, *129*, 14176-14177.

[4] M. Eddaoudi, J. Kim, N. Rosi, D. Vodak, J. Wachter, M. O'Keeffe, O. M. Yaghi, *Science* **2002**, *295*, 469-472.

[5] O. K. Farha, I. Eryazici, N. C. Jeong, B. G. Hauser, C. E. Wilmer, A. A. Sarjeant, R. Q. Snurr, S. T. Nguyen, A. Ö. Yazaydın, J. T. Hupp, *J. Am. Chem. Soc.* **2012**, *134*, 15016-15021.

[6] *Chem. Soc. Rev.* **2014**, *43*, 6173-6174.

[7] P. Deria, J. E. Mondloch, O. Karagiaridi, W. Bury, J. T. Hupp, O. K. Farha, *Chem. Soc. Rev.* **2014**, *43*, 5896-5912.

[8] Y.-H. Shih, Y.-C. Kuo, S. Lirio, K.-Y. Wang, C.-H. Lin, H.-Y. Huang, *Chem. Eur. J.* **2017**, *23*, 42-46.

[9] N. C. Burtch, H. Jasuja, K. S. Walton, *Chem. Rev.* **2014**, *114*, 10575-10612.

[10] A. P. Côté, A. I. Benin, N. W. Ockwig, M. O'Keeffe, A. J. Matzger, O. M. Yaghi, *Science* **2005**, *310*, 1166-1170.

[11] W. Saenger, *Principles of Nucleic Acid Structure*, Spinger-Verlag, New York, **1984**.

[12] S. K. Burley, G. A. Petsko, *Adv. Protein Chem.* **1988**, *39*, 125-189.

[13] G. R. Desiraju, A. Gavezzotti, *Chem. Commun.* **1989**, 621-623.

[14] C. A. Hunter, J. K. M. Sanders, *J. Am. Chem. Soc.* **1990**, *112*, 5525-5534.

[15] S. Grimme, *Angew. Chem. Int. Ed.* **2008**, *47*, 3430-3434.

[16] H. M. El-Kaderi, J. R. Hunt, J. L. Mendoza-Cortés, A. P. Côté, R. E. Taylor, M. O'Keeffe, O. M. Yaghi, *Science* **2007**, *316*, 268-272.

[17] M. Calik, T. Sick, M. Dogru, M. Döblinger, S. Datz, H. Budde, A. Hartschuh, F. Auras, T. Bein, *J. Am. Chem. Soc.* **2016**, *138*, 1234-1239.

[18] L. Ascherl, T. Sick, J. T. Margraf, S. H. Lapidus, M. Calik, C. Hettstedt, K. Karaghiosoff, M. Döblinger, T. Clark, K. W. Chapman, F. Auras, T. Bein, *Nature Chem.* **2016**, *8*, 310-316.

[19] S. Jin, K. Furukawa, M. Addicoat, L. Chen, S. Takahashi, S. Irle, T. Nakamura, D. Jiang, *Chem. Sci.* **2013**, *4*, 4505-4511.

[20] R.-N. Wang, X.-R. Zhang, S.-F. Wang, G.-S. Fu, J.-L. Wang, *PCCP* **2016**, *18*, 1258-1264.

[21] E. L. Spitler, W. R. Dichtel, *Nature Chem.* **2010**, *2*, 672-677.

[22] E. L. Spitler, B. T. Koo, J. L. Novotney, J. W. Colson, F. J. Uribe-Romo, G. D. Gutierrez, P. Clancy, W. R. Dichtel, *J. Am. Chem. Soc.* **2011**, *133*, 19416-19421.

[23] X. Feng, L. Chen, Y. Honsho, O. Saengsawang, L. Liu, L. Wang, A. Saeki, S. Irle, S. Seki, Y. Dong, D. Jiang, *Adv. Mater.* **2012**, *24*, 3026-3031.

[24] B. J. Smith, W. R. Dichtel, *J. Am. Chem. Soc.* **2014**, *136*, 8783-8789.

[25] F. J. Uribe-Romo, J. R. Hunt, H. Furukawa, C. Klock, M. O'Keeffe, O. M. Yaghi, *J. Am. Chem. Soc.* **2009**, *131*, 4570-4571.

[26] S. Wan, F. Gándara, A. Asano, H. Furukawa, A. Saeki, S. K. Dey, L. Liao, M. W. Ambrogio, Y. Y. Botros, X. Duan, S. Seki, J. F. Stoddart, O. M. Yaghi, *Chem. Mater.* **2011**, *23*, 4094-4097.

[27] S. Kandambeth, D. B. Shinde, M. K. Panda, B. Lukose, T. Heine, R. Banerjee, *Angew. Chem. Int. Ed.* **2013**, *52*, 13052-13056.

[28] S. Dalapati, M. Addicoat, S. Jin, T. Sakurai, J. Gao, H. Xu, S. Irle, S. Seki, D. Jiang, *Nature Commun.* **2015**, *6*.

[29] J. Guo, Y. Xu, S. Jin, L. Chen, T. Kaji, Y. Honsho, M. A. Addicoat, J. Kim, A. Saeki, H. Ihee, S. Seki, S. Irle, M. Hiramoto, J. Gao, D. Jiang, *Nature Commun.* **2013**, *4*.

[30] Q. Fang, Z. Zhuang, S. Gu, R. B. Kaspar, J. Zheng, J. Wang, S. Qiu, Y. Yan, *Nature Commun.* **2014**, *5*.

[31] S. Wu, S. Gu, A.-Q. Zhang, G. Yu, Z. Wang, c. Pan, X. Jian, *J. Mater. Chem. A* **2014**.

[32] P. Katekomol, J. Roeser, M. Bojdys, J. Weber, A. Thomas, *Chem. Mater.* **2013**, *25*, 1542-1548.

[33] P. Kuhn, M. Antonietti, A. Thomas, *Angew. Chem. Int. Ed.* **2008**, *47*, 3450-3453.

[34] F. J. Uribe-Romo, C. J. Doonan, H. Furukawa, K. Oisaki, O. M. Yaghi, *J. Am. Chem. Soc.* **2011**, *133*, 11478-11481.

[35] L. Stegbauer, K. Schwinghammer, B. V. Lotsch, *Chem. Sci.* **2014**, *5*, 2789-2793.

[36] D. D. Medina, J. M. Rotter, Y. Hu, M. Dogru, V. Werner, F. Auras, J. T. Markiewicz, P. Knochel, T. Bein, *J. Am. Chem. Soc.* **2015**, *137*, 1016-1019.

[37] J.-R. Song, J. Sun, J. Liu, Z.-T. Huang, Q.-Y. Zheng, *Chem. Commun.* **2014**, *50*, 788-791.

[38] S. Hug, M. E. Tauchert, S. Li, U. E. Pachmayr, B. V. Lotsch, *J. Mater. Chem.* **2012**, *22*, 13956-13964.

[39] M. Ciaccia, S. Di Stefano, *Org. Biomol. Chem.* **2015**, *13*, 646-654.

[40] D. Adam, F. Closs, T. Frey, D. Funhoff, D. Haarer, P. Schuhmacher, K. Siemensmeyer, *Phys. Rev. Lett.* **1993**, *70*, 457-460.

[41] M. Steinhart, S. Zimmermann, P. Göring, A. K. Schaper, U. Gösele, C. Weder, J. H. Wendorff, *Nano Lett.* **2005**, *5*, 429-434.

[42] I. Seguy, P. Jolinat, P. Destruel, J. Farenc, R. Mamy, H. Bock, J. Ip, T. P. Nguyen, *J. Appl. Phys.* **2001**, *89*, 5442-5448.

[43] L. Schmidt-Mende, A. Fechtenkötter, K. Müllen, E. Moons, R. H. Friend, J. D. MacKenzie, *Science* **2001**, *293*, 1119-1122.

[44] A. Benito-Hernández, U. K. Pandey, E. Cavero, R. Termine, E. M. García-Frutos, J. L. Serrano, A. Golemme, B. Gómez-Lor, *Chem. Mater.* **2013**, *25*, 117-121.

[45] C. Ruiz, E. M. García-Frutos, G. Hennrich, B. Gómez-Lor, *J Phys Chem Lett* **2012**, *3*, 1428-1436.

[46] Z. Chen, V. Stepanenko, V. Dehm, P. Prins, L. D. A. Siebbeles, J. Seibt, P. Marquetand, V. Engel, F. Würthner, *Chem. Eur. J.* **2007**, *13*, 436-449.

[47] V. Lemaur, D. A. da Silva Filho, V. Coropceanu, M. Lehmann, Y. Geerts, J. Piris, M. G. Debije, A. M. van de Craats, K. Senthilkumar, L. D. A. Siebbeles, J. M. Warman, J.-L. Brédas, J. Cornil, *J. Am. Chem. Soc.* **2004**, *126*, 3271-3279.

[48] D. Adam, P. Schuhmacher, J. Simmerer, L. Häussling, K. Siemensmeyer, K. H. Etzbachi, H. Ringsdorf, D. Haarer, *Nature* **1994**, *371*, 141.

[49] K. Senthilkumar, F. C. Grozema, F. M. Bickelhaupt, L. D. A. Siebbeles, *J. Chem. Phys.* **2003**, *119*, 9809-9817.

[50] J. Simmerer, B. Glüsen, W. Paulus, A. Kettner, P. Schuhmacher, D. Adam, K.-H. Etzbach, K. Siemensmeyer, J. H. Wendorff, H. Ringsdorf, D. Haarer, *Adv. Mater.* **1996**, *8*, 815-819.

[51] A. Bayer, J. Hübner, J. Kopitzke, M. Oestreich, W. Rühle, J. H. Wendorff, *J. Phys. Chem. B* **2001**, *105*, 4596-4602.

[52] C. Ruiz, U. K. Pandey, R. Termine, E. M. García-Frutos, G. López-Espejo, R. P. Ortiz, W. Huang, T. J. Marks, A. Facchetti, M. C. Ruiz Delgado, A. Golemme, B. Gómez-Lor, *ACS Appl. Mater. Interfaces* **2016**, *8*, 26964-26971.

[53] M. C. Scharber, N. S. Sariciftci, *Prog. Polym. Sci.* **2013**, *38*, 1929-1940.

[54] G. Yu, J. Gao, J. C. Hummelen, F. Wudl, A. J. Heeger, *Science* **1995**, *270*, 1789-1791.

[55] M. Brinkmann, *J. Polym. Sci., Part B: Polym. Phys.* **2011**, *49*, 1218-1233.

[56] X. Guo, N. Zhou, S. J. Lou, J. Smith, D. B. Tice, J. W. Hennek, R. P. Ortiz, J. T. L. Navarrete, S. Li, J. Strzalka, L. X. Chen, R. P. H. Chang, A. Facchetti, T. J. Marks, *Nature Photonics* **2013**, *7*, 825.

[57] M. Dogru, M. Handloser, F. Auras, T. Kunz, D. Medina, A. Hartschuh, P. Knochel, T. Bein, *Angew. Chem. Int. Ed.* **2013**, *52*, 2920-2924.

[58] M. Calik, F. Auras, L. M. Salonen, K. Bader, I. Grill, M. Handloser, D. D. Medina, M. Dogru, F. Loebermann, D. Trauner, A. Hartschuh, T. Bein, *J. Am. Chem. Soc.* **2014**, 17802-17807.

[59] N. Keller, D. Bessinger, S. Reuter, M. Calik, L. Ascherl, F. C. Hanusch, F. Auras, T. Bein, *J. Am. Chem. Soc.* **2017**, *139*, 8194-8199.

[60] D. D. Medina, M. L. Petrus, A. N. Jumabekov, J. T. Margraf, S. Weinberger, J. M. Rotter, T. Clark, T. Bein, *ACS Nano* **2017**, *11*, 2706-2713.

[61] M. L. Petrus, R. K. M. Bouwer, U. Lafont, D. H. K. Murthy, R. J. P. Kist, M. L. Bohm, Y. Olivier, T. J. Savenije, L. D. A. Siebbeles, N. C. Greenham, T. J. Dingemans, *Polymer Chemistry* **2013**, *4*, 4182-4191.

[62] D. Bessinger, L. Ascherl, F. Auras, T. Bein, *J. Am. Chem. Soc.* **2017**, *139*, 12035-12042.

2 Characterisation Techniques

2.1 X-ray Diffraction

X-ray diffraction (XRD) is one of the most powerful tools to determine the structure of crystalline materials and the first crucial step for solving the structure of a COF.

X-rays are generated when a beam of energetic charged particles such as electrons is directed onto a metal target. Electrons lose their energy by collision with the metal, changing their momentum, which results in the emission of a continuous radiation (Bremsstrahlung). However electrons with energy beyond a certain threshold can knock out inner-shell electrons from the target metal. When these voids are filled with electrons from higher energy levels, characteristic X-ray radiation is emitted. Their energy is hereby equal to the energy difference between the respective shells. In order to produce a monochromatic beam, the X-rays are filtered and collimated towards the sample.[1]

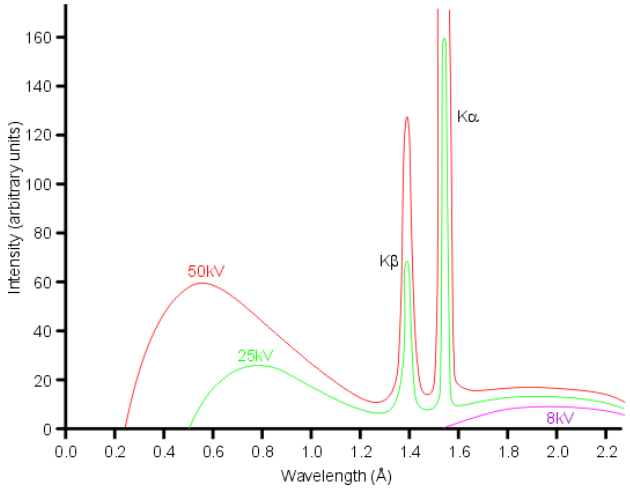

Figure 2.1 X-ray spectra from a copper target at different acceleration voltages.[2] The spectra of the continuous radiation (smooth bumps) are dependent on the acceleration voltages (red: 50 kV, green 25 kV), whereas the wavelength of the characteristic X-ray radiation (sharp peaks) remains unaffected. Beneath a certain voltage threshold, no characteristic X-ray radiation can be observed (purple: 8 kV).

The process by which a beam of light or other system of waves is spread out as a result of passing through a narrow aperture or across an edge, typically accompanied by interference between the wave forms produced.

Diffraction is a process by which a wave is spread out when passing a small aperture or edge. When this obstacle consists of a periodic array of objects or slits, the diffracted waves will interfere with each other, generating distinct intensity patterns. The effect of the diffraction is greatest when the wavelength and the width of the gap or object have approximately the same dimension. As the wavelength of X-rays are with 10 pm – 10 nm in the range of lattice constants in a crystal, the crystal lattice acts as a three-dimensional diffraction grating for X-rays, where the X-rays are diffracted by the electron shells of the irradiated atoms of the crystal. Depending on the distance of the atoms, this results in specific angles of diffraction. Constructive interference can only occur when parallel X-rays are phase-separated by an integer number *n*. For X-rays diffracted by a crystal lattice, this event happens when the Bragg equation is fulfilled:

$$n\lambda = 2dsin\theta$$

This equation connects the lattice spacing d and the diffraction angle θ with the wavelength λ of the X-rays and is used to determine the distance of lattice planes in the crystal:

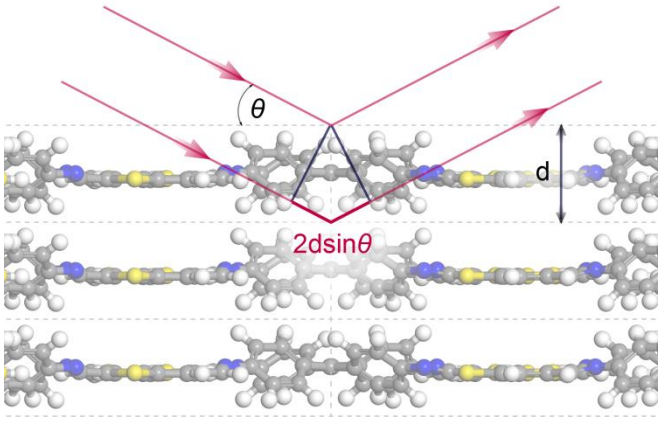

Figure 2.2 Schematic illustration of the Bragg equation. Constructive interference only occurs when the path difference 2dsinθ (dark pink) between two X-rays (light pink) is an integer of the wavelength.

The X-rays that interfere constructively are registered by a detector, whereby their intensity is plotted against 2θ.[3]

2.2 Grazing-incidence X-ray Scattering

Analysing thin films with conventional XRD scanning methods is difficult, as the signal from the film is very weak compared to a intense signal from the substrate underneath. Furthermore, obtaining detailed information about the preferred orientation of crystalline domains within the film, which is crucial for instance for the analysis of COFs grown on substrates, is not straight-forward. Thus, grazing-incidence X-ray scattering is the method of choice when investigating the nanoscale structure of thin films.

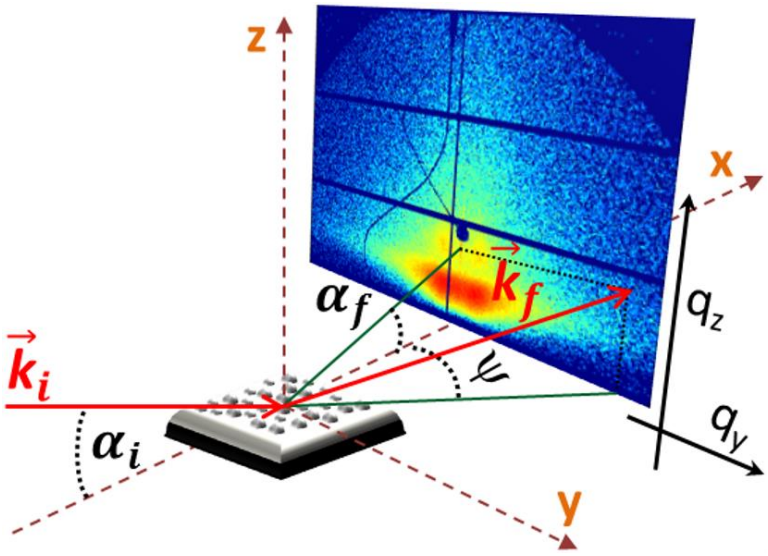

Figure 2.3 Illustration of the scattering geometry in a small-angle grazing-incidence scattering experiment.[4]

In a grazing-incidence X-ray scattering experiment, a monochromatic X-ray beam with a wavevector k_i is directed onto a surface under a very small incident angle α_i. This angle is typically in the range of the critical angle of the substrate, the angle below which total external reflection of the X-ray beam occurs.. The intensity of the scattered X-rays along k_f is then collected with an area detector as a function of α_f and Ψ. In order to be able to compare data from different setups, the position of the scattering spots is expressed as the wavelength-independent scattering vector q.[4] To further compare these q values to 2θ angles obtained from conventional (P)XRD measurements, they can be transformed via

$$q = \frac{4\pi}{\lambda}\sin(\frac{2\theta}{2})$$

with λ being the wavelength of the incident X-rays.

Grazing-incidence X-ray scattering allows for directly drawing conclusions about the geometry or orientation of crystalline phases. In general, the appearance of scatting spots instead of arcs indicates a preferred orientation of the crystallites on the surface. Figure 2.4 illustrates two extreme orientations of lattice planes and reveals the resulting scattering spots obtained at the 2D detector. When a set of lattice planes is aligned parallel to the substrate surface, the major intensity is obtained at $q_y = 0$. When the set of lattice planes is standing perpendicular to the substrate surface, the scattering spots appear directly at the substrate horizon.

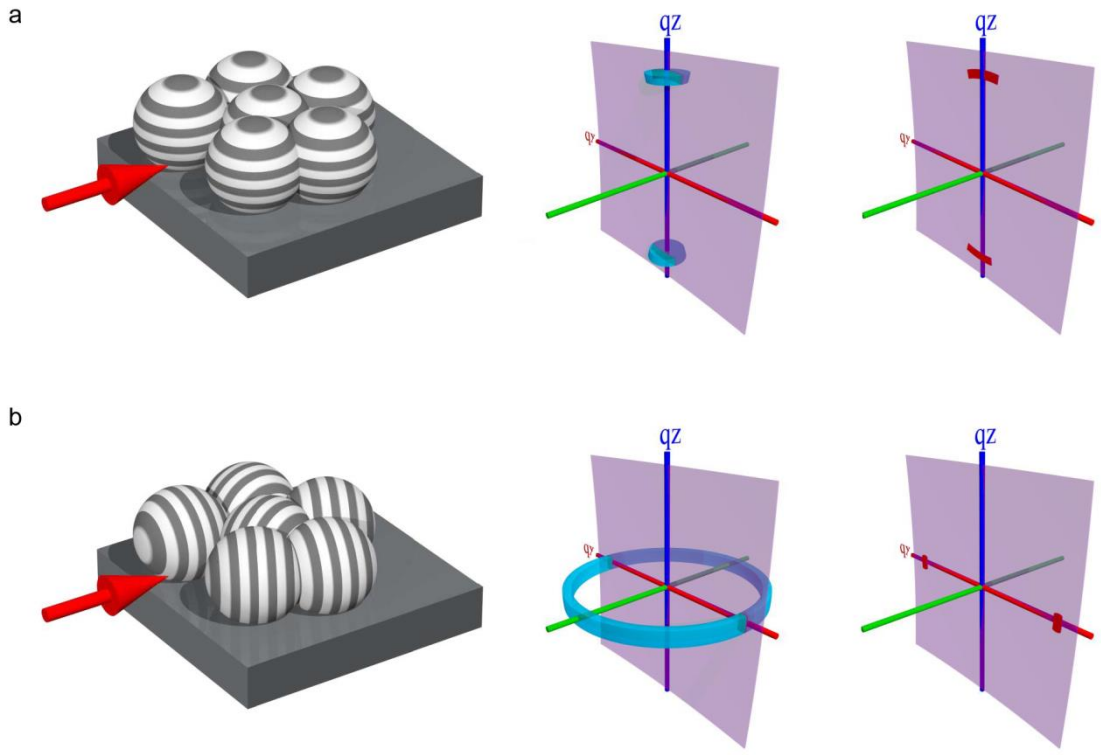

Figure 2.4 Realisation of scattering spots. Illustration of two extreme orientations of a set of lattice planes and the resulting scattering spots on the 2D detector.[5]

By indexing the resulting spots it is possible to draw conclusions about the orientation of COF domains on a substrate.[5]

2.3 Nitrogen sorption

Surface area, pore size distribution and the total pore volume are important features when characterizing a porous material. For COFs, the values obtained from (nitrogen) sorption analysis allow to draw conclusions about the quality of the respective material in terms of pore accessibility when compared to theoretical predictions

IUPAC defines the term "adsorption" as the enrichment of a or more components at an interface, distinguishing between chemisorption and physisorption, the latter being the more general phenomenon of and adsorbable gas getting in close contact to a solid surface: Weak interactions like van-der-Waals forces lead to the occupation of the respective interface, a process which is – in contrast to chemisorption – completely reversible.[6] At temperatures typically corresponding to the boiling point of the respective gas, an adsorption and desorption isotherm is recorded at different relative pressures p/p_0, where p is the equilibrium pressure and p_0 the saturation vapour pressure. Just recently, IUPAC has released a new guideline (Figure 2.3 and Table 2.1) adding two more types to the well-established six classes of sorption isotherms:[7]

Table 2.1 The eight types of sorption isotherms defined by IUPAC. [7]

Isotherm type	**Corresponding material and interpretation of the isotherm**
Ia	Micropore filling at low p/p_0 in mainly narrow micropores
Ib	Micropore filling in wider micropores and narrow mesopores
II	Unrestricted monolayer-multilayer adsorption in non- or macroporour materials
III	Weak interaction with substrate in non- or macroporour materials
IVa	Capillary condensation and hysteresis in mesoporous materials
IVb	Reversible isotherm of mesoporous materials with smaller width
V	Weak interaction with substrate plus pore filling in micro- to mesoporous materials
VI	Layer-by-layer absorption on highly uniform nonporous surface

Pores below a diameter of 2 nm are classified as micropores, a width between 2 and 50 nm corresponds to mesopores and macropores exceed a diameter of 50 nm.

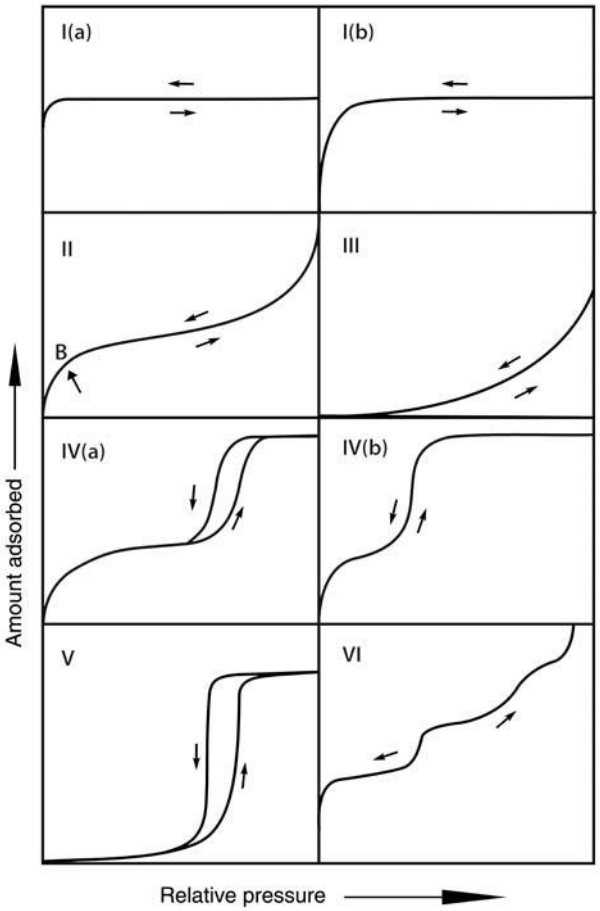

Figure 2.5 The eight major types of sorption isotherms according to the new IUPAC guideline.[7]

Typical COFs feature a pore size range of about 2 to 5 nm, some of them exhibiting distinct, reproducible hysteresis loops, which are typically located in the multilayer range of the isotherm and are associated with capillary condensation (Figure 2.6). In open-ended pores, this hysteresis occurs due to a delayed condensation process that originates from a metastable adsorption film. At this stage, the adsorption branch of the isotherm is not in its thermodynamic equilibrium with nucleation barriers present that prevent the formation of liquid bridges. When the pore is filled with the liquid-like condensate, desorption of the gas molecules occurs easily via an equilibrium vapour-liquid transition without nucleation.[8]

In more complex porous structures where wide pores exhibit only narrow necks, various forms of pore blocking and network effects alter the shape of the desorption branch.[7]

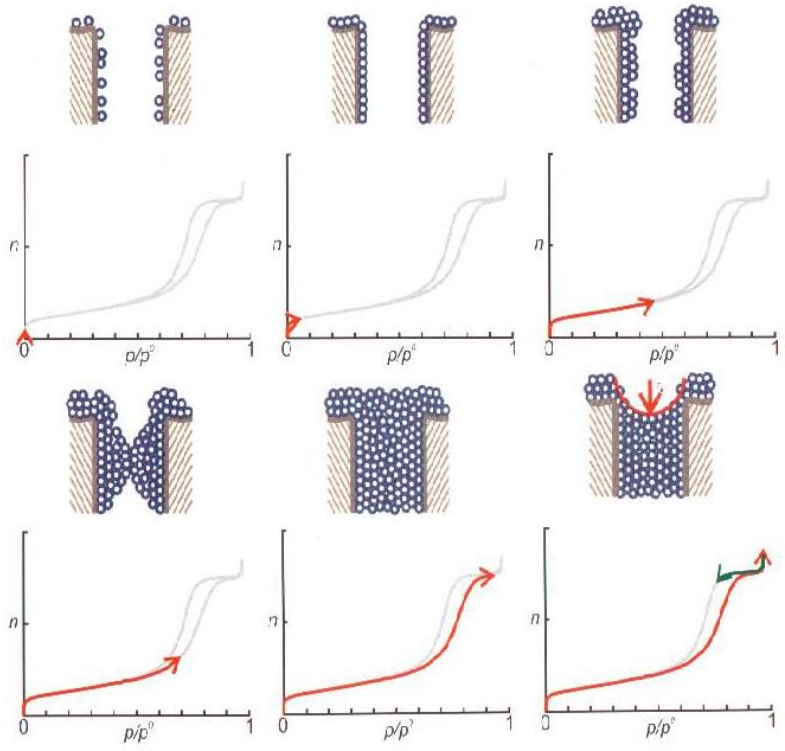

Figure 2.6 Schematic illustration of the capillary condensation process.[9]

Assuming that only monolayer adsorption occurs, all potential adsorption sites are equal, a uniform flat surface and no interaction between adjacent sites or particles, Langmuir presented a first model for the description of monolayer absorption and surface coverage Θ.

$$\theta = \frac{n^a}{n_m^a} = \frac{Kp}{1 + Kp}$$

Here, n^a refers to the adsorbed amount of gas, $n^a{}_m$ is the monolayer capacity, K is a rate constant of the sorption process and p is the respective pressure.

As is it also accounts for the formation of infinite multilayers, the method described by Brunauer, Emmett and Teller (BET) is an extension of the Langmuir model and now widely used to evaluate the surface area of porous materials. The BET theory assumes amongst others that each adsorbed molecule acts as a new adsorption site for a next one. Furthermore, the adsorption energy of the first layer differs from the adsorption energy of the following multilayers. Additionally, adsorbed molecules in the second and higher layers are assumed to behave liquid-like and the upmost layer is in equilibrium with the vapour phase.

To apply the BET method, the isotherm needs to be transformed into the BET plot, which then allows for the calculation of the monolayer capacity $n^a{}_m$ and the parameter *C*, which is exponentially related to the energy of monolayer adsorption.[10] [7]

$$\frac{\frac{p}{p_0}}{n^a(1-\frac{p}{p_0})} = \frac{C-1}{n_m^a C}\left(\frac{p}{p_0}\right) + \frac{1}{n_m^a C}$$

The BET area a_S can be calculated, when the molecular cross-sectional area σ_m representing the average area occupied by the adsorbing molecule and the mass *m* of the porous material are known.

$$a_S(BET) = n_m^a \sigma_m \frac{N_A}{m}$$

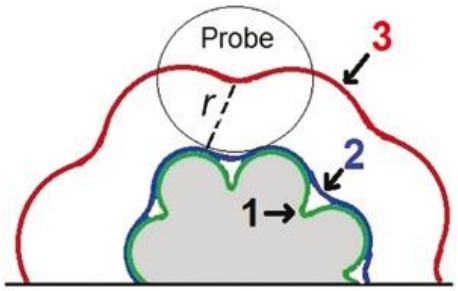

Figure 2.7 Possible surfaces in sorption experiments. 1. Van der Waals surface area, 2. Connolly surface area, 3. accessible surface area.

In order to derive a theoretical surface area from a structure model, the surface is typically defined in one of the following ways (Figure 2.7): The van der Waals surface is the superposition of the van der Waals spheres of all atoms in the structure. The Connolly surface is traced by rolling the bottom of a probe molecule with radius *r* over the van der Waals surface, whereas the accessible surface describes the area that the centre of this probe molecule can cover during the rolling process. The experimentally determined BET surface area is typically in between the simulated Connolly and accessible surface areas, mainly due to differences in the way the experimental and simulated surfaces are obtained. While the Connolly and accessible surfaces are generated using a single probe molecule, the sorption experiment relies on successively populating the sample surface with probe molecules. Especially in narrow pores, already adsorbed probe molecules can impede further adsorption of molecules, leading to a geometry-dependent reduction in probe density that is not

accounted for in the BET model. More reliable simulations should therefore include a continuous occupation with probe molecules instead of rolling one single probe molecule over the structure.

Furthermore, the pore size distribution (PSD) can be assessed from the recorded isotherms. The relative pressure where the pore condensation occurs depends hereby on the pore radius. The Kelvin equation correlates the pore radius r_p and the thickness of the adsorbed multilayer t_c, which is formed before condensation in the pore occurs.

$$\ln\left(\frac{p}{p_0}\right) = \frac{-2\gamma V_m}{RT(r_p - t_c)}$$

Here, γ is the surface tension of the bulk fluid and V_m is the molar liquid volume. This previously widely used equation however underestimates the pore size, as it does not account for enhanced surface forces that occur in narrow mesopores when the pore diameter deceeds 10 nm. Based on molecular simulations or DFT, the adsorbed phase can be described more accurately, and commercial software for a broad range of porous materials with different pore sizes is already available.[7]

2.4 Nuclear Magnetic Resonance Spectroscopy

In order to verify the structure and purity of organic materials like custom-made COF building blocks, nuclear magnetic resonance (NMR) spectroscopy is one of the most powerful analytic techniques, yielding in-depth information about the magnetic properties of atom nuclei within the sample.

When an electric current *I* is moving loop wise, it creates a magnetic dipole moment μ with its magnitude being the product of the area of the loop and the respective current.

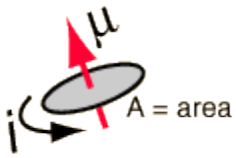

Figure 2.8 Schematic illustration of the origin of the magnetic dipole moment.[11]

$$\mu = IA$$

Considering a proton as a sphere consisting of an infinite amount of these current loops, the loops add up to the nuclear magnetic dipole moment μ_p of the proton. This dipole moment is proportional to the proton's angular momentum. When an infinitesimal current loop is placed into an external magnetic field B_0, it experiences a torque τ.

$$\tau = \mu_P \times B_0$$

This torque tries to align the magnetic momentum with the external magnetic field B_0, but instead of being oriented parallel to the magnetic field, the magnetic momentum will start processing around an axis parallel to the magnetic field lines with a frequency of procession ω, the Larmor frequency.

$$\omega = \frac{2\mu_P B_0}{\hbar}$$

Resulting of two possible spins of the proton, its energy levels will split when an external magnetic field is applied (Zeeman effect). The potential energy *U* which is associated with the magnetic field is

$$U = -\mu B_0$$

which leads to a difference in energy ΔU between the aligned and anti-aligned spins

$$\Delta U = 2\mu B_0$$

whereby the energy of spin-up is decreased by $|\mu B_0|$ and the spin-down is increased by $|\mu B_0|$. A slight population difference between spin-up and spin-down leads to a net or macroscopic magnetisation M_0 that is pointing into the direction of the main magnetic field B_0. When the nuclei are now exposed to radiofrequency radiation at the Larmor frequency by a field B_1, the nuclei in the lower energy state can gain enough energy to transition into the higher, antiparallel energy state. This causes the net magnetisation M_0 to spiral away from B_0: Now the majority of the nuclei are aligned antiparallel to the main field B_0 and precess in-phase, which creates a net transverse magnetization M_{xy} that precesses about B_0.and B_1.

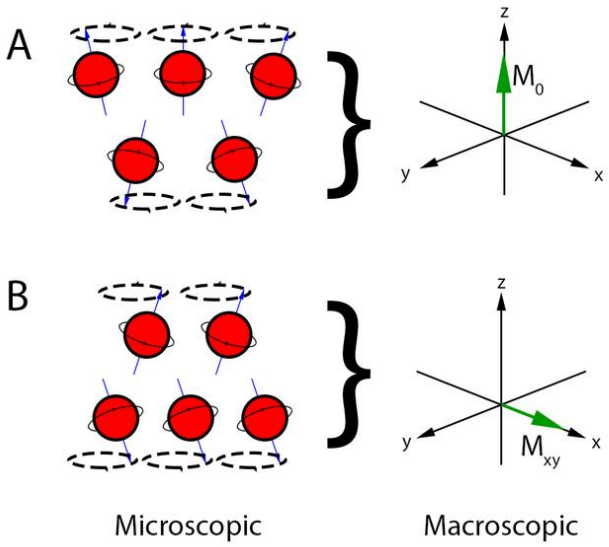

Figure 2.9 Illustration of protons in a magnetic field.[12] Before excitation (A), the majority of the nuclei are aligned parallel to the main magnetic field B_0. When a field B_1 is applied (B), protons in the lower-energy parallel state will be excited to the higher-energy antiparallel state. Furthermore, the protons will precess in-phase.

When the radiofrequency pulse is turned off, the precession about B_1 stops, but the net transversal magnetisation M_{xy} continues to precess about B_0 at the frequency ω and will finally relax back to the equilibrium parallel to B_0. The precession of the net magnetisation M_{xy}, however, creates a fluctuating magnetic field that is used to generate a current in a receiver coil.

The two main relaxation mechanisms after B_1 has been turned off are the spin-lattice (T_1, longitudinal relaxation) and the spin-spin (T_2, transverse relaxation). Here, T_1 describes hereby the reestablishment of the slight population difference between spin-up and spin-down, T_2 represents a dephasing of the coherent in-phase precession and therefore a decay of the transversal magnetization.

The relaxation processes result in a decay of the sinusoidal electromagnetic signal in the receiver coil, the free induction decay (FID). Via fourier transformation, this signal can be converted from the time domain into the frequency domain, yielding the NMR spectrum.

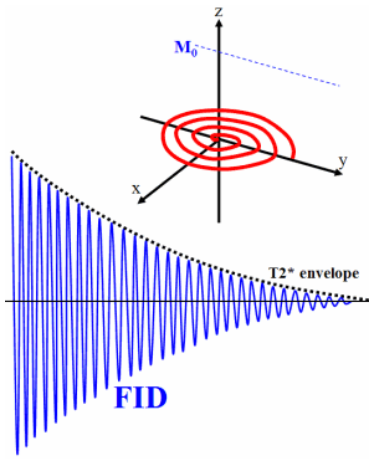

Figure 2.10 The free induction decay.[13]

Instead of using a relative scale that is dependent on the external magnetic field, all NMR signals are referenced to a particular compound

$$\delta = \frac{\omega - \omega_{ref}}{\omega_{ref}}$$

resulting in the B-field independent chemical shift δ. Depending on their chemical and magnetic environments, different protons have different chemical shifts and can thus be distinguished from each other.[14] [15]

2.5 Thermogravimetric analysis

Thermogravimetric analysis (TGA) is used to study the change in mass of a sample over time with increasing temperature.[16] A sample is heated under an atmosphere of choice (synthetic air, inert gasses, vacuum etc.) while a precision balance detects mass-losses or the increase in mass that can happen due to various processes such as evaporation, decomposition, oxidation or reduction. In the COF field, this method is mainly used to compare the temperature stability of different COF materials and allows to detect solvent molecules that have been trapped inside the channel system.

2.6 Infrared spectroscopy

The absorption of discrete frequencies of the electromagnetic spectrum in the infrared (IR) region between 400 cm^{-1} and 4000 cm^{-1} results in the excitation of vibrational - and in case of gases also rotational - modes in covalently bonded groups or atoms, allowing to study the properties of the chemical bonds or the molecular constitution of the respective molecule.[17] This transition from a lower to a higher vibrational state results in a stretching or bending of the covalent bonds, the atoms or groups start moving. Hereby, only vibrational modes that are associated with a temporary change of the electronic dipole can be excited by the electromagnetic field: In order to be capable of absorbing a photon of a certain frequency *v*, the temporary dipole must be able to vibrate at the same frequency.[18]

For the simple mechanistic model of two atoms connected through a spring, the energies E_{Vib} of these vibration frequencies ν_{osc} are

$$E_{Vib} = \mathrm{h}\nu_{osc}(\mathrm{v} + \frac{1}{2})$$

with v = 0, 1, 2,… and Δv = ± 1. There are only discrete levels with an equidistant energy gap in case of the idealised, harmonic oscillator (Figure 2.6, left), whereas the anharmonic oscillator (Figure 2.6, right) considers the effects of bond breaking and accounts for overtone and combination bands with Δv = ± 2, 3,…

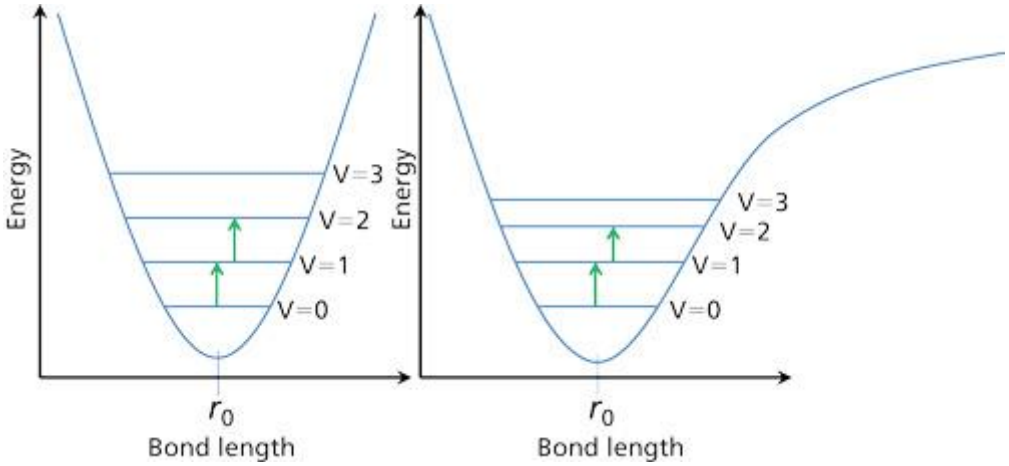

Figure 2.11 Energy diagrams for the harmonic (left) and anharmonic (right) oscillator.[19] In case of the idealised harmonic oscillator (left), the discrete energies are equally spaced. The anharmonic oscillator (right) however allows for a more accurate description of the system.

In COF synthesis, this technique is mainly used to validate the full conversion of starting materials into the respective COFs. Monitoring the disappearance of vibrations assigned to the reactive groups of the starting materials and the appearance of vibrations stemming from the newly formed bond between the building blocks allows for drawing conclusions about the degree of conversion in COF synthesis.

2.7 UV-Vis spectroscopy

Electromagnetic radiation in the range between ultraviolet (UV), visible (Vis) and near IR can cause the excitation of electrons in molecules, making UV-Vis spectroscopy a powerful tool for the investigation of electronic transitions from the ground state to a range of excited states.[17] For an organic molecule, n→π^* (non-binding orbital to unoccupied π-orbital), π→ π^* (occupied π-orbital to unoccupied π-orbital) as well as charge-transfer transitions (respective orbitals have no or only weak overlap) provide the most valuable insights into its electronic structure. In COF synthesis, the occurrence of new or disappearance of former transitions allows to monitor changes in the electronic structure when single building blocks are combined to a framework.

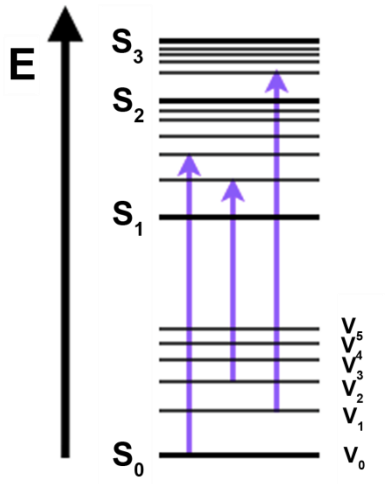

Figure 2.12 Simplified Jablonski diagram of electronic transitions.[20]

When light of a certain wavelength λ passes through a dilute sample, a certain ratio of the initial intensity I_0 is absorbed.

$$A(\lambda) = -log\frac{I(\lambda)}{I_0(\lambda)}$$

A(λ) is hereby related to the concentration of the absorbing species

$$A(\lambda) = -\varepsilon(\lambda)cL$$

This correlation can be used in COF synthesis for the thickness determination of thin films.

To study non-translucent, opaque materials such as COF powders, the diffuse reflectance R of the material diluted with a white standard is measured and approximated with the Kubelka-Munk-model

$$Kubleka - Munk = \frac{(1-R)^2}{2R}$$

to yield a spectrum comparable to a pure absorption spectrum.[21]

2.8 Transmission electron microscopy

Traditional light microscopes are limited to a resolution of around 200 nm. To image smaller objects such as the porous channel system of a COF with wall-to-wall distances below 10 nm, electron microscopy has been established as a powerful tool.[22] As the wavelengths of electrons are significantly shorter than those of visible light, electron microscopes can reach sub-nm resolution and image even on the atomic scale.

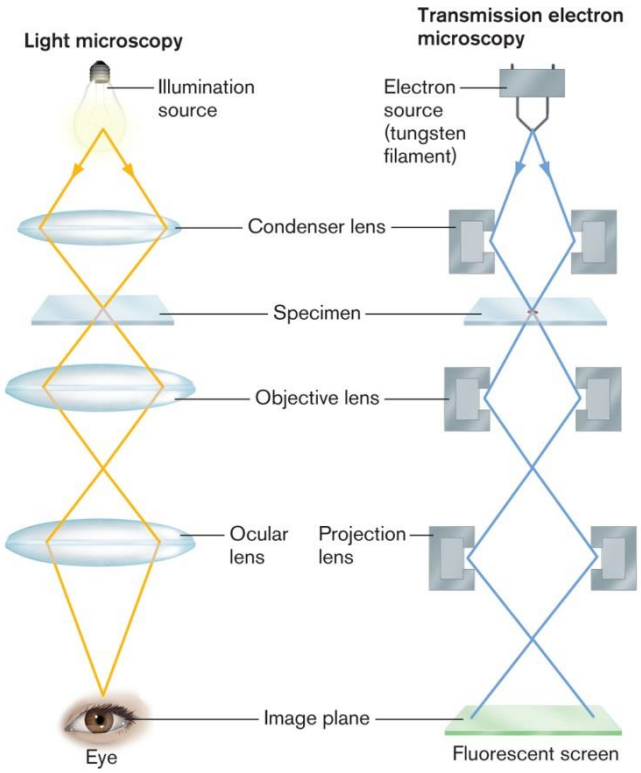

Figure 2.13 Illustration of the optical pathways in a classic light microscope and a transmission electron microscope.[23]

An electron beam is accelerated by a voltage and focused by a condenser system towards the thin sample. When this primary electron hits the sample, several processes such as scattering events, the generation of secondary or Auger electrons or the emission of X-rays can take place. The transmitted electrons are magnified through another lens system before being detected by a CCD camera or a fluorescent screen.[24]

2.9 References

[1] J. T. Bushberg, J. A. Seibert, E. M. J. Leidholdt, B. J. M., *The Essential Physics of Medical Imaging*, Lippincott Williams & Wilkins, Philadelphia, **2002**.

[2] http://pd.chem.ucl.ac.uk/pdnn/inst1/wavs1.gif, 21.11.2017.

[3] W. Borchardt-Ott, *Kristallographie - Eine Einführung für Naturwissenschaftler*, Springer-Verlag, Berlin Heidelberg, **2009**.

[4] G. Santoro, S. Yu, in *X-ray Scattering* (Ed.: A. E. Ares), InTech, Rijeka, **2017**, p. Ch. 02.

[5] http://meetings.chess.cornell.edu/ACABioSAS/TrackB/GISAXS_Yager.pdf, URL no longer accessible, 19.01.2016.

[6] K. S. W. Sing, D. H. Everett, R. A. W. Haul, L. Moscou, R. A. Pierotti, J. Rouquerol, T. Siemieniewska, *Pure Appl. Chem.* **1985**, *57*, 603.

[7] M. Thommes, K. Kaneko, V. Neimark Alexander, P. Olivier James, F. Rodriguez-Reinoso, J. Rouquerol, S. W. Sing Kenneth, *Pure Appl. Chem.* **2015**, *87*, 1051.

[8] M. Thommes, K. A. Cychosz, *Adsorption* **2014**, *20*, 233-250.

[9] https://www.chemie.uni-hamburg.de/ac/froeba/Gasadsorption08.pdf, 27.11.2017.

[10] S. Brunauer, P. H. Emmett, E. Teller, *J. Am. Chem. Soc.* **1938**, *60*, 309-319.

[11] http://hyperphysics.phy-astr.gsu.edu/hbase/magnetic/imgmag/mmom.gif, 21.11.2017.

[12] http://199.116.233.101/images/thumb/4/45/Proton_precession_Mxy.png/704px-Proton_precession_Mxy.png, 21.11.2017.

[13] http://www.revisemri.com/images/fid.gif, 21.11.2017.

[14] H. Günther, *NMR Spectroscopy : Basic Principles, Concepts and Applications in Chemistry*, Wiley-VCH, Weinheim, **2013**.

[15] J. H. Nelson, *Nuclear magnetic resonance spectroscopy*, Prentice Hall, Upper Saddle River, **2003**.

[16] *DIN 51006 – Thermische Analyse (TA) – Thermogravimetrie (TG) – Grundlagen* Beuth, Berlin, **2005**.

[17] M. Hesse, H. Meier, B. Zeeh, *Spektroskopische Methoden in der organischen Chemie*, Thieme, Stuttgart, **2002**.

[18] H. Günzler, H.-U. Gremlich, *IR-Spektroskopie - Eine Einführung*, Wiley-VCH, Weinheim, **2003**.

[19] http://alfresco.ubm-us.net/alfresco_images/pharma/2015/10/09/e9930a0c-89ea-4eb5-a7e4-318761f91e26/Bradley-Figure-1_web.jpg, 23.11.2017.

[20] https://chem.libretexts.org/@api/deki/files/79073/%253DScreen_shot_2011-03-01_at_9.34.55_AM.png, 28.02.18.

[21] H. G. Hecht, *J. Res. Natl. Bur. Stand. Sec. A* **1976**, *80A*, 567-583.

[22] D. B. Williams, C. B. Carter, *Transmission Electron Microscopy*, Plenum Press, New York, **1996**.

[23] https://digital.wwnorton.com/ebooks/epub/microbio4/OEBPS/Chapter02-06.xhtml, 28.02.2018.

[24] D. Brandon, W. D. Kaplan, *Microstructural Characterization of Materials*, John Wiley & Sons Ltd, Chichester, **2008**.

3 The Taming of the Screw

This chapter is based on the following publication:

Molecular docking sites designed for the generation of highly crystalline covalent organic frameworks

by Laura Ascherl, Torben Sick, Johannes T. Margraf, Saul H. Lapidus, Mona Calik, Christina Hettstedt, Konstantin Karaghiosoff, Markus Döblinger, Timothy Clark, Karena W. Chapman, Florian Auras, Thomas Bein

Nature Chem. **2016**, *8*, 310-316.

and was chosen as the front cover of the April issue 2016.

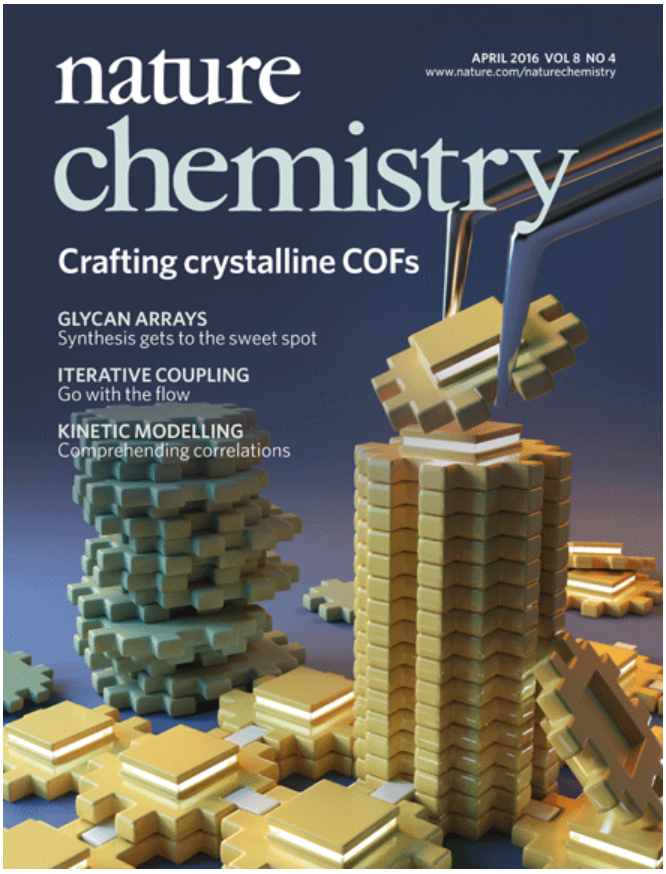

Cover image: Christoph Hohmann, Nano Initiative Munich (NIM)

3.1 Abstract

Covalent organic frameworks (COFs) formed by connecting multidentate organic building blocks through covalent bonds provide a platform for designing multifunctional porous materials with atomic precision. As they are promising materials for applications in optoelectronics, they would benefit from a maximum degree of long-range order within the framework, which has remained a major challenge. We have developed a synthetic concept to allow consecutive COF sheets to lock in position during crystal growth, and thus minimize the occurrence of stacking faults and dislocations. Hereby, the three-dimensional conformation of propeller-shaped molecular building units was used to generate well-defined periodic docking sites, which guided the attachment of successive building blocks that, in turn, promoted long-range order during COF formation. This approach enables us to achieve a very high crystallinity for a series of COFs that comprise tri- and tetradentate central building blocks. We expect this strategy to be transferable to a broad range of customized COFs.

3.2 Introduction

Controlling the crystallization of organic materials has remained challenging, particularly if a long-range ordered network is to be formed entirely from covalent bonds, as in the case of covalent organic frameworks (COFs). COFs have recently come into the limelight as gas storage or separation materials[1] [2], as new materials for applications in catalysis[3] and as promising candidates for realizing new optoelectronic-device concepts[4] [5]. COFs linked in two dimensions (2D-COFs) are of great interest, especially for optoelectronic devices. π-Stacking between the COF layers enables charge-carrier transport along self-assembled molecular columns[6] [7] and the formation of oriented host channels, which can be used to incorporate functional guest molecules[8]. COFs are realized via a reversible mechanism of covalent-bond formation, the most prominent linkage modes being boronate ester formation [9] [10] [11] [12] [13] [14], imine[15] [16] [17] and imide [18] condensation and trimerization processes based on borazine[19] and triazine[20]. The reversibility of the bond formation allows for constant self-healing during COF growth and is of key importance to obtain a highly crystalline product. Although 3D imine-linked COFs, such as COF-300 or molecular imine cages, can exhibit a rather high degree of order[15] [21] [22], most 2D-COFs are of moderate crystallinity, which possibly limits the accessible surface area and electronic transport in the framework.

Methods to enhance the crystallinity of layered COFs have focused mostly on the control of the intralayer interactions and layer planarity via the introduction of hydrogen bonds[23] [24]. Although these concepts have an indirect influence on the layer stacking, a direct and deterministic control of the stacking is highly desirable. Theoretical investigations of the layer stacking in these frameworks have established that a lateral offset between adjacent COF layers is energetically favourable, and results in inclined or serrated rather than fully eclipsed structures[25] [26]. Owing to the inherent symmetry of the layers, however, this offset will happen with the same probability along all the symmetry-equivalent directions. Consequently, if a successive COF layer nucleates at more than one location, the lateral offset of the growing islands is very likely to be in different directions, and so possibly causes lattice strain and defects, and in turn compromises crystallinity (Figure 3.1a).

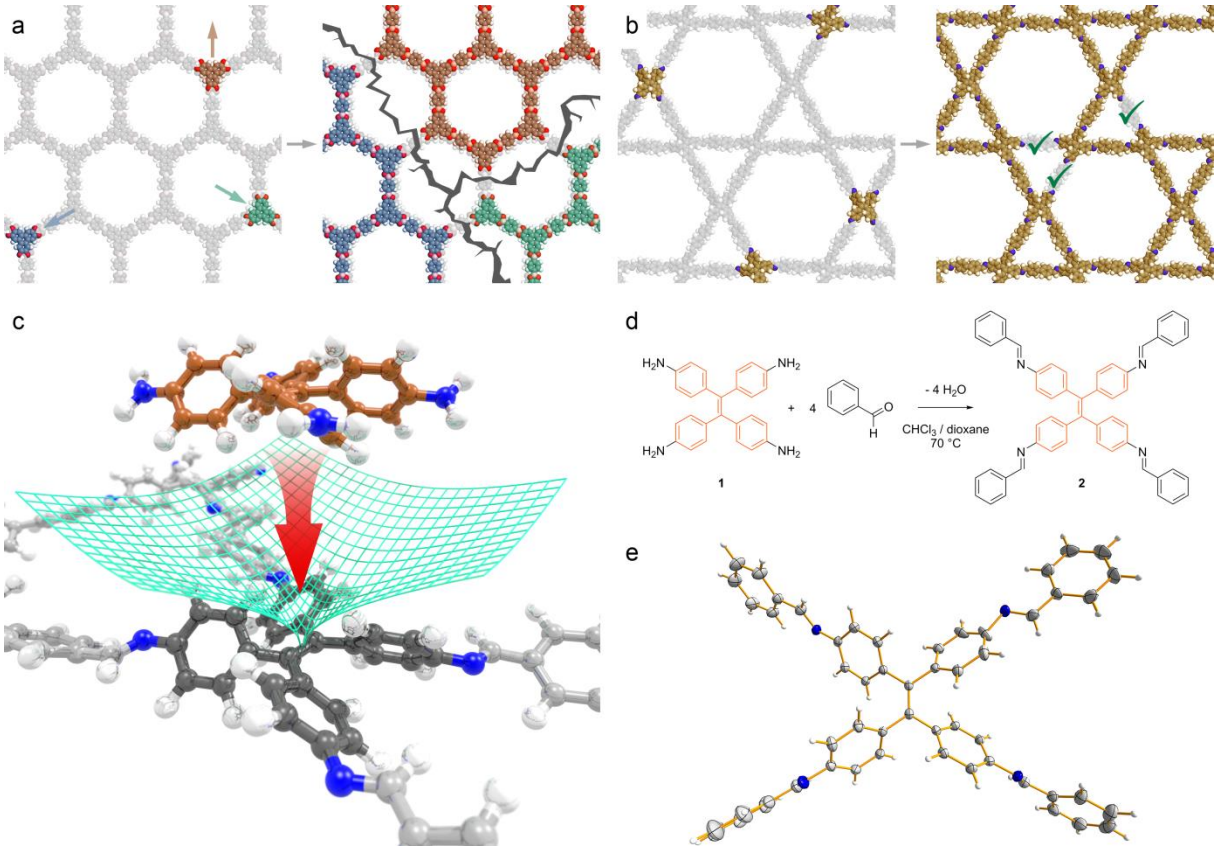

Figure 3.1 The self-repeating lock-and-key motif of propeller-shaped building blocks. a, Simultaneous nucleation of a successive COF layer (at three moieties for which the carbon atoms are shown in orange, blue and green, respectively; oxygen, red; hydrogen, white) at several positions over an initial COF layer (shown in light grey for clarity, with hydrogen atoms in white) offset in symmetry-equivalent directions (indicated by the orange, blue and green arrows) can lead to strain and lattice defects (visualized by cracks) during COF growth. **b**, If a successive COF layer (C, yellow; N,

blue; H, white) nucleates at unique attachment sites exactly over the nodes of the initial COF layer (shown in light grey with hydrogen atoms in white), the islands formed from these nucleation sites in the early steps of COF growth can merge into a defect-free layer (visualized by green ticks). **c**, Illustration of the guided attachment of the **4PE**-based building blocks (C, dark grey for the four core aromatic rings, light grey for the other carbons; N, blue; H, white). The molecular conformation of this building block (dark grey) causes a single minimum in the potential-energy hypersurface (green grid) for lateral displacement, which allows the successive layer (C, orange; N, blue; H, white) to lock in position (visualized by the red arrow). **d**, Synthesis of a **4PE**-based molecular model system via condensation of 1 with benzaldehyde. **e**, Asymmetric unit of the single-crystal X-ray structure of 2 that shows the solid-state geometry of the **4PE** unit. Blue, N; grey, C; white, H. The co-crystallized solvent molecule is omitted for clarity.

To preclude this error-prone network formation, we developed a concept to control 3D spatial relationships during the formation of COFs, in which the molecular conformation of the building blocks unambiguously defines the position of each building unit within adjacent COF layers (Figure 3.1b). We surmised that multidentate central units with a lock-and-key-like molecular conformation could be used to guide the attachment of the successive layers (Figure 3.1c). To implement this concept, we synthesized a set of highly crystalline hexagonal COFs with eclipsed 2D structures.

3.3 Results and Discussion

Inspired by stackable objects, we looked for screw- or propeller-shaped molecules that can lock into each other and thereby fix the lateral position for the attachment of successive COF layers (Figure 3.1c). As a first example for realizing this concept with imine-linked COFs we chose 1,1,2,2-tetrakis(4-aminophenyl)ethene (**1**). **1** is expected to yield fourfold connected and thus very stable COF structures, whereby a star-shaped, dual-pore arrangement of the COF seems to be favoured [27].

To study the molecular arrangement of the 1,1,2,2-tetrakis(4-aminophenyl)ethene (**4PE**) central unit inside a possible COF network, we first synthesized a molecular model system (**2**) by the fourfold imine condensation of **1** with benzaldehyde (Figure. 3.1d (for experimental details, see the Supplementary Information)). Single-crystal X-ray data confirm that the **4PE** unit adopts the desired propeller-like arrangement (Figure 3.1e) with both a left- and a right-turning entity present in the crystal structure (SI Figure 3.6).

We then applied 1 as a building block in a series of imine-linked COFs (Figure 3.2a), co-condensing the four-armed building block with linear dialdehydes. As to the choice of the linear building units, we decided to start with weakly interacting non-rigid molecules to avoid the layer stacking being dominated by these linear building blocks. We therefore selected biphenyl-4,4′-dicarboxaldehyde (**2P**) and, to achieve different pore sizes, the shorter terephthalaldehyde (**1P**) and its elongated homologue p-terphenyl-4,4″-dicarboxaldehyde (**3P**). To study whether the concept could also be transferred to linkers with stronger electronic interactions, we chose thieno[3,2-*b*]thiophene-2,5-dicarboxaldehyde (**TT**) as a further dicarboxaldehyde building block. A thienothiophene-bridged diboronic acid had already been applied successfully in previous COF studies by our group4.

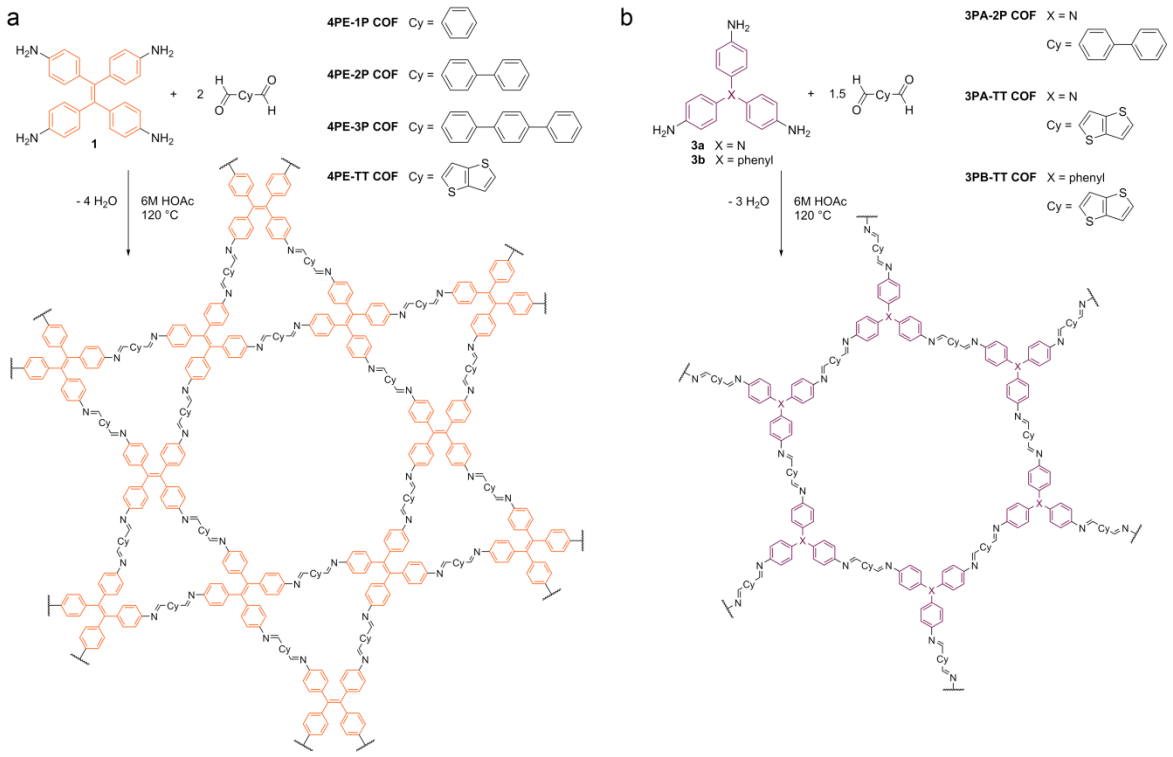

Figure 3.2 Synthetic scheme for the construction of the imine-linked COFs that comprise propeller-shaped building blocks. a, Construction of star-shaped, dual-pore **4PE**-based COFs via co-condensation of 1 with the linear dialdehyde bridging units **1P**, **2P**, **3P** and **TT**. **b**, Synthesis of the hexagonal **3PA**- and **3PB**-based COFs in combination with the linear dialdehyde bridging units **2P** and **TT**.

The corresponding **4PE-1P**, **4PE-2P**, **4PE-3P** and **4PE-TT** COFs were obtained via acid catalysis under solvothermal conditions (see Methods). In a way similar to molecular imine cages [28], the **4PE** COFs possess very high physicochemical stabilities. The frameworks are

stable in ambient air and were found to retain their crystallinity on stirring in a variety of protic and aprotic organic solvents and in boiling water (SI Figures 3.11 and 12).

Powder X-ray diffraction (PXRD) data from both high-resolution and high-energy synchrotron-based measurements confirmed the formation of highly crystalline frameworks (Figure 3.3a–c and SI Figure 3.8). In particular, the diffraction patterns of the new **4PE-2P**, **4PE-3P** and **4PE-TT** COFs display a large number of well-defined higher-order reflections (insets of Figure 3.3a–c). The high-energy data collected using an area detector provided an improved signal-to-noise ratio for the higher-angle reflections. For each COF, structural analysis via a Rietveld refinement was performed against both data sets simultaneously using density functional theory/local density approximation (DFT/LDA)-optimized structures as the starting models (Figure 3.3d–f). The Rietveld method refines the atom positions of these models to find the best match between the theoretical pattern and the experimental data. Refinements were undertaken in the *P*6 space group, as this was the highest symmetry predicted from the DFT modelling. The a lattice parameter was well constrained by the data. However, this sample illustrates the classic problem of a dominant zone with fewer and broad peaks corresponding to *hkl* reflections for $l \neq 0$. As such the c lattice dimension was defined less precisely. Bond lengths were constrained to the DFT-optimized values as the torsion between rigid moieties, such as rotations of the aromatic rings, was allowed to refine. The optimized models provide an excellent fit to the measured diffraction intensities (Figure 3.3). The unit-cell parameter a ranges from 4.12 nm for the **4PE-TT** COF to 5.48 nm for the **4PE-3P** COF. The c axis was found to be almost identical at 0.46–0.48 nm for all the **4PE**-based COFs, which indicates a similar layer stacking in all cases despite the differences in stiffness and electronic interactions between the **2P**, **3P** and **TT** building blocks.

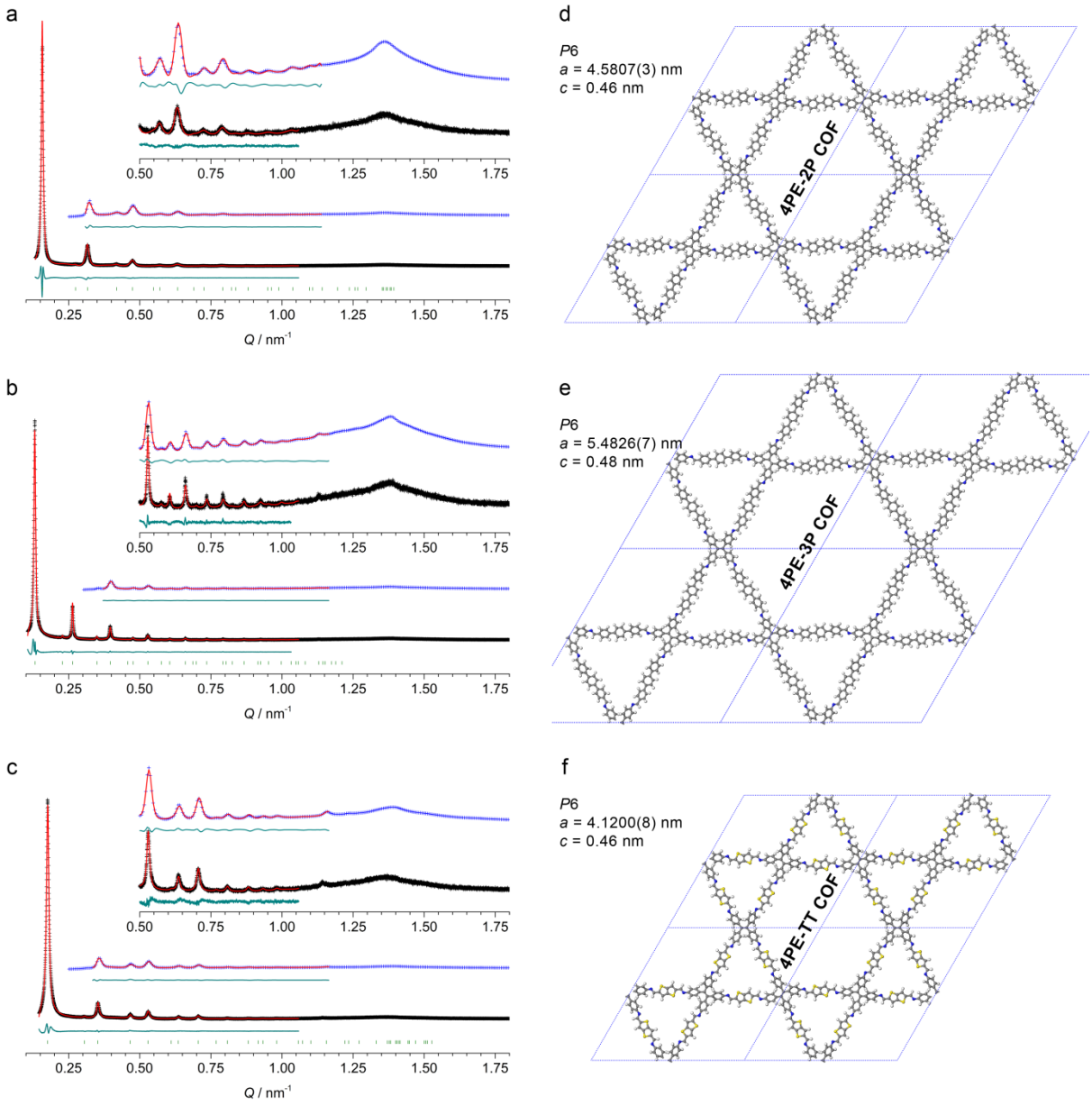

Figure 3.3 PXRD patterns and the corresponding Rietveld-refined structures illustrate the high degree of order within the 4PE-based COF networks. a–c, Experimental synchrotron PXRD data (black, high-resolution X-ray scattering; blue, high-energy X-ray total scattering) of the **4PE-2P** COF (**a**), **4PE-3P** COF (**b**) and **4PE-TT** COF (**c**). Simultaneous Rietveld refinements of the high-resolution and high-energy data sets (red lines) provide good fits to the experimental data with only minimal differences (the green lines show the difference plots between the experimental PXRD patterns and those obtained by Rietveld refinements). Bragg positions are indicated by light green ticks. $\lambda = 0.41417$ Å for the high-resolution data (black) and 0.2114 Å for the high-energy data (blue). Insets, magnified views onto the $Q > 0.5$ Å^{-1} region show well-defined higher-order reflections. **d–f**, The corresponding Rietveld-refined COF structures of the **4PE-2P** (**a**), **4PE-3P** (**b**) and **4PE-TT** (**c**) COFs assuming *P*6 symmetry (available as Supplementary Information).

Pair-distribution functions (PDFs) calculated for the optimized structure models provided an excellent match to the experimental data, and further confirmed the local structure (SI Figure 3.7). The best match between the experimental and simulated PDFs was achieved when the a lattice dimension was allowed to expand, which is in line with the systematic underestimation of bond lengths by the LDA method we used to build the starting models. The atomic displacement parameters perpendicular to the layers were significantly larger than those in the layer direction, which reflects the presence of an increased static and dynamic disorder in this non-bonded direction.

According to our simulations and the X-ray structure of the molecular fragment 2, the four core phenylene groups assume a screw-like arrangement, and thus allow the 4PE building block of a successive COF layer to lock in a single, well-defined lateral position. To vindicate the locking mechanism, DFT calculations were performed using the CASTEP code with the generalized gradient approximation PBE functional and applying a correction for dispersion interactions [29] [30] [31] [32] [33]. The simulation of the potential energy surface for the displacement of two **4PE-2P** layers confirms that the eclipsed structure is, indeed, thermodynamically favoured (SI Figure 3.13). Furthermore, the potential-energy hypersurface is steepest around the minimum and levels off considerably for displacements higher than 0.04 nm in any direction.

To understand the nature of these interactions, it is instructive to compare the potential-energy hypersurfaces obtained from pure and dispersion-corrected PBE calculations (SI Figure 3.9). The two methods predict the same qualitative features, most importantly the steep descent for displacements below 0.04 nm. As the PBE functional describes permanent multipole–multipole interactions only, without accounting for London-type interactions, the lock-and-key principle is primarily based on permanent electrostatic interactions between the aromatic rings. If dispersion interactions are included, the eclipsed structure is additionally stabilized by over 0.5 eV relative to the most-displaced geometry we considered. Furthermore, these interactions tilt the potential-energy hypersurface towards the minimum, which drives the key into the lock. This becomes particularly important for displacements beyond 0.04 nm, where the uncorrected PBE hypersurface is almost flat.

Regarding the interlayer distance (that is, the c lattice vector), the dispersion-corrected PBE calculations predict a value of 0.46 nm for both **4PE-2P** and **4PE-TT**, in excellent agreement

with the experiments. This confirms that this dimension is governed by interactions between the **4PE** units, and is relatively independent of the bridging moiety.

A perfectly defect-free crystal domain of *P*6 symmetry would be built up by **4PE** units that all have the same direction of rotation (Figure 3.4). As the introduction of even a single **4PE** column of the 'wrong' propeller enantiomer would cause considerable strain in the framework, synchronizing the molecular conformation of all the **4PE** units throughout a COF domain appears to be of key importance. We propose that this synchronization can only be achieved if the linear bridging unit is able to transmit information on the molecular configuration between adjacent **4PE** units during COF growth.

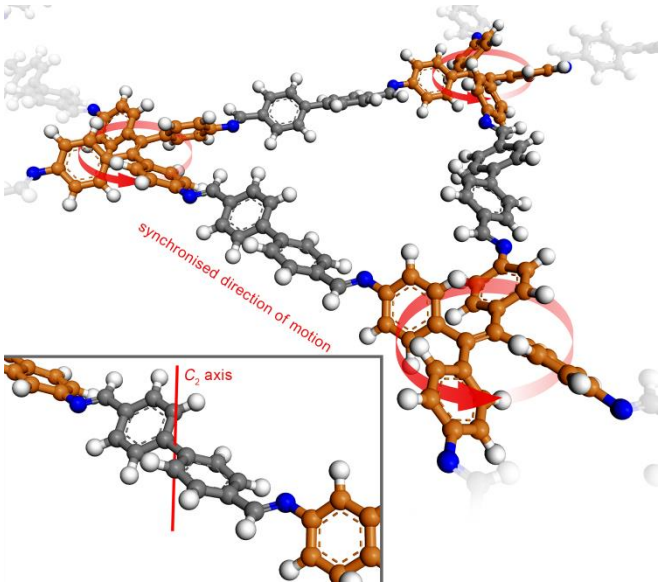

Figure 3.4 Fragment of the 4PE-2P COF structure. The direction of rotation (red arrows) of **4PE** entities (C, orange; N, blue; H, white) is synchronized via the molecular conformation of the linear bridging unit (C, grey; H, white). Inset, a cut-out showing the C_2-symmetric bridging unit that is crucial for transmitting information on the molecular conformation of the **4PE** entities.

Dividing the COF in a 'thought experiment' into phenylene–bridge–phenylene fragments we find a C_2 axis in the centre of the bridging unit (inset of Figure 3.4). Based on this consideration we can anticipate well-ordered systems for linear building blocks with a strong tendency to adopt a C_2-symmetric configuration, whereas mirror-symmetric bridging units cannot synchronize the **4PE** units. Indeed, the **2P** and **3P** units seem to be able to transfer this information efficiently, possibly via the tilt of their terminal phenylenes. If the bridging unit, however, is reduced to a single aromatic ring, as in the case of the **4PE-1P** COF, this mechanism might not be operational. In a *P*6-symmetric setting the rigid **1P** would be

required to assume an intermediate position, that is be co-planar with the *ab* plane. As both the cis and trans configurations of the terminal aldehydes have approximately the same energy, the **1P** building block cannot impose a synchronized direction of rotation on all the **4PE** entities, which possibly results in an increased defect density. Indeed, we observed a lower crystallinity for the **4PE-1P** COF compared with that of its larger homologues (SI Figure 3.8). Even though the relative ratios of the peak intensities correspond well to those of the proposed model, the broader and strongly asymmetrically shaped peaks could not be modelled so well by the data, which indicates the presence of considerably more disorder in this framework.

The TT bridging unit, on the other hand, proved to be capable of generating very well-ordered frameworks. Although this rigid building block is also expected to be co-planar with the ab plane in a *P*6-symmetric COF, the inherent C_2 symmetry of this molecule and its stronger electronic interaction with the imine bonds seem to provide a functional path for directing the conformation of adjacent **4PE** units.

Given their well-defined geometries, the new COFs are expected to form porous structures with two precisely defined pore sizes. The nitrogen sorption isotherms recorded at 77 K exhibit a type IV isotherm with two sharp steps and an H1 hysteresis loop (Figure 3.5a). Quenched-solid DFT calculations using an equilibrium model and assuming a cylindrical pore geometry show the existence of two types of pores with narrow size distributions in each of the COFs (Figure 3.5b) [34] [35]. The obtained pore diameters of 2.9, 3.8, 4.5 and 3.2 nm for the large hexagonal pores of the **4PE-1P**, **4PE-2P**, **4PE-3P** and **4PE-TT** COFs, respectively, are in very good agreement with the simulated pore sizes of 2.9, 3.8, 4.5 and 3.3 nm, respectively. For the smaller trigonal pores we obtained pore sizes of 1.6, 1.7, 1.8 and 1.6 nm, which are consistent with those of the simulated structures. The Brunauer–Emmett–Teller surface areas of the four COFs are 2,140 ± 50 m2 g−1 (**4PE-1P**), 2,070 ± 50 m2 g−1 (**4PE-2P**), 1,000 ± 50 m2 g−1 (**4PE-3P**) and 1,990 ± 50 m2 g−1 (**4PE-TT**) with total pore volumes of 1.31 cm3 g−1, 1.53 cm3 g−1, 0.844 cm3 g−1 and 1.24 cm3 g−1, respectively. Some of these surface areas are among the highest reported surface areas for imine-linked COFs [2] [27].

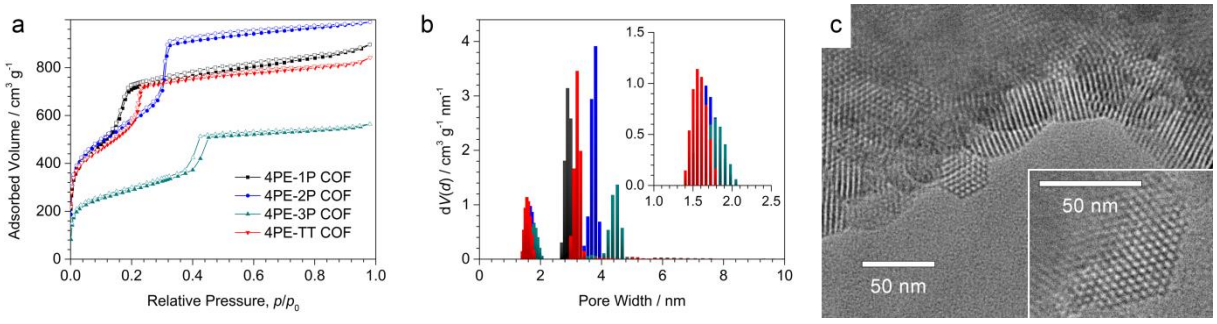

Figure 3.5 Porosity and real-space images of the 4PE-based COFs. a, Nitrogen sorption isotherms of the **4PE-1P** (black), **4PE-2P** (blue), **4PE-3P** (green) and **4PE-TT** (red) COFs exhibit type IV isotherms. Filled symbols, adsorption; open symbols, desorption. **b**, Corresponding pore-size distributions indicate the presence of both micro- and mesopores. Inset, enlargement of the microporous region. **c**, TEM images of **4PE-3P** COF that show the faceted COF crystallites with a hexagonal arrangement of the mesopores. Inset, magnified view onto a single COF crystallite.

Transmission electron microscopy (TEM) images of **4PE-3P** COF powder samples reveal the nanoscale morphology of individual COF crystallites (Figure 3.5c). Typical domain sizes range from 50 to 100 nm. Straight porous channels that extend through entire crystal domains can be observed. Domains oriented with their ab plane perpendicular to the viewing direction show the highly ordered hexagonal arrangement of the mesopores and exhibit clearly observable hexagonal facets, which highlights the crystallinity of this material. To the best of our knowledge this is the first time that such faceting has been observed for COF nanocrystals.

Having demonstrated that highly crystalline frameworks can be obtained for combinations of 1 with different linear building blocks, we decided to test the generality of our approach by extending our study to other propeller-shaped building blocks (Figure 3.2b). Triphenylamine (**3PA**) can be seen as a trigonal complement to **4PE** with comparable steric interactions between its aromatic rings. Although the terminal phenylenes of triphenylbenzene (**3PB**) are expected to interact less strongly with each other, the preferred conformation of this building block is propeller-like as well.

We employed both trigonal building blocks terminated with amino groups (3a and 3b) in the synthesis of imine-linked COFs using **2P** and **TT** as their linear counterparts. The resulting frameworks exhibited a very high crystallinity with sharp and well-defined higher-order reflections similar to those of the **4PE** COFs (SI Figures 3.9 and 10). Pawley refinement of

the **3PA**- and **3PB**-containing COFs based on *P*6-symmetric structure models produced the lattice parameters listed in Supplementary Table 2.

Similar to the case of the **4PE** COFs, the c axis seems to be determined by the nature of the propeller-shaped building block. The smaller tilt angle of the terminal aromatic rings of **3PB** compared with that of **4PE** (30° versus 44° according to our DFT simulations of the COFs) seems to allow for a closer layer stacking, and thus a reduced length of the c axis. Still, the high order caused by a single, well-defined lateral position is retained.

3.4 Conclusion

In this study, we utilized the inherent molecular conformation of rigid, propeller-shaped building units to define self-repeating docking sites for the attachment of consecutive COF layers. In this way, we were able to realize COFs that feature, to the best of our knowledge, an as yet unmatched degree of crystallinity and well-defined crystal facets.

Studying a series of COFs that comprise bridging units of different molecular symmetry and conformational flexibility enabled us to gain insights into the conveyance of configurational information during the COF formation, and highlights the importance of designing intra- and interlayer interactions. With the generality of this approach demonstrated for a number of combinations of different building blocks and bridging units, we expect this concept to be applicable to a broad variety of functional building blocks and to promote the establishment of COFs in catalysis and organic electronics.

3.5 Supporting Information

Unless stated otherwise, all reactions were performed in oven-dried glassware under ambient atmosphere. All reagents and solvents were obtained from commercial suppliers and used as received. 1,1,2,2-Tetrakis(4-nitrophenyl)ethene and 1,1,2,2-tetrakis(4-aminophenyl)ethene were synthesized following published procedures[36].

Nuclear magnetic resonance (NMR) spectra were recorded on Bruker AV 400 and AV 400 TR spectrometers. Proton chemical shifts are expressed in parts per million (δ scale) and are calibrated using residual undeuterated solvent peaks as an internal reference (DMSO-d_6: 2.50). Data for ^{1}H NMR spectra are reported in the following way: chemical shift (δ ppm) (multiplicity, coupling constant/Hz, integration). Multiplicities are reported as follows: s = singlet, d = doublet, t = triplet, q = quartet, m = multiplet, br = broad, or combinations thereof.

Infrared (IR) **spectra** were recorded on a Thermo Scientific Nicolet™ 6700 FT-IR spectrometer in transmission mode. IR data is reported in frequency of absorption (cm^{-1}).

UV-Vis spectra were recorded using a Perkin-Elmer Lambda 1050 spectrometer equipped with a 150 mm InGaAs integrating sphere. Diffuse reflectance spectra were collected with a Praying Mantis (Harrick) accessory and were referenced to barium sulfate powder as white standard.

Photoluminescence (PL) measurements were performed using a home-built setup consisting of a Horiba Jobin Yvon iHR 320 monochromator equipped with a photomultiplier tube and a liquid N_2-cooled InGaAs detector. The samples were illuminated with a pulsed (83 Hz) 365 nm LED at a light intensity of 500 mW cm^{-2}.

Thermogravimetric analysis (TGA) measurements were performed on a Netzsch Jupiter ST 449 C instrument equipped with a Netsch TASC 414/4 controller. The samples were heated from room temperature to 900 °C under a synthetic air atmosphere at a heating rate of 1 K/min.

The **nitrogen sorption** isotherms were recorded on a Quantachrome Autosorb 1 at 77.4 K in a pressure range from p/p_0 = 0.001 to 0.98. Prior to the measurement of the sorption isotherm the samples were outgassed for 24 h at 120°C under high vacuum. For the evaluation of the surface area the BET model was applied between 0.05 and 0.2 p/p_0. The calculations of the

pore size distribution were performed using the QSDFT equilibrium model with a carbon kernel for cylindrical pores.

Powder X-ray diffraction (PXRD) measurements were performed using a Bruker D8 Discover with Ni-filtered Cu K_α radiation and a LynxEye position-sensitive detector. Background correction was performed using spline-interpolated and intensity-adapted measurements of the empty sample holder.

The initial **structure models of the COFs** were built using the Forcite module of the Accelrys Materials Studio software package. We applied the space group with the highest possible symmetry, i.e. *P*6, taking into account the propeller-like conformation of the central building blocks. Using this coarse model we determined the unit cell parameters *via* Pawley refinement of our PXRD data. In order to obtain a more realistic picture of the local molecular arrangement, we then performed DFT geometry optimisations based on the refined unit cell parameters using the CASTEP module and the LDA/CA-PZ functional. These models were suitable for subsequent Rietveld refinements.

Synchrotron X-ray scattering measurements were undertaken for capillary-loaded samples of the samples at the Advanced Photon Source at Argonne National Laboratory. High-resolution powder X-ray diffraction data were collected at ambient temperature and at 100 K at beamline 11-BM with the use of 12-detector/analyzer system, with the data from the detectors corrected and merged into a single diffraction pattern. Samples were spun at 90 Hz to ensure good powder averaging.

High energy X-ray total scattering data suitable for diffraction and **pair distribution function** (PDF) analysis were collected at beamline 11-ID-B using high energy X-rays (58keV, 0.2114 Å wavelength) in combination with a large amorphous-Si based area detector from Perkin-Elmer. The two-dimensional scattering images were reduced to one-dimensional data within Fit2d. PDF's, $G(r)$, were extracted from the data within PDFgetX2, subtracting contributions from the background and inelastic scattering before Fourier transforming the data to Q_{max} = 19.8 $Å^{-1}$. There was no evidence for preferred orientation effects in the diffraction images. PDFs were calculated for the diffraction-optimised structural models within PDFgui.

Structural analysis of the powder diffraction data (both high resolution and high energy data) were undertaken by **Rietveld refinement**, as implemented within TOPAS. The high energy data collected using an area detector provided improved signal-to-noise for the higher angle

reflections. The DFT-optimised structures were used as starting models for the structural refinements. Refinements were undertaken in *P*6 space group, as this was the highest symmetry predicted from the DFT.

Single-crystal X-ray diffraction data were collected with an Xcalibur3 diffractometer equipped with a Spellman generator (voltage 50 kV, current 40 mA) and a Kappa CCD detector and using Mo K_α radiation (λ = 0.71073 Å). The data collection was performed with the CrysAlis CCD software [37] and the data reduction was achieved with the CrysAlis RED software. [38] The structure was solved with SIR-92, refined with SHELXL-97 and checked using PLATON.[39] The absorptions were corrected by the SCALE3 ABSPACK multiscan method.[40] Crystallographic data for the structure have been deposited with the Cambridge Crystallographic Data Centre, CCDC, 12 Union Road, Cambridge CB21EZ, UK. Copies of the data can be obtained free of charge on quoting the depository number CCDC 1055083 (http://www.ccdc.cam.ac.uk).

DFT calculations were performed with the CASTEP code using the generalised-gradient-approximation PBE functional. The energy cutoff for the planewave basis-set was set to 310.0 eV, ions were represented with ultrasoft pseudopotentials and k-point sampling was performed with a 1x1x4 Monkhorst-Pack grid (1x1x2 for the double layer structures). To account for dispersion interactions, we used the correction scheme of Tkatchenko and Scheffler.

Transmission electron microscopy (TEM) was performed on an FEI Titan Themis equipped with a field emission gun operated at 300 kV.

1,1,2,2-Tetrakis(4-nitrophenyl)ethene (4)

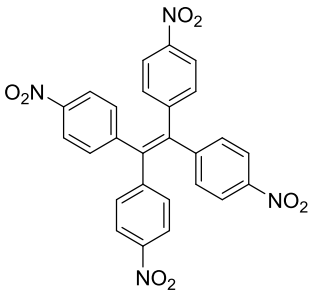

A mixture of 30 mL fuming nitric acid and 30 mL glacial acetic acid was cooled to 0°C. 1,1,2,2,-Tetraphenylethene (3.00 g, 9.00 mmol) was added in small portions and the mixture was allowed to warm to room temperature. After stirring for 3 h the solution was poured into ice water. The resulting precipitate was filtered off, washed with water and recrystallised from 1,4-dioxane to yield bright yellow crystals of **4** (2.05 g, 4.00 mmol, 44.4 %).

^{1}H NMR (400 MHz, DMSO-d_6): 8.11 (d, J = 8.00 Hz, 8 H), 7.37 (d, J = 8.00 Hz, 8 H).

1,1,2,2-Tetrakis(4-aminophenyl)ethene (1)

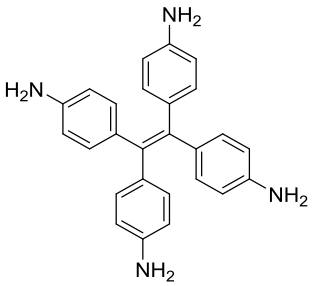

Under nitrogen, compound **4** (1.00 g, 1.95 mmol) was dissolved in 20 mL of THF. Raney Nickel (ca. 4 g) and hydrazine monohydrate (1.30 mL, 26.7 mmol) were added to the solution and the mixture was refluxed for 2 h. The solution was allowed to cool to 55 °C and the Raney Nickel was filtered off. All volatiles were evaporated under reduced pressure, yielding the title compound (0.75 g, 1.92 mmol, 98 %) as a yellow powder.

^{1}H NMR (400 MHz, DMSO-d_6): 6.57 (d, J = 8.00 Hz, 8 H), 6.26 (d, J = 8.00 Hz, 8 H), 4.85 (s, 8 H).

4PE(benzaldehyde)$_4$ (2)

In an argon atmosphere, dry benzaldehyde (53 mg, 0.5 mmol, 5 equiv.) was added to a suspension of **1** (39.2 mg, 0.10 mmol, 1 equiv.) in anhydrous 1,4-dioxane (0.5 mL) and $CHCl_3$ (2 mL). After addition of 5 beads of 3 Å molecular sieve, the reaction mixture was heated at 70 °C for 16 h. Upon slow cooling yellow needles formed, which were isolated by filtration and dried under reduced pressure. Crystals suitable for X-ray structure analysis were grown from a THF/1,2-dichloroethane (1:1 *v*:*v*) solution.

4PE-1P COF

1 (5.9 mg, 15 µmol, 1 equiv.) and 1P (4.0 mg, 30 µmol, 2 equiv.) were suspended in a mixture of 1,4-dioxane (149 µl) and mesitylene (33 µl). The resulting mixture was vortexed until complete dissolution of the reactants was achieved. Aqueous acetic acid (6 M, 18 µl) was added and the mixture kept in a glass tube at 120 °C for four days. The resulting bright-yellow precipitate was collected by filtration, washed with 1,4-dioxane and dried under reduced pressure. Analysis (calculated, found for C126H84N12): C (85.29, 83.92), H (5.23, 4.78), N (9.47, 9.31).

4PE-2P COF

1 (5.9 mg, 15 µmol, 1 equiv.) and 2B (6.3 mg, 30 µmol, 2 equiv.) were suspended in 1,4-dioxane (273 µl). The resulting mixture was vortexed until complete dissolution of the reactants was achieved. Aqueous acetic acid (6 M, 27 µl) was added and the mixture kept in a glass tube at 120 °C for four days. The resulting light-orange precipitate was collected by filtration, washed with 1,4-dioxane and dried under reduced pressure. Analysis (calculated, found for C162H108N12): C (87.22, 86.30), H (5.24, 4.97), N (7.53, 7.44).

4PE-3P COF

1 (5.9 mg, 15 µmol, 1 equiv.) and 3P (8.1 mg, 30 µmol, 2 equiv.) were suspended in a mixture of 1,4-dioxane (149 µl) and mesitylene (33 µl). The mixture was vortexed and aqueous acetic acid (6 M, 18 µl) added. The mixture was kept in a glass tube at 120 °C for four days to yield an ochre precipitate. The product was filtered, washed with 1,4-dioxane and dried under reduced pressure. Analysis (calculated, found for C198H132N12): C (88.49, 86.33), H (5.25, 5.04), N (6.25, 6.27).

4PE-TT COF

Under argon, 1 (11.7 mg, 30 µmol, 1 equiv.) and TT (11.8 mg, 60 µmol, 2 equiv.) were dissolved in 1 ml of a 1:9 v/v mixture of mesitylene and benzyl alcohol at 120 °C. The solution was cooled to room temperature and aqueous acetic acid (6 M, 100 µl) added. The mixture was kept in a glass tube at 120 °C for three days. The resulting red precipitate was collected by filtration, washed with DMF and dried under reduced pressure. Analysis (calculated, found for C126H72N12S12): C (70.76, 70.12), H (3.39, 3.72), N (7.86, 7.87), S (17.99, 17.30).

3PA-2P COF

Under argon, tris(4-aminophenyl)amine **3a** (8.7 mg, 30 µmol, 1 equiv.) and biphenyl-4,4'-dicarboxaldehyde (9.5 mg, 45 µmol, 1.5 equiv.) were dissolved in 500 µL of a 19:1 *v*:*v* mixture of anisole and 1,4-dioxane at 120 °C. Upon cooling to room temperature, aqueous acetic acid (6 M, 50 µL) was added and the reaction mixture was kept at 100 °C for 3 days, yielding an orange precipitate. The product was isolated via filtration.

3PA-TT COF

In an argon atmosphere, tris(4-aminophenyl)amine **3a** (8.7 mg, 30 µmol, 1 equiv.) and thieno[3,2-*b*]thiophene-2,5-dicarboxaldehyde (8.8 mg, 45 µmol, 1.5 equiv.) were dissolved in 500 µL of a 9:1 *v*:*v* mixture of mesitylene and benzyl alcohol at 120 °C. After cooling to room temperature, aqueous acetic acid (6 M, 50 µL) was added. The reaction mixture was kept at 120 °C for 4 days, yielding a dark purple precipitate. The product was isolated via filtration.

3PB-TT COF

In an argon atmosphere, tris(4-aminophenyl)benzene 3b (14.1 mg, 40 µmol, 1 equiv.) and thieno[3,2-*b*]thiophene-2,5-dicarboxaldehyde (11.8 mg, 60 µmol, 1.5 equiv.) were suspended in 1 mL of a 9:1 *v*:*v* mixture of anisole and ethanol. Aqueous acetic acid (6 M, 100 µL) was added and the resulting reaction mixture was kept at 100 °C for 5 days. The resulting yellow precipitate was isolated via filtration.

Single crystal structure of compound 2

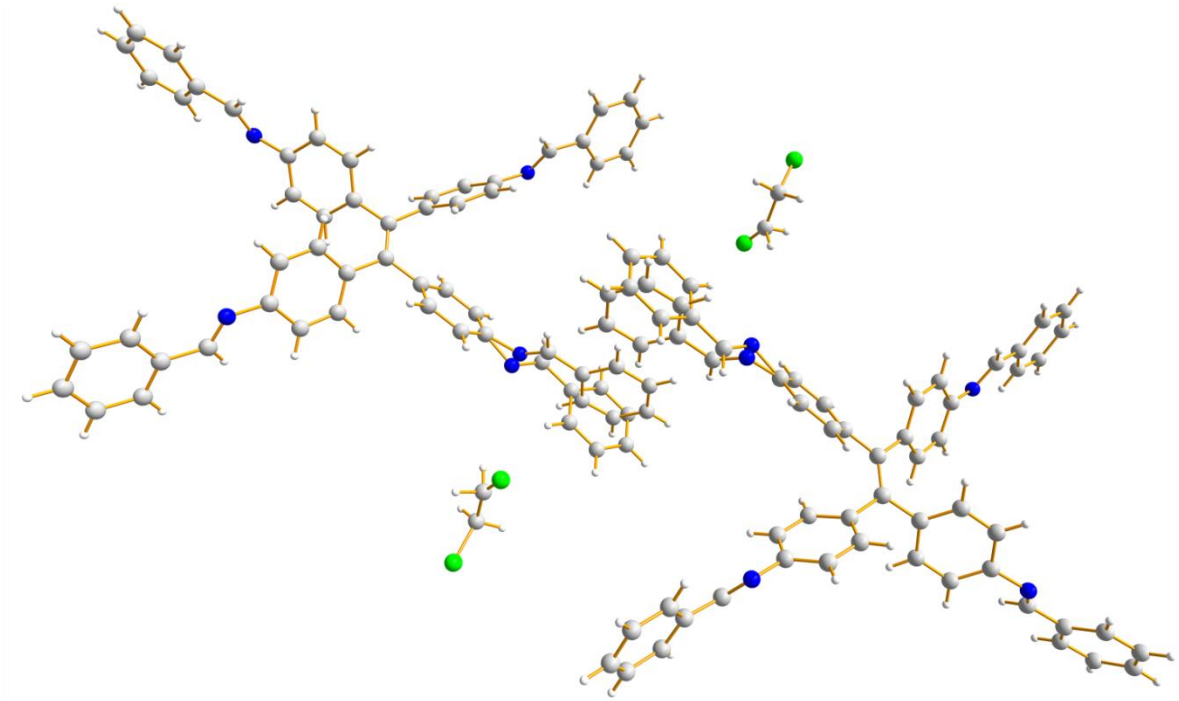

Figure 3.6 Single-crystal X-ray structure of compound 2. Colour scheme: carbon (grey), hydrogen (white), chlorine (green), nitrogen (blue). The structure contains one right-turning and one left-turning molecule per unit cell. The branches closest to the other molecule were refined having two positions with 50% occupancy each.

Table 3.1 Crystal structure data of compound 2.

Formula	$C_{56}H_{44}Cl_2N_4$
M	843.85
T / K	173(2)
Color, habit	yellow block
Cryst. Size / mm	0.2 x 0.2 x 0.1
Crystal system	triclinic
Space group	$P\bar{1}$
a / Å	9.3210(5)
b /Å	15.2640(9)
c / Å	16.6530(7)
α / °	74.721(4)
β / °	84.365(4)
γ / °	78.162(4)
V / Å^3	2234.5(2)
Z	2

ρ_{calcd} / g cm^{-3}	1.254
μ / mm^{-1}	0.188
Irradiation / Å	0.71073
F (000)	884
Index ranges	$-11 \leq h \leq 10$
	$-18 \leq k \leq 18$
	$-20 \leq l \leq 19$
Reflns. collected	17004
Reflns. unique	8138
Reflns. obsd.	5453
R_{int}	0.0330
Params. refined	669
θ range / °	4.098 - 25.350
R_1, wR_2 [I > 2σ(I)]	0.0526, 0.1212
R_1, $wR_{2\ (all\ data)}$	0.0874, 0.1422
GooF	1.022
δp_{max}, δp_{min} / e nm^{-3}	0.431, −0.335

Pair distribution analysis

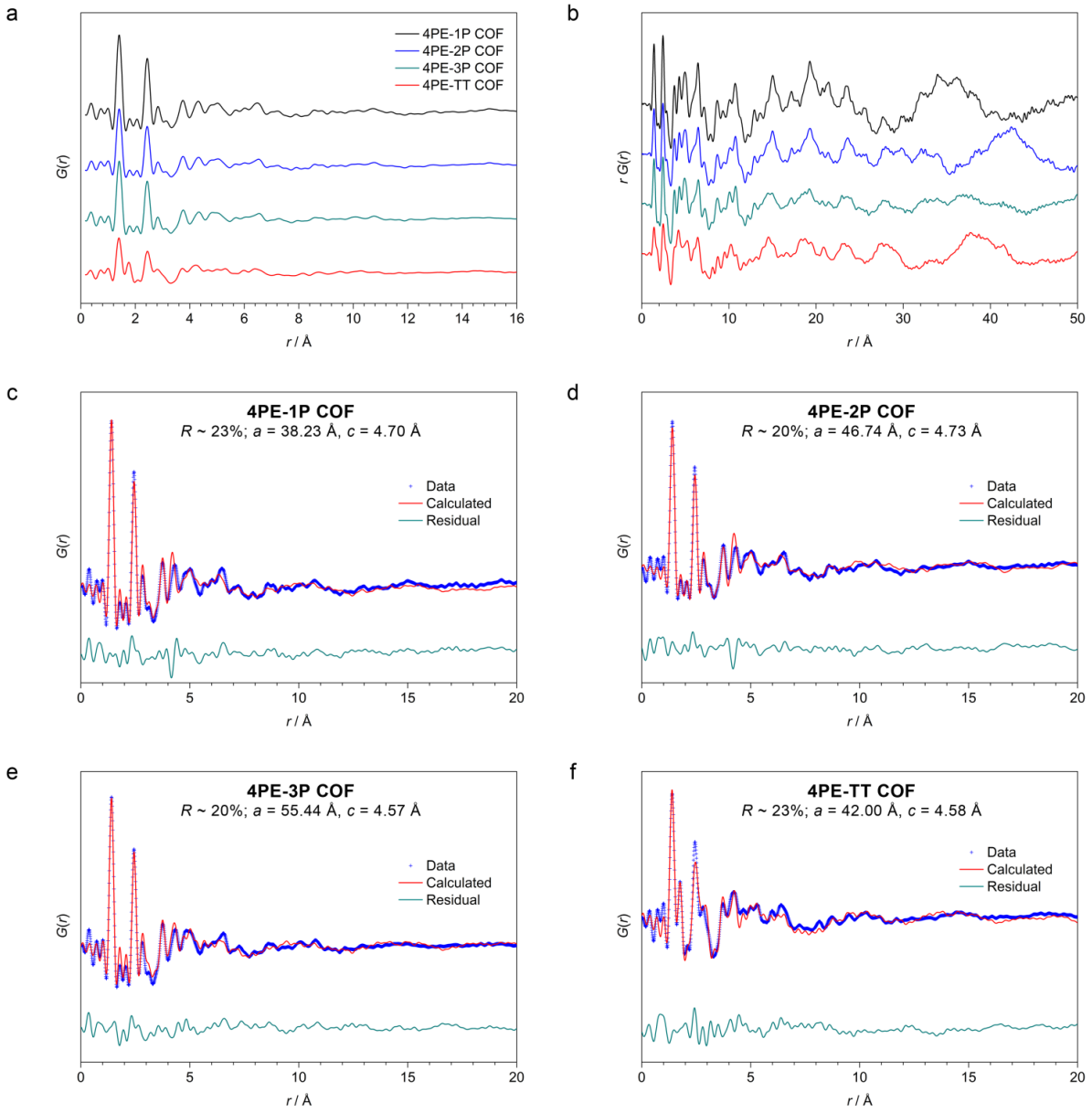

Figure 3.7 The PDF data for the COFs. a, PDF, G(r), and **b**, the r-multiplied G(r), which highlights features at longer distance. **c**, **d**, **e**, **f**, Fits of the structural models to the PDF data.

PXRD analysis and structure simulations of the 4PE-1P COF

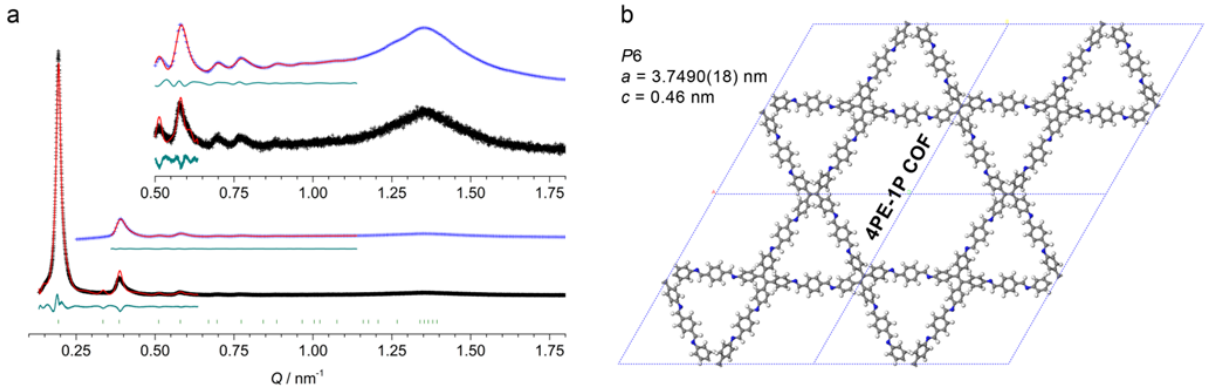

Figure 3.8 PXRD patterns Rietveld-refined structure of the 4PE-1P COF. a, Experimental synchrotron PXRD data (black: High-resolution X-ray scattering, blue: High energy X-ray total scattering) and Rietveld-refined patterns (red), difference plots (green) and Bragg positions (vertical ticks). **Insets**, magnified view onto the Q > 0.5 nm-1 region. **b**, Corresponding Rietveld-refined COF structure.

PXRD analysis and simulated structures of the 3PA- and 3PB-based COFs

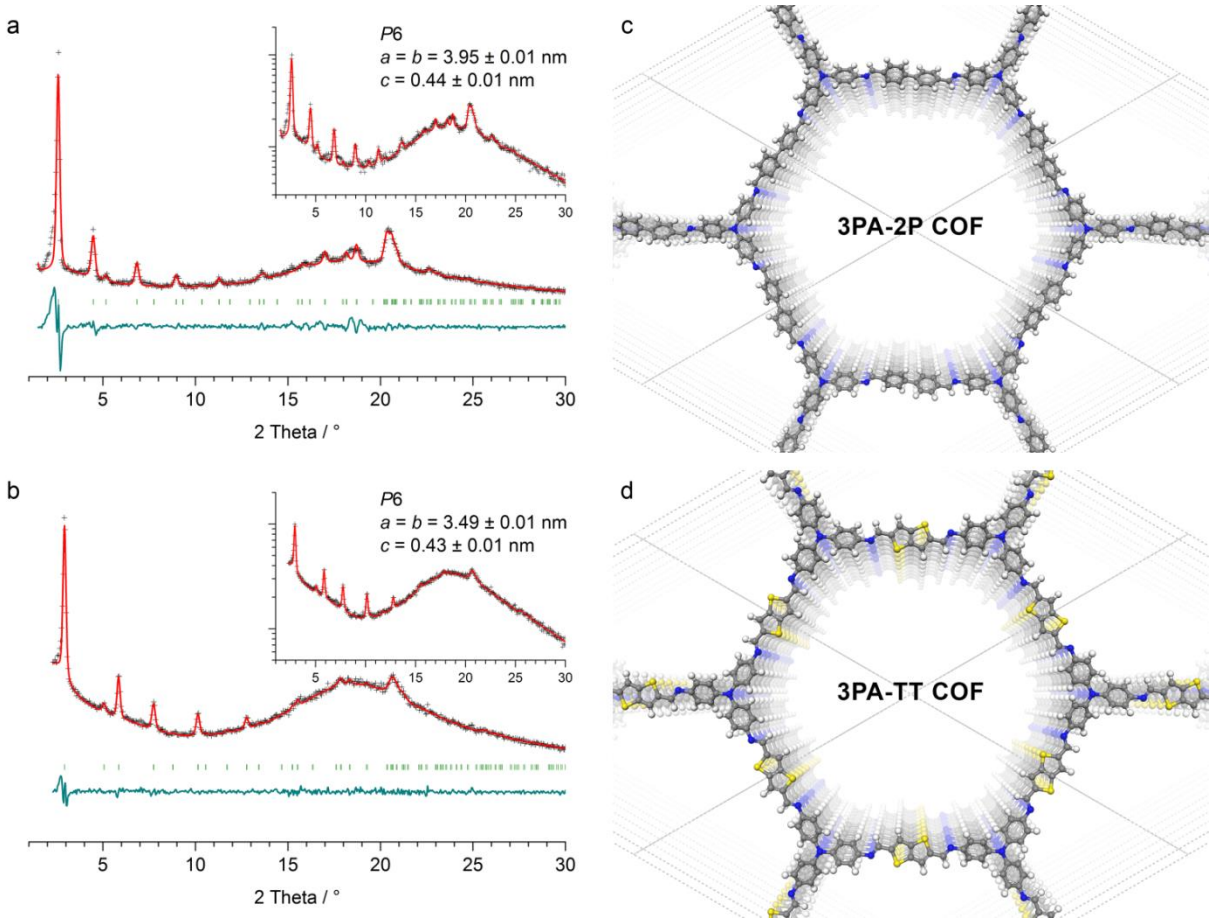

Figure 3.9 PXRD patterns of the triphenylamine (3PA) containing COFs and the corresponding simulated structures. a, **b**, Experimental (black symbols) and Pawley-refined (red) PXRD patterns, Bragg positions (green symbols) and difference plots (green) of the **3PA-2P** COF (**a**) and **3PA-TT** COF (**b**). **c**, **d** Simulated structures of the **3PA-2P** COF (**c**) and **3PA-TT** COF (**d**).

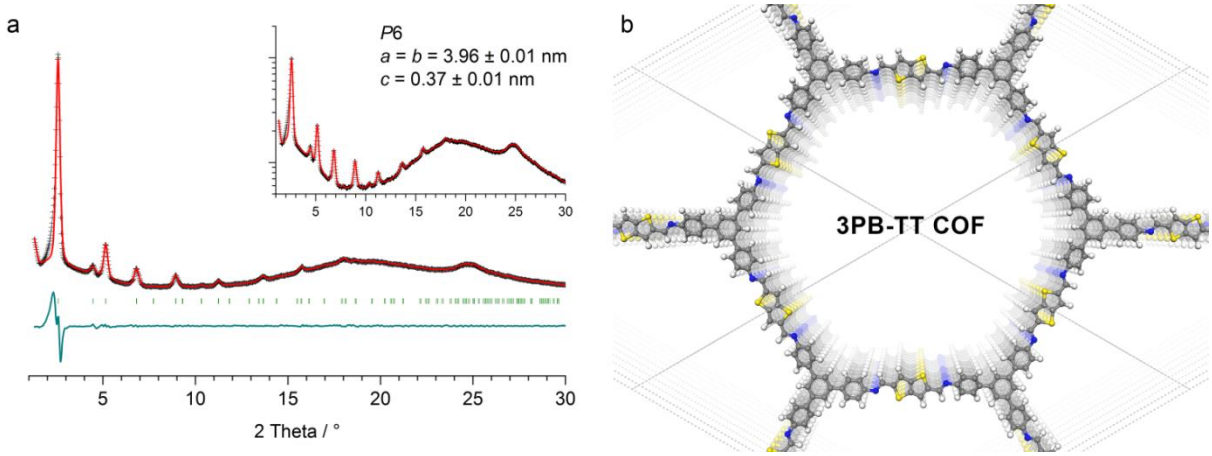

Figure 3.10 PXRD pattern of the triphenylbenzene (3PB) containing 3PB-TT COF and the corresponding simulated structure. a, Experimental (black symbols) and Pawley-refined (red) PXRD pattern, Bragg positions (green symbols) and difference plot (green). **b**, Simulated structure of the **3PB-TT** COF.

Stability tests

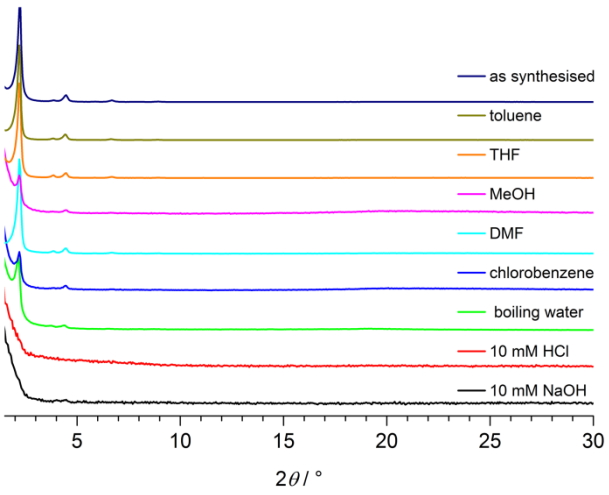

Figure 3.11 Stability tests of the 4PE-2P COF. Immersing the **4PE-2P** COF in common organic solvents or boiling water reveals the very high physiochemical stability of the new COF. The immersion times were 24 h for organic solvents and 4 h for water, acid and base, respectively.

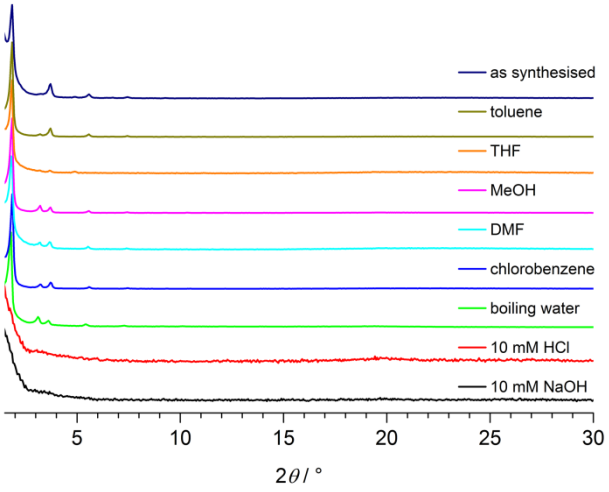

Figure 3.12 Stability tests of the 4PE-3P COF. The **4PE-3P** COF shows great physiochemical stability towards common organic solvents or boiling water. The immersion times were 24 h for organic solvents and 4 h for water, acid and base, respectively.

DFT simulations

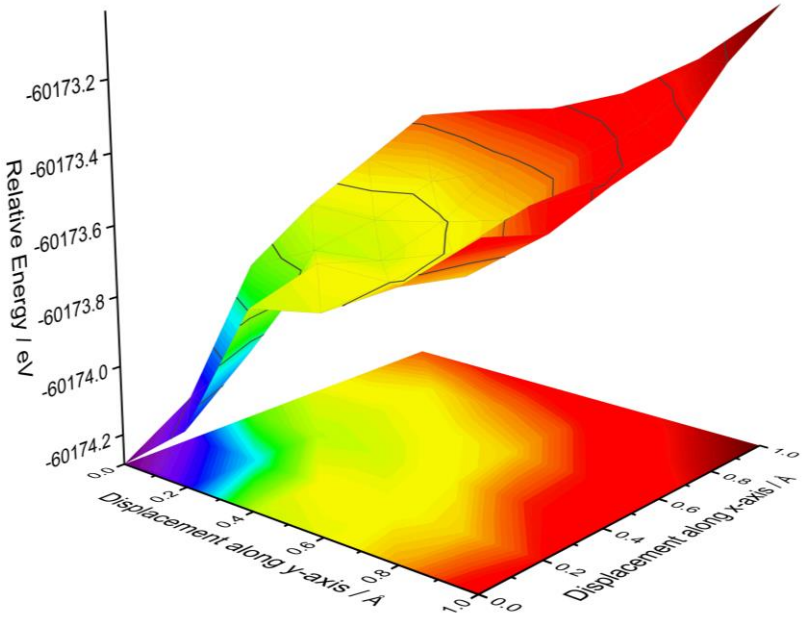

Figure 3.13 PBE+D potential energy surface for the horizontal displacement of two 4PE-2P layers relative to each other.

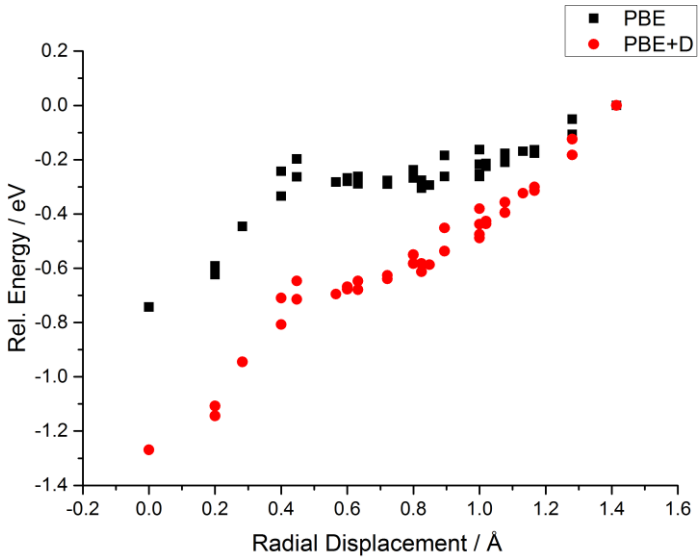

Figure 3.14 Comparison of the potential energy surfaces obtained from pure and dispersion-corrected PBE calculations. Plot of radial displacement versus relative energy for dispersion corrected (PBE+D) and uncorrected potential energy surface scans.

Optical spectroscopy

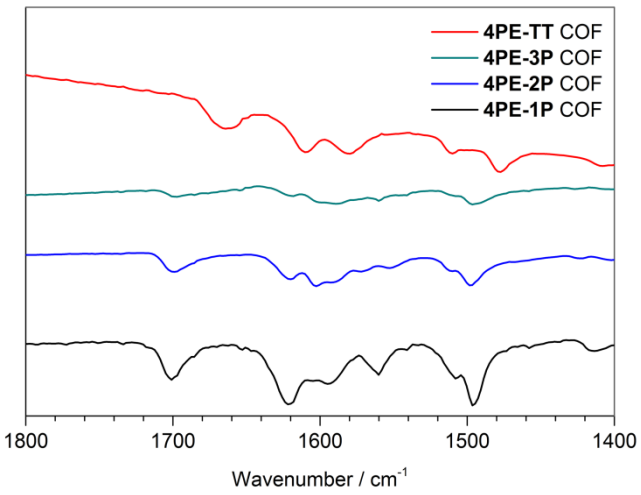

Figure 3.15 FT-IR spectra of the 4PE-based COFs. Enlargement of the fingerprint region below 1800 cm-1 showing the signals of the characteristic C=N stretching vibration (wavenumbers are given in the following table).

Table 3.2 C=N stretching vibrations of the **4PE**-based COFs.

	C=N / cm^{-1}
4PE-1P COF	1618
4PE-2P COF	1620
4PE-3P COF	1620
4PE-TT COF	1608

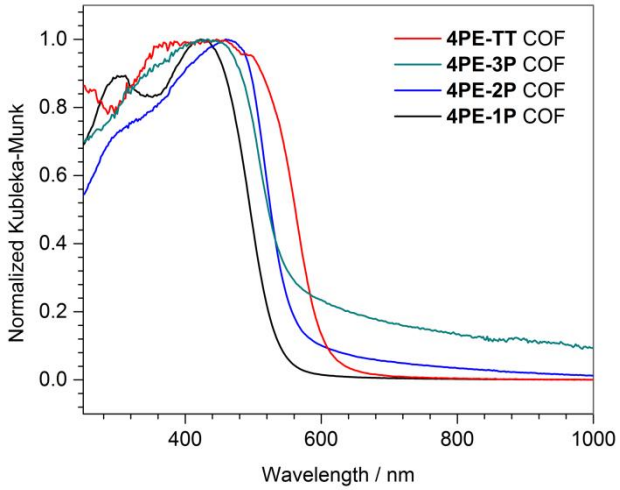

Figure 3.16 UV-vis diffuse reflectance spectra of the 4PE-containing COFs. The data are expressed in Kubelka-Munk units and normalised to the strongest absorption.

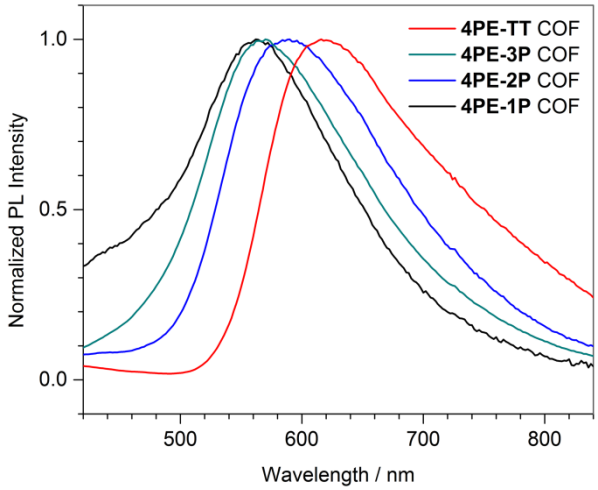

Figure 3.17 Photoluminescence emission spectra of the 4PE-based COFs. The COFs were measured as optically dense powders using 365 nm illumination.

Thermogravimetric analysis

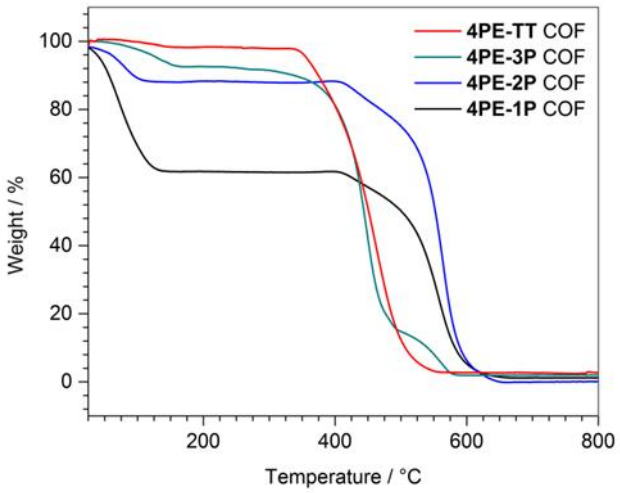

Figure 3.18 Thermogravimetric analysis of the 4PE-containing COFs. The samples were heated at 1 K min-1 in a constant flow of synthetic air.

NMR Spectroscopy

Compound 4

400 MHz, DMSO-d6

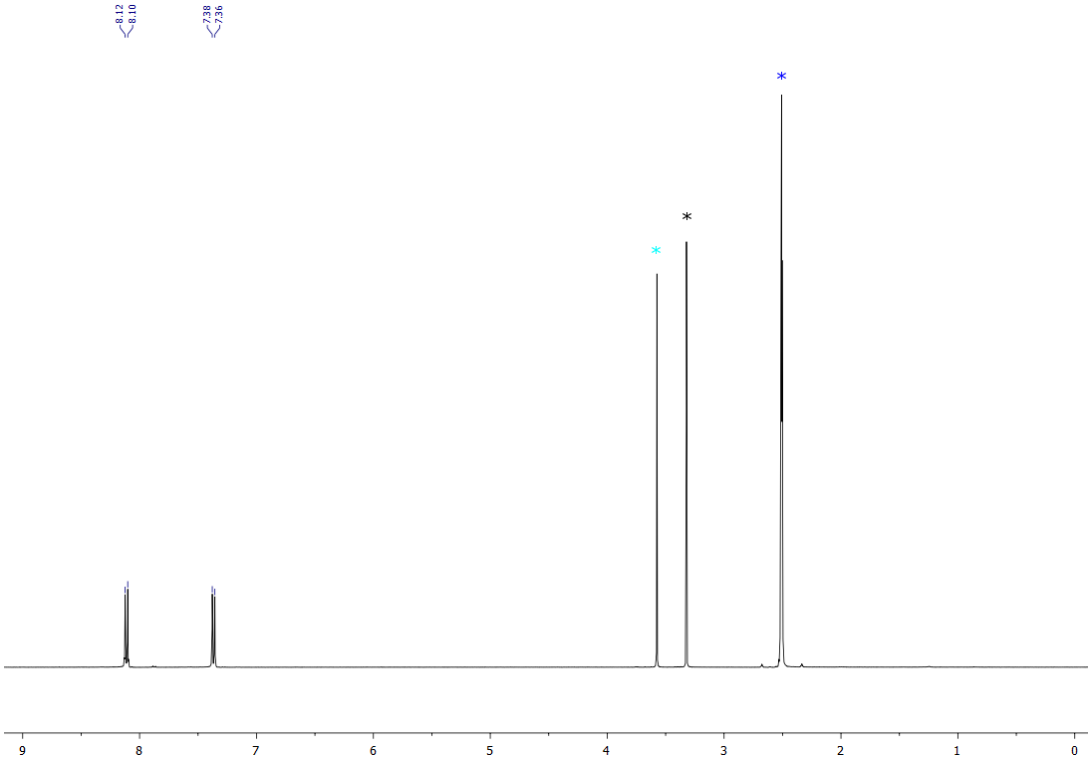

Solvent residues: 1,4-dioxane (cyan), water (black), DMSO (blue).

Compound 1

400 MHz, DMSO-d6

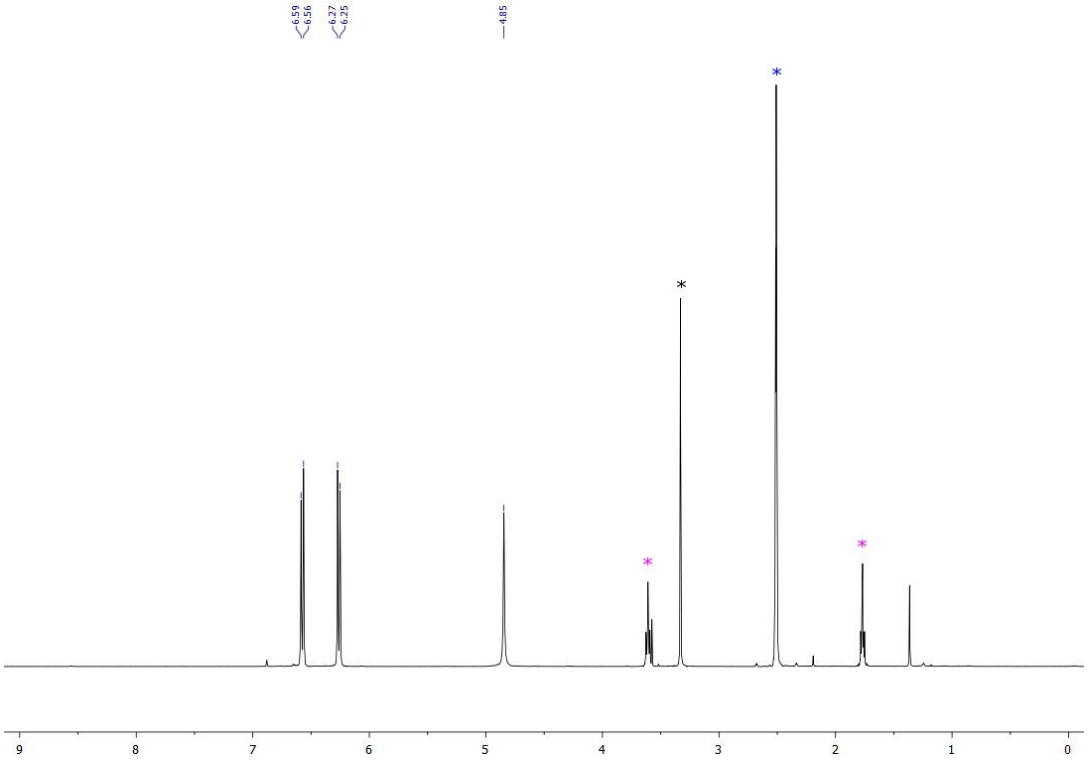

Solvent residues: THF (pink), water (black), DMSO (blue).

3.6 References

[1] C. J. Doonan, D. J. Tranchemontagne, T. G. Glover, J. R. Hunt, O. M. Yaghi, *Nature Chem.* **2010**, *2*, 235-238.

[2] M. G. Rabbani, A. K. Sekizkardes, Z. Kahveci, T. E. Reich, R. Ding, H. M. El-Kaderi, *Chem. Eur. J.* **2013**, *19*, 3324-3328.

[3] S.-Y. Ding, J. Gao, Q. Wang, Y. Zhang, W.-G. Song, C.-Y. Su, W. Wang, *J. Am. Chem. Soc.* **2011**, *133*, 19816-19822.

[4] M. Dogru, M. Handloser, F. Auras, T. Kunz, D. Medina, A. Hartschuh, P. Knochel, T. Bein, *Angew. Chem. Int. Ed.* **2013**, *52*, 2920-2924.

[5] M. Calik, F. Auras, L. M. Salonen, K. Bader, I. Grill, M. Handloser, D. D. Medina, M. Dogru, F. Loebermann, D. Trauner, A. Hartschuh, T. Bein, *J. Am. Chem. Soc.* **2014**, 17802-17807.

[6] S. Patwardhan, A. A. Kocherzhenko, F. C. Grozema, L. D. A. Siebbeles, *J. Phys. Chem. C* **2011**, *115*, 11768-11772.

[7] S. Jin, X. Ding, X. Feng, M. Supur, K. Furukawa, S. Takahashi, M. Addicoat, M. E. El-Khouly, T. Nakamura, S. Irle, S. Fukuzumi, A. Nagai, D. Jiang, *Angew. Chem. Int. Ed.* **2013**, *52*, 2017-2021.

[8] G. H. V. Bertrand, V. K. Michaelis, T.-C. Ong, R. G. Griffin, M. Dincă, *Proc. Natl Acad. Sci. USA* **2013**, *110*, 4923-4928.

[9] A. P. Côté, A. I. Benin, N. W. Ockwig, M. O'Keeffe, A. J. Matzger, O. M. Yaghi, *Science* **2005**, *310*, 1166-1170.

[10] E. L. Spitler, W. R. Dichtel, *Nature Chem.* **2010**, *2*, 672-677.

[11] M. Dogru, A. Sonnauer, A. Gavryushin, P. Knochel, T. Bein, *Chem. Commun.* **2011**, *47*, 1707-1709.

[12] E. L. Spitler, J. W. Colson, F. J. Uribe-Romo, A. R. Woll, M. R. Giovino, A. Saldivar, W. R. Dichtel, *Angew. Chem. Int. Ed.* **2012**, *51*, 2623-2627.

[13] D. D. Medina, V. Werner, F. Auras, R. Tautz, M. Dogru, J. Schuster, S. Linke, M. Döblinger, J. Feldmann, P. Knochel, T. Bein, *ACS Nano* **2014**, *8*, 4042-4052.

[14] D. D. Medina, J. M. Rotter, Y. Hu, M. Dogru, V. Werner, F. Auras, J. T. Markiewicz, P. Knochel, T. Bein, *J. Am. Chem. Soc.* **2015**, *137*, 1016-1019.

[15] F. J. Uribe-Romo, J. R. Hunt, H. Furukawa, C. Klock, M. O'Keeffe, O. M. Yaghi, *J. Am. Chem. Soc.* **2009**, *131*, 4570-4571.

[16] S. Wan, F. Gándara, A. Asano, H. Furukawa, A. Saeki, S. K. Dey, L. Liao, M. W. Ambrogio, Y. Y. Botros, X. Duan, S. Seki, J. F. Stoddart, O. M. Yaghi, *Chem. Mater.* **2011**, *23*, 4094-4097.

[17] J. Guo, Y. Xu, S. Jin, L. Chen, T. Kaji, Y. Honsho, M. A. Addicoat, J. Kim, A. Saeki, H. Ihee, S. Seki, S. Irle, M. Hiramoto, J. Gao, D. Jiang, *Nature Commun.* **2013**, *4*.

[18] Q. Fang, Z. Zhuang, S. Gu, R. B. Kaspar, J. Zheng, J. Wang, S. Qiu, Y. Yan, *Nature Commun.* **2014**, *5*.

[19] K. T. Jackson, T. E. Reich, H. M. El-Kaderi, *Chem. Commun.* **2012**, *48*, 8823-8825.

[20] P. Kuhn, M. Antonietti, A. Thomas, *Angew. Chem. Int. Ed.* **2008**, *47*, 3450-3453.

[21] Y.-B. Zhang, J. Su, H. Furukawa, Y. Yun, F. Gándara, A. Duong, X. Zou, O. M. Yaghi, *J. Am. Chem. Soc.* **2013**, *135*, 16336-16339.

[22] J. T. A. Jones, T. Hasell, X. Wu, J. Bacsa, K. E. Jelfs, M. Schmidtmann, S. Y. Chong, D. J. Adams, A. Trewin, F. Schiffman, F. Cora, B. Slater, A. Steiner, G. M. Day, A. I. Cooper, *Nature* **2011**, *474*, 367.

[23] S. Kandambeth, D. B. Shinde, M. K. Panda, B. Lukose, T. Heine, R. Banerjee, *Angew. Chem. Int. Ed.* **2013**, *52*, 13052-13056.

[24] D. B. Shinde, S. Kandambeth, P. Pachfule, R. R. Kumar, R. Banerjee, *Chem. Commun.* **2015**, 310-313.

[25] E. L. Spitler, B. T. Koo, J. L. Novotney, J. W. Colson, F. J. Uribe-Romo, G. D. Gutierrez, P. Clancy, W. R. Dichtel, *J. Am. Chem. Soc.* **2011**, *133*, 19416-19421.

[26] M. Dogru, T. Bein, *Chem. Commun.* **2014**, *50*, 5531-5546.

[27] T.-Y. Zhou, S.-Q. Xu, Q. Wen, Z.-F. Pang, X. Zhao, *J. Am. Chem. Soc.* **2014**, 15885-15888.

[28] T. Hasell, M. Schmidtmann, C. A. Stone, M. W. Smith, A. I. Cooper, *Chem. Commun.* **2012**, *48*, 4689-4691.

[29] J. Clark Stewart, D. Segall Matthew, J. Pickard Chris, J. Hasnip Phil, I. J. Probert Matt, K. Refson, C. Payne Mike, *Z. Kristallog. – Cryst. Mater.* **2005**, *220*, 567-570.

[30] J. P. Perdew, K. Burke, M. Ernzerhof, *Phys. Rev. Lett.* **1996**, *77*, 3865-3868.

[31] H. J. Monkhorst, J. D. Pack, *Phys. Rev. B* **1976**, *13*, 5188-5192.

[32] E. R. McNellis, J. Meyer, K. Reuter, *Phys. Rev. B* **2009**, *80*, 205414.

[33] A. Tkatchenko, M. Scheffler, *Phys. Rev. Lett.* **2009**, *102*, 073005.

[34] K. S. W. Sing, *Pure Appl. Chem.* **1985**, *57*, 603-613.

[35] M. Thommes, *Chem. Ing. Tech.* **2010**, *82*, 1059-1073.

[36] J. Lu, J. Zhang, *J. Mater. Chem. A* **2014**, *2*, 13831-13834.

[37] CrysAlis CCD, version 1.171.27p5 beta (release 01–04–2005 CrysAlis171.NET; compiled Apr 1 2005,17:53:34); Oxford Diffraction Ltd.: Oxfordshire, U. K.

[38] CrysAlis RED, version 1.171.27p5 beta (release 01–04–2005 CrysAlis171.NET; compiled Apr 1 2005, 17:53:34); Oxford Diffraction Ltd.: Oxfordshire, U. K.

[39] a) SIR-92, A Program for Crystal Structure Solution: A. Altomare, G. L. Cascarano, C. Giacovazzo, A. Guagliardi, J Appl Crystallogr, 1993, 26, 343–350.b) A. Altomare, M. C. Burla, M. Camalli, G. L. Cascarano, C. Giacovazzo, A. Guagliardi, A. G. G. Moliterni, G. Polidori, R. Spagna, J Appl Crystallogr, 1999, 32, 115–119.c) G. M. Sheldrick, SHELXS-97, Program for Crystal Structure Solution, University of Göttingen, Göttingen, Germany, 1997. d) G. M. Sheldrick, SHELXL-97, Program for the Refinement of Crystal Structures, University of Göttingen: Göttingen, Germany, 1999. e) L. A. Spek, PLATON, A Multipurpose Crystallographic Tool, Utrecht University: Utrecht, The Netherlands, 1999.

[40] SCALE3 ABSPACK - An Oxford Diffraction program (1.0.4, gui:1.0.3); Oxford Diffraction Ltd.: Oxfordshire, U. K., 2005.

4 Every Stack you Make

This chapter is based on the following publication:

Synchronized offset stacking – a concept for growing large-domain and highly crystalline 2D covalent organic frameworks

by Florian Auras, Laura Ascherl, Amir H. Hakimioun, Johannes T. Margraf, Fabian C. Hanusch, Stephan Reuter, Derya Bessinger, Markus Döblinger, Christina Hettstedt, Konstantin Karaghiosoff, Simon Herbert, Paul Knochel, Timothy Clark, Thomas Bein

J. Am. Chem. Soc. **2016**, *138*, 16703-16710.

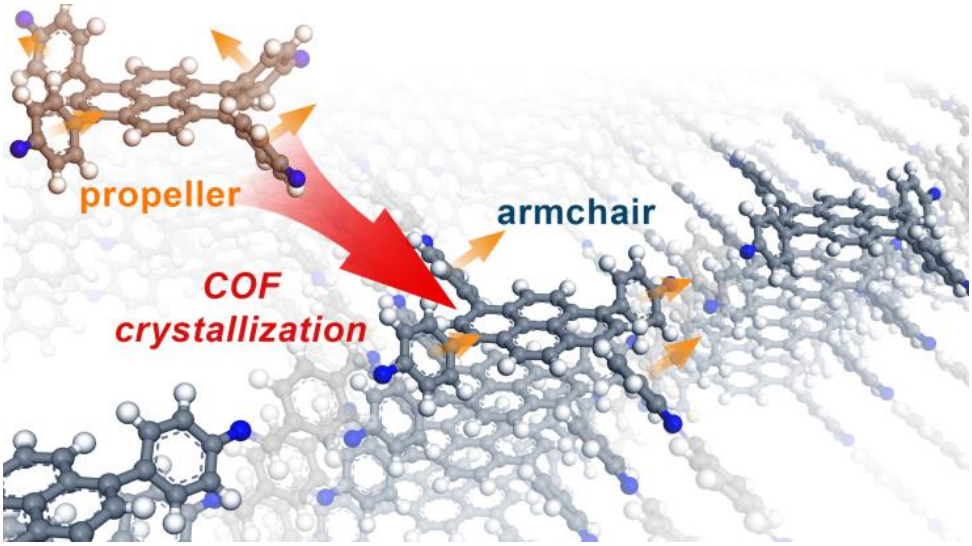

4.1 Abstract

Covalent organic frameworks (COFs), formed by reversible condensation of rigid organic building blocks, are crystalline and porous materials of great potential for catalysis and organic electronics. Particularly with a view of organic electronics, achieving a maximum degree of crystallinity and large domain sizes while allowing for a tightly π-stacked topology would be highly desirable. We present a design concept that uses the 3D geometry of the building blocks to generate a lattice of uniquely defined docking sites for the attachment of consecutive layers, thus allowing us to achieve a greatly improved degree of order within a given average number of attachment and detachment cycles during COF growth. Synchronization of the molecular geometry across several hundred nanometers promotes the growth of highly crystalline frameworks with unprecedented domain sizes. Spectroscopic data indicate considerable delocalization of excitations along the π-stacked columns and the feasibility of donor-acceptor excitations across the imine bonds. The frameworks developed in this study can serve as a blueprint for the design of a broad range of tailor-made 2D COFs with extended π-conjugated building blocks for applications in photocatalysis and optoelectronics.

4.2 Introduction

Growing extended and high quality crystals of molecular framework materials has remained a challenge, particularly in the case of covalent organic frameworks (COFs), where the connections between the individual building blocks are formed by covalent bonds. COFs are porous long-range ordered materials that have recently attracted considerable scientific attention as candidates for gas storage and separation,[1] [2] catalysis,[3] [4] and as new materials for organic electronics and optoelectronics.[5] [6] [7] In view of the last potential application, COFs that are covalently linked in two dimensions while held together by π-stacking in the third dimension (referred to as 2D-COFs), are of particular interest.[8] [9] The self-assembled π-stacked columns that are formed in these materials enable electronic transport across the layers.[10] [11] Additionally, if the linkage between the individual building blocks that constitute the 2D layers is π-conjugated, as for example in the case of imine-linked frameworks, the conductivity might be extended to the other two dimensions. The aligned open channels that surround the molecular stacks can be used to alter the properties or extend the functionality of the host material through the incorporation of guest molecules, such as fullerenes,[5] [12] [13] tetracyanoquinodimethane,[14] or iodine.[15] [16]

In view of these potential applications it is essential to construct highly crystalline (i.e. a maximum degree of coherent long-range order within a crystal domain) frameworks with large crystal domains and to be able to select from a broad range of specialized building blocks. Possible applications in gas separation or catalysis require fully accessible pores that are not blocked due to stacking faults or amorphous regions. The factor of crystallinity becomes even more important if applications in electronics or optoelectronics are intended, as stacking faults could disrupt the conductive π-stacked columns, and defect sites and grain boundaries could act as traps and recombination sites for excitons or charges.

COFs are synthesized via reversible formation of covalent bonds, the most widely applied linkage motifs to date being boronate esters,[17] [18] [19] [20] imines,[21] [22] [23] [24] and hydrazones.[25] [26] In all of these cases, this reversibility of the bond formation under reaction conditions provides the growing COF crystal with a functional self-healing mechanism, a factor of key importance for obtaining a long-range ordered network.[27] However, as the formation and cleavage of these covalent bonds involve several reaction partners and intermediates, these processes will inherently be more complex and typically slower than for example the coordinative network formation in metal-organic frameworks (MOFs), or the crystallization of small organic molecules, which is driven mainly by Coulomb and dispersion interactions. As a result, crystalline COF structures can be achieved only on very small length scales of typically a few tens to hundred nanometers. If it were possible, however, to direct the attachment of a building block to the growing COF domain such that the correct orientation is highly favored over all other possible attachment geometries, one could expect to obtain enhanced crystallinity within a given number of average attachment and detachment cycles per building block. This could ultimately pave the way for the development of COF single crystals.

We have recently developed a concept for growing highly crystalline 2D COFs that exhibit well-defined hexagonal facets and are devoid of amorphous regions between the individual crystallites.[28] In this concept, the 3D molecular conformation generates a uniquely defined docking site for the attachment of a successive COF layer, thus greatly lowering the probability of stacking faults and strained regions due to defects within the individual layers. While we have realized this deterministic approach to COF growth using propeller-shaped central building blocks, it would be desirable to formulate a geometric concept that imposes less strict boundary conditions on the selection of building blocks. Additionally, enabling

significant π-orbital overlap between extended opto- and electroactive building blocks such as acenes, porphyrins, or tetrathiafulvalenes would be a prerequisite for highly conductive frameworks.

Here, we present a design concept for growing highly crystalline COFs with domain sizes on the order of half a micrometer based on the synchronized offset-stacking of the building blocks. The core moiety of the multidentate building block is hereby allowed to π-stack, thus providing the framework with a very stable interlayer distance and enabling electronic contact between the layers. The four phenylene substituents on this core serve a dual purpose. They bear the chemical functionality used to cross-link the framework, but also define the magnitude and direction of the offset between two COF layers. In this way, the molecular geometry of the central building block gives rise to a uniquely defined docking site that can guide the attachment of successive layers. Implementing this concept, we synthesized a series of highly crystalline pyrene-based COFs with a slip-stacked quasi-quadratic structure. Time-resolved and steady-state optical spectroscopy revealed considerable delocalization of excitations along the π-stacked columns and, depending on the selection of the building blocks, electronic coupling and charge-transfer transitions across the imine bonds.

4.3 Results and discussion

To implement our concept we chose 1,3,6,8-tetrakis(4-aminophenyl)pyrene (**1**) as central building block. Pyrene-based building blocks used in previous COF studies were found to produce appreciably well-ordered networks.[2] [29] [30]As is the case for most imine-linked COFs, the amine functionality required to cross-link the network is not directly attached to the core, but added in the form of a 4-aminophenyl substituent. In addition to practical reasons such as straightforward synthesis *via* cross-coupling reactions and a more core-independent reactivity of the aniline groups compared to a directly attached amine, these anilines provide the non-planarity of the building block that is required to generate a geometric docking site.

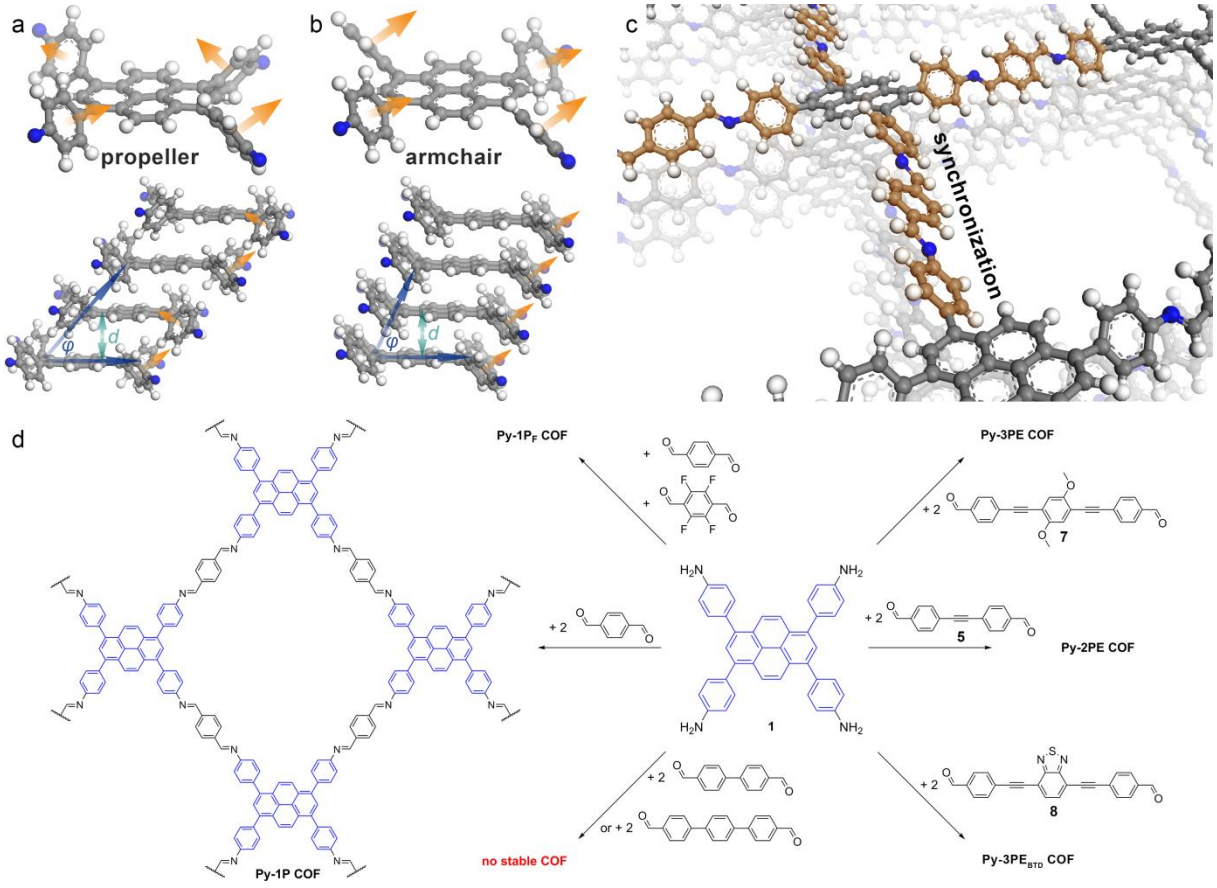

Figure 4.1 Possible molecular conformations and corresponding stacking arrangements of 1,3,6,8-tetrakis(4-aminophenyl)pyrene when incorporated into a COF (C, grey; H, white; N, blue). In the 'propeller' conformation (**a**) the normal vectors of the phenylenes describe a circle. These molecules form offset stacks of alternating left- and right-handed propellers, whereby the phenylenes arrange in an edge-on-face sequence. In the 'armchair' configuration (**b**) the normal vectors of the phenylenes point into the same direction. Owing to the reduced steric demands in this configuration the molecules can stack more closely and with reduced lateral offset. (**c**) Forming defect-free COF domains requires ensuring the same stacking direction of neighboring pyrene stacks. We propose that this can be achieved by synchronizing the orientation of the phenylenes across flat, cofacially stacked bridges. (**d**) Chemical structures of the building blocks used in the synthesis of the new pyrene-based COFs.

Steric repulsion between the phenylene hydrogens and the six hydrogen atoms of the core causes the four phenylenes to be rotated against the pyrene by typically 40-60°.[31] In contrast to smaller building blocks such as 1,1,2,2-tetrakis(4-aminophenyl)ethene,[28] the phenylenes on the pyrene are not sterically coupled and thus the molecule can in theory adopt several geometric configurations; the most symmetrical ones are shown in Figures 4.1a and b.

In order to study possible stacking modes of the tetraphenylpyrene subunit when incorporated into a COF, we synthesized a molecular model compound **2** by imine condensation between **1** and four equivalents of benzaldehyde (see the Supporting Information for experimental details). This model compound was found to crystallize in the 'propeller' configuration also observed for the parent tetraphenylpyrene,[31] with slipped stacks of alternating right- and left-handed propellers (SI, Figure 4.6). Because of the sterically demanding edge-on-face configuration of the four phenylenes, the angle φ at which the pyrene layers are offset is 48.9°. The average spacing of the pyrenes d in this arrangement is approximately 0.41 nm, considerably larger than typical distances of π-stacked acenes. [11]

We then simulated a possible COF structure for this stacking motif, linking **1** with the smallest aromatic dialdehyde, i.e. terephthalaldehyde (SI, Figure 4.7a). Balancing the attractive interactions between the pyrene cores and the steric demands of the edge-on-face stacked phenylenes leads to the formation of fairly offset pyrene stacks in the framework (Figure 4.1a). We find φ = 50.9°, and d = 0.42 nm for the simulated COF, in good agreement with the experimental parameters for the molecular crystals of **2**.

As this 'propeller' structure is not particularly close-packed, we reasoned that there might be another geometric arrangement that could allow for stronger interactions between the COF layers and thus produce a thermodynamically more stable framework. The 'armchair' configuration, in which the normal vectors of the four phenylenes point in the same direction, would allow for the cofacial arrangement of both the pyrene cores and the phenylenes (Figure 4.1b). The distances in this geometry would be determined by the π-π interactions. Although this molecular configuration has, to the best of our knowledge, not yet been observed in molecular crystals of tetraphenylpyrene derivatives, recent examples of tetra(2-pyridyl)ethene complexes have shown that external interactions, for example the complexation of a transition metal ion, can provide sufficient driving force for the transition from the 'propeller' to the 'armchair' configuration.[32]

Simulating the above COF with the pyrenes in the 'armchair' configuration indeed led to a much closer-packed framework (SI, Figure 4.7b). Here the pyrenes form slip-stacked columns with greatly reduced offset and shorter core-to-core distances of φ = 70.3° and d = 0.39 nm, respectively (Figure 4.1b).

Comparing the two molecular configurations regarding their ability to direct the attachment of successive COF layers reveals further differences. The ‘armchair’ conformation generates a uniquely defined docking site in which the stacking distance and the lateral offset are defined by the π-π interactions between the pyrene cores and the phenylenes, respectively (SI, Figure 4.8b). Here, also the direction of the offset is uniquely defined through the tilt of the phenylenes with respect to the core. In the case of the ‘propeller’ configuration, however, a single building block can only define the stacking distance and the magnitude of the offset. As in this configuration the phenylenes of a single molecule do not possess a preferred direction, the second building block can attach in two positions (SI, Figure 4.8a). Directional information that can be transferred to successive building blocks *via* the chains of edge-on-face oriented phenylenes only exists once a dimer has formed.

At this stage, it remains difficult to predict which of the above configurations will be present in our COFs, because this might also be influenced by the choice of the linear building block. As the two conformers stack at very different offset angles, however, the experimentally determined unit cell might allow for conclusions regarding the molecular geometry.

In a defect-free crystal, all pyrene stacks would be offset in the same direction. As the incorporation of a pyrene stack with the ‘wrong’ offset direction would cause immense strain and a large number of defects to compensate it, the synchronization of all pyrene stacks throughout a crystal domain is of key importance. In the ‘armchair’ case, we anticipate that this can be achieved if the linear building block is able to transport information about the orientation of the phenylene moieties from one pyrene to its neighbors, ensuring coplanar orientation (Figure 4.1c). This synchronization mechanism is expected to work well with flat and rigid linear building blocks, such as terephthalaldehyde, whereas twisted molecules such as biphenyl-4,4’-dicarbaldehyde fail to ensure the coplanar orientation of the phenylenes and hence are not expected to form a stable framework. For geometric reasons the ‘propeller’ conformation, on the other hand, cannot incorporate aligned and closely packed linear building blocks. We thus expected it to be less sensitive to the flatness of the linear units, but also less effective for achieving long-range synchronization.

We used the 1,3,6,8-tetrakis(4-aminophenyl)pyrene building block (**1**) in the solvothermal synthesis of imine-linked COFs in combination with a series of linear dialdehydes (Figure 4.1d, see the SI for experimental details). Regarding the choice of the building blocks, in view of the above considerations we reasoned that the differences between the twisted biphenyl and

terphenyl dialdehydes and their flat ethynylene-bridged counterparts should provide us with clear conclusions about the preferred stacking mode in our COFs. The flat building blocks, and in particular the 2,1,3-benzothiadiazole-substituted **8**, would moreover allow us to study the electronic coupling between the pyrene cores and their π-conjugated electron-rich (**7**) or –deficient (**8**) counterparts.

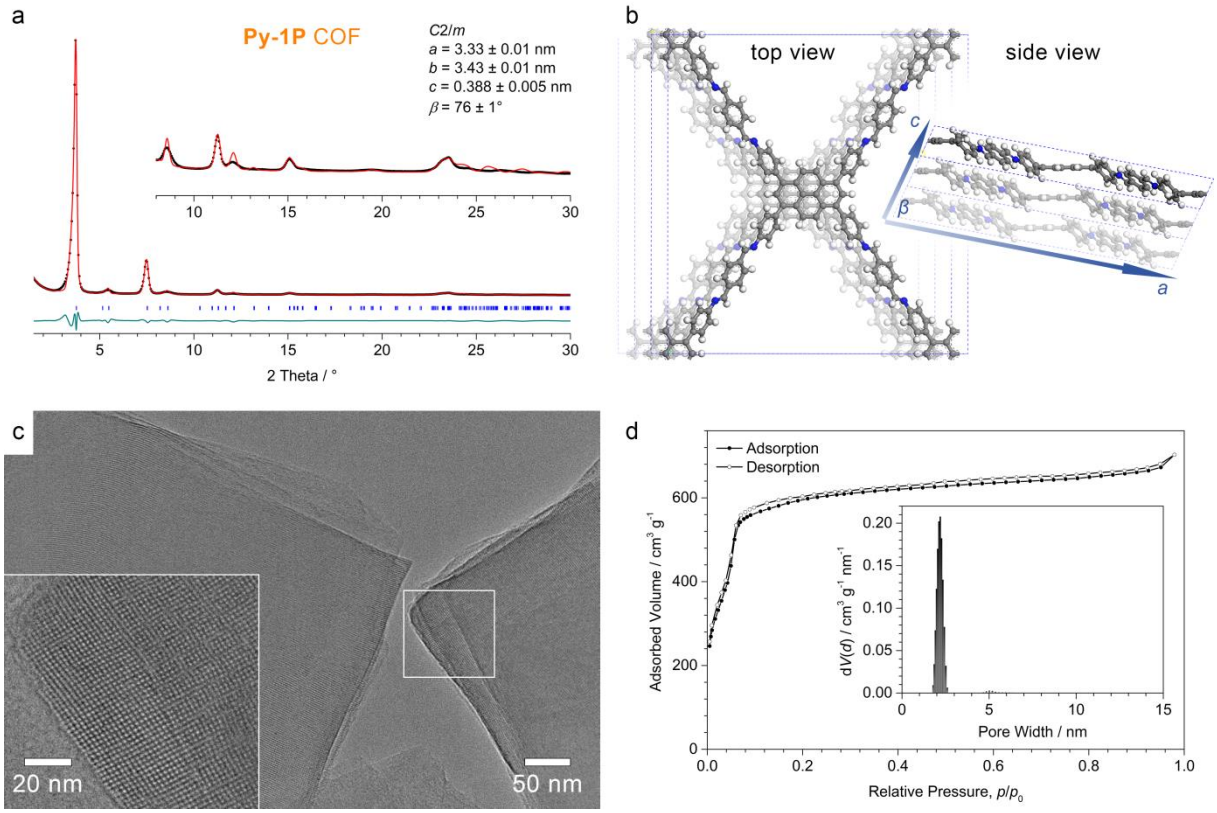

Figure 4.2 (**a**) Experimental PXRD pattern (black dots) of the **Py-1P** COF. Rietveld refinement (red line) provides a very good fit to the experimental data with only minimal differences (the green line shows the difference plot between the experimental PXRD pattern and the one obtained by Rietveld refinement; Rwp = 4.91%, Rp = 10.32%). Bragg positions are indicated by blue ticks. Inset, magnified view of the 2θ > 8° region. (**b**) The corresponding unit cell with the viewing direction normal to the pyrene core (left) and onto the side (right). (**c**) High resolution TEM image showing the large crystal domains of the **Py-1P** COF. Inset, magnified view showing the pseudo-quadratic arrangement of the mesopores. The white frame indicates the magnified area. (**d**) Nitrogen sorption isotherm recorded at 77 K. Inset, QSDFT calculation using an equilibrium model yields the very narrow pore-size distribution that is anticipated for a fully crystalline lattice.

The powder X-ray diffraction pattern of the **Py-1P** COF exhibits a large number of well-defined reflections and only very weak background, confirming the formation of a highly

crystalline framework (Figure 4.2a). In the following we use the term ‘crystallinity’ to refer to the degree of coherent long-range order within a COF domain (as opposed to the domain size). Rietveld refinement using the ‘armchair’ configuration and assuming *C*2/*m* symmetry reproduced the experimental pattern very well and yielded the lattice harameters a = 3.33 ± 0.01 nm, b = 3.43 ± 0.01 nm, c = 0.388 ± 0.005 nm, β = 76 ± 1 ° (Figure 4.2b).

Since the unit cell of the **Py-1P** COF contains a large number of light atoms and the reflections are broadened even for this well-crystallized framework, it was not possible to refine the coordinates of individual atoms and thus directly observe the conformation of the tetraphenylpyrene. Given the differences in stacking behavior between the two possible structures, however, it is possible to draw conclusions on the molecular geometry from the following considerations:

The comparison between the experimental pattern and the theoretical patterns calculated from the two simulated COF structures yields a good match for the ‘armchair’ configuration with only slightly shifted reflection positions, whereas the ‘propeller’ structure does not resemble the experimental pattern very well ,, Figures 4.7c and 4.7d).

The lattice parameters c and β (see above), which can be refined with high accuracy from the position and splitting of the double-peak at 2θ = 23.4° and which are very sensitive to the packing of the pyrenes, provide a second indication in favor of the less offset and closer-packed ‘armchair’ configuration.

The packing geometry of the ‘armchair’ structure was further confirmed by density functional theory (DFT) calculations using the CASTEP code with the generalized-gradient-approximation (GGA) PBE functional and a correction for dispersion interactions (see the SI for details). These quantum-mechanical simulations yielded β = 75.2°, in very good agreement with the experimental unit cell.

In order to obtain independent experimental evidence for the presence of the ‘armchair’ configuration in the **Py-1P** COF, we synthesized this framework using a 1:1 mixture of terephthalaldehyde and 2,3,5,6-tetrafluoroterephthalaldehyde. This mixture has been found to add an additional electrostatic stabilization to COFs *via* the formation face-on-face oriented stacks of alternating fluorinated and non-fluorinated phenylenes.[33] The PXRD pattern of this **Py-1P$_F$** COF exhibits the same sequence of reflections and in particular contains the double-peak that stems mainly from the 111 and 001 reflections, here slightly shifted to 23.6° (SI,

Figure 4.9). The unit cell parameters for this double-layer COF after Rietveld refinement in the space group *P*2/*m* are a = 3.38 ± 0.02 nm, b = 3.40 ± 0.02 nm, c = 0.772 ± 0.01 nm, β = 75 ± 2 °. The experimental finding that the forced face-to-face arrangement of the bridges in the **Py-1P$_F$** COF gives rise to a framework that is almost identical to the non-fluorinated **Py-1P** COF, is another strong indication for the presence of cofacially stacked bridges and hence 'armchair'-type pyrenes in our COFs.

In conclusion, based on the above findings we offer strong theoretical and experimental evidence for the presence of the 'armchair' configuration of the tetraphenylpyrenes in the **Py-1P** COF. To the best of our knowledge, this is the first time that the crystallization of a COF framework has been observed to change the geometry of one of its constituents into a conformation that does not occur in molecular solids.

Transmission electron microscopy (TEM) images of the **Py-1P** COF reveal that this material crystallizes in the form of platelets with very large domain sizes of 300-500 nm (Figure 4.2c). Domains oriented with their crystallographic *a*-*b* plane perpendicular to the viewing direction show the highly ordered pseudo-quadratic arrangement of the mesopores. Moreover, the individual crystallites feature well-defined facets that are devoid of any visible amorphous regions.

With pore diagonals of 2.00 nm, 2.44 nm, and 2.76 nm (bridge-to-bridge and the two pyrene-to-pyrene distances, respectively) in the refined structure, the **Py-1P** COF is at the border between micro- and mesoporosity. Its type IV nitrogen sorption isotherm, which is typical for mesoporous materials, exhibits a sharp step and an H1 hysteresis loop at low p/p_0 values, confirming the expected small pore size (Figure 4.2d). The pore diameter calculated by quenched-solid density functional theory (QSDFT) using an equilibrium model and assuming a cylindrical pore geometry is 2.20 nm, in very good agreement with the averaged pore diagonals. The Brunauer–Emmett–Teller (BET) surface area of the **Py-1P** COF is 2210 ± 50 m^2 g^{-1} with a total pore volume of 1.09 ± 0.03 cm^3 g^{-1}. These values are in excellent agreement with the Connolly surface and total pore volume of 2160 m^2 g^{-1} and 0.98 cm^3 g^{-1}, respectively, confirming that the pores are open and fully accessible.

The formation of the COF during the solvothermal synthesis proceeds, similar to other imine-linked frameworks,[34] *via* an initially formed amorphous network that is converted into the crystalline **Py-1P** COF over the course of several hours (SI, Figure 4.11). After 1 d the main

reflections hardly change in intensity any more, indicating nearly full conversion to the crystalline COF. Weaker reflections, however, continue to become more distinct, suggesting an ongoing recrystallization of the material accompanied by further improvements in crystal quality. In combination with our lock-and-key design of the building blocks, this mechanism can reliably produce fully crystallized nano- to microcrystalline COFs. Even larger crystals can be anticipated if future improvements in the linkage chemistry could suppress the fast condensation of the amorphous network.

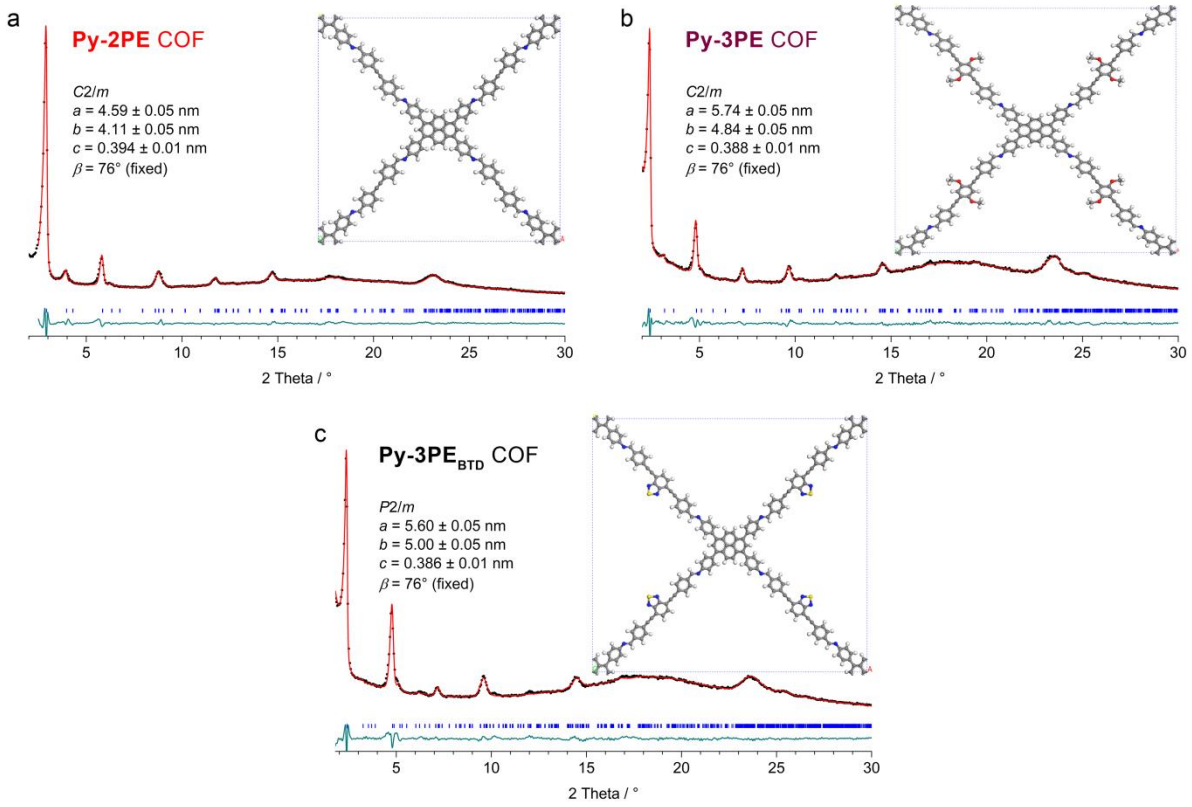

Figure 4.3 Experimental PXRD patterns (black dots), Pawley-refined patterns (red lines), difference plots (green lines), and Bragg positions (blue ticks) of (**a**) the **Py-2PE**, (**b**) the **Py-3PE**, and (**c**) the **Py-3PE$_{BTD}$** COFs, respectively. Insets, the corresponding refined unit cells. Compared to the **Py-1P** COF, the reflection intensities of these COFs appear weaker due to the inclusion of trapped oligomers in the pores that cannot be fully removed without compromising the crystallinity of the framework.

In order to broaden the scope of the above concept we used a series of directly linked and ethynylene-bridged building blocks in the COF syntheses. As expected from the above geometric considerations, the twisted biphenyl (**2P**) and terphenyl (**3P**) derived building blocks fail to produce stable crystalline frameworks. The **Py-2P** COF forms in the reaction

solution, but quickly loses its long-range order upon evaporation of the solvent (SI, Figure 4.10).

If an acetylene bridge, however, is introduced between the phenylenes, the molecule can adopt a planar configuration that should allow for the synthesis of well-ordered 'armchair' type frameworks.[35] Indeed, we were able to obtain crystalline COF materials using the acetylene-bridged building blocks (Figures 4.3a and 4.3b). Pawley refinements carried out in the space group *C*2/*m* with the angle β fixed at 76° (i.e. assuming similar stacking offset as for the **Py-1P** COF) yielded the lattice parameters a = 4.59 ± 0.05 nm, b = 4.11 ± 0.05 nm, c = 0.394 ± 0.01 nm, β = 76° (fixed) and a = 5.74 ± 0.05 nm, b = 4.84 ± 0.05 nm, c = 0.388 ± 0.01 nm, β = 76° (fixed) for the **Py-2PE** and the **Py-3PE** COFs, respectively.

This concept allows us also to incorporate additional electronic functionality into the building blocks and thus modulate the electronic structure of the resulting frameworks. We demonstrate this by applying a 2,1,3-benzothiadiazole-modified (BTD) version of the 3PE building block. Pawley refinement of the **Py-3PE$_{BTD}$** COF in the space group *P*2/*m*, assuming the most symmetric arrangement of the BTD units in the framework, produced the lattice parameters a = 5.60 ± 0.05 nm, b = 5.00 ± 0.05 nm, c = 0.386 ± 0.01 nm, β = 76° (fixed) (Figure 4.3c).

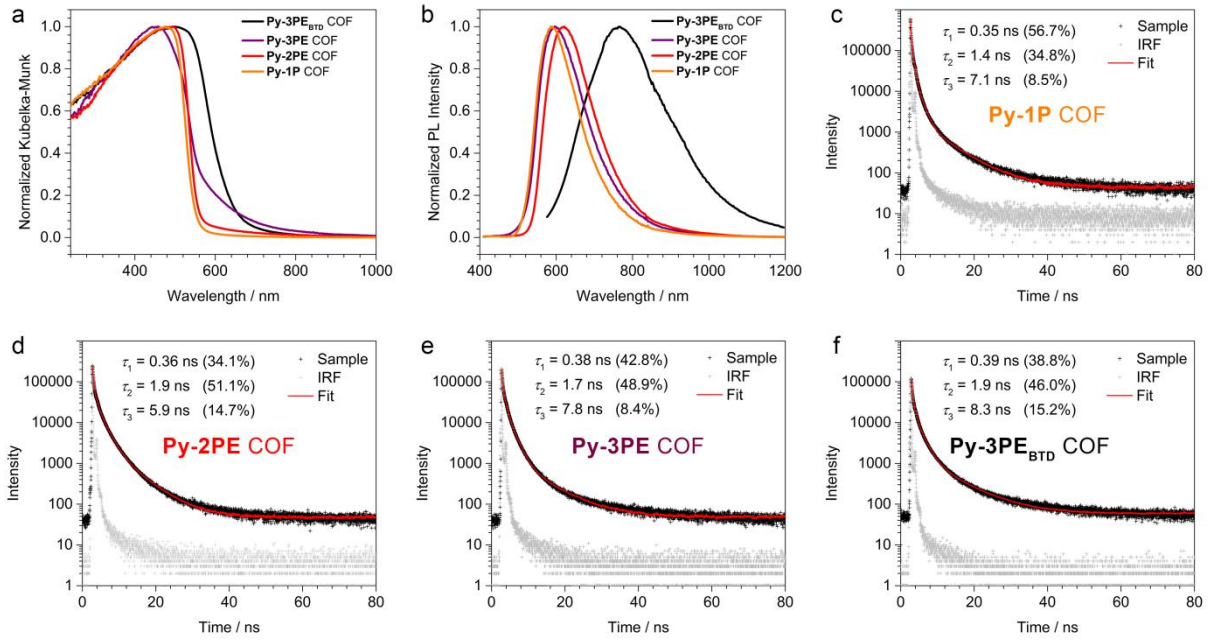

Figure 4.4 Diffuse reflectance (**a**) and PL spectra (**b**) of the four COFs. (**c**)-(**f**), TCSPC traces (black), instrument response functions (IRF, grey), and the corresponding tri-exponential

deconvolution fits of the COFs (red lines). The fraction of collected photons corresponding to the respective lifetimes are given in brackets. Photoexcitation was achieved with a picosecond diode laser at 403 nm.

The new pyrene-based COFs are intensely colored solids ranging from bright orange (**Py-1P** and **Py-2PE** COFs) to deep red (**Py-3PE$_{BTD}$** COF). UV-VIS diffuse reflectance spectra corroborate these observations (Figure 4.4a). Compared to a solution of compound **1**, the framework absorption edge is red-shifted by about 100-150 nm, indicating considerable electronic delocalization across the pyrene stacks (SI, Figure 4.16). The **Py-1P** and **Py-2PE** COFs feature particularly sharp absorption onsets around 560 nm, whereas the absorption spectrum of the **Py-3PE** COF is more curved in the normalized representation due to an overlap of the pyrene and the acetylene bridge absorption. In all three cases, the steepest rise in the absorption spectrum is at almost the same wavelength, indicating that the optical transitions are dominated by the central pyrene building block and only slightly affected by the additional π-conjugation of the acetylenes. This interpretation is supported by the corresponding photoluminescence (PL) spectra (Figure 4.4b), showing similar emission at around 600 nm.

In order to obtain a better understanding of the electronic processes in these materials, we determined the absolute external photoluminescence quantum yields (PLQYs) using an integrating sphere (SI, Table S2),[36] [37] and studied the PL decay dynamics *via* time-correlated single photon counting (TCSPC). All three COFs exhibit PLQYs of around 0.2% and tri-exponential decay curves with almost identical lifetimes. These results confirm that, irrespective of the length of the π-conjugated bridge, the electronic processes are dominated by the tetraphenylpyrene moiety.

Placing a strongly electron-withdrawing BTD group into the bridge, however, does change the band gap of the material. The red-shifted absorption and emission spectra are indicative of a charge-transfer excitation at energies below the π-π* transition of the individual building blocks. This is supported by the significantly lower PLQY of the **Py-3PE$_{BTD}$** COF. The recombination of the emissive states, however, appears at very similar time constants as for the other three COFs, highlighting the strong influence of the central building block on the optoelectronic properties.

4.4 Conclusion

In this study, we used the three-dimensional geometry of a tetraphenylpyrene-derived building block to generate a periodic lattice of synchronized docking sites for the attachment of consecutive COF layers. This way we were able to grow highly crystalline 2D COFs with domain sizes on the order of half a micrometer that feature well-defined facets and are devoid of any observable amorphous regions. In combination with future improvements in the linkage chemistry, this geometric guidance could pave the way for the development of COF single crystals. Our design principle also allows for the simultaneous incorporation of π-stacked central building blocks and π-stacked bridges, thus enabling electronic communication between all subunits of the framework. Studying the optoelectronic properties of a series of pyrene-based COFs revealed significant delocalization of excitations along the pyrene stacks and showed that charge-transfer excitations are possible across the imine bonds. The frameworks developed in this study can serve as a blueprint for designing a broad range of tailor-made 2D COFs with extended π-conjugated building blocks for applications in photocatalysis and optoelectronics.

4.5 Supporting information

Nuclear magnetic resonance (NMR) spectra were recorded on Bruker AV 400 and AV 400 TR spectrometers. Proton chemical shifts are expressed in parts per million (δ scale) and are calibrated using residual undeuterated solvent peaks as an internal reference ($CDCl_3$: 7.26, DMSO-d_6: 2.50). Data for ^{1}H NMR spectra are reported in the following way: chemical shift (δ ppm) (multiplicity, coupling constant/Hz, integration). Multiplicities are reported as follows: s = singlet, d = doublet, t = triplet, q = quartet, m = multiplet, br = broad, or combinations thereof. Magic angle spinning (MAS) **solid-state Nuclear magnetic resonance** (ssNMR) spectra were recorded using a Bruker Avance III-500 spectrometer.

Powder X-ray diffraction (PXRD) measurements were performed using a Bruker D8 Discover with Ni-filtered Cu K_α radiation and a LynxEye position-sensitive detector. Background correction was performed using spline-interpolated and intensity-adapted measurements of the empty sample holder.

The **structure models of the COFs** were built using the Forcite module of the Accelrys Materials Studio software package. For each COF structure we applied the space group with the highest possible symmetry, taking into account the rotation of the phenylenes versus the pyrene core. Structure refinements using either the Rietveld (**Py-1P** and **Py-1P$_F$** COFs) or the Pawley method (**Py-2PE**, **Py-3PE**, **Py-3PE$_{BTD}$** COFs) were then carried out as implemented in the Reflex module of the Materials Studio software. Pseudo-Voigt peak profiles were used and peak asymmetry was corrected using the Finger-Cox-Jephcoat method. A crystallite size of 500 nm along *a* and *b* and 200 nm along *c*, and lattice strain parameters of 0.8%, 0.8% and 0.5% along *a*, *b*, *c*, respectively, were assumed throughout the refinements.

DFT calculations were performed using CASTEP with the PBE functional and a 350 eV plane-wave basis set cut-off. [38] The D2-dispersion correction was employed to describe non-covalent interactions.[39] The Brouillion zone was sampled with a 1x1x6 Monkhorst-Pack grid.[40] The structure optimization was performed in a two-step process: First the lattice and atom positions were optimized until the maximum stress was reduced to below 0.15 GPa. In a second step, the lattice was frozen and the atoms were further optimized until the forces on all atoms were below 0.05 eV Å^{-1}.

Single-crystal X-ray diffraction data were collected with an Xcalibur3 diffractometer equipped with a Spellman generator (voltage 50 kV, current 40 mA) and a Kappa CCD

detector, and using Mo K_α radiation (λ = 0.71073 Å). The data collection was performed with the CrysAlis CCD software[41] and the data reduction was achieved with the CrysAlis RED software. The structure was solved with SIR-92, refined with SHELXL-97 and checked using PLATON.[42] The absorptions were corrected by the SCALE3 ABSPACK multiscan method.[43] Crystallographic data for the structure have been deposited with the Cambridge Crystallographic Data Centre, CCDC, 12 Union Road, Cambridge CB21EZ, UK. Copies of the data can be obtained free of charge on quoting the depository number CCDC 1503281 (http://www.ccdc.cam.ac.uk).

Transmission electron microscopy (TEM) was performed on an FEI Titan Themis equipped with a field emission gun operated at 300 kV.

The **nitrogen sorption** isotherms were recorded on a Quantachrome Autosorb 1 at 77 K in a pressure range from p/p_0 = 0.001 to 0.98. Prior to the measurement of the sorption isotherm the samples were outgassed for 24 h at 120 °C under high vacuum. For the evaluation of the surface area the BET model was applied between 0.06 and 0.11 p/p_0. The calculations for obtaining the pore size distribution were performed using the QSDFT equilibrium model with a carbon kernel for cylindrical pores. The Connolly Surface was calculated based on the Rietveld-refined structure model using a nitrogen-sized probe (r = 3.58 Å) and a grid interval of 0.25 Å.

Thermogravimetric analysis (TGA) measurements were performed using a Netzsch Jupiter ST 449 C instrument equipped with a Netsch TASC 414/4 controller. The samples were heated in nitrogen atmosphere from room temperature to 900 °C at a heating rate of 1 K min^{-1}.

UV-VIS spectra were recorded using a Perkin-Elmer Lambda 1050 spectrometer equipped with a 150 mm InGaAs integrating sphere. **Diffuse reflectance spectra** were collected with a Praying Mantis (Harrick) accessory and were referenced to barium sulfate powder as white standard. The specular reflection of the sample surface was removed from the signal using apertures that allow only light scattered at angles > 20 ° to pass.

Photoluminescence (PL) measurements were performed using a home-built setup consisting of a Horiba Jobin Yvon iHR 320 monochromator equipped with a photomultiplier tube and a liquid N_2-cooled InGaAs detector. The samples were illuminated with a pulsed (83 Hz) 365 nm LED at a light intensity of 500 mW cm^{-2}. **Absolute photoluminescence quantum yields** (PLQY) were obtained applying the method outlined by de Mello *et al.*,[36] using a 150 mm

Spectralon integrating sphere and a 403 nm diode laser (pulse power 0.3 µJ cm^{-2}, pulse rate 40 MHz). Three individual spectra were recorded per sample, i.e. (a) the empty sphere, (b) the sample inside the sphere, but not directly illuminated, and (c) the sample inside the sphere and directly illuminated.

Time-correlated single photon counting (TCSPC) measurements were performed using a PicoQuant FluoTime 300 spectrometer equipped with a 403 nm picosecond diode laser (pulse power 0.3 µJ cm^{-2}).

Building block syntheses

Unless stated otherwise, all reactions were performed in oven-dried glassware under argon atmosphere. All reagents and solvents were obtained from commercial suppliers and used as received.

1,3,6,8-tetrakis(4-aminophenyl)pyrene (1)[16]

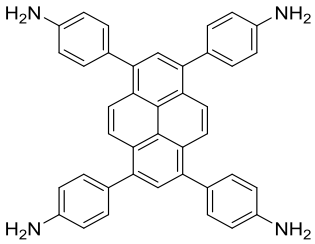

A reaction mixture containing 1,3,6,8-tetrabromopyrene (1482 mg, 2.86 mmol, 1.0 eq.), 4-aminophenylboronic acid pinacol ester (3010 mg, 13.7 mmol, 4.8 eq.), K_2CO_3 (2175 mg, 15.7 mmol, 5.5 eq.) and $Pd(PPh_3)_4$ (330 mg, 0.29 mmol, 10 mol%) in 32 mL 1,4-dioxane and 8 mL H_2O was heated to reflux (115 °C) for 3 d. After cooling to room temperature, H_2O was added. The resulting precipitate was collected via filtration and was washed with H_2O and MeOH. Recrystallization from 1,4-dioxane, followed by drying under high vacuum furnished the title compound, co-crystallized with approximately 1.5 dioxane molecules per formula unit, as a bright yellow powder (1792 mg, 2.56 mmol, 90%).

^{1}H NMR (400 MHz, DMSO-d_6): 8.13 (s, 4 H), 7.79 (s, 2 H), 7.34 (d, J = 8.4 Hz, 8 H), 6.77 (d, J = 8.5 Hz, 8 H), 5.30 (s, 8 H), 3.56 (s, 12 H, dioxane).

^{13}C NMR (100 MHz, DMSO-d_6): 148.2, 137.1, 131.0, 129.0, 127.6, 126.7, 126.1, 124.4, 113.9, 66.3 (dioxane).

Py(Benzaldehyde)$_4$ (2)

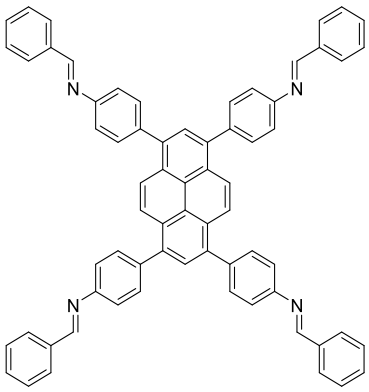

Benzaldehyde (106 mg, 1 mmol) and ca. 100 mg of $MgSO_4$ were added to a suspension of compound **1** (28 mg, 0.04 mmol) in 2 mL of dry $CHCl_3$. The reaction container was sealed and heated at 70 °C overnight. The resulting yellow solution was evaporated to dryness, yielding the title compound as a yellow solid. Crystals suitable for X-ray structure analysis were grown by slow evaporation of the solvent from a concentrated DCM solution.

4-((trimethylsilyl)ethynyl)benzaldehyde (3)

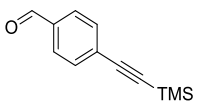

4-Bromobenzaldehyde (5550 mg, 30 mmol, 1.0 eq.), $Pd(PPh_3)_2Cl_2$ (421 mg, 0.60 mmol, 2 mol%), and CuI (228 mg, 1.2 mmol, 4 mol%) were dissolved in 30 mL of dry THF. Et_3N (4554 mg, 45 mmol, 1.5 eq.) and trimethylsilylacetylene (3094 mg, 31.5 mmol, 1.05 eq.) were added and the resulting reaction mixture was stirred overnight at room temperature. After completion, all volatiles were removed under reduced pressure. The resulting solid was extracted with pentane, filtered through celite and dried under reduced pressure, yielding colorless crystals (6.01 g, 29.7 mmol, 99%).

^{1}H NMR (400 MHz, $CDCl_3$): 10.00 (s, 1 H), 7.81 (m, 2 H), 7.60 (m, 2 H), 0.27 (s, 9 H).

^{13}C NMR (100 MHz, $CDCl_3$): 191.5, 135.7, 132.6, 129.6, 129.5, 104.0, 99.2, -0.1.

4-ethynylbenzaldehyde (4)

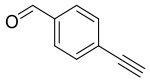

Compound 2 (1598 mg, 7.9 mmol, 1.0 eq.) was dissolved in 50 mL of MeOH, followed by the addition of KOH (560 mg, 10 mmol, 1.25 eq.). The reaction mixture was stirred at room temperature for 1 h. Brine was added, followed by extraction with EtOAc and drying over $MgSO_4$. Evaporation of all volatiles yielded the title compound as an off-white solid (1008 mg, 7.7 mmol, 98%)

^{1}H NMR (400 MHz, DMSO-d_6): 10.02 (s, 1 H), 7.91 (m, 2 H), 7.69 (m, 2 H), 4.54 (s, 1 H).

^{13}C NMR (100 MHz, DMSO-d_6): 192.5, 135.8, 132.4, 129.6, 127.5, 84.6, 82.7.

4,4'-(ethyne-1,2-diyl)dibenzaldehyde (5)

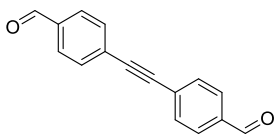

A reaction mixture containing 4-bromobenzaldehyde (740 mg, 4.0 mmol, 1.0 eq.), compound 3 (521 mg, 4.0 mmol, 1.0 eq.), $Pd(PPh_3)_4$ (115 mg, 0.1 mmol, 2.5 mol%), and CuI (19 mg, 0.1 mmol, 2.5 mol%) in 30 mL of dry THF and 10 mL Et_3N was heated to 85 °C and stirred overnight. After cooling to room temperature, all volatiles were removed under reduced pressure. Purification via silica gel column chromatography using DCM as eluent, followed by recrystallization from hot DCE yielded the title compound as white needles (824 mg, 3.5 mmol, 88 %).

^{1}H NMR (400 MHz, $CDCl_3$): 10.04 (s, 1 H), 7.90 (m, 2 H), 7.71 (m, 2 H).

^{13}C NMR (100 MHz, $CDCl_3$): 191.4, 136.1, 132.5, 129.8, 128.8, 92.3.

1,4-diiodo-2,5-dimethoxybenzene (6)[44]

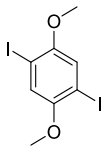

ICl (3491 mg, 21.5 mmol, 4.3 eq.) was added dropwise to 25 mL MeOH at 10 °C. To this solution was added 1,4-dimethoxybenzene (691 mg, 5.0 mmol, 1.0 eq.) and the resulting mixture was heated to 75 °C and stirred at this temperature for 4 h. Upon cooling to room temperature a white solid precipitated, which was collected by filtration, washed with cold MeOH and dried under high vacuum at 50 °C. Yield: 1129 mg, 2.89 mmol, 58 %.

^{1}H NMR (400 MHz, $CDCl_3$): 7.20 (s, 2 H), 3.83 (s, 6 H).

^{13}C NMR (100 MHz, $CDCl_3$): 153.5, 121.8, 85.6, 57.4.

Compound 7

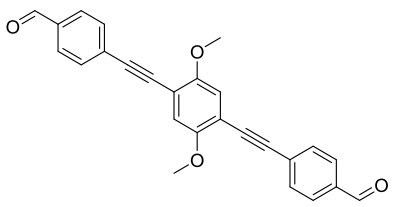

A reaction mixture containing compound 6 (780 mg, 2.0 mmol, 1.0 eq.), compound 4 (521 mg, 4.0 mmol, 2.0 eq.), $Pd(PPh_3)_4$ (115 mg, 0.1 mmol, 5 mol%), and CuI (19 mg, 0.1 mmol, 5 mol%) in 15 mL of dry THF and 5 mL Et_3N was refluxed overnight at 85 °C. After cooling to room temperature, all volatiles were removed under reduced pressure. Purification by silica gel column chromatography using $CHCl_3$ as eluent, followed by recrystallization from hot DCE afforded the title compound as a yellow powder (650 mg, 1.64 mmol, 82%).

^{1}H NMR (400 MHz, $CDCl_3$): 10.02 (s, 2 H), 7.87 (m, 4 H), 7.71 (m, 4 H), 7.06 (s, 2 H), 3.93 (s, 6 H).

^{13}C NMR (100 MHz, $CDCl_3$): 191.5, 154.3, 135.7, 132.3, 129.7, 129.5, 115.8, 113.5, 94.6, 89.8, 56.6.

Compound 8

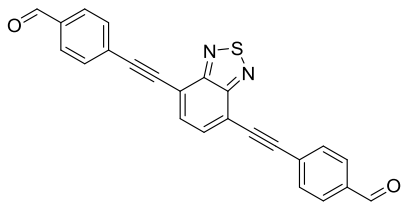

A reaction mixture consisting of 4,7-dibromo-2,1,3-benzothiadiazole (1176 mg, 4.0 mmol, 1.0 eq.), compound 4 (1041 mg, 8.0 mmol, 2.0 eq.), $Pd(PPh_3)_4$ (231 mg, 0.2 mmol, 5 mol%), and CuI (38 mg, 0.1 mmol, 5 mol%) in 30 mL of dry THF and 10 mL Et_3N was heated to reflux (85 °C) for 36 h. After cooling to room temperature, all volatiles were removed under reduced pressure and the residue was dissolved in a minimal amount of hot $CHCl_3$. Repeated purification by silica gel column chromatography using $CHCl_3$ as eluent yielded the title compound as a bright yellow powder (897 mg, 2.29 mmol, 57 %).

^{1}H NMR (400 MHz, $CDCl_3$): 10.06 (s, 2 H), 7.93 (m, 4 H), 7.86 (s, 2 H), 7.83 (m, 4 H).

^{13}C NMR (100 MHz, $CDCl_3$): 191.3, 154.3, 136.1, 132.8, 132.5, 129.6, 128.5, 117.2, 96.6, 88.7.

COF syntheses

Unless stated otherwise, all COF syntheses were performed under argon atmosphere. Commercially available reagents were used as received. Solvents were obtained in high purity grade from commercial suppliers and were, unless shipped under argon, degassed and saturated with argon prior to use.

Py-1P COF

Compound **1** (14.0 mg, 20 µmol, 1.0 eq.) and terephthalaldehyde (5.4 mg, 40 µmol, 2.0 eq.) were filled into a reaction tube, followed by the addition of mesitylene (667 µL), 1,4-dioxane (333 µL), and 6 M acetic acid (100 µL). The tube was sealed and the reaction mixture was heated at 120 °C for 7 d. After cooling to room temperature, the precipitate was collected by filtration, washed with MeCN and dried in air, yielding a bright orange, hard and brittle powder.

Py-1P$_F$ COF

Compound **1** (14.0 mg, 20 µmol, 1.0 eq.), terephthalaldehyde (2.7 mg, 20 µmol, 1.0 eq.), and 2,3,5,6-tetrafluoroterephthalaldehyde (4.1 mg, 20µmol, 1.0 eq.) were filled into a reaction tube, followed by the addition of mesitylene (667 µL), 1,4-dioxane (333 µL), and 6 M acetic acid (100 µL). The tube was sealed and the reaction mixture was heated at 120 °C for 3 d. After cooling to room temperature, the precipitate was collected by filtration, washed with MeCN and dried in air, yielding an orange powder.

Py-2P COF

Compound **1** (7.0 mg, 10 µmol, 1.0 eq.) and 4,4'-biphenyldicarboxaldehyde (4.2 mg, 20 µmol, 2.0 eq.) were filled into a reaction tube, followed by the addition of mesitylene (333 µL), 1,4-dioxane (167 µL), and 6 M acetic acid (50 µL). The tube was sealed and the reaction mixture was heated at 120 °C for 3 d. After cooling to room temperature, the precipitate was collected by filtration, yielding an orange powder. This framework was found to lose its crystallinity upon evaporation of the solvent.

Py-2PE COF

Compound **1** (14.0 mg, 20 µmol, 1.0 eq.) and compound **5** (9.4 mg, 40 µmol, 2.0 eq.) were filled into a reaction tube, followed by the addition of mesitylene (667 µL), 1,4-dioxane (400 µL), BnOH (400 µL), and 6 M acetic acid (100 µL). The tube was sealed and the reaction mixture was heated at 120 °C for 3 d. After cooling to room temperature, the precipitate was collected by filtration and dried in air, yielding an orange powder.

Py-3PE COF

Compound **1** (14.0 mg, 20 µmol, 1.0 eq.) and compound **7** (15.8 mg, 40 µmol, 2.0 eq.) were filled into a reaction tube, followed by the addition of mesitylene (667 µL), BnOH (333 µL), and 6 M acetic acid (100 µL). The tube was sealed and the reaction mixture was heated at 120 °C for 5 d. After cooling to room temperature, the precipitate was collected by filtration and dried in air, yielding an orange-brown powder.

Py-3PE$_{BTD}$ COF

Compound **1** (14.0 mg, 20 µmol, 1.0 eq.) and compound **8** (15.7 mg, 40 µmol, 2.0 eq.) were filled into a reaction tube, followed by the addition of mesitylene (667 µL), BnOH (333 µL), and 6 M acetic acid (100 µL). The tube was sealed and the reaction mixture was heated at 120 °C for 5 d. After cooling to room temperature, the precipitate was collected by filtration and dried in air, yielding a dark red, brittle powder.

NMR-Spectra of compound 1

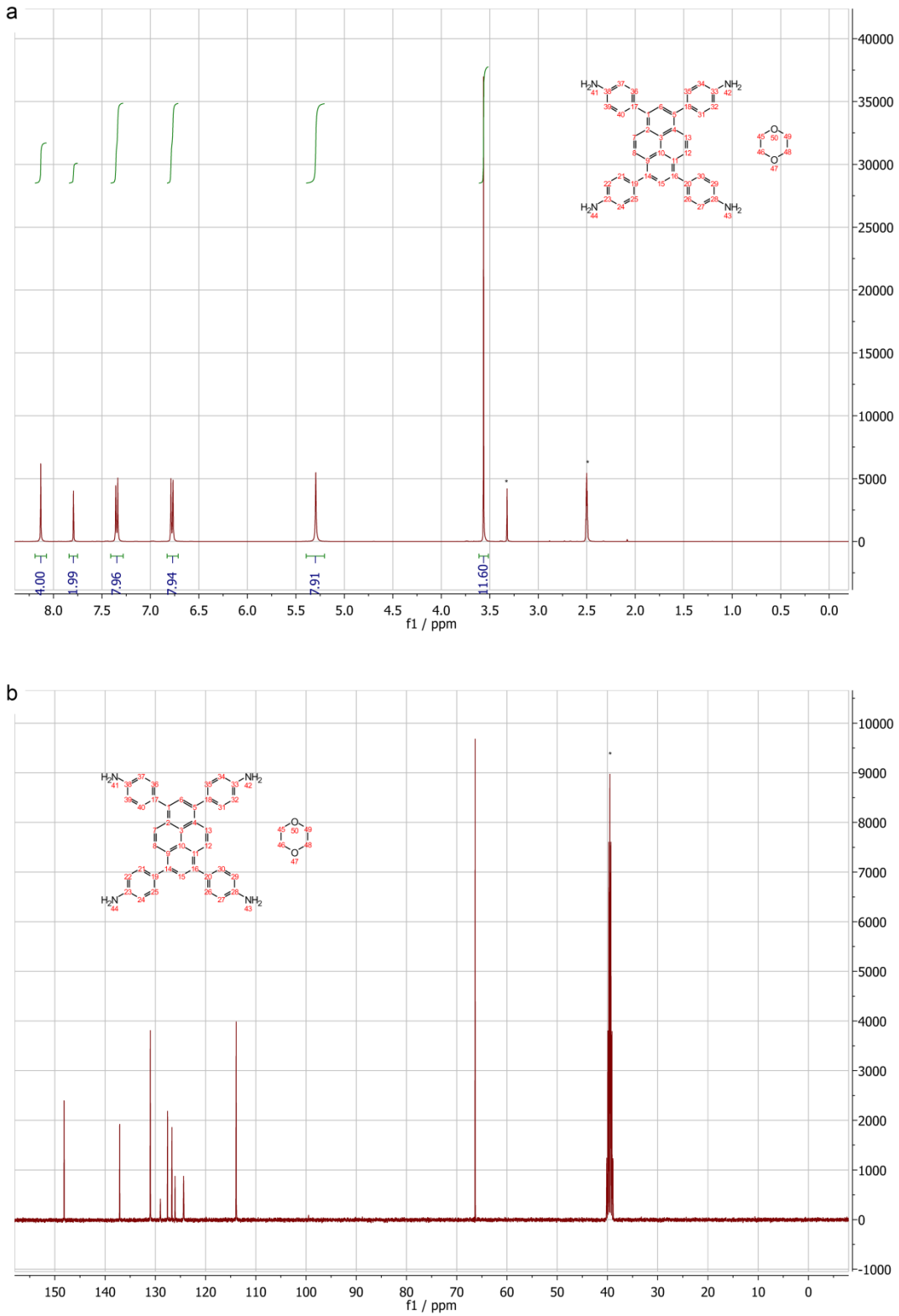

Figure 4.5 (**a**) ^{1}H and (**b**) ^{13}C NMR spectra of compound **1**. The signals of the residual undeuterated solvent and of H_2O/HDO in the ^{1}H spectrum are marked with an asterisk.

Single crystal structure of compound 2

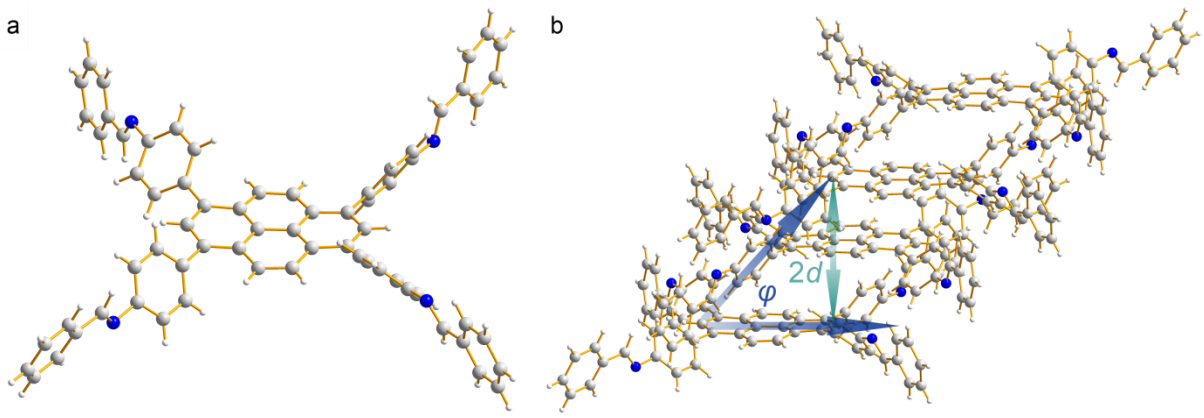

Figure 4.6 Single-crystal X-ray structure of compound 2 showing (**a**) the asymmetric unit (C, grey; H, white; N, blue) and (**b**) a stack of four alternating left- and right-handed propellers. One of the four imine-linked branches in the asymmetric unit was refined having two positions with 50% occupancy each (for clarity, only one is displayed). The co-crystallized DCM solvent molecules were omitted for clarity.

Table 4.1 Crystal structure data of compound **2**.

Formula	$C_{139}H_{98}Cl_6N_8$
M	2092.95
T / K	173(2)
Color, habit	yellow rod
Cryst. Size / mm	0.2 x 0.2 x 0.1
Crystal system	triclinic
Space group	$P\bar{1}$
a / Å	10.7899(8)
b /Å	15.7375(10)
c / Å	17.8183(13)
α / °	72.675(2)
β / °	80.347(3)
γ / °	70.518(3)
V / Å^3	2715.1(3)
Z	2

ρ_{calcd} / g cm^{-3}	1.280
μ / mm^{-1}	0.217
λ / Å	0.71073
F (000)	1090
Index ranges	$-12 \leq h \leq 12$
	$-18 \leq k \leq 18$
	$-21 \leq l \leq 21$
Reflns. collected	41933
Reflns. unique	9206
Reflns. obsd.	6745
R_{int}	0.0706
Params. refined	703
ϑ range / °	2.008 - 25.350
R_1, wR_2 [I > 2σ(I)]	0.0577, 0.1401
R_1, wR_2 (all data)	0.0841, 0.1549

Modelling and refinement of the Py-1P COF

The hypothetical **Py_{prop}-1P** COF with the pyrenes adopting a 'propeller' configuration was modelled as a double layer structure based on the geometry and stacking that had been observed in the single crystal structure of the model compound **2**. Force-field based optimization of the molecular geometry and the unit cell yielded the framework shown in Figure 5.7a. The optimized unit cell parameters are a = 3.23 nm, b = 3.57 nm, c = 1.07 nm, α = 90.0° (fixed), β = 60.6°, γ = 90.0° (fixed).

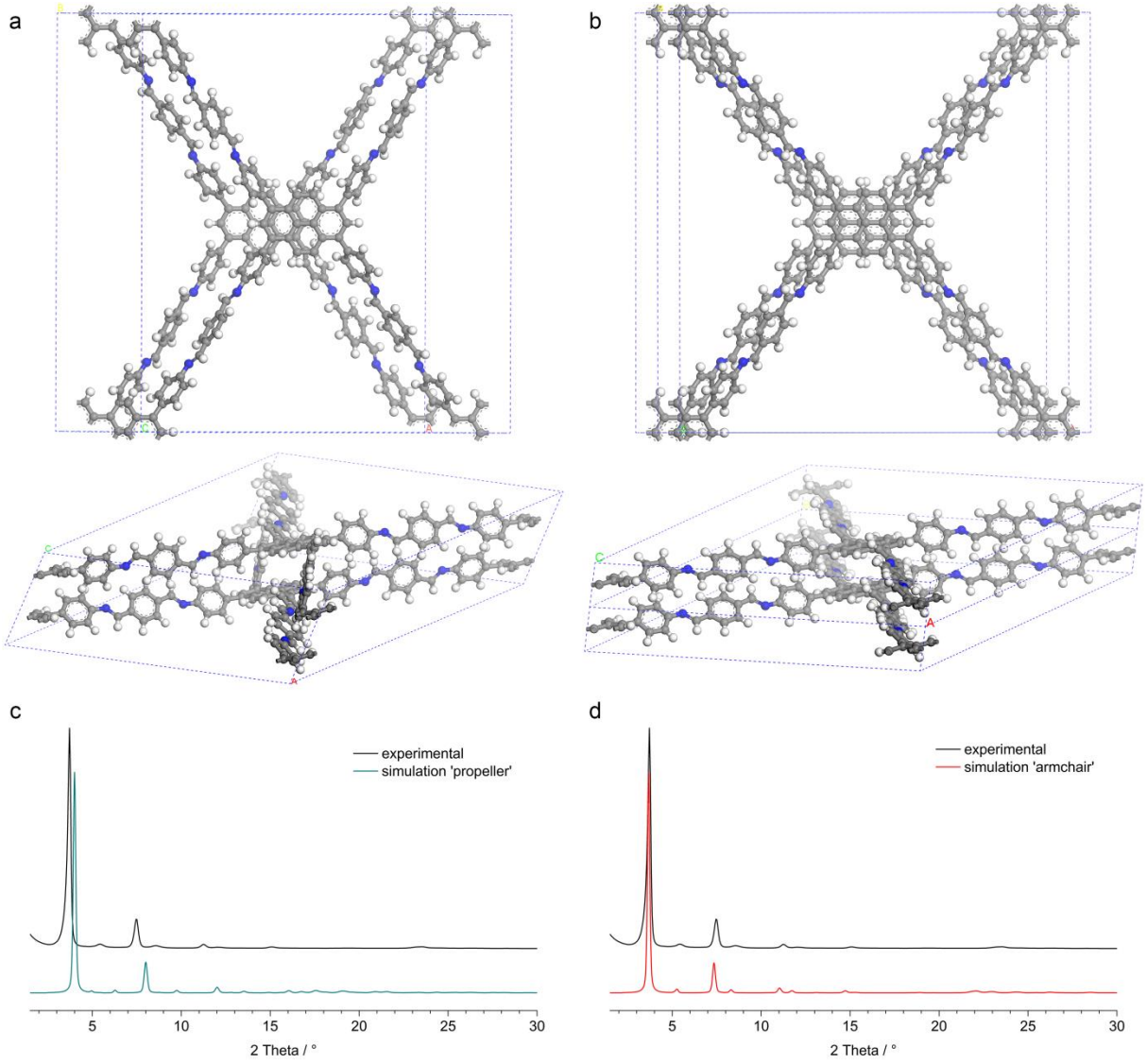

Figure 4.7 Comparison of the simulated **Py-1P** COF structures (C, grey; H, white; N, blue) with the pyrene (**a**) in the 'propeller' conformation and (**b**) in the 'armchair' configuration. (**c**) and (**d**), the experimental PXRD pattern of the **Py-1P** COF and the calculated patterns based on the above simulated structures. The 'armchair' pattern closely resembles the experimental data, whereas the

‘propeller’ structure features a much smaller angle β and thus would give rise to a significantly different sequence of reflections, particularly at $2\vartheta > 10°$.

The ‘armchair’ Py-1P COF was initially modelled using force-field methods. In a second step, this model was refined using density functional theory (CASTEP, PBE, D2 dispersion correction). The DFT-optimized unit cell parameters are a = 3.54 nm, b = 3.39 nm, c = 0.437 nm, α = 90.0° (fixed), β = 75.2°, γ = 90.0° (fixed).

Defining the stacking direction and offset

In the ‘propeller’ configuration, the second pyrene can attach in two symmetry-equivalent positions with the offset to the left or to the right (Figure 4.8a). This initial dimer, however, defines the direction of the stack via the chains of alternating edge-on-face oriented phenylenes (note that only one of the two symmetry-equivalent stacks is shown in the figure). Incorporation of a pyrene that is slipped into the opposite direction creates a stacking fault that is possibly unfavorable for electrostatic and electronic reasons, but would geometrically be feasible.

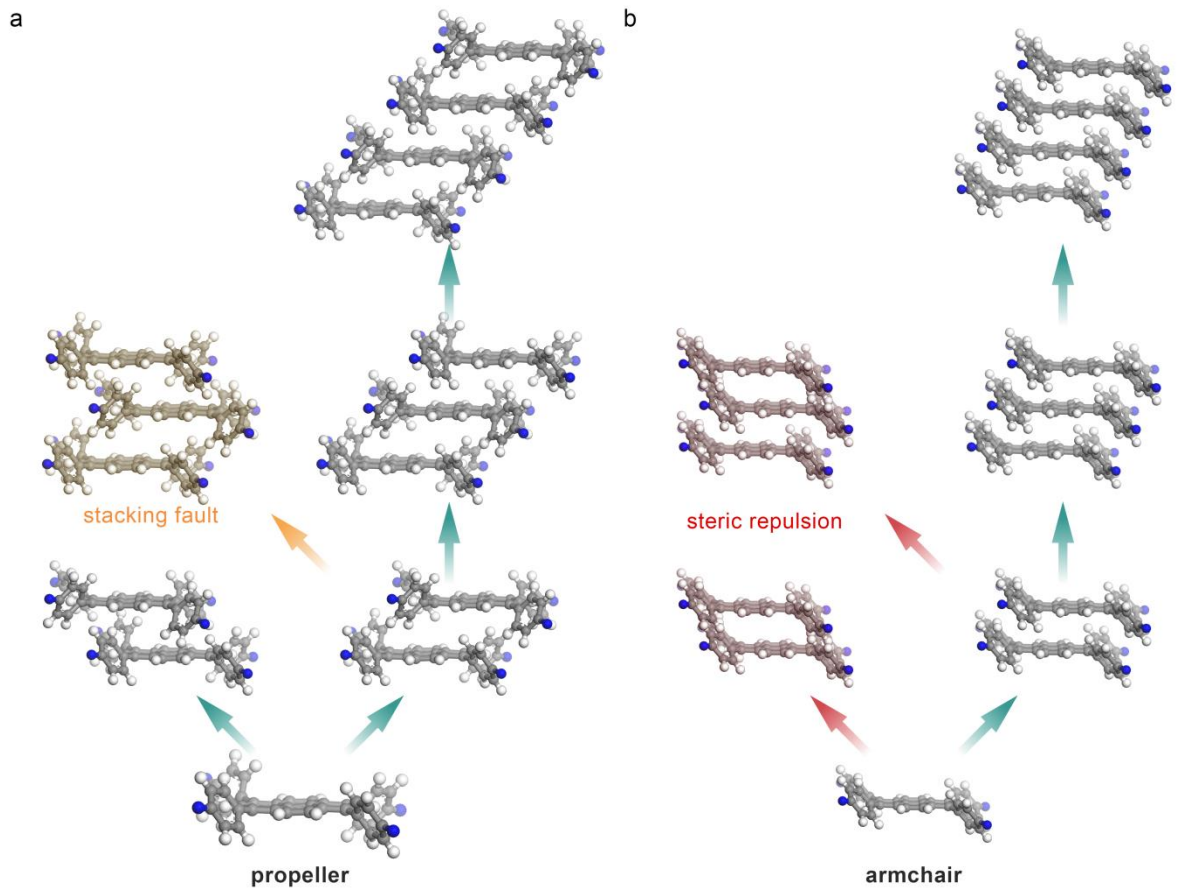

Figure 4.8 Possible arrangements for the attachment of successive tetraphenylpyrene building blocks (C, grey; H, white; N, blue) in the ‘propeller’ (**a**) and the ‘armchair’ configuration (**b**).

The ‘armchair’ configuration imposes much stricter geometric boundary conditions (Figure 4.8b). Here, the orientation of the phenylenes in the first layer defines the magnitude and the direction of stacking offset. Incorporation of a building block that is slipped in the opposite direction would lead to steric repulsion of the phenylenes and would hence create immense

strain in the growing COF domain. This more pronounced geometric guidance for the attachment of a successive COF layer is suggested to lead to a reduced defect density in the resulting framework and hence support the growth of particularly crystalline COFs.

Modelling and refinement of the Py-1P$_F$ COF

For modelling of the **Py-1P$_F$** COF, we started from the *C*2/*m* symmetric model of the **Py-1P** COF and extended the unit cell to two layers. In both layers we replaced two of the four bridging units with their tetrafluoro-substituted analogues, thus generating a sequence of alternating fluorinated and non-fluorinated bridges along the stacking direction. We chose the highest possible symmetry, i.e. *P*2/*m* for our model and optimized the geometry via force-field methods. Less ordered distributions of the fluorinated and non-fluorinated bridges can also be expected to exist in the COF, but could not be distinguished on the basis of our PXRD data.

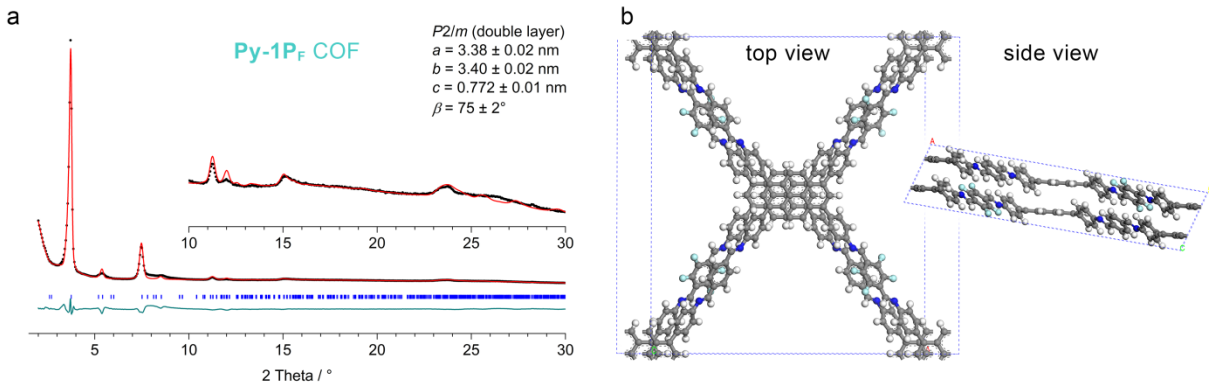

Figure 4.9 (**a**) Experimental PXRD pattern (black), Rietveld refinement (red), difference plot (green), and Bragg positions (blue) of the **Py-1P$_F$** COF. R_{wp} = 6.05%, R_p = 16.6%. (**b**) The refined double-layer unit cell. Viewing direction normal to the pyrene (left) and onto the side of the pyrenes (right).

PXRD analysis of the Py-2P COF

The reaction of **1** with 4,4'-biphenyldicarboxaldehyde was found to form an initially periodically ordered framework. Given the twisted geometry of the linear building block we did not anticipate a similarly close-packed armchair-type structure as for the other COFs containing flat bridges. Indeed, the reflection at the highest 2ϑ angle, which is typically related to the stacking direction in these materials, is at about 22 ° compared to around 23.5 ° for all the other COFs in this study (Figure 4.9, black line). This framework was found to be unstable towards the evaporation of the solvent and lost most of its order within 1 h in ambient air atmosphere. Similar degradation was observed for storage in argon or removal of the solvent under reduced pressure.

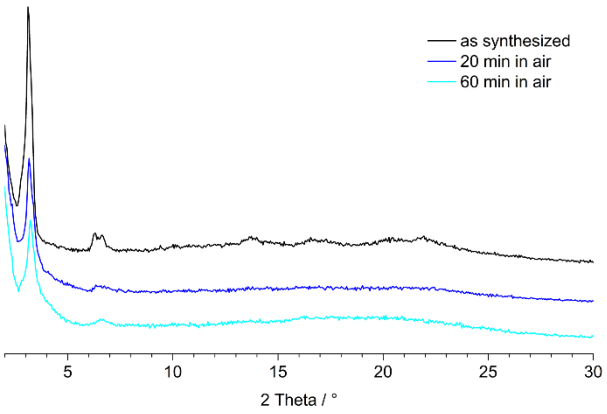

Figure 4.10 PXRD patterns of the **Py-2P** framework directly from the reaction mixture (black) and after drying in ambient air for 20 min (blue) and 60 min (light blue).

Py-1P COF crystallization kinetics

In order to better understand the COF formation process, we studied the crystallization kinetics during the solvothermal synthesis. Identical reaction mixtures, prepared as described in Section C, were heated at 120 °C for times ranging from 1 h to 7 d. The resulting solids were collected by filtration, washed with MeCN and dried in air.

Similar to a recent literature report, we observed the formation of an amorphous precipitate from the initially homogeneous reaction solutiuon already after 10 min.[34] The solids formed after 1 h and all longer reaction times correspond to about 90% yield based on the starting materials, indicating that a quasi-equilibrium between the precipitate and dissolved building blocks is formed quickly and that this remains relatively unchanged by the crystallization of the framework. This initially amorphous network then slowly crystallizes to form the COF, possibly by mass transfer through the solution phase. First weak reflections appear after 1.5 h and grow strongly in intensity between 2 and 8 h. After this time, the strongest reflections hardly change in intensity, but higher-order reflections become more distinct, indicating that the degree of order is still further improving.

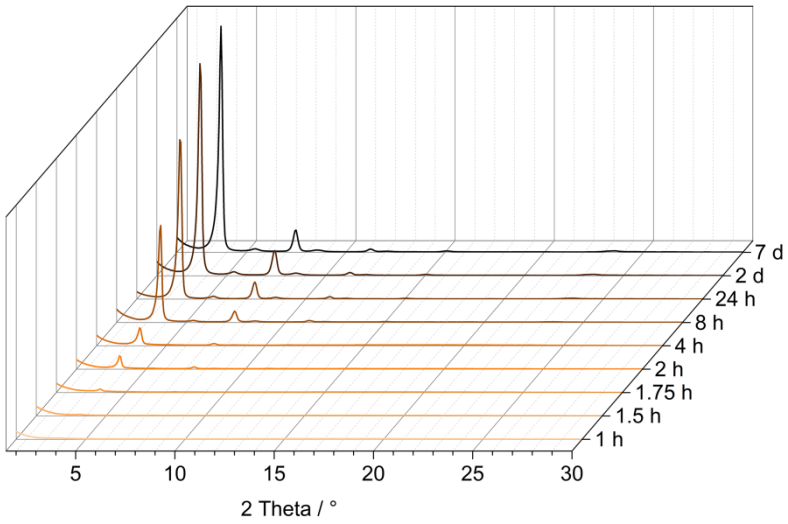

Figure 4.11 Crystallization kinetics of the **Py-1P** COF.

Py-1P COF crystallization: Solvent mixtures

COFs are commonly synthesized in mixtures composed of a polar solvent (e.g. 1,4-dioxane, BnOH) and a less polar aromatic solvent (mesitylene, 1,2-dichlorobenzene). The use of a solvent mixture rather than a single solvent allows for better matching the reactivity of the precursors and for fine-tuning the equilibrium between precipitation and re-dissolution of the building blocks, thus fostering the formation of a crystalline framework. The geometric design principle presented in this work can enhance the formation of highly ordered COF structures, but it still requires a functioning self-healing mechanism. The selection of an optimized solvent mixture therefore remains a crucial step in the development of each COF.

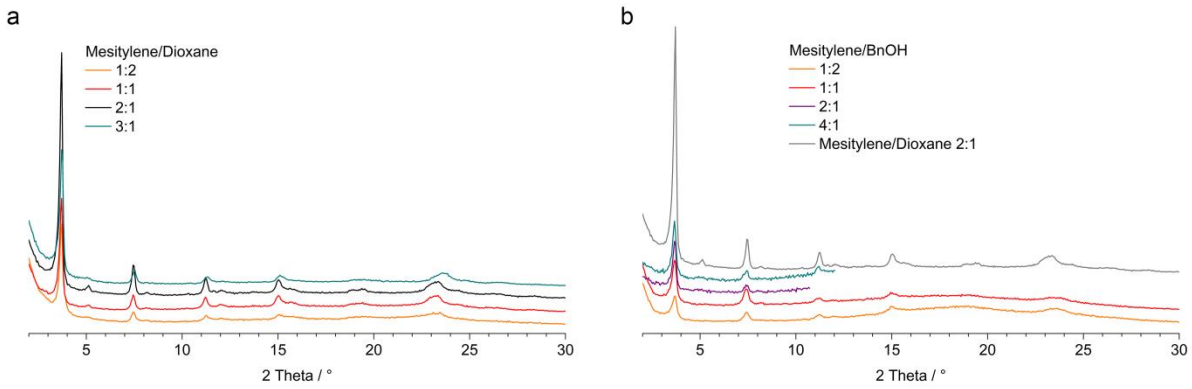

Figure 4.12 Crystallinity of the **Py-1P** COF synthesized in (**a**) mesitylene/1,4-dioxane and (**b**) mesitylene/BnOH solvent mixtures. The diffraction patterns are vertically offset for clarity.

Solid-state NMR

The $^{13}C(^{1}H)$ cross-polarization (CP) magic angle spinning (MAS) solid-state NMR (ssNMR) spectra exhibit a set of signals between 110 and 160 ppm that originate from the aromatic carbons in the framework. In the spectrum of the **Py-1P** COF (Figure 4.13a) the expected 12 carbon signals (5 from the pyrene core, 4 from the pyrene phenyls, 3 from the imine bridge) are resolved at δ = 118, 119, 121, 124, 127, 129, 131, 132, 137, 138, 149, and 156 ppm. In the spectra of the other COFs the signals overlap more strongly, but the peaks originating from the acetylene bridges (**Py-2PE**, **Py-3PE**, **Py-3PE$_{BTD}$**) and the methoxy groups (**Py-3PE**) are clearly resolved. The ssNMR spectrum of the **Py-1P$_F$** COF appears much less well resolved than the **Py-1P** COF. We attribute this to the statistical distribution of fluorinated and non-fluorinated bridges in the framework that creates a range of similar, but not exactly equivalent environments for each carbon atom.

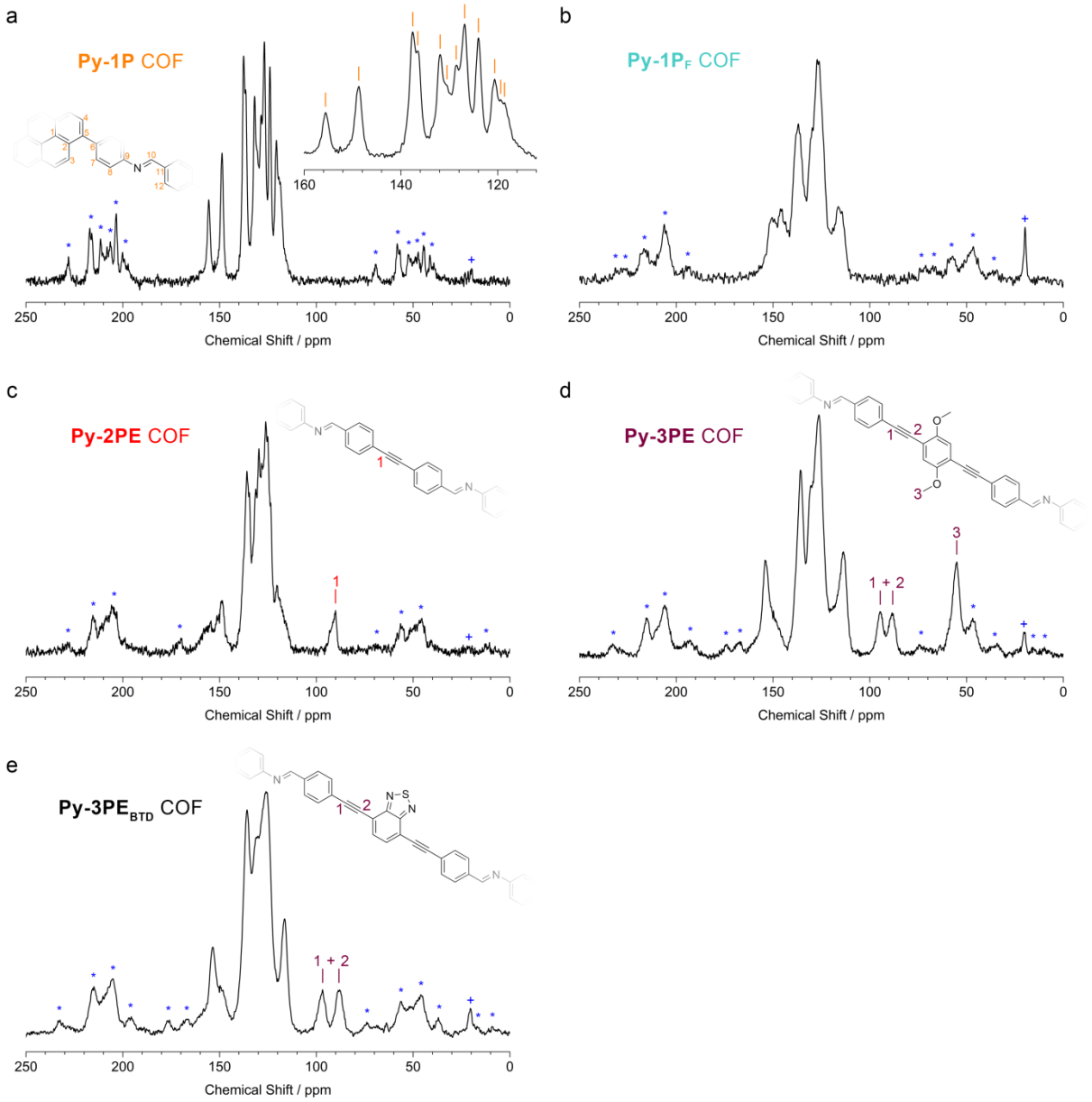

Figure 4.13 $^{13}C(^{1}H)$ cross-polarization magic angle spinning solid-state NMR spectra of the COFs. The peaks that could be assigned to specific carbon atoms are indicated in the framework structures. Spinning side bands are marked with asterisks. The spectra show also traces of residual MeCN from washing the COFs after the synthesis (marked with a cross at 20 ppm).

Themogravimetric analysis

Thermogravimetric analysis (TGA) reveals the high thermal stability of the pyrene-based COFs with decomposition temperatures above 400 °C (Figure 4.14). The **Py-1P** and **Py-2PE** COFs are particularly stable and start to decompose only above 500 °C, which places them among the most stable COFs to date.[8]

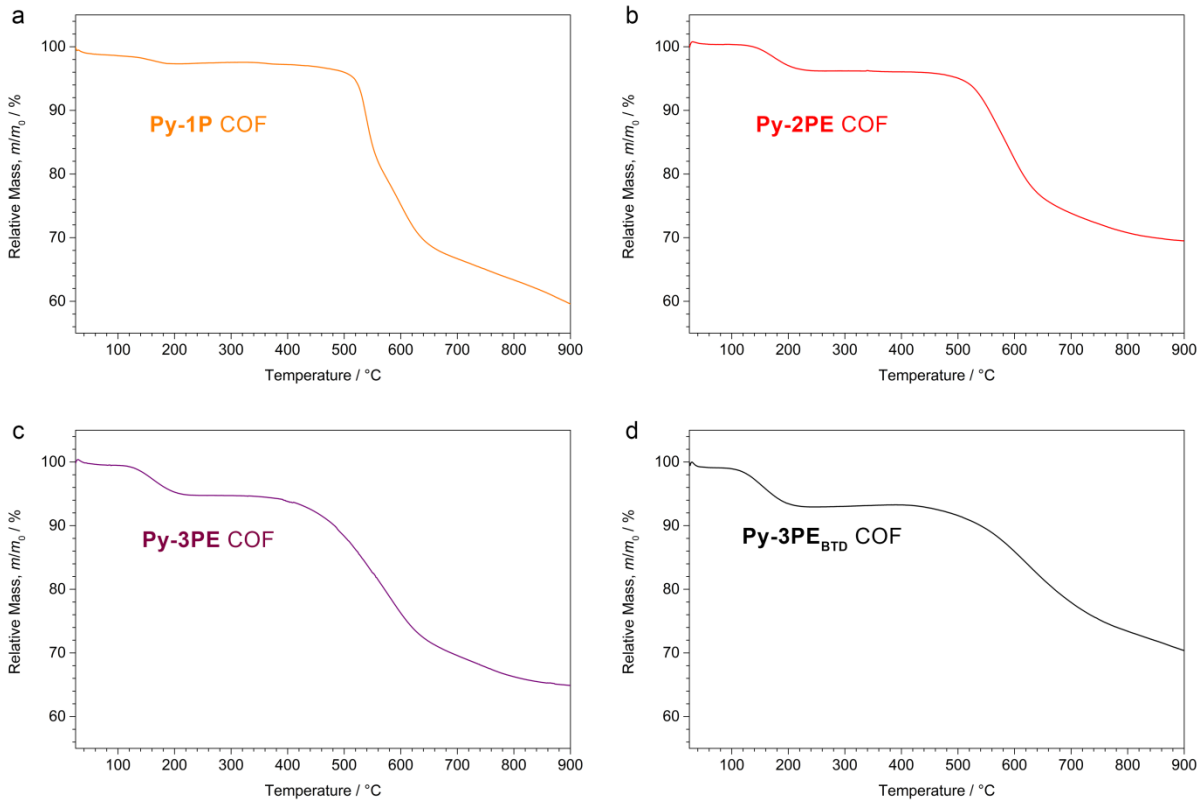

Figure 4.14 Thermogravimetric analysis of the **Py-1P**, **Py-2PE**, **Py-3PE**, and **Py-3PE$_{BTD}$** COFs, respectively, measured in nitrogen atmosphere at a heating rate of 1 K min^{-1}. The initial mass loss between 50 and 200 °C can be attributed to the desorption of water and residual MeCN (from washing the COFs after synthesis).

IR spectroscopy

We noted that the IR spectra of the **Py-1P** and the **Py-1P$_F$** COFs are almost identical, despite the intense absorption bands of the fluorinated terephthalaldehyde building block. In order to evaluate these findings, we synthesized a COF using only the tetrafluorinated terephthalaldehyde (denoted as **Py-1P$_{100\%\ F}$** COF) as the linear building block. This COF showed again a very similar IR spectrum as the parent **Py-1P** COF, a finding that is consistent with a recent literature report on related porphyrin-based COFs with fluorinated bridges.[33]

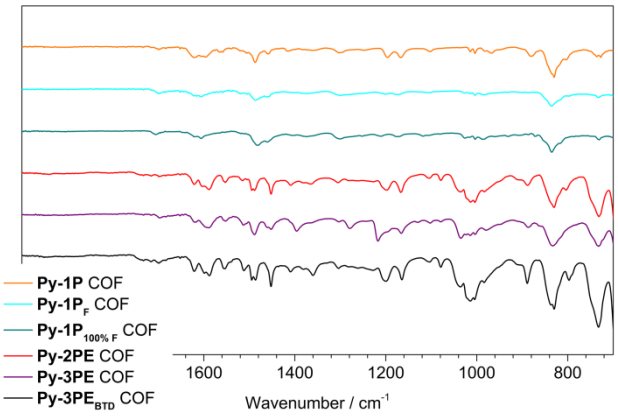

Figure 4.15 ATR-IR spectra of the pyrene-based COFs.

Additional UV-VIS spectra and PLQY data

UV-VIS absorption spectra of the COF precursors were measured under argon using 50 µM solutions in 1,4-dioxane. For recording the diffuse reflectance spectra, the COF powders were mixed with $BaSO_4$ to achieve 10-20 % reflectivity in the spectral regions where the COF absorbs strongly. The specular reflection component was removed from the signal.

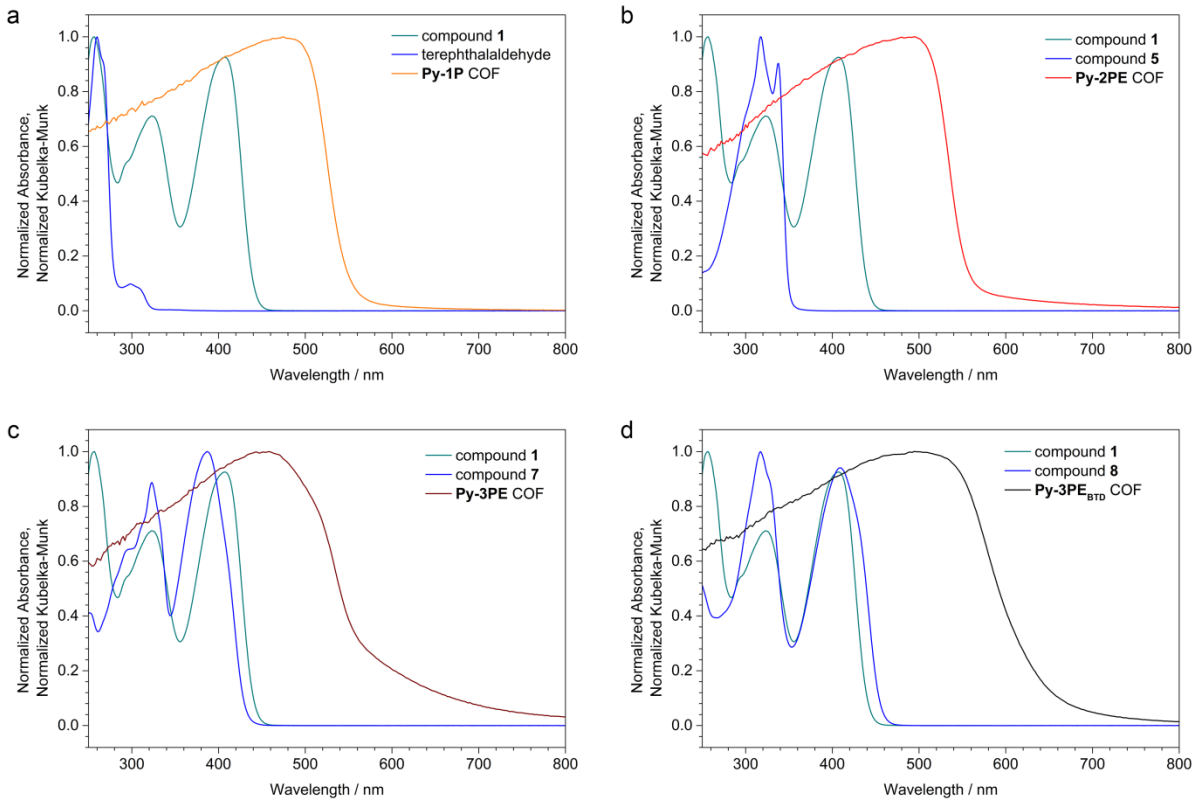

Figure 4.16 Normalized absorption spectra of the COF precursors (blue and green, respectively) and normalized diffuse reflectance spectra of the four COFs indicated in the figures (orange, red, purple, black, respectively).

Table 4.2 External photoluminescence quantum yields.

COF	PLQY (%)
Py-1P	0.2
Py-2PE	0.23
Py-3PE	0.15
Py-3PE$_{BTD}$	0.03

4.6 References

[1] C. J. Doonan, D. J. Tranchemontagne, T. G. Glover, J. R. Hunt, O. M. Yaghi, *Nature Chem.* **2010**, *2*, 235-238.

[2] M. G. Rabbani, A. K. Sekizkardes, Z. Kahveci, T. E. Reich, R. Ding, H. M. El-Kaderi, *Chem. Eur. J.* **2013**, *19*, 3324-3328.

[3] S.-Y. Ding, J. Gao, Q. Wang, Y. Zhang, W.-G. Song, C.-Y. Su, W. Wang, *J. Am. Chem. Soc.* **2011**, *133*, 19816-19822.

[4] S. Lin, C. S. Diercks, Y.-B. Zhang, N. Kornienko, E. M. Nichols, Y. Zhao, A. R. Paris, D. Kim, P. Yang, O. M. Yaghi, C. J. Chang, *Science* **2015**, *349*, 1208-1213.

[5] M. Dogru, M. Handloser, F. Auras, T. Kunz, D. Medina, A. Hartschuh, P. Knochel, T. Bein, *Angew. Chem. Int. Ed.* **2013**, *52*, 2920-2924.

[6] M. Calik, F. Auras, L. M. Salonen, K. Bader, I. Grill, M. Handloser, D. D. Medina, M. Dogru, F. Loebermann, D. Trauner, A. Hartschuh, T. Bein, *J. Am. Chem. Soc.* **2014**, 17802-17807.

[7] S.-L. Cai, Y.-B. Zhang, A. B. Pun, B. He, J. Yang, F. M. Toma, I. D. Sharp, O. M. Yaghi, J. Fan, S.-R. Zheng, W.-G. Zhang, Y. Liu, *Chem. Sci.* **2014**, *5*, 4693-4700.

[8] A. P. Côté, A. I. Benin, N. W. Ockwig, M. O'Keeffe, A. J. Matzger, O. M. Yaghi, *Science* **2005**, *310*, 1166-1170.

[9] E. L. Spitler, J. W. Colson, F. J. Uribe-Romo, A. R. Woll, M. R. Giovino, A. Saldivar, W. R. Dichtel, *Angew. Chem. Int. Ed.* **2012**, *51*, 2623-2627.

[10] S. Jin, X. Ding, X. Feng, M. Supur, K. Furukawa, S. Takahashi, M. Addicoat, M. E. El-Khouly, T. Nakamura, S. Irle, S. Fukuzumi, A. Nagai, D. Jiang, *Angew. Chem. Int. Ed.* **2013**, *52*, 2017-2021.

[11] S. Patwardhan, A. A. Kocherzhenko, F. C. Grozema, L. D. A. Siebbeles, *J. Phys. Chem. C* **2011**, *115*, 11768-11772.

[12] D. D. Medina, V. Werner, F. Auras, R. Tautz, M. Dogru, J. Schuster, S. Linke, M. Döblinger, J. Feldmann, P. Knochel, T. Bein, *ACS Nano* **2014**, *8*, 4042-4052.

[13] J. Guo, Y. Xu, S. Jin, L. Chen, T. Kaji, Y. Honsho, M. A. Addicoat, J. Kim, A. Saeki, H. Ihee, S. Seki, S. Irle, M. Hiramoto, J. Gao, D. Jiang, *Nature Commun.* **2013**, *4*.

[14] G. H. V. Bertrand, V. K. Michaelis, T.-C. Ong, R. G. Griffin, M. Dincă, *Proc. Natl Acad. Sci. USA* **2013**, *110*, 4923-4928.

[15] H. Ding, Y. Li, H. Hu, Y. Sun, J. Wang, C. Wang, C. Wang, G. Zhang, B. Wang, W. Xu, D. Zhang, *Chem. Eur. J.* **2014**, *20*, 14614-14618.

[16] S. Jin, T. Sakurai, T. Kowalczyk, S. Dalapati, F. Xu, H. Wei, X. Chen, J. Gao, S. Seki, S. Irle, D. Jiang, *Chem. Eur. J.* **2014**, *20*, 14608-14613.

[17] E. L. Spitler, W. R. Dichtel, *Nature Chem.* **2010**, *2*, 672-677.

[18] E. L. Spitler, B. T. Koo, J. L. Novotney, J. W. Colson, F. J. Uribe-Romo, G. D. Gutierrez, P. Clancy, W. R. Dichtel, *J. Am. Chem. Soc.* **2011**, *133*, 19416-19421.

[19] X. Feng, L. Liu, Y. Honsho, A. Saeki, S. Seki, S. Irle, Y. Dong, A. Nagai, D. Jiang, *Angew. Chem. Int. Ed.* **2012**, *51*, 2618-2622.

[20] B. J. Smith, W. R. Dichtel, *J. Am. Chem. Soc.* **2014**, *136*, 8783-8789.

[21] F. J. Uribe-Romo, J. R. Hunt, H. Furukawa, C. Klock, M. O'Keeffe, O. M. Yaghi, *J. Am. Chem. Soc.* **2009**, *131*, 4570-4571.

[22] S. Wan, F. Gándara, A. Asano, H. Furukawa, A. Saeki, S. K. Dey, L. Liao, M. W. Ambrogio, Y. Y. Botros, X. Duan, S. Seki, J. F. Stoddart, O. M. Yaghi, *Chem. Mater.* **2011**, *23*, 4094-4097.

[23] S. Kandambeth, D. B. Shinde, M. K. Panda, B. Lukose, T. Heine, R. Banerjee, *Angew. Chem. Int. Ed.* **2013**, *52*, 13052-13056.

[24] S. Dalapati, M. Addicoat, S. Jin, T. Sakurai, J. Gao, H. Xu, S. Irle, S. Seki, D. Jiang, *Nature Commun.* **2015**, *6*.

[25] F. J. Uribe-Romo, C. J. Doonan, H. Furukawa, K. Oisaki, O. M. Yaghi, *J. Am. Chem. Soc.* **2011**, *133*, 11478-11481.

[26] L. Stegbauer, K. Schwinghammer, B. V. Lotsch, *Chem. Sci.* **2014**, *5*, 2789-2793.

[27] M. Calik, T. Sick, M. Dogru, M. Döblinger, S. Datz, H. Budde, A. Hartschuh, F. Auras, T. Bein, *J. Am. Chem. Soc.* **2016**, *138*, 1234-1239.

[28] L. Ascherl, T. Sick, J. T. Margraf, S. H. Lapidus, M. Calik, C. Hettstedt, K. Karaghiosoff, M. Döblinger, T. Clark, K. W. Chapman, F. Auras, T. Bein, *Nature Chem.* **2016**, *8*, 310-316.

[29] X. Chen, N. Huang, J. Gao, H. Xu, F. Xu, D. Jiang, *Chem. Commun.* **2014**, *50*, 6161-6163.

[30] Y. Wu, H. Xu, X. Chen, J. Gao, D. Jiang, *Chem. Commun.* **2015**, *51*, 10096-10098.

[31] X. Feng, H. Tomiyasu, J.-Y. Hu, X. Wei, C. Redshaw, M. R. J. Elsegood, L. Horsburgh, S. J. Teat, T. Yamato, *J. Org. Chem.* **2015**, *80*, 10973-10978.

[32] D. M. D'Alessandro, F. R. Keene, P. J. Steel, C. J. Sumby, *Aust. J. Chem.* **2003**, *56*, 657-664.

[33] X. Chen, M. Addicoat, S. Irle, A. Nagai, D. Jiang, *J. Am. Chem. Soc.* **2013**, *135*, 546-549.

[34] B. J. Smith, A. C. Overholts, N. Hwang, W. R. Dichtel, *Chem. Commun.* **2016**, *52*, 3690-3693.

[35] J. Nafe, S. Herbert, F. Auras, K. Karaghiosoff, T. Bein, P. Knochel, *Chem. Eur. J.* **2015**, *21*, 1102-1107.

[36] J. C. de Mello, H. F. Wittmann, R. H. Friend, *Adv. Mater.* **1997**, *9*, 230-232.

[37] S. Fernandez, M. A. Ganiek, M. Karpacheva, F. C. Hanusch, S. Reuter, T. Bein, F. Auras, P. Knochel, *Org. Lett.* **2016**, *18*, 3158-3161.

[38] J. P. Perdew, K. Burke, M. Ernzerhof, *Phys. Rev. Lett.* **1996**, *77*, 3865-3868.

[39] S. Grimme, *J. Comput. Chem.* **2006**, *27*, 1787-1799.

[40] H. J. Monkhorst, J. D. Pack, *Phys. Rev. B* **1976**, *13*, 5188-5192.

[41] CrysAlis CCD, version 1.171.27p5 beta (release 01–04–2005 CrysAlis171.NET; compiled Apr 1 2005,17:53:34); Oxford Diffraction Ltd.: Oxfordshire, U. K.

[42] a) SIR-92, A Program for Crystal Structure Solution: A. Altomare, G. L. Cascarano, C. Giacovazzo, A. Guagliardi, J Appl Crystallogr, 1993, 26, 343–350.b) A. Altomare, M. C. Burla, M. Camalli, G. L. Cascarano, C. Giacovazzo, A. Guagliardi, A. G. G. Moliterni, G. Polidori, R. Spagna, J Appl Crystallogr, 1999, 32, 115–119.c) G. M. Sheldrick, SHELXS-97, Program for Crystal Structure Solution, University of Göttingen, Göttingen, Germany, 1997. d) G. M. Sheldrick, SHELXL-97, Program for the Refinement of Crystal Structures, University of Göttingen: Göttingen, Germany, 1999. e) L. A. Spek, PLATON, A Multipurpose Crystallographic Tool, Utrecht University: Utrecht, The Netherlands, 1999.

[43] SCALE3 ABSPACK - An Oxford Diffraction program (1.0.4, gui:1.0.3); Oxford Diffraction Ltd.: Oxfordshire, U. K., 2005.

[44] Y.-L. Zhao, L. Liu, W. Zhang, C.-H. Sue, Q. Li, O. Š. Miljanić, O. M. Yaghi, J. F. Stoddart, *Chem. Eur. J.* **2009**, *15*, 13356-13380.

5 Fifty Shades of Red

This chapter is based on the article

Solvatochromic covalent organic frameworks

by Laura Ascherl, Matthias Hennemann, Daniele Di Nuzzo, Alexander G. Hufnagel, Michael Beetz, Richard H. Friend, Timothy Clark, Thomas Bein and Florian Auras

which is currently under review at *Nature Communications*.

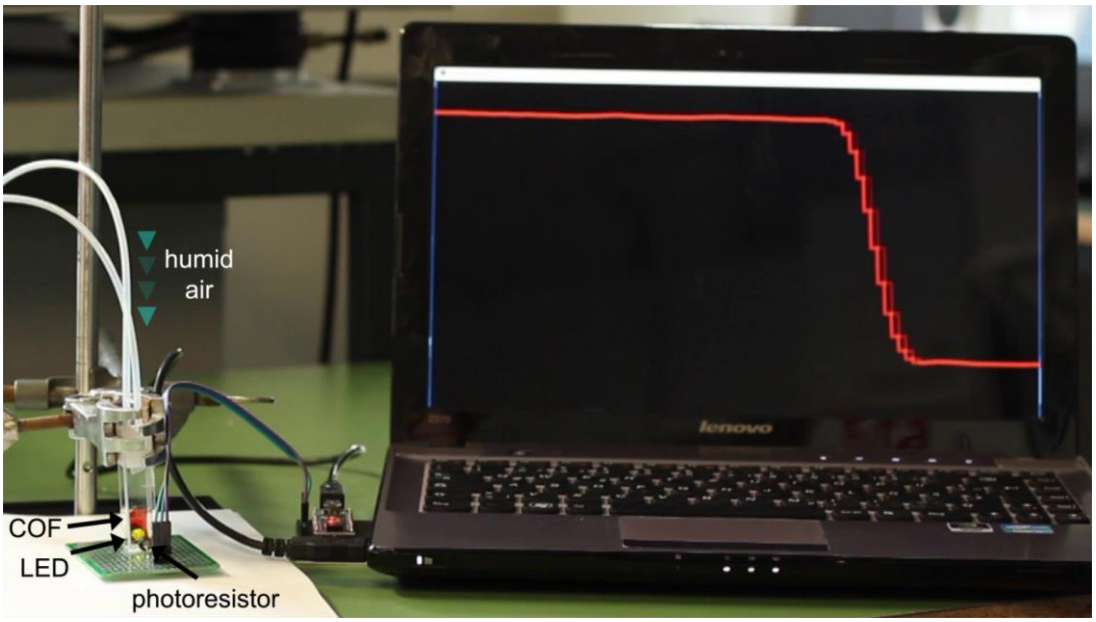

Ultrafast humidity sensing with a solvatochromic COF film as a vapour-sensitive light filter between an LED and a light-dependent resistor

5.1 Abstract

Covalent organic frameworks (COFs) are an emerging class of highly tuneable crystalline, porous materials. By combining electron-rich and -deficient building blocks, we have synthesized the first COFs that change their electronic structure reversibly depending on the surrounding atmosphere. These COFs can act as solid-state supramolecular solvatochromic sensors that show a strong colour change when exposed to humidity or solvent vapours, dependent on the vapour concentration and the solvent polarity. The excellent accessibility of the pores in vertically oriented films results in ultrafast response times below 200 ms, outperforming commercial humidity sensors by more than an order of magnitude. Employing a solvatochromic COF film as a vapour-sensitive light filter, we constructed a fast humidity sensor with full reversibility and stability over at least 4000 cycles. Considering their immense chemical diversity and modular design, COFs with fine-tuned solvatochromic properties could broaden the range of possible applications for these materials in sensing and optoelectronics.

5.2 Introduction

With covalent organic frameworks (COFs) already being in their early teens, the scientific community has gained a profound understanding regarding the synthesis of highly porous, crystalline and stable frameworks.[1] [2] If these materials are to evolve from a purely academic research field, however, one of the next major challenges will be the realisation of COFs that can compete with other materials in practical applications.

COFs are formed via reversible cross-linking of rigid organic building blocks, whereby boronate esters,[3] [4] [5] [6] imines[7] [8] [9] [10] and hydrazones[11] [12] represent the most prominent linkage motifs. Potential for application has mainly been demonstrated in the fields of gas storage,[13] [14] [15] catalysis and photocatalysis,[16] [17] and in electronics and optoelectronics.[18] [19] [20] [21] [22] However, functionalities arising from the combination of the well-defined porosity and the semiconducting properties of the COF backbone are still under-explored.

Taking particular advantage of their tuneable porosity and the resulting capability of selectively hosting specific guest molecules, a predestined ambit for COFs could be the sensing of ions or molecules. The COF-based sensing materials reported thus far are able to

detect heavy metal ions,[23] [24] pH changes,[25] or organic explosives[26] [27] via fluorescence quenching.

A more general scope for application, however, would be the detection of water and solvent vapours in the gas phase with the possibility of differentiating between various substances. COFs featuring this kind of "nosing" capability could be a powerful tool for detecting harmful volatile organic compounds in workplace environments, or for real-time monitoring the water content of gases and solvents in industrial processes. Such on-line analysis would require an easy read-out possibility, preferably via a colour change of the detector material, in combination with full reversibility over multiple cycles and sufficient photochemical stability.

Reversible colour changes of solvated organic molecules as a function of the solvent polarity are known as solvatochromism. This effect occurs when the ground and excited states of a molecule are of different polarity, thus rendering the energy of intramolecular electronic transitions sensitive to changes in the polarity of the surrounding medium.[28] Charge-transfer transitions, as they occur in the archetypical Reichardt's dye (2,6-diphenyl-4-(2,4,6-triphenylpyridinium)phenolate, betaine 30), display the highest sensitivity in this context.[29]

The solvatochromic effect has mostly been exploited for defining solvent polarity scales such as the $E_T(30)$ and the normalized E_T^N scales through measuring solvent-dependent energy shifts of the absorption onset.[30] For detecting target molecules in a stream of gas or liquid, however, the requirement for a dissolved molecular dye would be highly impractical.

A suitably designed COF, on the other hand, could constitute a supramolecular periodic analogue of the aforementioned solvatochromic dyes, with the added benefit of being an insoluble, chemically and photochemically stable material.[31] [32] The modular COF design allows matched combinations of electron-rich and -deficient building, generating a periodic lattice of covalently linked donor-acceptor pairs that promote charge-transfer transitions.[33] [34] For optimal performance and fast response times, COFs can be grown as thin films with their pores oriented vertically to the substrate, thus exposing their high internal surface area to the analyte.[35] [36]

We have developed oriented thin films of tetrakis(4-aminophenyl)pyrene-based COFs that show an ultrafast and fully reversible solvatochromic response upon exposure to various polar and non-polar vapours. The newly developed COFs derive their high degree of crystallinity from geometric interlocking of the covalently linked 2D sheets into a synchronised offset-

stacked pattern.[10] [37] The charge-transfer character of the optical transitions and hence the sensitivity to changes in polarity inside the COF pores can be tuned through the aldehyde counterpart used for assembling the COF. In this context, the strong donor-acceptor contrast realized between tetraphenylpyrene and thieno[3,2-*b*]thiophene yields the most pronounced solvatochromism. Oriented thin films of this COF with the pores extending vertically from the substrate exhibit millisecond-response times to changes in the surrounding atmosphere and fully retain their structure and function over several thousand cycles.

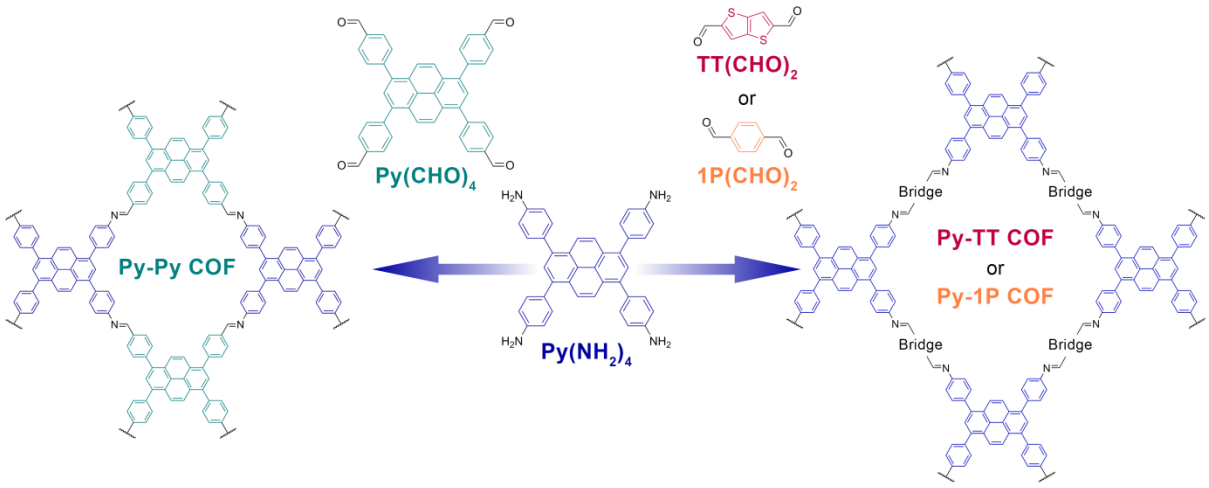

Figure 5.1 Synthesis of the imine-linked COFs. Combining the tetraphenylpyrene tetraamine $Py(NH_2)_4$ with the tetradentate pyrene aldehyde $Py(CHO)_4$ in a 1:1 molar ratio yields the microporous **Py-Py** COF (left), whereas the combination of $Py(NH2)_4$ with linear dialdehydes in a 1:2 molar ratio produces the mesoporous **Py-TT** and **Py-1P** COFs, respectively (right).

5.3 Results and Discussion

We selected the electron-rich 1,3,6,8-tetrakis(4-aminophenyl)pyrene, $Py(NH_2)_4$, as a basis for constructing solvatochromic COFs. Pyrene-based COFs have not only proven to yield extremely well-ordered frameworks with large crystal domains in our recent studies, [37] but are also geometrically compatible with a wide range of aromatic and heteroaromatic aldehyde counterparts,[33] [34] [38] enabling us to optimize the solvatochromic response within a single COF family.

Combinations with more electron-deficient aldehyde counterparts are expected to produce electronic transitions with a varying degree of charge-transfer character across the conjugated imine bond. For optimal solvatochromic response, however, these charge-transfer transitions

are not only required to possess sufficient oscillator strength, but also be sensitive to polarity changes in the pores.

In light of these considerations, we chose three increasingly electron-deficient aldehyde counterparts (Figure 5.1). Pairing $Py(NH_2)_4$ with the tetradentate 1,3,6,8-tetrakis(4-formylphenyl)pyrene, $Py(CHO)_4$, in the **Py-Py** COF is anticipated to produce the smallest donor-acceptor contrast in this context, derived mainly from the slightly polarized imine bond. Switching from pairing two quaterdentate building blocks to a combination of the quaterdentate amine with a linear acene dialdehyde, $1P(CHO)_2$, as realised in the **Py-1P** COF, increases the polarity within the linear bridge. An even stronger charge-transfer character can be achieved in combinations with electron-deficient heterocycles, such as the thieno-[3,2-*b*]thiophene-2,5-dicarboxaldehyde, $TT(CHO)_2$, in the **Py-TT** COF.

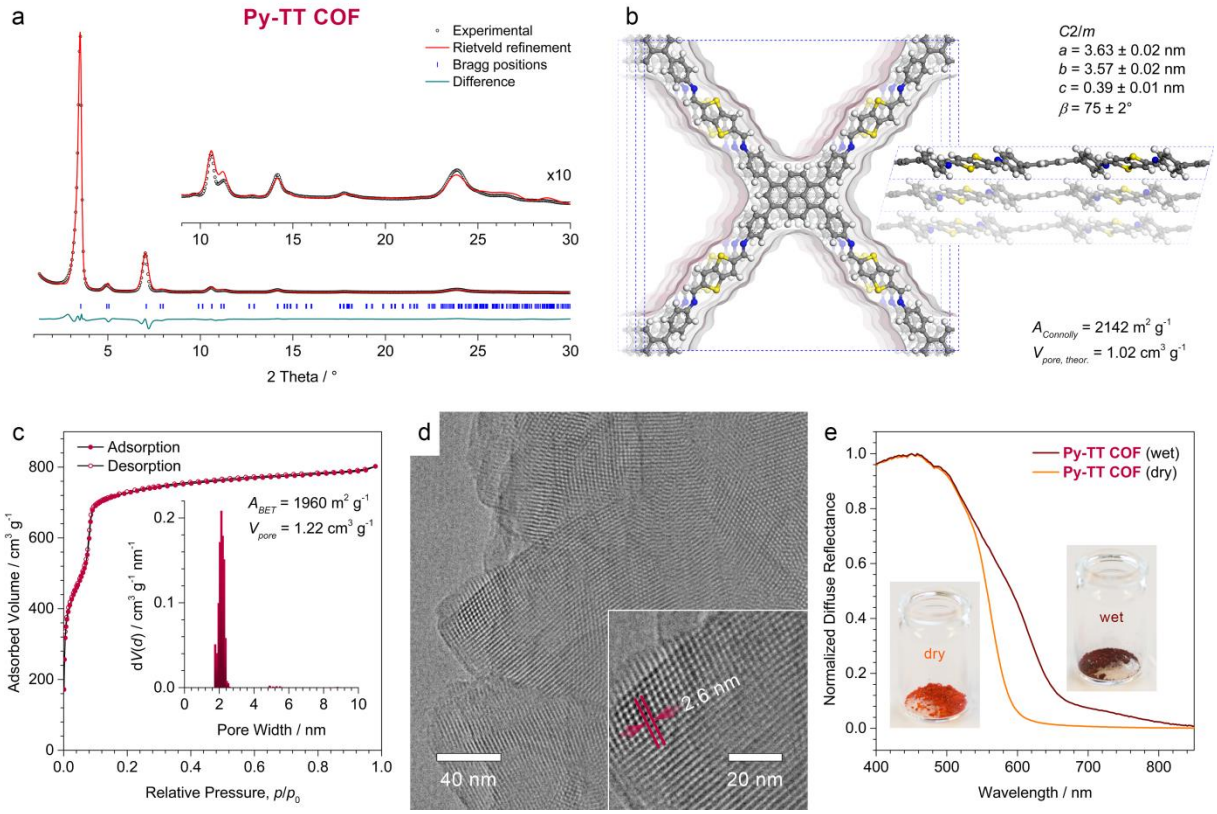

Figure 5.2 Structure analysis and solvatochromism of the Py-TT COF bulk powder. (**a**) Experimental PXRD pattern (black dots) of the **Py-TT** COF powder. Rietveld refinement (red line) using the structure model displayed in (**b**) provides a very good fit to the experimental data with only minimal differences between the experimental and the refined patterns (green line). R_{wp} = 5.1%, R_p = 10.9%. Bragg positions are indicated by blue ticks. Inset, magnified view of the 2θ > 9° region. (**b**) Top view (left) and side view (right) of the corresponding unit cell reveal the pseudo-quadratic, offset-

stacked structure that is typical for pyrene-based COFs. The structure has a Connolly surface of 2142 $m^2 g^{-1}$ with a pore volume of 1.02 $cm^3 g^{-1}$. (**c**) Nitrogen sorption isotherm of the **Py-TT** COF recorded at 77 K. Inset, QSDFT calculation using an equilibrium model yields a very narrow pore-size distribution with a maximum at 2.1 nm. (**d**) High resolution TEM image showing the large crystal domains of the **Py-TT** COF. Inset, magnified view onto a COF crystallite visualizing the pseudo-quadratic arrangement of the COF pores with a periodicity of 2.6 ± 0.1 nm. (**e**) Diffuse reflectance spectra of the dry (orange) and water vapour-saturated (brown) **Py-TT** COF powder showing a strong solvatochromic red-shift.

The **Py-Py**, **Py-1P** and **Py-TT** COFs were initially synthesized as bulk powders under solvothermal conditions (see Supporting Information for details).

The powder X-ray diffraction (PXRD) pattern of the **Py-TT** COF contains a number of sharp reflections, including several well-defined higher-order reflections, and is devoid of any visible amorphous background (Figure 5.2a). Rietveld refinement in the monoclinic space group *C*2/*m* using the force-field optimized structure model shown in Figure 5.2b provides a very good fit to the experimental data. Owing to the large number of light atoms in the unit cell and the peak broadening due to the inherent flexibility of imine-linked COFs, it is not possible to refine the coordinates of individual atoms. We therefore observe some deviations in the intensities of higher-index reflections that are primarily attributed to slight differences between the structure model and the actual COF structure.

With pore diagonals of 2.4 and 2.0 nm (corner-to-corner and bridge-to-bridge, respectively) in the refined structure model, the **Py-TT** COF is expected to be a mesoporous material. Its nitrogen sorption isotherm exhibits a type IVb isotherm shape with a sharp step at $p/p_0 = 0.08$, confirming the mesoporosity (Figure 5.2c). [39] Quenched solid density functional theory (QSDFT) analysis using an equilibrium model for cylindrical pores yields a very narrow pore size distribution with a maximum of 2.1 nm, in excellent agreement with the structure model. The Brunauer-Emmett-Teller (BET) surface of the **Py-TT** COF is 1960 ± 50 $m^2 g^{-1}$ with a total pore volume of 1.22 ± 0.05 $cm^3 g^{-1}$. These results are in very good agreement with the porosity values derived from the structure model, confirming that the pores of the framework are fully open and accessible.

Transmission electron microscopy (TEM) reveals the formation of a periodic framework with domain sizes of 50 - 200 nm (Figure 5.2d). High-resolution TEM confirms the pseudo-

quadratic geometry of the COF with a periodicity of 2.6 ± 0.1 nm, in excellent agreement with the pore-to-pore repeat distance of 2.5 nm in the refined structure model.

The isostructural **Py-1P** COF is an equally well-crystallized framework with a slightly smaller unit cell due to the shorter terephthalaldehyde bridge (SI, Figure 5.4). The **Py-Py** COF has a similar pseudo-quadratic overall geometry, but is composed of alternating columns of the pyrene amine and aldehyde. The symmetry of the framework is thus reduced to *P*2/*m* with a considerably smaller unit cell owing to the reduced length of the bridge between the pyrene centres (SI, Figures 5.5).

Following our initial considerations, COFs comprising donor-acceptor motifs of alternating electron-rich and -deficient building blocks are expected to show a solvatochromic response towards molecules in their pores. Indeed, exposing the initially orange-red **Py-TT** COF powder to an atmosphere of 98% relative humidity causes a colour change to dark brown within few seconds (Figure 5.2e). The corresponding diffuse reflectance spectra reveal that this colour change stems from the appearance of new optical transitions in the 550-850 nm range. This effect is fully reversible as the colour reverts to the initial orange-red hue upon drying. The **Py-1P** and **Py-Py** COFs also respond to water vapour (SI, Figures 5.4e and 5.5e). The colour shifts, however, are less pronounced, presumably owing to the much smaller donor-acceptor contrast between their building blocks. The origin of the solvatochromic colour shifts in our COFs will be discussed in more detail below.

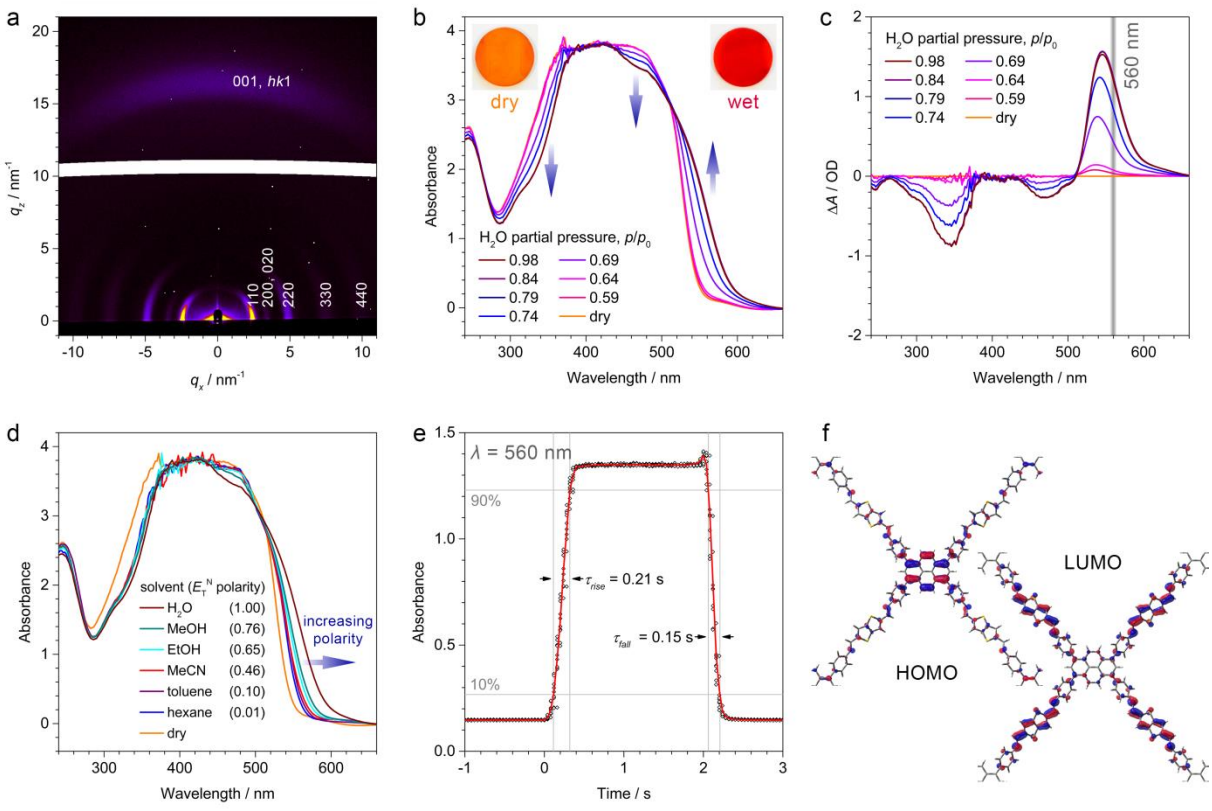

Figure 5.3 Solvatochromism of Py-TT COF oriented thin films. (**a**) GIWAXS pattern of a 360 nm thick **Py-TT** COF film grown on a sapphire substrate. The intensity of *hk*0 reflections is concentrated directly above the sample horizon, whereas the 001 and other low-index *hk*1 reflections appear close to the substrate normal. (**b**) UV-Vis absorption spectra of the **Py-TT** COF film recorded at different partial pressures of H_2O in N_2. Increasing water content causes a strong absorption increase in the 520-640 nm region, accompanied by a reduced absorption in the 440-500 nm and 280-380 nm regions. Insets, photographs of the COF film in the dry and water-saturated states. (**c**) Corresponding plot of the humidity-induced absorbance changes, A_{humid}-A_{dry}, at different H_2O partial pressures. The grey line indicates the wavelength used for the response time measurements (see below). (**d**) UV-Vis spectra of the same COF film in saturated atmospheres of various solvents. The solvatochromic shift increases monotonically with increasing E_T^N polarity of the solvents. (**e**) Solvatochromic response of the **Py-TT** COF film towards step-changes between dry and H_2O-saturated N_2 streams. 10 individual data sets (black dots) recorded at λ = 560 nm have been averaged (red line). The response times τ_{rise} and τ_{fall} are determined between the 10% and 90% thresholds. (**f**) DFT-simulated frontier orbitals of a single-layer **Py-TT** molecular fragment. A cut-out of the structure is shown in this figure; see the SI for the complete model system. The HOMO is centred on the electron-rich pyrene core. The LUMO is mostly located on the electron-deficient TT bridge, causing a strong charge-transfer character of the lowest-energy optical transition.

We anticipated that growing the solvatochromic COF as an oriented film with the pores extending from the substrate surface would greatly facilitate the diffusion of guest molecules into and out of the framework and thus strongly accelerate the response to changes in the surrounding atmosphere. Supported COF thin films would moreover simplify handling, improve re-usability, and facilitate the read-out procedure in possible applications (see below).

The growth of oriented COF films on non-epitaxial substrates has recently also been realized for imine-linked frameworks.[34] We adapted this method for the growth of the **Py-TT**, **Py-1P**, and **Py-Py** COFs. Solvothermal syntheses in slightly diluted solutions yielded smooth and homogeneous films of the three frameworks on fused silica, sapphire, or indium-tin-oxide (ITO) substrates with tuneable thickness between 160 and 360 nm, depending on the reaction time (see the SI for details).

The 2D grazing-incidence wide angle X-ray scattering (GIWAXS) pattern of the **Py-TT** COF film exhibits a number of well-defined reflections that can be indexed as shown in Figure 5.3a. The distribution of the reflections indicates that the COF film is highly textured with the imine-linked layers extending parallel to the substrate surface (Figure 5.6a,b). Individual COF domains grow hereby at random rotation about the substrate normal (planar disorder) (Figure 5.6c,d). We found that this texture is identical for different substrates (c-cut sapphire, fused silica, polycrystalline ITO), suggesting that the uniaxial preferred orientation is generated by the anisotropy of the framework.[34] [36]

The electronic coupling throughout the film was analysed for films grown on ITO substrates with electron- or hole-selective contact layers (TiO_2 or MoO_x, respectively). Transport measurements of these vertical-stack single-carrier devices yield charge-carrier mobilities of $(4.02 \pm 0.04) \times 10^{-6}$ and $(1.02 \pm 0.01) \times 10^{-7}$ $cm^2\ V^{-1}\ s^{-1}$ for holes and electrons, respectively (SI, Figure 5.7).

In accordance with the GIWAXS results, TEM analysis of a **Py-TT** COF film removed from the substrate shows a highly textured morphology with the *ab*-plane perpendicular to the viewing direction, i.e. parallel to the substrate (SI, Figure 5.6e,f). The pores consequently extend at an angle of 75° vs. the substrate surface (i.e. 15° vs. the viewing direction) and hence are fully accessible to the surrounding atmosphere.

As for the COF powder, exposing the **Py-TT** COF film to a humidified N_2 flow results in a colour change from orange to dark red. Transmission UV-Vis spectra recorded at different H_2O partial pressures reveal the appearance of an absorption band in the 520-640 nm region and a simultaneous decrease in absorption across the 440-500 nm and 280-380 nm spectral regions (Figure 5.3b). Plotting the change in absorbance ΔA enables us to identify a strong humidity-induced absorption band with a maximum at 545 nm that is accompanied by two bleach bands with minima at 345 and 470 nm (Figure 5.3c). The COF film exhibits the highest sensitivity towards humidity changes between H_2O partial pressures of 0.64 and 0.79. Above this, the absorption change saturates, possibly due to condensation in the COF pores.

The **Py-TT** COF was found to respond in a similar way to a range of organic solvents (Figure 5.3d). The magnitude of the colour change upon exposure to a saturated atmosphere increases monotonically with the E_T^N polarity of the respective solvent (SI, Figure 5.8).[30] The **Py-TT** COF thus represents a solid-state supramolecular analogue to the commercially available molecular solvatochromic dyes with the added benefit of being sensitive even to vapours diluted in a carrier gas.

Oriented films of the **Py-TT** COF with their pores extending towards the film surface display a very fast response towards step-changes between dry and H_2O-saturated gas streams (Figure 5.3e). For a 360 nm thick film, we measure a response time (τ_{rise}) of 0.21 s for the absorption increase upon change from dry to humid atmosphere, while the transition to the dry state is even faster with τ_{fall} = 0.15 s. As the solvent molecules need to diffuse through the entire film in order to saturate the solvatochromic colour change, we anticipated a strong correlation between film thickness and response time. Indeed, both response times get shorter for thinner films, whereby the fastest response of 0.11 s/0.09 s (rise/fall) was achieved using a 160 nm thick COF film (SI, Figure 5.9). To the best of our knowledge, this represents the fastest response time of a solvatochromic sensing system reported to date, and places it among the fastest nanostructured humidity sensors.[40] [41] [42] [43]

In addition to this extremely fast response, the **Py-TT** COF films display excellent reversibility and reproducibility during repeated switching (SI, Figure S7a). Furthermore, the COF film is stable over at least 4000 humidity and solvent vapour switching cycles and storage in ambient air for 250 d, without showing any apparent changes in its absorption spectra and GIWAXS patterns (SI, 5.10b-e).

For a possible application as a high performance solvatochromic sensor, easy read-out, fast response times, reversibility, and reproducibility are of key importance. Employing the COF thin film as a vapour-sensitive light filter, a continuous read-out was realized in combination with a green LED and a light-dependent resistor (SI, Figure 5.18). A video of this proof of concept is included as Supporting Information.

In order to shed light on the origin of the solvent-induced colour-changes of our COFs, we first probed for chemical or structural changes that might alter the coupling between the building blocks or the COF layers. Solid-state nuclear magnetic resonance measurements, however, provide no indication of a different chemical environment in the water-saturated COF (SI, Figure 5.12). If the **Py-TT** COF is exposed to a water-saturated atmosphere, the PXRD reflection intensities, especially of *hk*0 reflections, are reduced considerably (SI, Figure 5.11a,b). This effect, however, is fully reversible and can be attributed to modified structure factors due to the water molecules in the pores (SI, Figure 5.11c,d). All reflection positions, peak shapes and widths, and hence the unit cell and framework symmetry remain unchanged during the humidity cycles. Given the three-dimensional configuration and interlocked stacking of the COF layers, even minor deformations or rotations of the bridges would be reflected in modified unit cell parameters. The absence of structural changes is further supported by the extreme stability of the material, which seems hardly possible if deformations or sliding of the COF layers were involved.

The **Py-TT** COF displays a positive solvatochromism, i.e. the absorption is red-shifted with increasing polarity. In well-studied molecular dyes such as phenol blue,[44] this is observed for combinations of a low-polarity ground state with a polar first excited state.[28] In that case, the excited state is stabilized to a larger extent than the ground state with increasing polarity of the surrounding medium, hence lowering the energy required for photoexcitation.

DFT calculations (B3LYP/6-31G(d)) of the frontier orbitals carried out for a single-layer **Py-TT** molecular fragment show that the highest occupied molecular orbital (HOMO) is mostly localized on the electron-rich pyrene (Figure 5.3f and SI, Figure 5.19). In contrast, the LUMO is centred on the electron-deficient TT bridges, leading to a pronounced charge-transfer character of the lowest-energy optical transition. While this symmetrical charge-transfer alone would not result in a change of dipole moment upon excitation, facile lattice vibrations in the COF will lead to unsymmetrical structures that give highly dipolar excited states. This

excited-state symmetry breaking is well stablished for linear molecular quadrupoles and should be equally applicable in COFs.[45] [46]

A strong charge-transfer character of the lowest-energy optical transition in polar environments in the **Py-TT** COF is further supported by its photoluminescence (PL) characteristics (SI, Figure 5.14). If the COF is exposed to a humid atmosphere, the PL is red-shifted, indicating a stabilisation of the excited state by the pore medium. This is accompanied by a reduction in PL intensity by more than 95% compared to the dry material, suggesting that under these conditions there is sufficient dielectric screening at optical frequencies to overcome the Coulomb barrier and sustain the charge-separated state.[47] [48] This sensitivity to the brought-in charge-transfer character causes the solvatochromic response.

In summary, there is strong evidence that the solvatochromism of our COFs is of purely electronic nature with no structural or chemical changes involved.

We furthermore found the solvatochromic response to depend on the crystallinity of the framework. While crystalline films of the **Py-1P** COF display a colour shift from yellow to orange when exposed to solvent or water vapour, a chemically identical amorphous **Py-1P** network does not show any solvatochromism (SI; Figure 5.15). We thus conclude that the solvatochromic function requires a combination of a precisely defined, accessible porosity and an appropriate electronic structure of the COF backbone.

5.4 Conclusion

We have developed the first solvatochromic covalent organic frameworks that show strong colour shifts when exposed to solvent or water vapours. Growing these COFs as highly crystalline vertically oriented thin films, we have realized optically homogeneous coatings that can act as fully reversible, solid-state supramolecular solvatochromic sensors. The excellent accessibility of the pores in these films results in ultrafast response times of below 200 ms, thus outperforming commercial humidity sensors by more than an order of magnitude. As a proof of concept, we constructed a simple and fast humidity sensor device by using the COF film as a vapour-sensitive light filter between an LED and a light-dependent resistor. Experimental data and DFT calculations strongly suggest that the solvatochromism is of purely electronic origin and does not involve structural or chemical changes in the framework – a fact that we believe is not only key to the extremely fast response times and outstanding stability of the material, but might also have implications for the use of COFs in

the broader context of optoelectronics. In particular, the observation that in these materials electronic transitions can be manipulated reversibly and that intramolecular charge-transfer can be facilitated via the inclusion of chemically inert guest molecules could impact the development of stimuli-responsive organic electronics. Future chemical modifications to the COF backbone or the pore walls could be used to adapt the sensitivity and selectivity of the solvatochromic response, broadening the range of possible applications for these materials.

5.5 Supporting information

Nuclear magnetic resonance (NMR) spectra were recorded on Bruker AV 400 and AV 400 TR spectrometers. Proton chemical shifts are expressed in parts per million (δ scale) and are calibrated using residual undeuterated solvent peaks as an internal reference (DMSO-d_6: 2.50). Data for ^{1}H NMR spectra are reported in the following way: chemical shift (δ ppm) (multiplicity, coupling constant, integration). Multiplicities are reported as follows: s = singlet, d = doublet, t = triplet, q = quartet, m = multiplet, or combinations thereof. Magic angle spinning (MAS) **solid-state nuclear magnetic resonance** (ssNMR) spectra were recorded with a Bruker Avance III-500 spectrometer using 2.5 mm diameter ZrO_2 rotors at a spinning frequency of 20 kHz.

Powder X-ray diffraction (PXRD) measurements were performed using a Bruker D8 Discover with Ni-filtered Cu K_α radiation and a LynxEye position-sensitive detector.

2D **grazing-incidence wide angle X-ray scattering** (GIWAXS) data were recorded with an Anton Paar SAXSpace system equipped with a GeniX Cu K_α microsource and a Dectris Eiger R 1M detector. The samples were positioned at a tilt angle of 2.3° and a sample-detector distance of 135 mm.

The **structure models of the COFs** were constructed using the Accelrys Materials Studio software package. For each COF structure we applied the space group with the highest possible symmetry, taking into account the rotation of the phenylenes versus the pyrene core. Structure refinements using the Rietveld method were carried out as implemented in the Reflex module of the Materials Studio software. Pseudo-Voigt peak profiles were used and peak asymmetry was corrected using the Finger-Cox-Jephcoat method. **Connolly surfaces** were generated using an N_2-sized probe (r = 0.184 nm) at a 0.025 nm grid interval.[49]

Nitrogen sorption isotherms were recorded on a Quantachrome Autosorb 1 at 77 K. Prior to the measurements, the samples were outgassed for 24 h at 120°C under high vacuum. For the evaluation of the surface areas the BET model was applied in the ranges $0.005 \leq p/p_0 \leq 0.025$ (**Py-TT** COF), $0.002 \leq p/p_0 \leq 0.023$ (**Py-1P** COF), and $0.0002 \leq p/p_0 \leq 0.004$ (**Py-Py** COF), respectively. Total pore volumes were determined at $p/p_0 = 0.9$ to minimize the contributions of textural porosity. Pore size distributions were calculated using the QSDFT equilibrium model with a carbon kernel for cylindrical pores.

Transmission electron microscopy (TEM) was performed with an FEI Titan Themis equipped with a field emission gun operated at 300 kV.

Scanning electron microscopy (SEM) was performed with an FEI Helios NanoLab G3 UC eqiupped with a Schottky field-emission electron source operated at 1 - 30 kV.

UV-Vis spectra were recorded using a Perkin-Elmer Lambda 1050 spectrometer equipped with a 150 mm InGaAs integrating sphere. Time-resolved absorption measurements were performed at fixed detector gain and slit settings. **Diffuse reflectance spectra** were collected with a Praying Mantis (Harrick) accessory and were referenced to barium sulfate powder as white standard. The specular reflection of the sample surface was removed from the signal by spatial filtering.

Gas flow experiments were performed using a gas flow controller system (F-201-C-RBA-33-V, Bronkhorst Hi-Tec) and a liquid mass flow controller with a controlled evaporation mixer (W-101A-110, Bronkhorst Hi-Tec), where the solvents were evaporated at temperatures above their boiling points. Solvents were obtained from commercial suppliers in high-purity anhydrous grades and were used as received. The flow cell was home-built from a 10 x 10 mm fused silica cuvette (Hellma Analytics) equipped with a tightly fitting PTFE lid and 2 mm diameter PP hoses connected to the gas flow system. Individual vapour pressures were calculated using the Bronkhorst Fluidat software tool.[50] In this context the terms “dry” and “wet” refer to H_2O partial vapour pressures of $p/p_0 = 0$ and $p/p_0 = 0.98$, respectively.

Steady-state **humidification** of the bulk powders was performed using a home-built humidification chamber with a saturated potassium sulfate solution to reach a relative humidity of 98%.[51]

Photoluminescence (PL) measurements were performed using a home-built setup consisting of a Horiba Jobin Yvon iHR 320 monochromator equipped with a photomultiplier tube and a liquid N_2-cooled InGaAsdetector. The samples were illuminated with a 378 nm diode laser (pulse power 0.99 nJ cm^{-2}, pulse rate 40 MHz).

FT-IR spectra were recorded using a Perkin Elmer Spectrum BX FT-IR System.

Density functional theory (DFT) calculations were performed with Gaussian 16[52] using the B3LYP[53] [54] [55] [56] hybrid density functional and the 6-31G(d) [57] [58] [59] [60] [61] [62] basis set.

Building block syntheses

All reactions were performed in oven-dried glassware under argon atmosphere using standard Schlenk and glovebox techniques. Commercially available reagents were used as received. Solvents were obtained in high-purity grades from commercial suppliers and were, unless shipped under argon, degassed and saturated with argon prior to use.

1,3,6,8-tetrakis(4-aminophenyl)pyrene, Py(NH_2)$_4$ [37] [63]

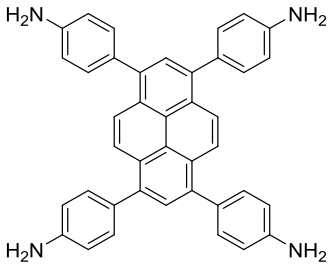

A reaction mixture containing 1,3,6,8-tetrabromopyrene (1482 mg, 2.86 mmol, 1.0 eq.), 4-aminophenylboronic acid pinacol ester (3010 mg, 13.7 mmol, 4.8 eq.), K_2CO_3 (2175 mg, 15.7 mmol, 5.5 eq.), and $Pd(PPh_3)_4$ (330 mg, 0.29 mmol, 10 mol%) in 32 mL 1,4-dioxane and 8 mL degassed H_2O was refluxed at 115 °C for 3 d. After cooling to room temperature, H_2O (50 mL) was added. The resulting precipitate was collected via filtration and washed subsequently with H_2O (50 mL) and MeOH (100 mL). Recrystallization from 1,4-dioxane, followed by drying under high vacuum yielded the title compound, co-crystallized with approximately 1.5 dioxane molecules per formula unit, as a bright yellow powder (1792 mg, 2.56 mmol, 90%).

^{1}H NMR (400 MHz, DMSO-d_6): 8.13 (s, 4 H), 7.79 (s, 2 H), 7.34 (d, J = 8.4 Hz, 8 H), 6.77 (d, J = 8.5 Hz, 8 H), 5.30 (s, 8 H), 3.56 (s, 12 H, dioxane).

^{13}C NMR (100 MHz, DMSO-d_6): 148.2, 137.1, 131.0, 129.0, 127.6, 126.7, 126.1, 124.4, 113.9, 66.3 (dioxane).

1,3,6,8-tetrakis(4-formylphenyl)pyrene, Py(CHO)$_4$[64]

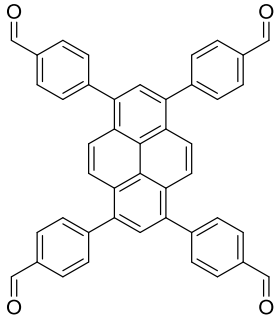

1,3,6,8-tetrabromopyrene (371 mg, 0.72 mmol, 1.0 eq.), 4-formylphenylboronic acid (480 mg, 3.20 mmol, 4.8 eq.), K_2CO_3 (547 mg, 3.66 mmol, 5.5 eq.) and $Pd(PPh_3)_4$ (83 mg, 0.066 mmol, 10 mol%) were refluxed at 115 °C in 8 mL 1,4-dioxane and 2 mL H_2O for 3 d. After cooling to room temperature, H_2O (20 mL) was added. The precipitate was collected by filtration and was washed with H_2O and MeOH. The resulting yellow powder was dried under vacuum (378 mg, 0.61 mmol, 85%).

^{1}H NMR (400 MHz, DMSO-d_6): 10.16 (s, 4 H), 8.18 (s, 4 H), 8.09 (d, J = 8.20 Hz, 8 H), 8.04 (s, 2 H), 7.86 (d, J = 8.20, 8 H).

Due to the low solubility of this compound in common deuterated solvents, no ^{13}C NMR spectra could be recorded.

COF syntheses

COF bulk powder syntheses were performed under argon atmosphere in PTFE-sealed glass reaction tubes (6 mL volume). Solvents and acetic acid were obtained in high-purity grades from commercial suppliers and were, unless shipped under argon, degassed and saturated with argon prior to use.

Py-TT COF

$Py(NH_2)_4$ (14.0 mg, 20 µmol, 1.0 eq.) and thieno-[3,2-*b*]thiophene-2,5-dicarboxaldehyde (7.8 mg, 40 µmol, 2.0 eq.) were filled into a reaction tube, followed by the addition of mesitylene (667 µL), benzyl alcohol (333 µL), and 6 M acetic acid (100 µL). The tube was sealed and kept at 120 °C for 3 d. After cooling to room temperature, the precipitate was collected by filtration, washed with MeCN and dried in air, yielding a bright red powder.

Py-1P COF

$Py(NH_2)_4$ (14.0 mg, 20 µmol, 1.0 eq.) and terephthalaldehyde (5.4 mg, 40 µmol, 4.0 eq.) were filled into a reaction tube, followed by the addition of mesitylene (667 µL), 1,4-dioxane (333 µL), and 6 M acetic acid (100 µL). The tube was sealed and heated at 120 °C for 3 d. After cooling to room temperature, the precipitate was collected by filtration, yielding a bright orange powder.

Py-Py COF

$Py(NH_2)_4$ (3.5 mg, 5.1 µmol, 1.02 eq.) and $Py(CHO)_4$ (3.1 mg, 5 µmol, 1.0 eq.) were filled into a reaction tube, followed by the addition of mesitylene (333 µL), benzyl alcohol (167 µL), and 6 M acetic acid (50 µL). The tube was sealed and kept at 120 °C for 3 d. After cooling to room temperature, the precipitate was collected by filtration, washed with MeCN and dried in air, yielding a bright yellow powder.

COF thin films were synthesized in 100 mL autoclaves equipped with a 28 mm diameter glass liner. Fused silica (Spectrosil 2000), sapphire (UQG Optics, *c*-axis cut), and ITO-coated glass (VisionTec, 12-15 ohms/sq) substrates were cleaned in detergent solution, water, acetone, and isopropanol, and activated with an O_2-plasma for 5 min directly before use. The

substrates were placed horizontally in PTFE sample holders with the activated surface face-down.

Py-TT COF films

$Py(NH_2)_4$ (7.0 mg, 10 µmol, 1.0 eq.) and thieno-[3,2-*b*]thiophene-2,5-dicarboxaldehyde (4.0 mg, 20 µmol, 2.0 eq.) were filled into an autoclave, followed by the addition of mesitylene (1333 µL) and benzyl alcohol (666 µL). A substrate (fused silica, sapphire or ITO) was inserted, followed by the addition of 6 M acetic acid (200 µL). The autoclave was sealed and heated to 120 °C for 4 d. After cooling to room temperature, the substrate was immersed in dry MeCN and dried with compressed air. Thinner films were grown at shorter reaction times ranging from 4 h to 2 d.

Py-1P COF films

$Py(NH_2)_4$ (7.0 mg, 10 µmol, 1.0 eq.) and terephthalaldehyde (2.75 mg, 20 µmol, 2.0 eq.) were filled into an autoclave, followed by the addition of mesitylene (1333 µL) and benzyl alcohol (666 µL). An ITO substrate was inserted, followed by the addition of 6 M acetic acid (200 µL). The autoclave was sealed and heated to 120 °C for 3 d. After cooling to room temperature, the substrate was rinsed with dry MeCN and dried with compressed air.

The **amorphous Py-1P network** was grown under identical synthesis conditions as the Py-1P COF, but employing a TiO_2 (anatase) coated ITO substrate.[65]

Py-Py COF films

$Py(NH_2)_4$ (7.0 mg, 10 µmol, 1.0 eq.) and $Py(CHO)_4$ (6.2 mg, 10 µmol, 1.0 eq.) were filled into an autoclave, followed by the addition of mesitylene (1333 µL) and benzyl alcohol (666 µL). A substrate (sapphire or ITO) was inserted, followed by the addition of 6 M acetic acid (200 µL). The autoclave was sealed and heated to 120 °C for 3 d. After cooling to room temperature, the substrate was rinsed with dry MeCN and dried with compressed air.

Py-1P COF structure analysis

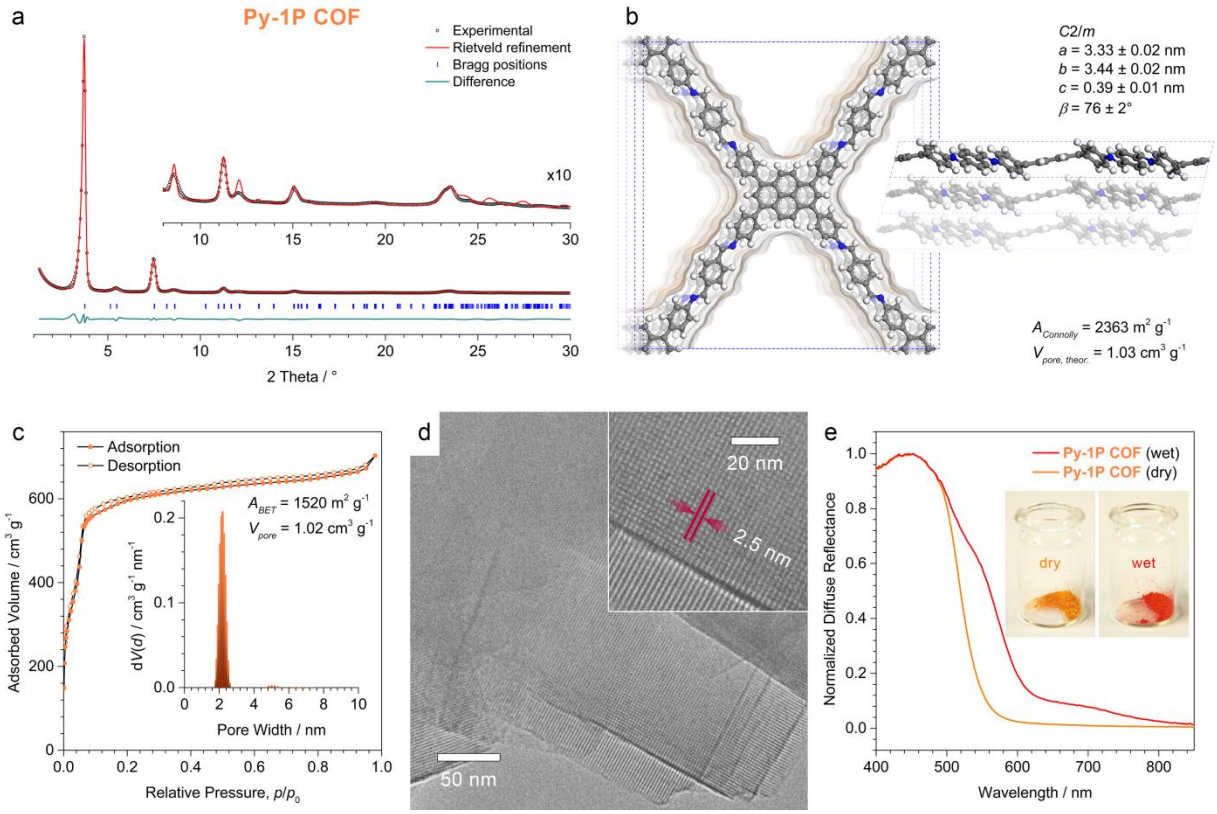

Figure 5.4 Structure analysis and solvatochromism of the Py-1P COF bulk powder. (**a**) Experimental PXRD pattern (black dots) of the **Py-1P** COF powder. Rietveld refinement (red line) using the structure model displayed in (**b**) provides a very good fit to the experimental data with only minimal differences between the experimental and the refined patterns (green line). R_{wp} = 3.4%, R_p = 8.4%. Bragg positions are indicated by blue ticks. Inset, magnified view of the 2θ > 8° region. (**b**) Top view (left) and side view (right) of the corresponding unit cell showing the pseudo-quadratic, offset-stacked structure that is typical for pyrene-based COFs. Crystallographic data are available as Supporting Information. The structure has a Connolly surface of 2363 m^2 g^{-1} with a pore volume of 1.03 cm^3 g^{-1}. (**c**) Nitrogen sorption isotherm of the **Py-1P** COF recorded at 77 K. Inset, QSDFT calculation using an equilibrium model yields a very narrow pore-size distribution with a maximum at 2.1 nm. (**d**) High resolution TEM image showing the very large crystal domains of the **Py-1P** COF. Inset, magnified view onto a COF crystallite revealing the pseudo-quadratic arrangement of the COF pores with a periodicity of 2.5 ± 0.1 nm. (**e**) Diffuse reflectance spectra of the dry (orange) and water vapour saturated (red) **Py-1P** COF powder showing a strong solvatochromic red-shift.

The PXRD pattern of the **Py-1P** COF contains a number of sharp reflections including several well-defined higher-order reflections, indicating that this COF is equally well-crystallized as the **Py-TT** COF (Figure 5.4a). Rietveld refinement in the monoclinic space group *C*2/*m* using

the force-field optimized structure model shown in Figure 5.4b provides a very good fit to the experimental data. As discussed in the main article, the large number of light atoms in the unit cell and the peak broadening due to the inherent flexibility of imine-linked COFs precludes the refinement of individual atom coordinates. We therefore observe minor deviations in the intensities of higher-index reflections that are primarily attributed to slight differences between the structure model and the actual COF structure.

N_2 sorption confirms that this COF is mesoporous with a pore-size distribution peaking at 2.1 nm (Figure 5.4c). The total pore volume of 1.02 cm^3 g^{-1} derived from the sorption isotherm matches the theoretical porosity very well, indicating that the pores are open and accessible.

This COF forms particularly large crystallites that can reach several hundred nanometres in size and are terminated by well-defined facets (Figure 5.4d). High-resolution TEM reveals the pseudo-quadratic geometry with a periodicity of 2.5 ± 0.1 nm, in excellent agreement with the pore-to-pore repeat distance of 2.4 nm in the refined structure model.

Py-Py COF structure analysis

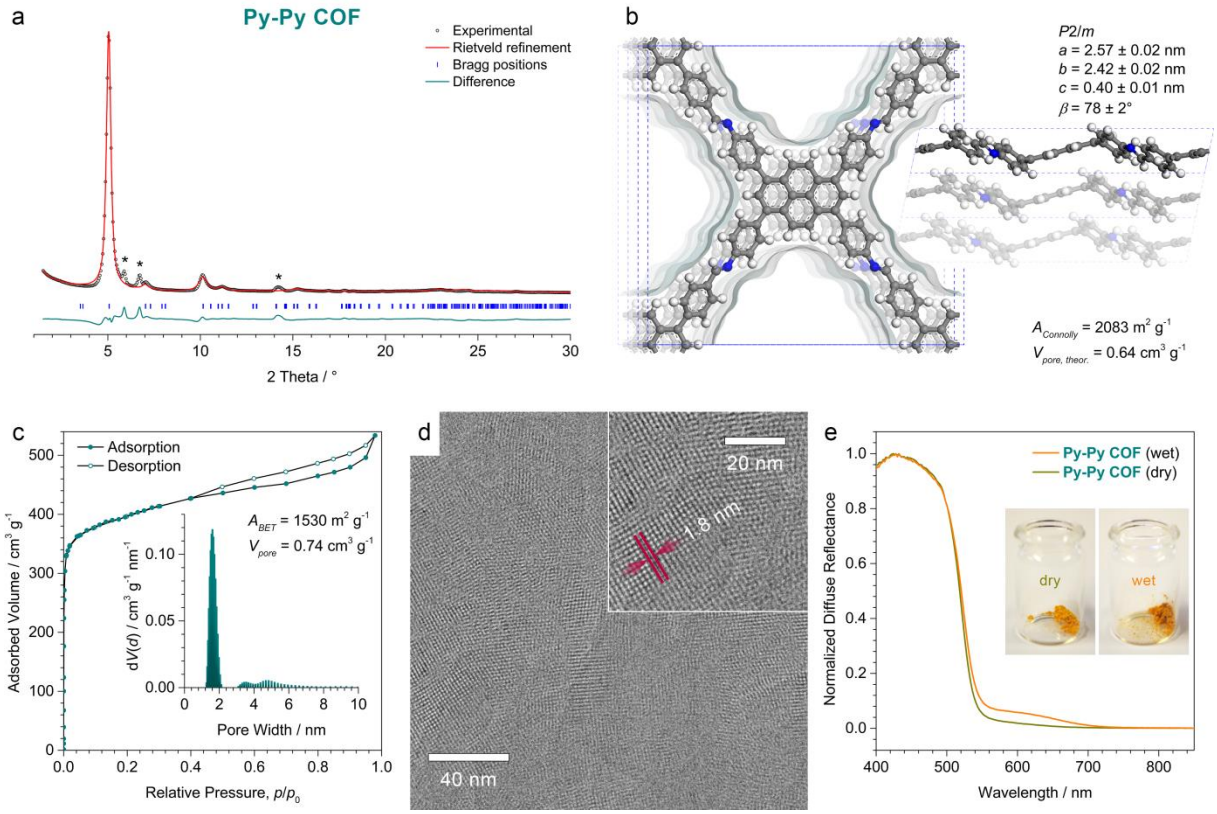

Figure 5.5 Structure analysis and solvatochromism of the Py-Py COF bulk powder. (**a**) Experimental PXRD pattern (black dots) of the **Py-Py** COF powder. The reflections marked with asterisks stem from residual $Py(CHO)_4$ starting material that could not be removed by washing due to its limited solubility. Rietveld refinement (red line) using the structure model displayed in (**b**) provides a good fit to the experimental data with only minor differences between the experimental and the refined patterns (green line). R_{wp} = 7.2%, R_p = 18.1%. Bragg positions are indicated by blue ticks. (**b**) Top view (left) and side view (right) of the corresponding unit cell showing the pseudo-quadratic, offset-stacked structure formed by alternating pyrene amine (centre) and aldehyde (corners) columns. Crystallographic data are available as Supporting Information. The structure has a Connolly surface of 2083 m^2 g^{-1} with a pore volume of 0.64 cm^3 g^{-1}. (**c**) Nitrogen sorption isotherm of the **Py-Py** COF recorded at 77 K. Inset, QSDFT calculation using an equilibrium model yields a narrow pore-size distribution with a maximum at 1.6 nm. (**d**) High resolution TEM image showing the crystal domains of the **Py-Py** COF. Inset, magnified view onto a COF crystallite revealing the pseudo-quadratic arrangement of the COF pores with a periodicity of 1.8 ± 0.1 nm. (**e**) Diffuse reflectance spectra of the dry (green) and water vapour saturated (orange) **Py-Py** COF powder showing a small solvatochromic red-shift.

The **Py-Py** COF features a pseudo-quadratic overall geometry similar to the **Py-TT** and **Py-1P** COFs, but is composed of alternating columns of pyrene amine and pyrene aldehyde moieties. Rietveld refinement of the **Py-Py** COF in the space group *P*2/*m* yields a considerably smaller unit cell than for the other COFs in this study, in line with the reduced length of the pore walls due to the altered connectivity of this framework (Figure 5.5a,b).

The consequently smaller pores give rise to a type I nitrogen sorption isotherm with a QSDFT pore-size distribution peaking at 1.6 nm (Figure 5.5c).

High-resolution TEM confirms the anticipated pseudo-quadratic geometry of the framework with a periodicity of 1.8 ± 0.1 nm, in very good agreement with the pore-to-pore repeat distance of 1.7 nm in the refined structure model (Figure 5.5d).

Py-TT COF film morphology

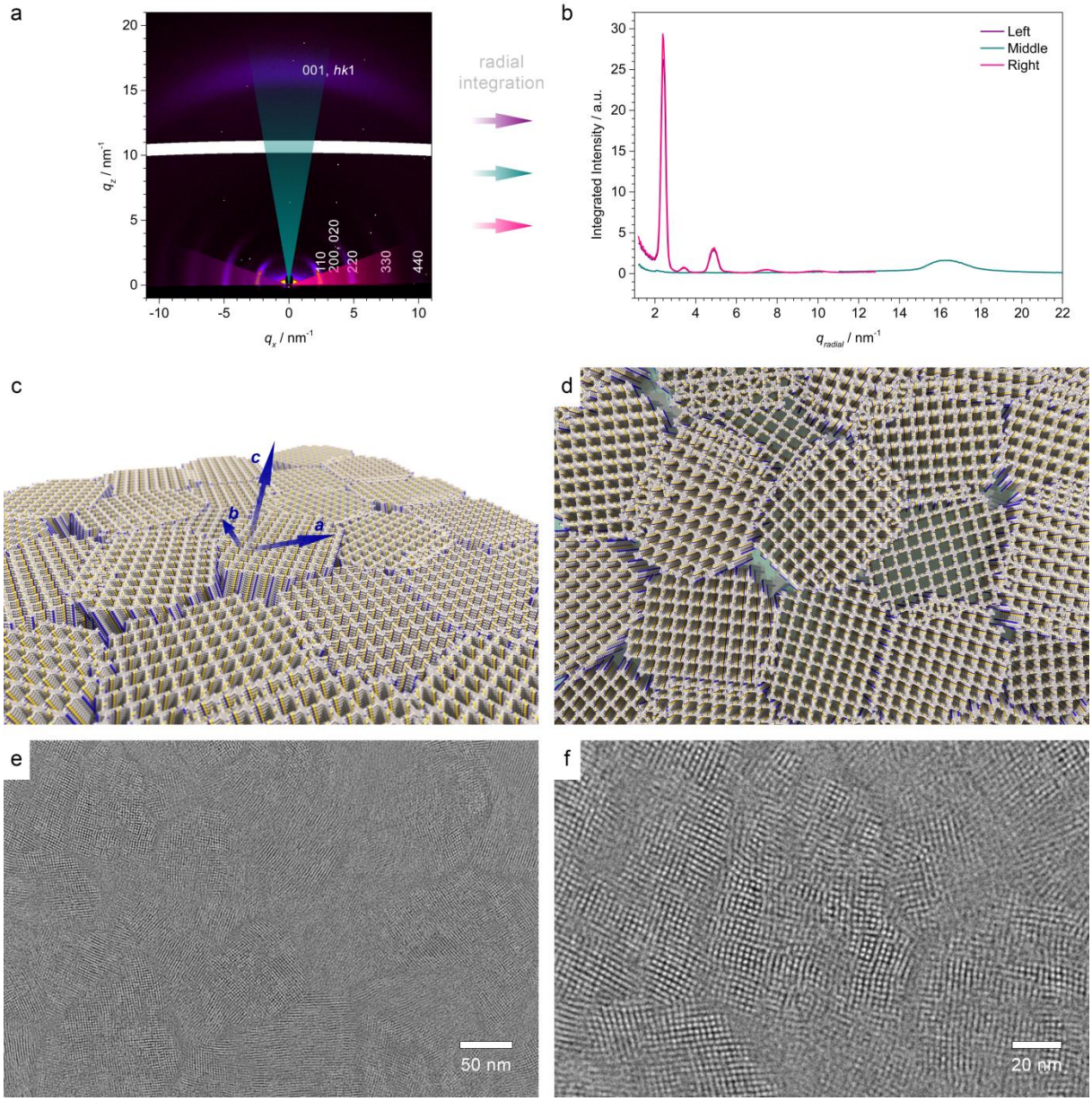

Figure 5.6 Morphology characterisation of the Py-TT COF films. (**a**) GIWAXS pattern of a 360 nm thick **Py-TT** COF film grown on a sapphire substrate. (**b**) Radial integration over the purple, green, and pink segments in the GIWAXS pattern (20° opening) shows that the COF film is highly textured with the crystallographic *ab*-plane parallel to the substrate. Most of the intensity of the 110, 020 and 200, 220, 330 and 440 reflections is confined to the segments directly above the sample horizon (purple and pink lines), while the middle segment contains the 001 reflection and contributions from other low-index *hk*1 reflections (green line; see discussion below). (**c**,**d**) Illustration of the polycrystalline film morphology. Individual COF domains grow with their *ab*-plane parallel to the substrate and at random rotation about the substrate normal. The unit cell axes are indicated for

one crystallite. (**e**) High-resolution TEM image of **Py-TT** COF film revealing its polycrystalline, highly textured morphology with domain sizes around 50 nm. (**f**) Magnified view confirming the orientation of the pores towards the film surface.

The **Py-TT** COF films are highly textured with the imine-linked COF layers extending parallel to the substrate surface. This texture is identical for single-crystalline (*c*-cut sapphire), amorphous (fused silica), and polycrystalline (ITO) substrates, suggesting that the preferred orientation is generated by the anisotropy of the framework.[36] [34] Consistently, individual COF domains grow at random rotation about the substrate normal (planar disorder) without any preferential alignment of their *a* and *b* axes with respect to the sapphire hexagonal plane. Due to the highly anisotropic unit cell, the *d*-spacings of the (001), (111) and other low-index (*hk*1) sets of lattice planes are almost identical. The corresponding reflections, however, appear under different angles relative to the substrate normal and give rise to an arc with $q \approx 16\ nm^{-1}$.

Py-TT COF single carrier devices

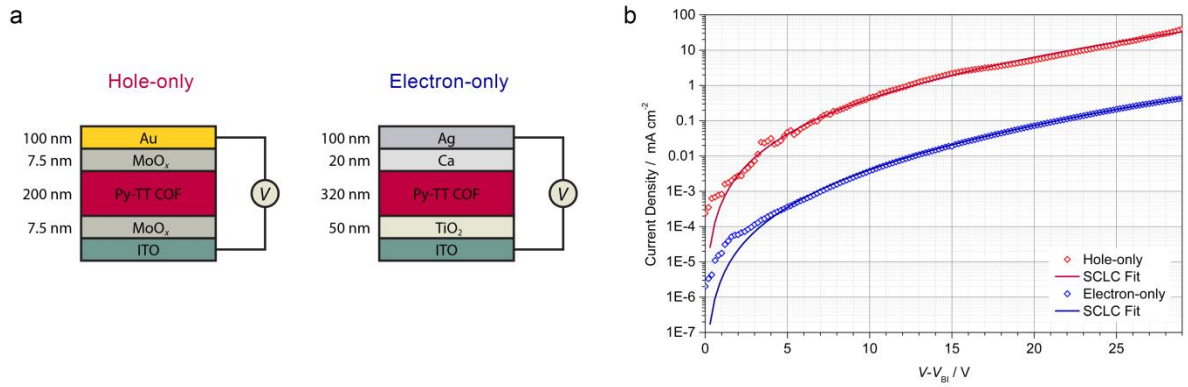

Figure 5.7 Electronic transport properties of Py-TT COF films. (**a**) Schematic illustrations of the hole-only and electron-only devices. (**b**) *J-V* curves of the single carrier devices measured in the dark (symbols) and the corresponding fits using the SCLC model (red and blue lines).

Owing to their sheet-like structure, the electronic properties of 2D COFs tend to be highly anisotropic with the highest conductivity and mobility typically along the π-stacked columns.[34] [21] [66] Electronic transport measurements can thus be used to draw conclusions about the COF crystallite orientation.

Vertical electronic transport was investigated by constructing single carrier devices. **Py-TT** COF films were grown as described above using MoO_x-coated (hole-only) or TiO_2-coated

(electron-only) ITO substrates. The devices were completed by thermal evaporation of MoO_x and Au (hole-only), or Ca and Al (electron-only) electrodes through a shadow mask. COF layer thicknesses were determined from SEM cross-sections of the devices. The devices were measured in the dark with carrier injection from the top contact (MoO_x/Au or Ca/Ag, respectively).

Assuming Ohmic injection, the current in the devices will be space-charge limited. In the space-charge-limited regime, the current density follows a modified Mott-Gurney law, taking into account the dependence of the mobility on the electric field (Poole-Frenkel model, exponential term in equation below).[67] [68] [69]

$$J(V) = \frac{9}{8}\varepsilon_0\varepsilon_r\mu_0\frac{(V-V_{BI})^2}{d^3}exp\left(\beta\sqrt{\frac{(V-V_{BI})}{d}}\right)$$

ε_0 vacuum permittivity

ε_r relative permittivity

μ_0 zero-field mobility

V_{BI} built-in voltage

d COF layer thickness

β field effect mobility coefficient

Table 5.1 SCLC analysis of the Py-TT COF single-carrier devices.

	μ_0 / cm^2 V^{-1} s^{-1}	ε_r (fixed)	V_{BI} / V*	d / nm	β / cm$^{0.5}$ V$^{-0.5}$	Adjusted R^2
hole-only	(4.02 ± 0.04) x 10^{-6}	3.5	1.4	200	4.5 x 10^{-3}	0.984
electron-only	(1.02 ± 0.01) x 10^{-7}	3.5	4.2	320	6.5 x 10^{-3}	0.999

*The built-in voltages were extrapolated from the *J-V* curves. The built-in voltage of the hole-only device could stem from a slight modification of the oxygen stoichiometry (de-doping) of the bottom MoO_x layer during the solvothermal COF synthesis.

To the best of our knowledge, this represents the highest hole-only SCLC mobility of any COF to date,[66] and also is the first measurement of a vertical transport electron mobility.

Lateral transport measurements across gap electrodes deposited on either on the COF film surface (200 µm gap) or on the substrate (50 µm gap) did not show any measurable

conductivity, suggesting that the highest conductivity is indeed along the π-stacked columns and that the orientation of the COF crystallites is unchanged throughout the entire film.

Solvent-induced spectral changes

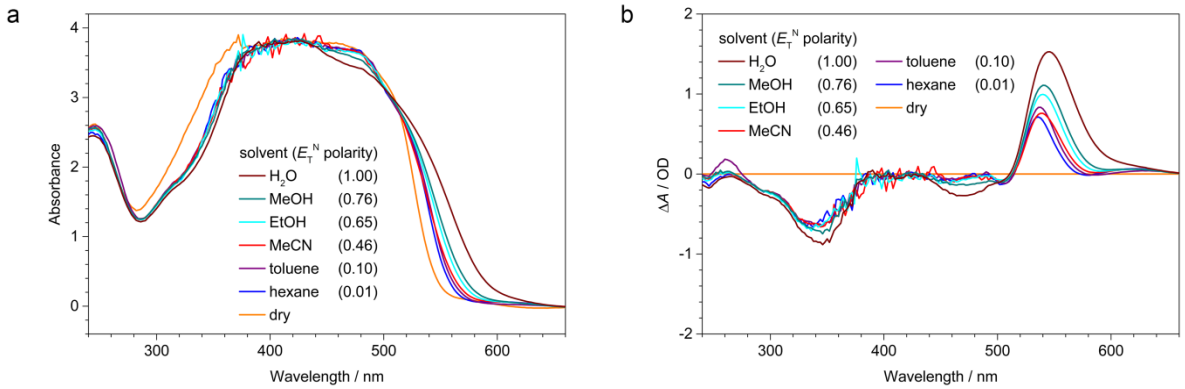

Figure 5.8 Solvent-induced absorption changes of the Py-TT COF. (**a**) UV-Vis spectra of the **Py-TT** COF film exposed to different solvent-saturated N_2 streams. (**b**) Plot of the absorption change, $A_{solvent}$ - A_{dry}, showing a strong solvent-induced absorbance in the 520-640 nm region that is accompanied by two bleach bands extending over the 440-500 and 280-380 nm regions. The magnitude of the solvent-induced spectral changes increases with increasing E_T^N polarity of the respective solvent.

Thickness-dependent response times

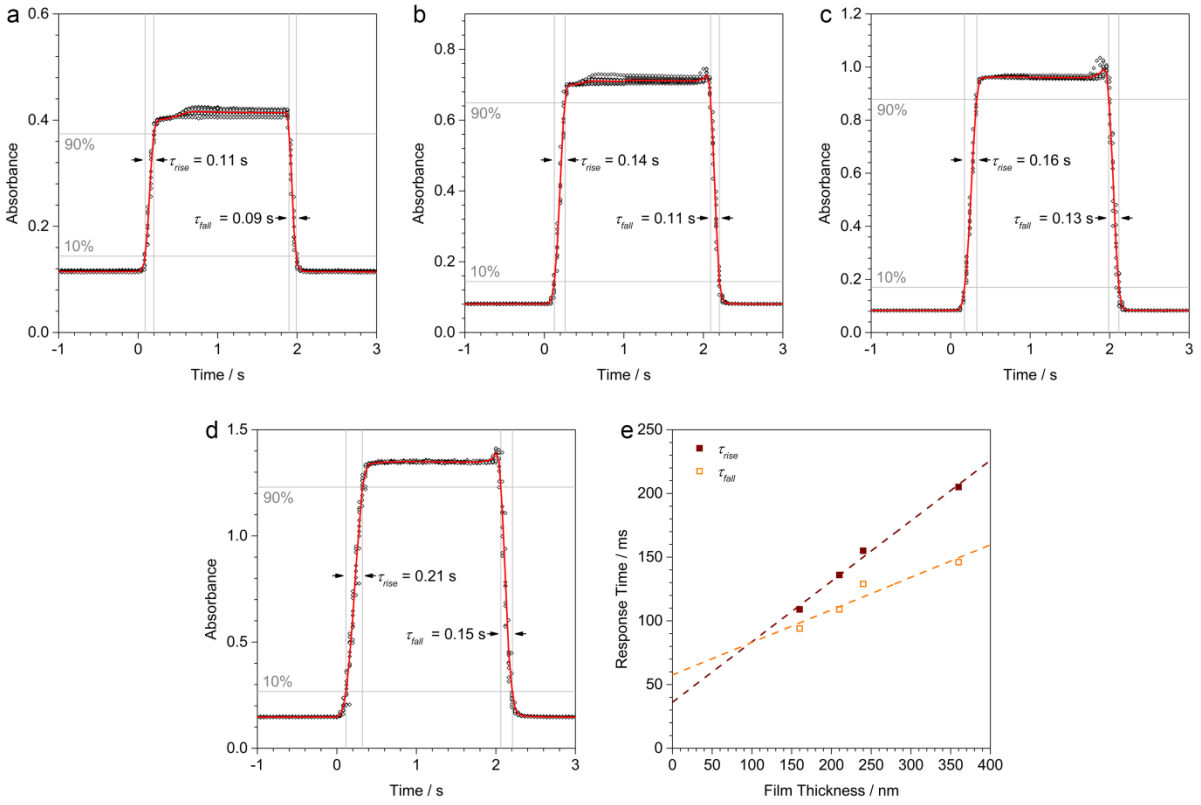

Figure 5.9 Film thickness-dependent response times of oriented Py-TT COF films. (**a-d**) Response times at λ = 560 nm derived from the averages (red lines) of 10 humidity cycles (dry to water-saturated). COF film thicknesses of 160, 210, 240, and 360 nm were realized via reaction times of 4 h, 1 d, 2 d, and 4 d, respectively. The spikes at the end of each "wet" period stem from pressure fluctuations during switching of the gas streams that cause a momentary increase of the water content in the COF film. (**e**) Correlation between the COF film thickness and the respective response times. The data might contain an offset of 30 - 50 ms that is associated with experimental factors, such as a temporary mixing of the dry and water-saturated gas flows during switching. The dashed lines are added as a guide to the eye.

Reproducibility and stability

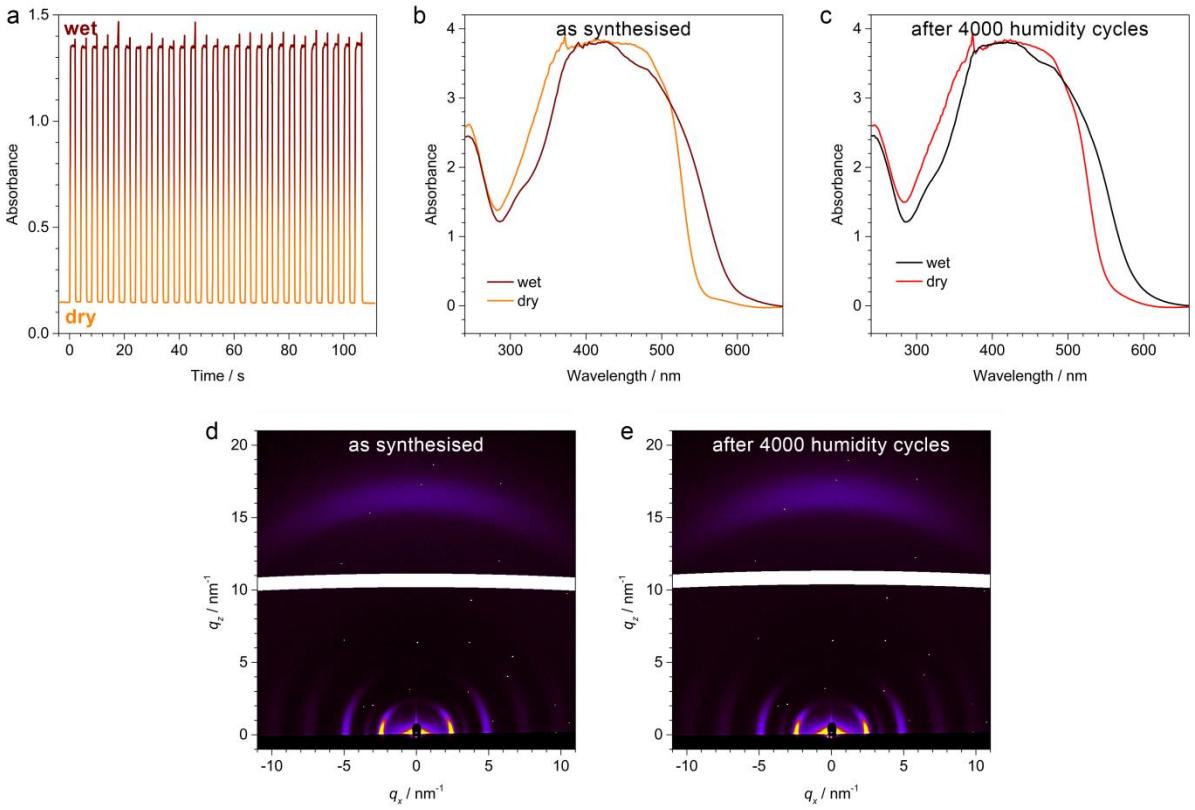

Figure 5.10 Reproducibility of the solvatochromic response and stability of the Py-TT COF films towards repeated humidity cycling and storage in ambient air. (**a**) Repeated humidity cycling (dry to water-saturated) underlines the complete reversibility of the solvatochromic response of the COF film. The spikes at the end of each "wet" period stem from pressure fluctuations during switching of the gas streams that cause a momentary increase of the water content in the COF film. (**b,c**) Absorption spectra of the as-synthesized **Py-TT** COF film and the same sample after 4000 humidity cycles and storage in ambient air for 250 d. The optical properties and solvatochromic response remain virtually unchanged. (**d,e**) The corresponding GIWAXS patterns confirm that the crystallinity and texture are fully retained. The white dots originate from damaged and deactivated pixels on the detector.

Humidity-dependent PXRD analysis

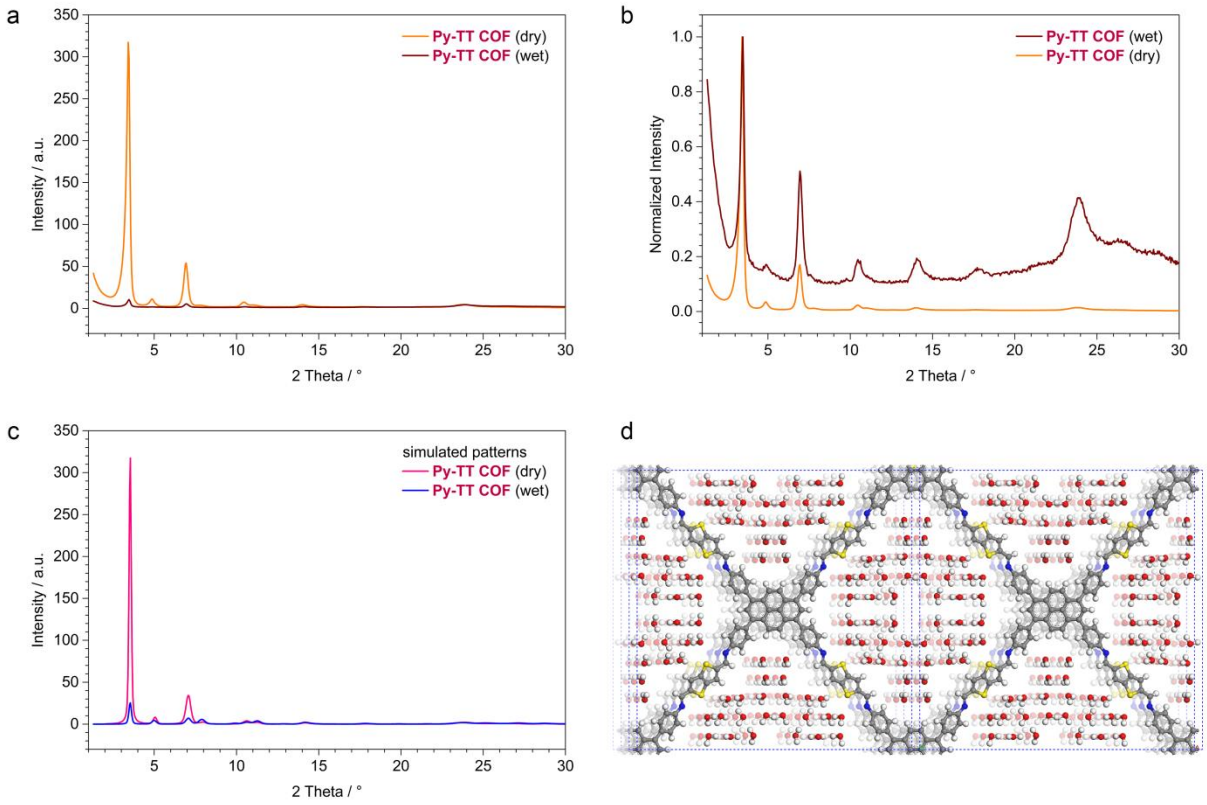

Figure 5.11 Comparison of the Py-TT COF PXRD patterns recorded in the dry and water-saturated states. (**a**) PXRD patterns of the dry (orange) and the water vapour-saturated **Py-TT** COF (brown). The reflection intensities, in particular at low angles, are significantly reduced in the water-saturated material. (**b**) The normalized representation of the PXRD patterns indicates no structural changes upon exposure to humidity as the reflection positions remain identical. (**c**,**d**) The observed reduction of reflection intensities can be reproduced in silico by filling the pores of the **Py-TT** COF structure model with water molecules.

Solid-state NMR spectroscopy

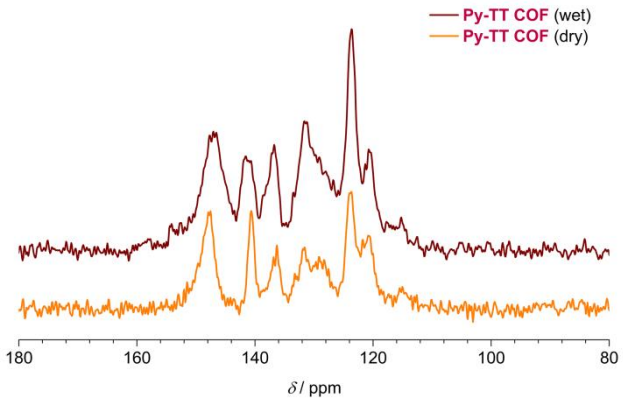

Figure 5.12 $^{13}C(^{1}H)$ cross-polarisation (cp) magic angle spinning (MAS) solid-state NMR spectra of Py-TT COF powder in the dry and water-saturated states. The spectrum exhibits a series of signals in the 110-160 ppm range originating from the 13 aromatic carbon atoms in the framework. Interactions with water molecules in the water-saturated framework might be the cause of minor changes in some peak intensities, but no shifts that would indicate an altered chemical environment are observed.

Analysis of the Py-1P and Py-Py COF films

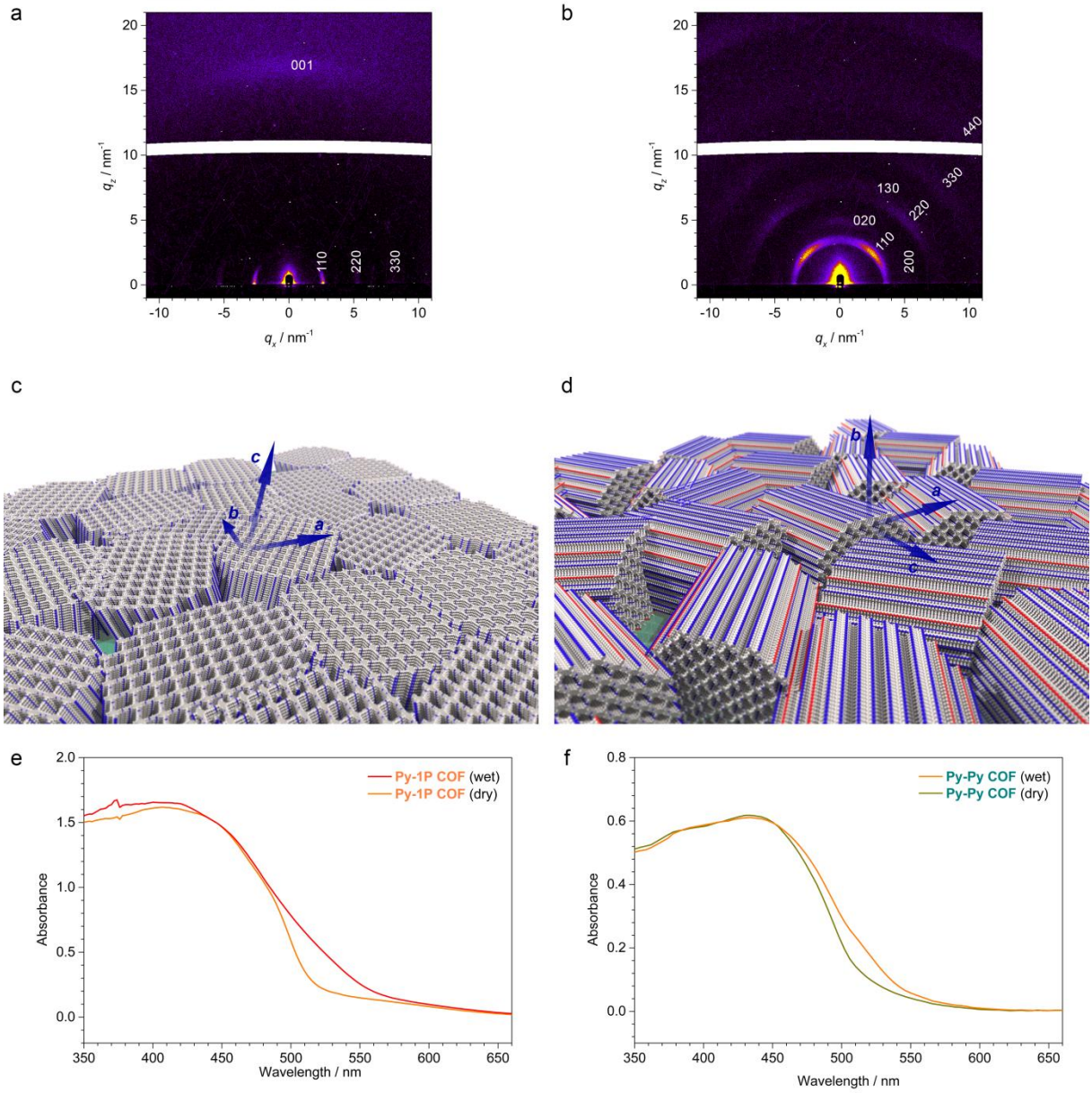

Figure 5.13 Structure characterisation and solvatochromism of Py-1P and Py-Py COF films. (**a**) GIWAXS pattern of a **Py-1P** COF film grown on an ITO substrate. The intensity of *hk*0 reflections is concentrated directly above the sample horizon, indicating a predominant orientation of the COF layers parallel to the substrate. (**b**) GIWAXS pattern of a **Py-Py** COF film grown on a sapphire substrate. In contrast to the other COFs in this study, this framework grows with the *ac*-plane parallel to the substrate, possibly due to interactions of the aldehyde building block with the substrate. (**c**,**d**) Illustrations of the polycrystalline **Py-1P** and **Py-Py** COF films. The unit cell axes are indicated for one crystallite. (**e**,**f**) Solvatochromic response of the COF films towards a water-saturated atmosphere.

Both COFs exhibit a humidity-induced absorption in the 480-560 nm region, which is, however, much narrower and less pronounced than observed for the **Py-TT** COF.

Py-TT COF photoluminescence spectra

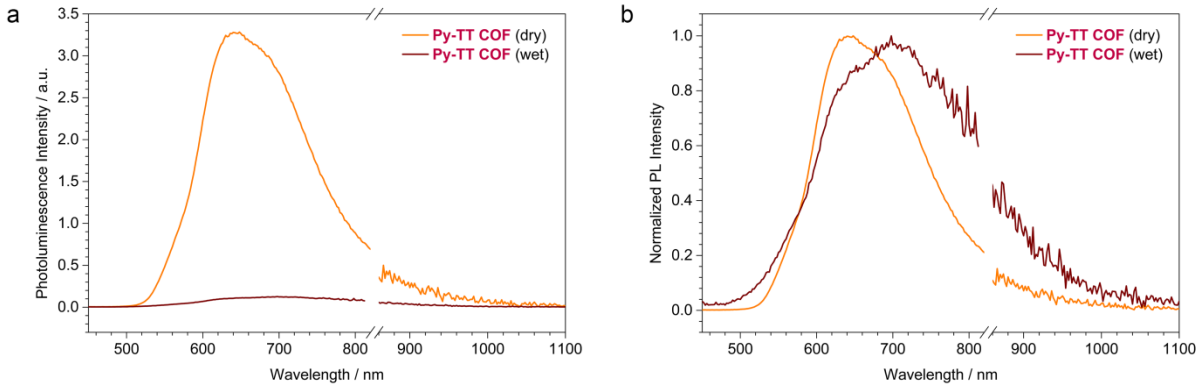

Figure 5.14 PL spectra of the dry and water-saturated Py-TT COF. (**a**) The dry **Py-TT** COF exhibits a moderately intense red PL, which is quenched by more than 95% upon exposure to humid atmosphere. (**b**) The normalized representation of the spectra reveals that this quenching is accompanied by a spectral shift towards lower energies, indicating changes in the electronic structure of the emissive states.

Analysis of an amorphous Py-1P network

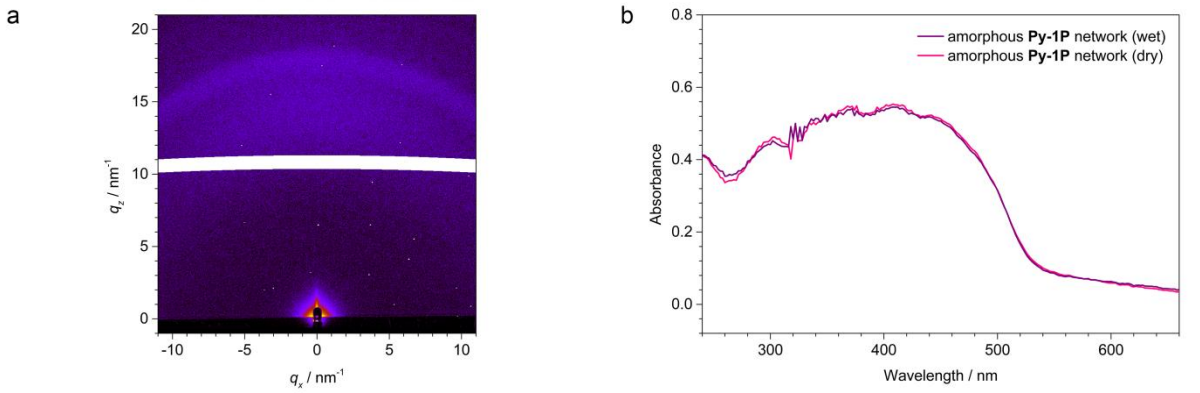

Figure 5.15 Characterisation and humidity exposure of an amorphous Py-1P network. (**a**) GIWAXS pattern of the **Py-1P** network grown on TiO_2-coated ITO confirming that the film is fully amorphous. The diffuse arcs at q = 14 and q = 17.5 originate from the substrate. (**b**) Absorption spectra of this amorphous network in dry (pink) and water vapour-saturated atmospheres (purple). Despite being composed of the same building blocks as the solvatochromic **Py-1P** COF, this network does not exhibit any measurable solvatochromic response.

Additional COF characterisation

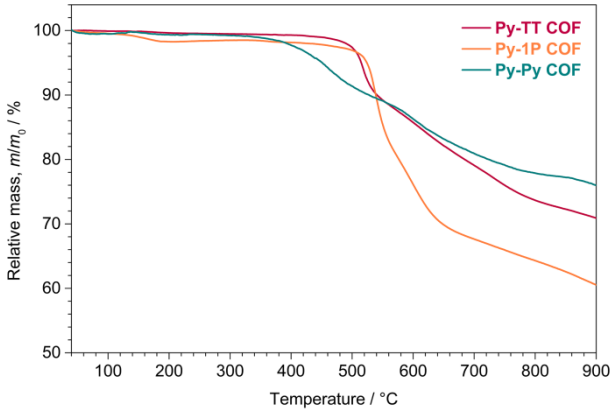

Figure 5.16 Thermogravimetric analysis. Thermogravimetric analysis of the three COFs measured under an N_2 atmosphere at a heating rate of 1 K min^{-1}. Thermal decomposition starts only at 350 °C in the **Py-Py** COF. The **Py-TT** and **Py-1P** COFs display an even higher stability with decomposition temperatures above 500 °C, placing them among the most stable COFs to date.[6] [70]

IR spectroscopy

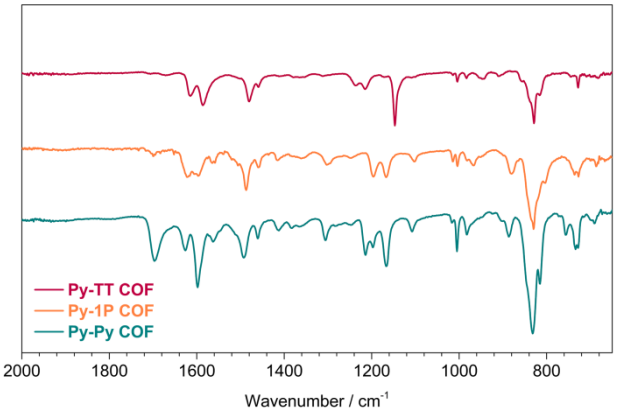

Figure 5.17 Fourier-transform IR spectra of the COF powders. IR spectroscopy confirms the formation of imine-linked frameworks with characteristic imine vibration bands around 1620 cm^{-1}.

Table 5.2 Imine C=N stretching vibration frequencies.

	ν(C=N) / cm^{-1}
Py-TT COF	1615
Py-1P COF	1621
Py-Py COF	1626

Py-TT COF based humidity sensor

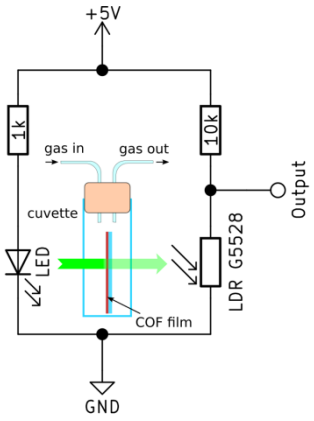

Figure 5.18 Circuit diagram of the COF-based humidity sensor. The light emitted from the green LED is transmitted through the **Py-TT** COF film and detected via a light-dependent resistor. In a dry atmosphere, the COF is almost transparent to green light, whereas it becomes increasingly opaque with increasing humidity.

To demonstrate the applicability of a solvatochromic COF film for sensing, we constructed a simple humidity sensor based on the circuit shown in Figure 5.18. The **Py-TT** COF film acts as a humidity-responsive attenuator to the light emitted from a common 5 mm green InGaN LED. Detection of the transmitted light is achieved by a CdS-based light-dependent resistor (LDR, type: GL5528, peak response at 540 nm) connected as a variable voltage divider with a 10 kΩ resistor. Both LED and LDR are shielded with black heat shrink tubing to minimize ambient light effects. The COF film is placed between the LED and LDR in an optical cuvette equipped with a gas inlet and outlet.

The analog output signal can be probed between the LDR and the 10 kΩ resistor. We used a development board equipped with an ATMEGA328P microcontroller for read-out and digitalisation. This signal can be monitored on a PC in real-time or be logged over an extended period of time. The microcontroller was programmed using the Arduino IDE (v. 1.6.5) and the graphical display was programmed in Processing (v. 3.3.5).

A video of the **Py-TT** COF humidity sensor in operation is available as Supporting Information.

DFT simulations

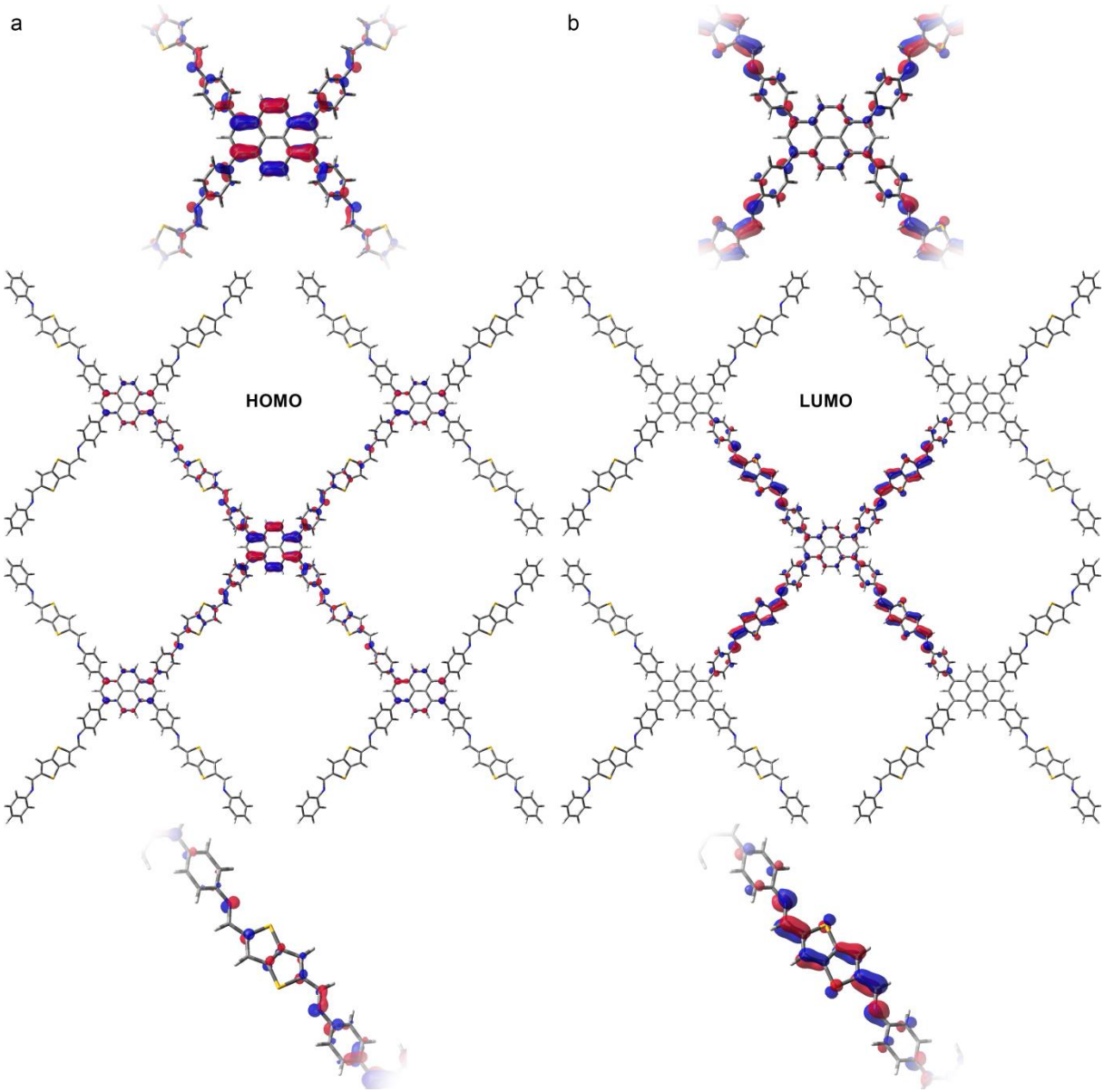

Figure 5.19 DFT-simulated frontier orbitals. The HOMO (**a**) and LUMO (**b**) were calculated for a single-layer **Py-TT** molecular fragment using the B3LYP hybrid functional and a 6-31G(d) split-valence basis set. Insets, magnified views onto the central pyrene (top) and one of the four pyrene-TT-pyrene bridges (bottom).

5.6 References

[1] J. W. Colson, W. R. Dichtel, *Nature Chem.* **2013**, *5*, 453.

[2] F. Beuerle, B. Gole, *Angew. Chem.* **2017**, *3*, 533–543.

[3] E. L. Spitler, W. R. Dichtel, *Nature Chem.* **2010**, *2*, 672-677.

[4] B. J. Smith, W. R. Dichtel, *J. Am. Chem. Soc.* **2014**, *136*, 8783-8789.

[5] M. Calik, T. Sick, M. Dogru, M. Döblinger, S. Datz, H. Budde, A. Hartschuh, F. Auras, T. Bein, *J. Am. Chem. Soc.* **2016**, *138*, 1234-1239.

[6] A. P. Côté, A. I. Benin, N. W. Ockwig, M. O'Keeffe, A. J. Matzger, O. M. Yaghi, *Science* **2005**, *310*, 1166-1170.

[7] F. J. Uribe-Romo, J. R. Hunt, H. Furukawa, C. Klock, M. O'Keeffe, O. M. Yaghi, *J. Am. Chem. Soc.* **2009**, *131*, 4570-4571.

[8] S. Wan, F. Gándara, A. Asano, H. Furukawa, A. Saeki, S. K. Dey, L. Liao, M. W. Ambrogio, Y. Y. Botros, X. Duan, S. Seki, J. F. Stoddart, O. M. Yaghi, *Chem. Mater.* **2011**, *23*, 4094-4097.

[9] S. Kandambeth, A. Mallick, B. Lukose, M. V. Mane, T. Heine, R. Banerjee, *J. Am. Chem. Soc.* **2012**, *134*, 19524-19527.

[10] L. Ascherl, T. Sick, J. T. Margraf, S. H. Lapidus, M. Calik, C. Hettstedt, K. Karaghiosoff, M. Döblinger, T. Clark, K. W. Chapman, F. Auras, T. Bein, *Nature Chem.* **2016**, *8*, 310-316.

[11] F. J. Uribe-Romo, C. J. Doonan, H. Furukawa, K. Oisaki, O. M. Yaghi, *J. Am. Chem. Soc.* **2011**, *133*, 11478-11481.

[12] L. Stegbauer, K. Schwinghammer, B. V. Lotsch, *Chem. Sci.* **2014**, *5*, 2789-2793.

[13] C. J. Doonan, D. J. Tranchemontagne, T. G. Glover, J. R. Hunt, O. M. Yaghi, *Nature Chem.* **2010**, *2*, 235-238.

[14] Z. Li, X. Feng, Y. Zou, Y. Zhang, H. Xia, X. Liu, Y. Mu, *Chem. Commun.* **2014**, *50*, 13825-13828.

[15] M. G. Rabbani, A. K. Sekizkardes, Z. Kahveci, T. E. Reich, R. Ding, H. M. El-Kaderi, *Chem. Eur. J.* **2013**, *19*, 3324-3328.

[16] S.-Y. Ding, J. Gao, Q. Wang, Y. Zhang, W.-G. Song, C.-Y. Su, W. Wang, *J. Am. Chem. Soc.* **2011**, *133*, 19816-19822.

[17] S. Lin, C. S. Diercks, Y.-B. Zhang, N. Kornienko, E. M. Nichols, Y. Zhao, A. R. Paris, D. Kim, P. Yang, O. M. Yaghi, C. J. Chang, *Science* **2015**, *349*, 1208-1213.

[18] M. Dogru, M. Handloser, F. Auras, T. Kunz, D. Medina, A. Hartschuh, P. Knochel, T. Bein, *Angew. Chem. Int. Ed.* **2013**, *52*, 2920-2924.

[19] X. Feng, L. Chen, Y. Honsho, O. Saengsawang, L. Liu, L. Wang, A. Saeki, S. Irle, S. Seki, Y. Dong, D. Jiang, *Adv. Mater.* **2012**, *24*, 3026-3031.

[20] S. Jin, X. Ding, X. Feng, M. Supur, K. Furukawa, S. Takahashi, M. Addicoat, M. E. El-Khouly, T. Nakamura, S. Irle, S. Fukuzumi, A. Nagai, D. Jiang, *Angew. Chem. Int. Ed.* **2013**, *52*, 2017-2021.

[21] M. Calik, F. Auras, L. M. Salonen, K. Bader, I. Grill, M. Handloser, D. D. Medina, M. Dogru, F. Loebermann, D. Trauner, A. Hartschuh, T. Bein, *J. Am. Chem. Soc.* **2014**, 17802-17807.

[22] J. Guo, Y. Xu, S. Jin, L. Chen, T. Kaji, Y. Honsho, M. A. Addicoat, J. Kim, A. Saeki, H. Ihee, S. Seki, S. Irle, M. Hiramoto, J. Gao, D. Jiang, *Nature Commun.* **2013**, *4*.

[23] Z. Li, Y. Zhang, H. Xia, Y. Mu, X. Liu, *Chem. Commun.* **2016**, *52*, 6613-6616.

[24] S.-Y. Ding, M. Dong, Y.-W. Wang, Y.-T. Chen, H.-Z. Wang, C.-Y. Su, W. Wang, *J. Am. Chem. Soc.* **2016**, *138*, 3031-3037.

[25] Y. Zhang, X. Shen, X. Feng, H. Xia, Y. Mu, X. Liu, *Chem. Commun.* **2016**, *52*, 11088-11091.

[26] G. Das, B. P. Biswal, S. Kandambeth, V. Venkatesh, G. Kaur, M. Addicoat, T. Heine, S. Verma, R. Banerjee, *Chem. Sci.* **2015**, *6*, 3931-3939.

[27] M. R. Rao, Y. Fang, S. De Feyter, D. F. Perepichka, *J. Am. Chem. Soc.* **2017**, *139*, 2421-2427.

[28] C. Reichardt, in *Solvents and Solvent Effects in Organic Chemistry*, Wiley-VCH, **2010**.

[29] K. Dimroth, C. Reichardt, *Liebigs Ann. Chem.* **1969**, *727*, 93-105.

[30] C. Reichardt, *Chem. Rev.* **1994**, *94*, 2319-2358.

[31] S. Kandambeth, D. B. Shinde, M. K. Panda, B. Lukose, T. Heine, R. Banerjee, *Angew. Chem. Int. Ed.* **2013**, *52*, 13052-13056.

[32] C. R. DeBlase, K. E. Silberstein, T.-T. Truong, H. D. Abruña, W. R. Dichtel, *J. Am. Chem. Soc.* **2013**, *135*, 16821-16824.

[33] N. Keller, D. Bessinger, S. Reuter, M. Calik, L. Ascherl, F. C. Hanusch, F. Auras, T. Bein, *J. Am. Chem. Soc.* **2017**, *139*, 8194-8199.

[34] D. Bessinger, L. Ascherl, F. Auras, T. Bein, *J. Am. Chem. Soc.* **2017**, *139*, 12035-12042.

[35] J. W. Colson, A. R. Woll, A. Mukherjee, M. P. Levendorf, E. L. Spitler, V. B. Shields, M. G. Spencer, J. Park, W. R. Dichtel, *Science* **2011**, *332*, 228-231.

[36] D. D. Medina, V. Werner, F. Auras, R. Tautz, M. Dogru, J. Schuster, S. Linke, M. Döblinger, J. Feldmann, P. Knochel, T. Bein, *ACS Nano* **2014**, *8*, 4042-4052.

[37] F. Auras, L. Ascherl, A. H. Hakimioun, J. T. Margraf, F. C. Hanusch, S. Reuter, D. Bessinger, M. Döblinger, C. Hettstedt, K. Karaghiosoff, S. Herbert, P. Knochel, T. Clark, T. Bein, *J. Am. Chem. Soc.* **2016**, *138*, 16703-16710.

[38] X. Chen, N. Huang, J. Gao, H. Xu, F. Xu, D. Jiang, *Chem. Commun.* **2014**, *50*, 6161-6163.

[39] M. Thommes, K. Kaneko, V. Neimark Alexander, P. Olivier James, F. Rodriguez-Reinoso, J. Rouquerol, S. W. Sing Kenneth, *Pure Appl. Chem.* **2015**, *87*, 1051.

[40] J. Lee, H. T. Chang, H. An, S. Ahn, J. Shim, J.-M. Kim, *Nature Commun.* **2013**, *4*, 2461.

[41] K. Szendrei, P. Ganter, O. Sànchez-Sobrado, R. Eger, A. Kuhn, B. V. Lotsch, *Adv. Mater.* **2015**, *27*, 6341-6348.

[42] S. Borini, R. White, D. Wei, M. Astley, S. Haque, E. Spigone, N. Harris, J. Kivioja, T. Ryhänen, *ACS Nano* **2013**, *7*, 11166-11173.

[43] M. A. Squillaci, L. Ferlauto, Y. Zagranyarski, S. Milita, K. Müllen, P. Samorì, *Adv. Mater.* **2015**, *27*, 3170-3174.

[44] L. G. S. Brooker, R. H. Sprague, *J. Am. Chem. Soc.* **1941**, *63*, 3214-3215.

[45] B. Dereka, A. Rosspeintner, M. Krzeszewski, D. T. Gryko, E. Vauthey, *Angew. Chem. Int. Ed.* **2016**, *55*, 15624-15628.

[46] A. I. Ivanov, B. Dereka, E. Vauthey, *J. Chem. Phys.* **2017**, *146*, 164306.

[47] A. A. Bakulin, A. Rao, V. G. Pavelyev, P. H. M. van Loosdrecht, M. S. Pshenichnikov, D. Niedzialek, J. Cornil, D. Beljonne, R. H. Friend, *Science* **2012**, *335*, 1340-1344.

[48] A. Petrozza, F. Laquai, I. A. Howard, J.-S. Kim, R. H. Friend, *Phys. Rev. B* **2010**, *81*, 205421.

[49] T. Düren, F. Millange, G. Férey, K. S. Walton, R. Q. Snurr, *J. Phys. Chem. C* **2007**, *111*, 15350-15356.

[50] www.fluidat.com.

[51] http://www.omega.com/temperature/z/pdf/z103.pdf.

[52] Gaussian 16, Revision A.03 (Gaussian, Inc., Wallingford, CT, USA, 2016).

[53] A. D. Becke, *J. Chem. Phys.* **1993**, *98*, 1372-1377.

[54] A. D. Becke, *J. Chem. Phys.* **1993**, *98*, 5648-5652.

[55] F. J. Devlin, J. W. Finley, P. J. Stephens, M. J. Frisch, *J. Phys. Chem.* **1995**, *99*, 16883-16902.

[56] C. Lee, W. Yang, R. G. Parr, *Phys. Rev. B* **1988**, *37*, 785-789.

[57] R. Ditchfield, W. J. Hehre, J. A. Pople, *J. Chem. Phys.* **1971**, *54*, 724-728.

[58] W. J. Hehre, R. Ditchfield, J. A. Pople, *J. Chem. Phys.* **1972**, *56*, 2257-2261.

[59] P. C. Hariharan, J. A. Pople, *Theoret. Chim. Acta* **1973**, *28*, 213-222.

[60] P. C. Hariharan, J. A. Pople, *Mol. Phys.* **1974**, *27*, 209-214.

[61] M. S. Gordon, *Chem. Phys. Lett.* **1980**, *76*, 163-168.

[62] M. M. Francl, W. J. Pietro, W. J. Hehre, J. S. Binkley, M. S. Gordon, D. J. DeFrees, J. A. Pople, *J. Chem. Phys.* **1982**, *77*, 3654-3665.

[63] S. Jin, T. Sakurai, T. Kowalczyk, S. Dalapati, F. Xu, H. Wei, X. Chen, J. Gao, S. Seki, S. Irle, D. Jiang, *Chem. Eur. J.* **2014**, *20*, 14608-14613.

[64] M. G. Rabbani, A. K. Sekizkardes, O. M. El-Kadri, B. R. Kaafarani, H. M. El-Kaderi, *J. Mater. Chem.* **2012**, *22*, 25409-25417.

[65] M. Tountas, Y. Topal, E. Polydorou, A. Soultati, A. Verykios, A. Kaltzoglou, T. A. Papadopoulos, F. Auras, K. Seintis, M. Fakis, L. C. Palilis, D. Tsikritzis, S. Kennou, M. Koutsoureli, G. Papaioannou, M. Ersöz, M. Kus, P. Falaras, D. Davazoglou, P. Argitis, M. Vasilopoulou, *ACS Appl. Mater. Interfaces* **2017**, *9*, 22773-22787.

[66] D. D. Medina, M. L. Petrus, A. N. Jumabekov, J. T. Margraf, S. Weinberger, J. M. Rotter, T. Clark, T. Bein, *ACS Nano* **2017**, *11*, 2706-2713.

[67] P. N. Murgatroyd, *J. Phys. D: Appl. Phys.* **1970**, *3*, 151.

[68] P. W. M. Blom, M. J. M. d. Jong, C. T. H. F. Liedenbaum, *Polym. Adv. Technol.* **1998**, *9*, 390-401.

[69] D. Kabra, L. P. Lu, M. H. Song, H. J. Snaith, R. H. Friend, *Adv. Mater.* **2010**, *22*, 3194-3198.

[70] Q. Fang, Z. Zhuang, S. Gu, R. B. Kaspar, J. Zheng, J. Wang, S. Qiu, Y. Yan, *Nature Commun.* **2014**, *5*.

6 Take my Breath Away

This chapter is based on the article

Breathing covalent organic frameworks

by Laura Ascherl, Simon Krause, Stephan Reuter, Stefan Kaskel, Florian Auras and Thomas Bein

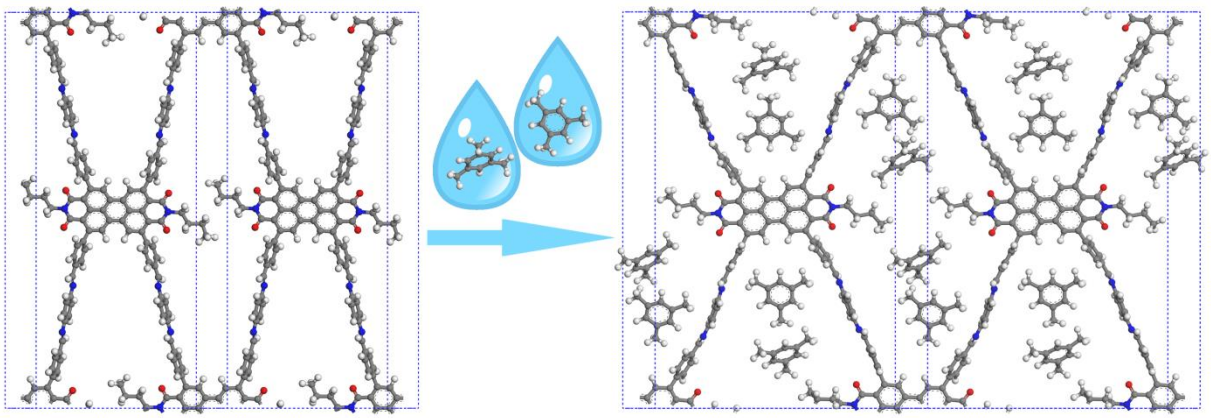

Illustration of the “wine-rack” breathing mode of a PDI-based COF upon contact with mesitylene

6.1 Abstract

Despite intriguing opportunities for potential applications, establishing reversibly flexible 2D COF materials that can undergo phase transitions upon contact with an external stimulus has remained a major challenge. Introducing a high degree of lateral displacement between individual COF layers teamed with strong π-stacking has enabled us to realise the first breathing 2D COFs. This new subclass of crystalline materials can change its crystal structure and electronic properties reversibly upon exposure to various solvents. During these "wine-rack"-type breathing transitions, the distance between the central core units is changed, allowing a modulation of the in-plane electronic coupling.

6.2 Introduction

The idea that highly ordered crystalline materials can undergo reversible structural phase transitions as a result of external stimuli might seem contradictory at a first glance. Terms like "rigidity" often used in the context of porous compounds like zeolites, metal organic frameworks (MOFs) or covalent organic frameworks (COFs) do their bit to shape a very biased image of this family of materials. It is therefore hardly surprising that the first evidence for flexibility observed in certain MOFs – so called Soft Porous Crystals (SPCs) – whipped the community into a frenzy and stimulated the investigation of this "third generation of host materials". Multiple external triggers like the accommodation of guest molecules,[1] [2] electric fields,[3] [4] temperature,[5] [6] pressure[7] [8] or irradiation[9] [10] were found to induce structural changes in some MOFs and various "breathing" mechanisms including stretching, twisting or scissoring of linkers were examined.[11] Potential for application of such dynamic materials has been demonstrated for size-exclusive molecular sieving,[12] gas storage, [13] sensing,[14] and drug delivery.[15] However, the ability to reversibly switch the conformation of the SPCs also enables the manipulation of physical properties like the optical band gap[16], resistance[17] or magnetic moment[18] and illustrates the potential impact of breathing materials beyond sieving or guest-accommodation. Despite various attempts, there is no means to develop breathing MOFs by design and the observation of structural flexibility still remains a serendipitous find.

Whereas breathing is a common feature in MOFs, little has been reported about structural dynamics in COFs. Especially with regard to two-dimensional (2D) COFs, reversible flexibility has not been observed so far. Due to their unique π-stacked structure and the

opportunity to grow these materials as highly oriented films, introducing breathing capabilities could enable the realisation of membranes whose 1D channels could be reversibly opened and closed upon applying an external stimulus. As the 2D sheets can enable in-plane electron transport, it could be also possible to reversibly modulate the electronic coupling between the chromophores by altering the degree of conjugation.

We have now been able to realise the first 2D COFs that can change their structure reversibly upon contact with solvent molecules, and in addition we have furthermore been able to inhibit these breathing capabilities by simple molecular adaptations. Our new COFs based on perylene-3,4,9,10-tetracarboxylic acid diimide (PDI) fully retain their crystallinity during phase transition and pave the way for the development of a new family of dynamic porous materials. PDIs have a longstanding and successful history as industrial pigments and are especially appreciated for their excellent thermal, chemical and photo-stability.[19] As they also feature extremely high photoluminescence quantum yields, show high charge-carrier mobilities and have a strong electron-accepting character, PDIs are one of the most extensively studied class of materials in organic electronics and have been investigated with a view on various applications ranging from dye lasers,[20] organic photovoltaics[21] or solar collectors[22] to organic field-effect transistors.[23] Incorporating PDIs in a highly ordered fashion into a flexible COF system further enabled us to reversibly tune its electronic structure.

6.3 Results and Discussion

Irreversible crystal-to-amorphous phase transitions are an unwanted form of structural flexibility. They are common for 2D COFs that are based on very fragile central building blocks and/or weak layer-to-layer interactions, suggesting that delamination might play a crucial role in this degradation process. Hypothetical, reversible crystal-to-crystal breathing motions in 2D COFs would however involve flexibility within the sheet and thus require maximal stability along the stacking direction. In breathing pillared MOFs, the nearest relatives to flexible 2D COFs, structural transitions involve a displacement or rotation of the linear bridges at a distance where they do not obstruct each other. We thus concluded that key to implementing dynamic behaviour in 2D COFs was to separate linear bridging units from

adjacent layers as far apart as possible and yet to guarantee sufficient stability between the π-stacked multidentate core units to defy shear forces.

We found that in pyrene-based COFs, which have been well-studied within our group, an offset-angle of roughly 74.0° between the π-stacked layers and an average spacing of 3.9 Å lead to a net lateral displacement of 1.1 Å along the sheets.[24] [25] [26] In order to increase that distance to keep the bridges further apart, a smaller offset angle might be necessary. Molecules of *N*,*N*-bis(*n*-octyl)-2,5,8,11-tetraphenylperylene-3,4:9,10-bis(dicarboximide) were found to self-assemble into π–π slip-stacked crystals with an offset angle of 43° and a PDI-to-PDI distance of 3.5 Å, resulting in a lateral displacement 3.3 Å,[27] three times the size of the offset in pyrene-COFs. Furthermore, PDI molecules preferably crystallize in form of highly anisotropic needles along the stacking direction, underlining a strong π-stacking character and suggesting that the use of PDIs as COF nodes, might enable the resulting frameworks to breathe.

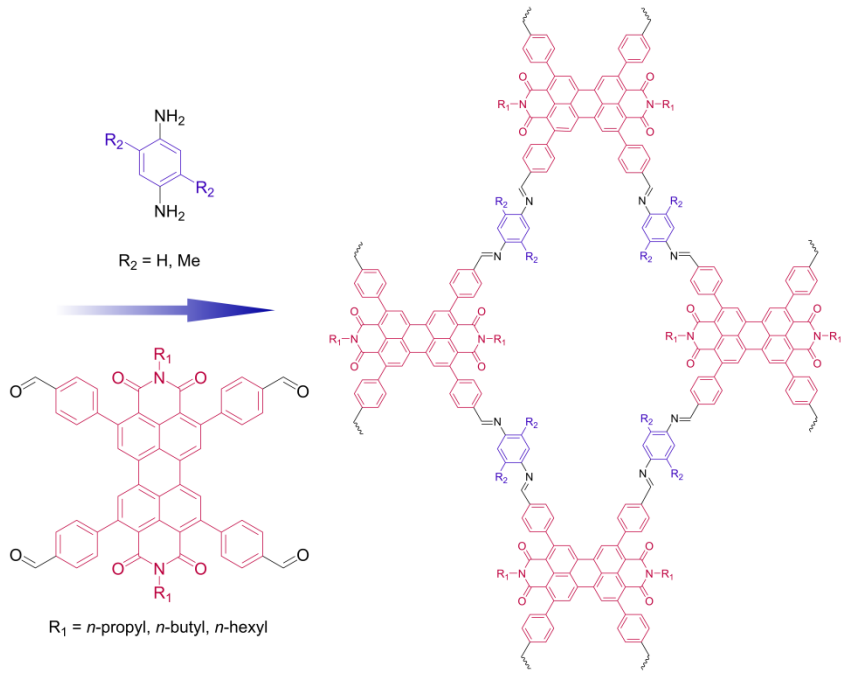

Figure 6.1 Synthesis of the imine-linked PDI-COFs. The combination of tetraphenylcarboxaldeyde-dialkyl-PDIs (red) with linear diamines (blue) in a molar ratio of 1 : 2 yields the PDI-COFs.

Tuning the optical, physical or electronic properties of PDIs can be achieved through modifications at various positions within the molecule. Even though the ketone lone pairs are the actual driving force for the striking lateral displacement, the utilisation of different amines

during the imide formation can also affect the stacking behaviour of PDI, whereby short and long axis offset of the PDI core can be directed via the substituents.[28] Additionally this position allows for controlling the solubility of the molecule, which is of key importance for a successful COF building block. Well-studied and easily achieved modifications at the bay-area of the PDI also influence the stacking behaviour.[29] Additionally they allow tuning electronic properties of the respective PDI[19] and might be possible anchoring points for introducing functional groups like amines or aldehydes to cross-link the building blocks during COF synthesis. Due to the close proximity of substituents in the bay position, the resulting PDIs tend to deviate from an ideal flat structure and adopt a distorted molecular conformation with twisted naphthalene entities.[30] This however is detrimental for potential applications where a high degree of crystallinity and effective electronic coupling is required and disqualifies the substitutions at the bay-position for COF linkers in this context. To preclude this unwanted distortion, a new mean of introducing substituents at the *ortho*-positions of the PDI via CH activation has been recently developed.[31]

In view of the above considerations, we synthesised *ortho*-functionalised tetraphenylcarboxaldeyde-dialkyl-PDIs (alkyl = propyl, butyl, hexyl) with different chain lengths and applied them in combination with the linear linker *p*-phenylenediamine (**1P**) in solvothermal, acid-catalysed COF syntheses (Figure 6.1).

The powder X-ray diffraction (PXRD) pattern of the **PDI$_{Hex}$-1P** COF exhibits a large number of well-defined reflections (Figure 6.2a) but does not resemble any common sequence of COF reflexes, indicating a rather complex structure type. Rietveld refinement using a small β angle typical for PDIs and assuming $P\bar{1}$ symmetry reproduced our experimental pattern very well, yielding the lattice parameters a = 2.12 ± 0.05 nm, b = 4.48 ± 0.05 nm, c = 0.49 ± 0.05 nm, α = 90° (fixed), β = 45 ± 5°, γ = 90° (fixed) and revealing that we indeed succeeded in synthesising the desired 2D COFs with large lateral layer displacement (Figure 6.2b).

Following our initial considerations, the **PDI$_{Hex}$-1P** COF is expected to show dynamic response towards external stimuli. Indeed, exposing the powder to various solvents causes instant structural transitions observable via PXRD (Figure 6.2c). The refinement of the solvent-saturated structure ($P\bar{1}$ symmetry, a = 2.73 ± 0.05 nm, b = 4.44 ± 0.05 nm, c = 0.50 ± 0.05 nm, α = 90° (fixed), β = 45 ± 5°, γ = 90° (fixed)) reveals that the structural transition consists in a "wine-rack"[32] breathing mode, which is reflected in a significant elongation of

the *a*-axis and a stretching of the hexyl chain. The **PDI$_{Pro}$-1P** and **PDI$_{Bu}$-1P** COFs exhibit similar structures in the dry and solvent saturated states and their structure refinements as well as breathing studies can be found in the Supporting Information.

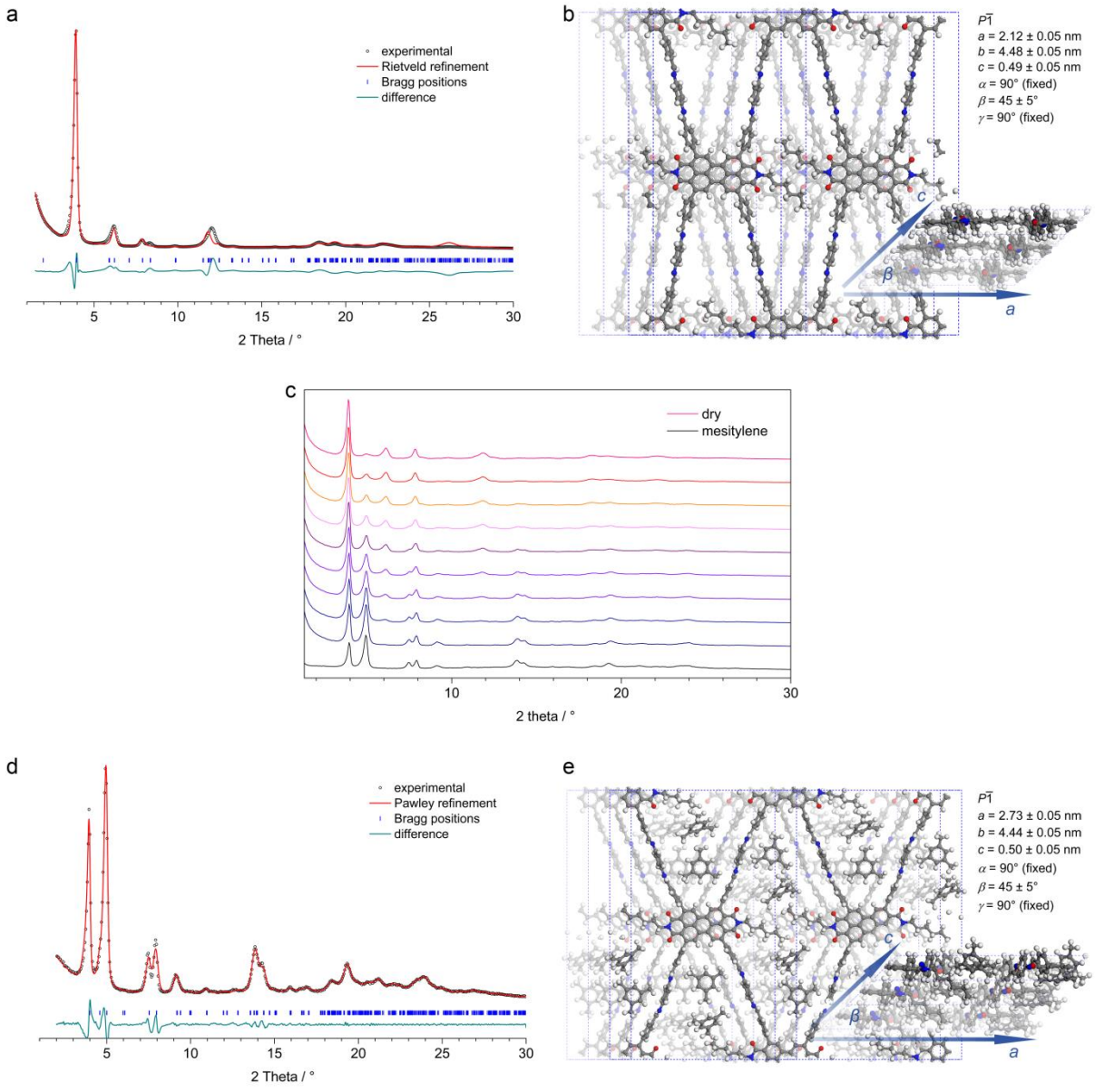

Figure 6.2 Dynamic behaviour of a PDI-based COF. (**a + d**) Experimental PXRD patterns (black dots) of the **PDI$_{Hex}$-1P** COF powder in the dry (**a**) and solvent-saturated (**c**) state. Refinements (red lines) using the structure models displayed in (**b + e**) provide a very good fit to the experimental data with only minimal differences between the experimental and the refined patterns (green lines). (**b + e**) Top views (left) and side views (right) of the corresponding unit cells reveal a rhombic, highly offset-stacked structures. (**c**) Breathing series of the **PDI$_{Hex}$-1P** COF with mesitylene.

Following our initial considerations, the **PDI$_{Hex}$-1P** COF is expected to show dynamic response towards external stimuli. Indeed, exposing the powder to various solvents causes instant structural transitions observable via PXRD (Figure 6.2c). The refinement of the solvent-saturated structure ($P\bar{1}$ symmetry, a = 2.73 ± 0.05 nm, b = 4.44 ± 0.05 nm, c = 0.50 ± 0.05 nm, α = 90° (fixed), β = 45 ± 5°, γ = 90° (fixed)) reveals that the structural transition consists in a "wine-rack"[32] breathing mode, which is reflected in a significant elongation of the a-axis and a stretching of the hexyl chain. The **PDI$_{Pro}$-1P** and **PDI$_{Bu}$-1P** COFs exhibit similar structures in the dry and solvent saturated states and their structure refinements as well as breathing studies can be found in the Supporting Information.

We reasoned that it might be possible to inhibit the breathing capabilities of the COF by introducing sterically demanding groups at the bridging units. Applying 2,5-dimethyl-1,4-phenylenediamine (**1P$_{Me}$**) as linear linker were able to realize a COF material that crystallizes in a significantly different structure. Compared to its highly rhombic relatives (Figure 6.3c), the **PDI$_{Pro}$-1P$_{Me}$** COF appears widened and bears more resemblance to the solvent-saturated structures. Transmission electron microscopy (TEM) confirms our observations: Whereas crystallites of **PDI$_{Bu}$-1P** appear in form of highly faceted rhombi with a sharp angle of 40 ± 5°, the pore structure of the **PDI$_{Pro}$-1P$_{Me}$** COF appears almost pseudo-quadratic (Figure 6.3e). In contrast to **PDI$_{Bu}$-1P**, exposing the **PDI$_{Pro}$-1P$_{Me}$** COF to various solvents is not accompanied by any structural transformations (Figure 6.3b), confirming the validity of our above-made assumption.

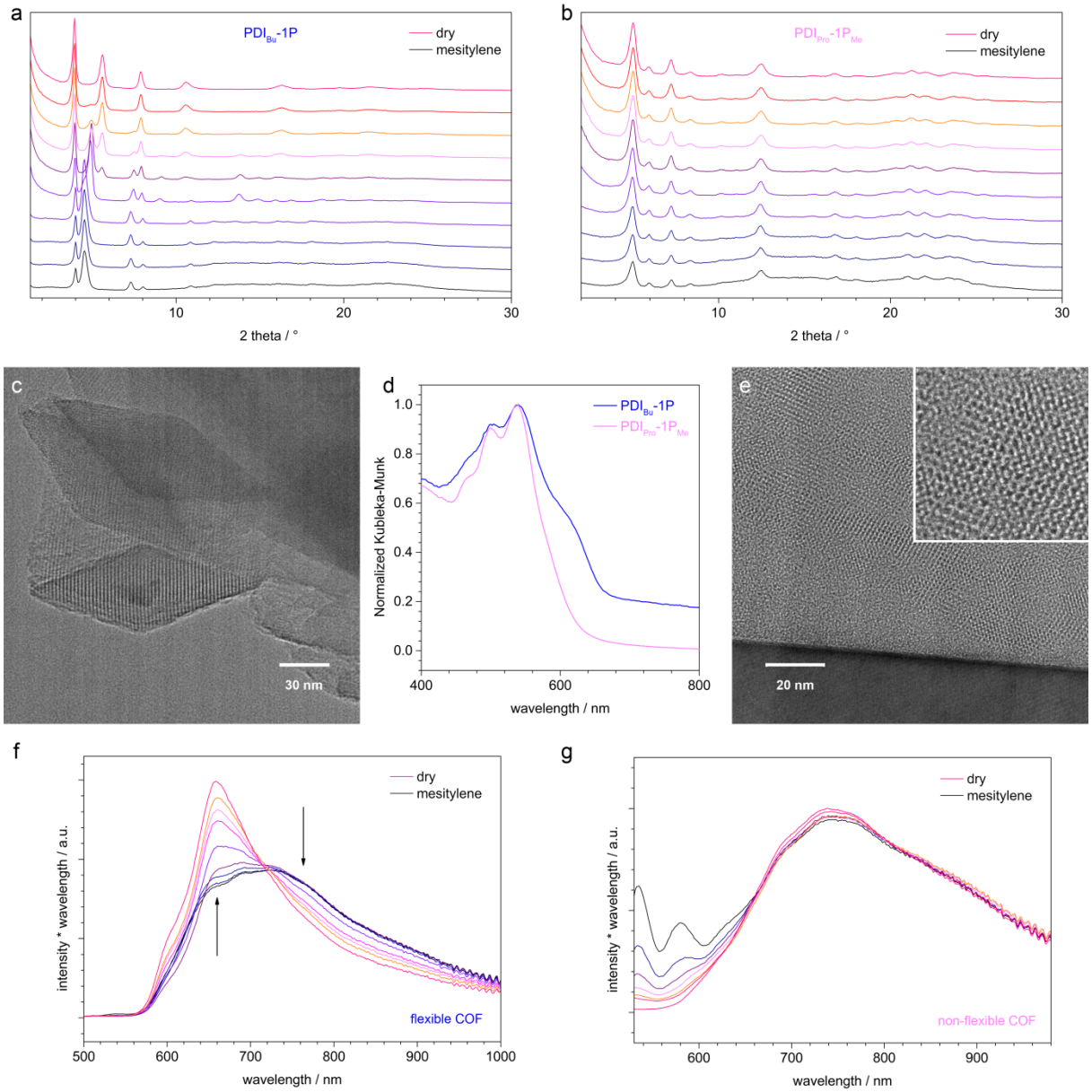

Figure 6.3 Correlation of geometric and electronic structure in PDI-based COFs. (a + b) Mesitylene evaporation series of the breathing **PDI$_{Bu}$-1P** and the rigid **PDI$_{Pro}$-1P$_{Me}$** COFs. **(c)** High resolution TEM image showing highly faceted, rhombic crystal domains of the **PDI$_{Bu}$-1P** COF. (**d**) High resolution TEM of a FIB lamella prepared from the **PDI$_{Pro}$-1P$_{Me}$** COF, revealing a pseudo-quadratic pore arrangement (Inset). **(d)** Diffuse reflectance UV-Vis analysis of the onset area reveals a trident absorption feature typical for PDIs around 540 nm for both COFs and an additional shoulder at 615 nm in case of the **PDI$_{Bu}$-1P** COF. **(f + g)** Photoluminescence analysis of the **PDI$_{Bu}$-1P (f)** and the **PDI$_{Pro}$-1P$_{Me}$ (g)** COFs upon evaporation of mesitylene reveals that structural transitions of the COFs have an influence on the position of the PL emission maxima. The y-scale in this representation is the measured intensity multiplied by the wavelength, rendering the areas under the curves proportional to

the number of photons.[33] [34] The artefacts in **(g)** at 550 nm are due to interference effects caused by mesitylene.

Studying the photoluminescence (PL) properties of the **PDI$_{Bu}$-1P** and the **PDI$_{Pro}$-1P$_{Me}$** COF enabled us to gain intriguing insights into the relationship between the electronic and crystal structure of our COFs (Figure 6.3f, g). The PL of the dry, non-flexible **PDI$_{Pro}$-1P$_{Me}$** COF appears as a broad signal around 750 nm with some vibrational fine structure. In line with the H-type aggregation of the cofacially stacked PDI columns, the highest-energy transition has a lower intensity than the lower-energy transitions. The PL line shape remains unaffected by exposure to solvents. In contrast, the spectrum of **PDI$_{Bu}$-1P** exhibits a sharp luminescence band at 660 nm. Upon exposure of this COF to mesitylene, the PL spectrum changes drastically, re-transforming upon drying (indicated by black arrows) and exhibiting an isosbestic point. We attribute this behaviour to the structural transitions that are triggered by the solvent molecules. Regarding the breathing COF in the solvent-saturated state, the PDI molecules within one layer are laterally separated as the unit cell is elongated along *a*, resulting in electronic properties that are mainly dominated by interactions within the π-stacked columns, similar to the widened **PDI$_{Pro}$-1P$_{Me}$** COF. When the COF is in its contracted, dry form, however, the PDI molecules within one sheet converge, allowing for additional electronic coupling and enabling previously forbidden optical transitions. Our findings are reminiscent of studies on fluorescent J-aggregates by Würthner et al., where PDI molecules are designed to adopt a hydrogen-bonded, head-to-head arrangement in organic solvents.[35] This bead-like arrangement can be achieved by applying the principles of reticular design and simply incorporating the PDIs in a highly ordered way in a COF, with the added benefit of being able to switch between the two electronic states.

Differences in the electronic structure are further illustrated by the presence of an additional absorption feature at 615 nm in the diffuse reflectance UV-Vis spectra of the dry COF powders (Figure 6.3d). IR (Figure 6.11) and toluene sorption studies (Figure 6.9) further reveal differences between the flexible and the non-flexible materials.

6.4 Conclusion

We have developed the first flexible two-dimensional covalent organic frameworks that show reversible crystal-to-crystal phase transitions triggered by solvent molecules. By employing perylene-3,4,9,10-tetracarboxylic acid diimides as multidentate building blocks, adjacent COF

sheets can be kept laterally separated, allowing linear linkers to move freely. At the same time, these core units enable very strong π-interactions and inhibit delamination of the 2D sheets. Photoluminescence spectroscopy allowed us to observe that the in-plane electronic coupling of adjacent PDI molecules can be reversibly switched on and off during the wine-rack breathing transition. Moreover, the introduction of sterically demanding groups enabled us to lock the breathing mechanism, keeping the COF in an open, decoupled form. We believe that our findings will lay the groundwork for developing a new family of flexible 2D COFs and broaden the scope of applications for this unique class of materials.

6.5 Supporting information

Unless otherwise stated, all reactions were performed in oven-dried glassware under argon atmosphere in a glove box or using standard Schlenk techniques. The reagents and solvents were obtained from commercial suppliers and used as received.

Terminology

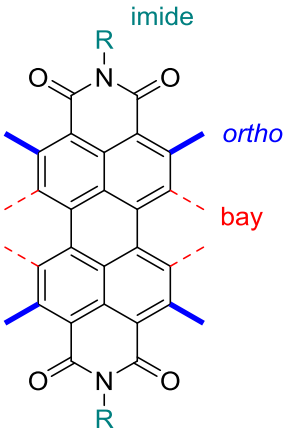

Figure 6.4 Nomenclature in PDI-chemistry.

Linker syntheses

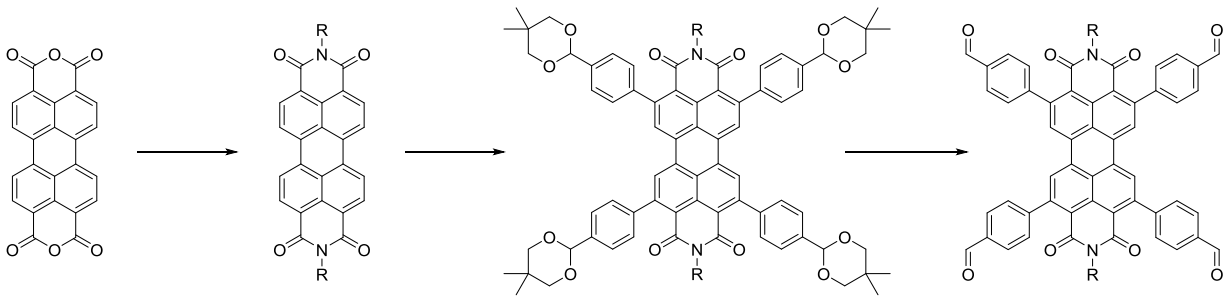

Figure 6.5 Synthesis scheme towards the Tetraphenylcarboxaldeyd-PDI building blocks.

Neopentyl acetal phenyl boronic acid neopentyl ester (1)

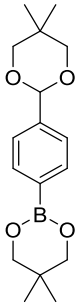

Formylphenylboronic acid (5000 mg, 33 mmol, 1 eq), 2,2-dimethylpropane-1,3-diol (1740 mg, 167 mmol, 5 eq), *p*-toluenesulfonic acid (250 mg, 1.32 mmol, 0.04 eq) and 5 g Na_2SO_4 were refluxed in toluene at 125 °C for 3.5 h. The reaction mixture was allowed to come to ambient temperature and the solvent was removed by rotary evaporation. The solid residue was dissolved in DCM (250 ml) and washed with water and brine. The organic phase was dried with Na_2SO_4, filtered through a cotton wool plug and dried via rotary evaporation and subsequently under high vacuum to yield the product in form of white, shiny platelets (9150 mg, 30 mmol, 91 %).

^{1}H NMR (400 MHz, $CDCl_3$): 7.82 (d, *J* = 8.3 Hz, 2 H), 7.51 (d, *J* = 8.3 Hz, 2 H), 5.40 (s, 1 H), 3.78 (d, *J* = 3.6 Hz, 2 H), 3.77 (s, 3 H), 3.65 (d, *J* = 3.6 Hz, 2 H), 1.30 (s, 3 H), 1.02 (s, 6 H), 0.80 (s, 3 H).

Dipropyl-PDI (2a)

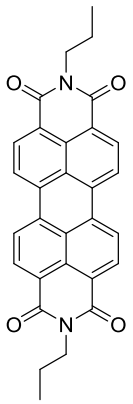

Perylenetetracarboxylic dianhydride (1960 mg, 5 mmol, 1 eq) and propylamine (2.05 ml, 25 mmol, 5 eq) were refluxed in DMF (36 ml) at 150 °C for 4 h. The mixture was allowed to come to room temperature and quenched with 1 M HCl (50 ml). The dark brown precipitate was filtered off and stirred in 100 ml 1 M NaOH at 50 °C for 30 min, before being filtered again. The precipitate was treated with 1 M HCl until neutrality and washed with water to yield the title compound in form of poorly soluble, purple shiny crystallites (2182 mg, 4.6 mmol, 92 %).

Tetra(neopentylesterphenyl)dipropyl-PDI (2b)[31]

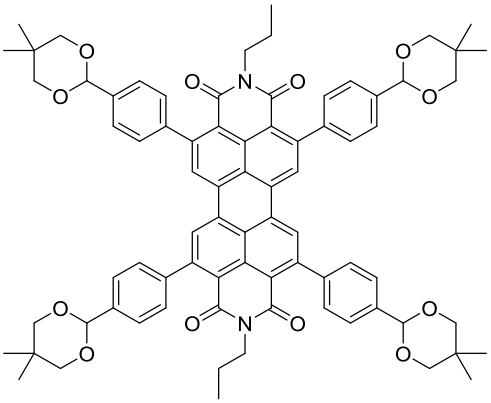

2a (380 mg, 0.8 mmol, 1 eq), **1** (1460 mg, 4.8 mmol, 6 eq) and $RuH_2(CO)(PPh_3)_3$ (176 mg, 0.192 mmol, 0.24 eq) were refluxed in 8 ml of a 9 : 1 mixture of mesitylene and pinacolone at 160 °C for 4 d. The solvents were removed under reduced pressure and the crude product was

purified via column chromatography (silica, DCM : cyclohexane, 20 : 1 and aluminium oxide, DCM) to yield the bright red title compound in 19 % yield (192 mg, 0.16 mmol).

^{1}H NMR (400 MHz, $CDCl_3$): 8.28 (s, 4H), 7.65 (d, *J* = 8.1 Hz, 8H), 7.42 (d, *J* = 8.3 Hz, 8H), 5.50 (s, 4H), 3.90 (dd, *J* = 9.1, 6.5 Hz, 4H), 3.80 (d, *J* = 11.0 Hz, 8H), 3.69 (d, *J* = 10.9 Hz, 8H), 1.64 – 1.55 (m, 8H), 0.86 (t, *J* = 7.3 Hz, 6H).

Tetraphenylcarboxaldeyde-dipropyl-PDI (2c)

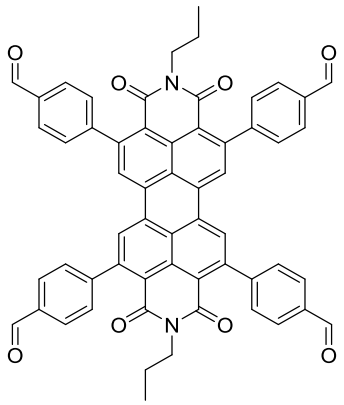

2b (192 mg, 0.16 mmol) was stirred in a mixture of TFA (10 ml), water (1 ml) and $CHCl_3$ (50 ml) for 24 h at room temperature. The mixture was quenched with saturated K_2CO_3 solution and extracted with $CHCl_3$. The combined organic phases were dried with $MgSO_4$. After removing the excess solvent, the title compound was obtained as a dark red powder in 98 % yield (135 mg, 0.15 mmol).

^{1}H NMR (400 MHz, $CDCl_3$): 10.12 (s, 4H), 8.35 (s, 4H), 8.05 (d, *J* = 8.0 Hz, 8H), 7.58 (d, *J* = 7.9 Hz, 8H), 3.89 (dd, *J* = 9.1, 6.5 Hz, 4H), 1.64 – 1.55 (m, 4H), 0.85 (t, *J* = 7.4 Hz, 6H).

Dibutyl-PDI (3a)

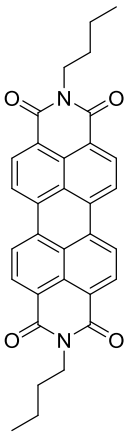

Perylenetetracarboxylic dianhydride (1960 mg, 5 mmol, 1 eq) and *n*-butylamine (2.47 ml, 25 mmol, 5 eq) were refluxed in 36 ml DMF at 150 °C for 3 h. After coming to room temperature, the mixture was quenched with 50 ml 1 M HCl. The precipitate was filtered and stirred in 100 ml 1 M NaOH at 50 °C for 30 min. The precipitate was filtered again, treated with 1 M HCl to neutrality and washed with water to yield the title compound in form of poorly soluble, purple shiny crystallites (2287 mg, 4.6 mmol, 91 %).

Tetra (neopentyl ester phenyl) dibutyl-PDI (3b)[31]

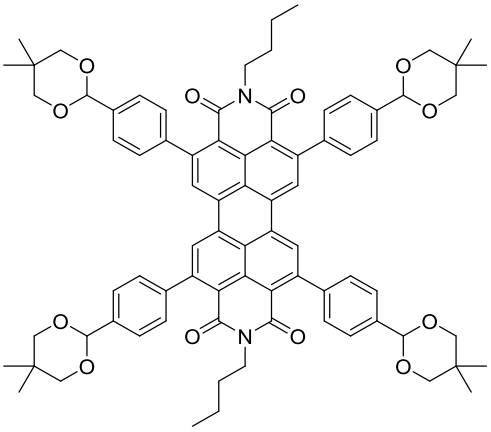

3a (500 mg, 1.0 mmol, 1.0 eq), **1** (2160 mg, 7.1 mmol, 7.1 eq) and $RuH_2(CO)(PPh_3)_3$ (190 mg, 0.2 mmol, 0.2 eq) were refluxed in a mixture of 5 ml mesitylene and 5 ml pinacolone at 140 °C for 24 h. The solvents were removed under reduced pressure and the crude product was purified via column chromatography (silica, DCM : cyclohexane 3 : 1 and aluminium

oxide, DCM). The pure title compound was obtained as a bright red powder in 14 % yield (181 mg, 0.14 mmol).

^{1}H NMR (400 MHz, $CDCl_3$): 8.27 (s, 4H), 7.65 (d, *J* = 8.1 Hz, 8H), 7.42 (d, *J* = 8.3 Hz, 8H), 5.50 (s, 4H), 3.93 (t, *J* = 7.3 Hz, 4H), 3.81 (d, *J* = 11.1Hz, 8H), 3.69 (d, *J* = 10.7 Hz, 8H), 1.29 - 1.23 (m, 8H), 0.85 (t, *J* = 7.4 Hz, 6H).

Tetraphenylcarboxaldeyde-dibutyl-PDI (3c)

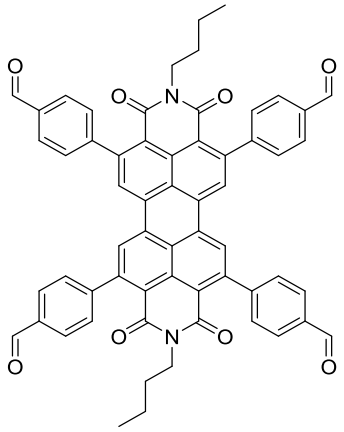

3b (181 mg, 0.14 mmol) was stirred at room temperature for 3 d in a mixture of $CHCl_3$ (50 ml), TFA (10 ml) and water (1 ml). The solution was neutralized with K_2CO_3, washed with water and dried with $MgSO_4$. The title compound was obtained as red powder (127 mg, 0.14 mmol, 98 %).

^{1}H NMR (400 MHz, $CDCl_3$): 10.12 (s, 4H), 8.35 (s, 4H), 8.05 (d, *J* = 8.0 Hz, 8H), 7.58 (d, *J* = 7.9 Hz, 9H), 3.92 (t, *J* = 8.1 Hz, 4H), 1.33 – 1.20 (m, 8H), 0.85 (t, *J* = 7.3 Hz, 6H).

Dihexyl-PDI (4a)

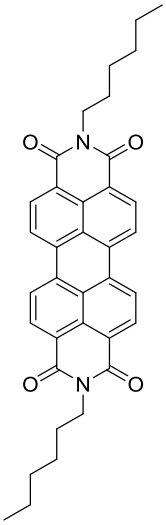

Perylenetetracarboxylic dianhydride (543 mg, 1.4 mmol, 1 eq) and *n*-hexylamine (0.9 ml, 7 mmol, 5 eq) were refluxed in 10 ml DMF at 150 °C for 4 h. The reaction mixture was allowed to come to room temperature and quenched with 50 ml 1 M HCl. The dark brown precipitate was filtered and stirred in 100 ml 1 M NaOH at 50 °C for 30 min. After filtering it again, the precipitate was treated with 1 M HCl until neutrality and washed with water to yield the poorly soluble title compound in 95 % yield (743 mg, 1.3 mmol).

Tetra (neopentyl ester phenyl) dihexyl-PDI (4b)[31]

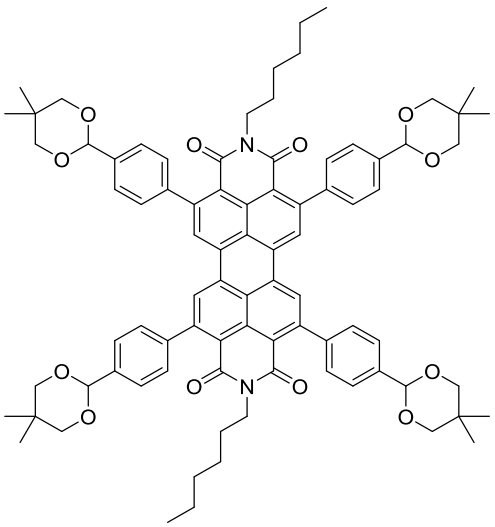

4a (500 mg, 1.0 mmol, 1.0 eq), **1** (2160 mg, 7.1 mmol, 7.1 eq) and $RuH_2(CO)(PPh_3)_3$ (190 mg, 0.2 mmol, 0.2 eq) were refluxed in 5 ml of a 1 : 1 mixture of mesitylene and pinacolone

for 24 h at 140 °C. The solvents were removed under reduced pressure and the crude product was purified via column chromatography (silica, DCM : *n*-hexane 1 : 1 and aluminium oxide, DCM) to obtain the title compound as a bright red powder (202 mg, 0.15 mmol, 15 %).

^{1}H NMR (400 MHz, $CDCl_3$): 8.28 (s, 4H), 7.65 (d, *J* = 8.0 Hz, 8H), 7.43 (d, *J* = 8.3 Hz, 8H), 5.50 (s, 4H), 3.93 (t, *J* = 8.1 Hz, 4H), 3.81 (d, *J* = 11.1 Hz, 8H), 3.69 (d, *J* = 10.6 Hz, 8H), 1.27 – 1.19 and 0.85 – 0.79 (m, 22H).

Tetraphenylcarboxaldeyde-dihexyl-PDI (4c)

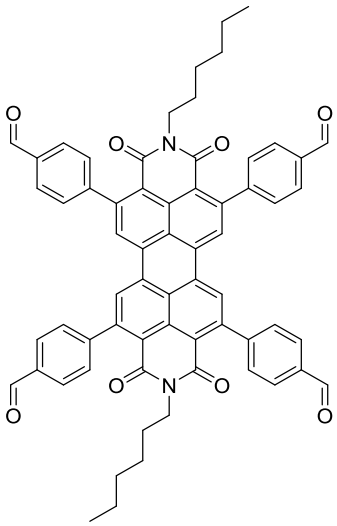

4b (202 mg, 0.15 mmol) was stirred in a mixture of TFA (10 ml), water (1 ml) and $CHCl_3$ (50 ml) for 24 h at room temperature. The mixture was quenched with saturated K_2CO_3 solution and extracted with $CHCl_3$. The organic phases were dried with $MgSO_4$ and after removing the excess solvent under reduced pressure, the title compound was obtained as a red powder in 99 % yield (148 mg, 0.15 mmol).

^{1}H NMR (400 MHz, $CDCl_3$): 10.12 (s, 4H), 8.35 (s, 4H), 8.05 (d, *J* = 8.3 Hz, 8H), 7.58 (d, *J* = 8.1 Hz, 8H), 3.91 (t, *J* = 8.1 Hz, 4H), 1.37 – 1.12 and 0.94 – 0.75 (m, 22H).

COF syntheses

PDI_{Pro}-1P COF

Compound **2b** (17.8 mg, 20 µmol, 1.0 eq.) and 1,4-phenylenediamine (4.4 mg, 40 µmol, 2.0 eq.) were filled into a reaction tube, followed by the addition of mesitylene (333 µL) and dioxane (666 µL), and 6 M acetic acid (100 µL). The sealed tube was kept at 120 °C for 3 days and hence allowed to cool down to room temperature. The formed precipitate was collected by filtration, washed with MeCN and dried in air to yield a dark brown powder.

PDI_{Bu}-1P COF

Compound **3b** (18.4 mg, 20 µmol, 1.0 eq.) and 1,4-phenylenediamine (4.4 mg, 40 µmol, 2.0 eq.) were filled into a reaction tube, followed by the addition of mesitylene (333 µL) and dioxane (666 µL), and 6 M acetic acid (100 µL). The tube was sealed, heated at 120 °C for 3 days and hence allowed to cool down to room temperature. The formed precipitate was collected by filtration, washed with MeCN and dried in air, yielding a dark brown powder.

PDI_{Hex}-1P COF

Compound **4b** (9.8 mg, 10 µmol, 1.0 eq.) and 1,4-phenylenediamine (2.2 mg, 20 µmol, 2.0 eq.) were filled into a reaction tube, followed by the addition of mesitylene (83 µL) and dioxane (167 µL), and 6 M acetic acid (25 µL). The sealed tube was kept at 120 °C for 3 days. The mixture was then allowed to cool down to room temperature. The precipitate was collected by filtration, washed with MeCN and dried in air to yield a dark brown powder.

PDI_{Pro}-$1P_{Me}$ COF

Compound **2b** (8.9 mg, 10 µmol, 1.0 eq.) and 2,5-dimethyl-1,4-phenylenediamine (2.7 mg, 20 µmol, 2.0 eq.) were filled into a reaction tube, followed by the addition of mesitylene (166 µL) and dioxane (333 µL), and 6 M acetic acid (50 µL). The sealed tube was kept at 120 °C for 4 days and hence allowed to cool down to room temperature. The formed precipitate was collected by filtration, washed with MeCN and dried in air, yielding a red powder.

PDI_{Bu}-1P COF structure analysis

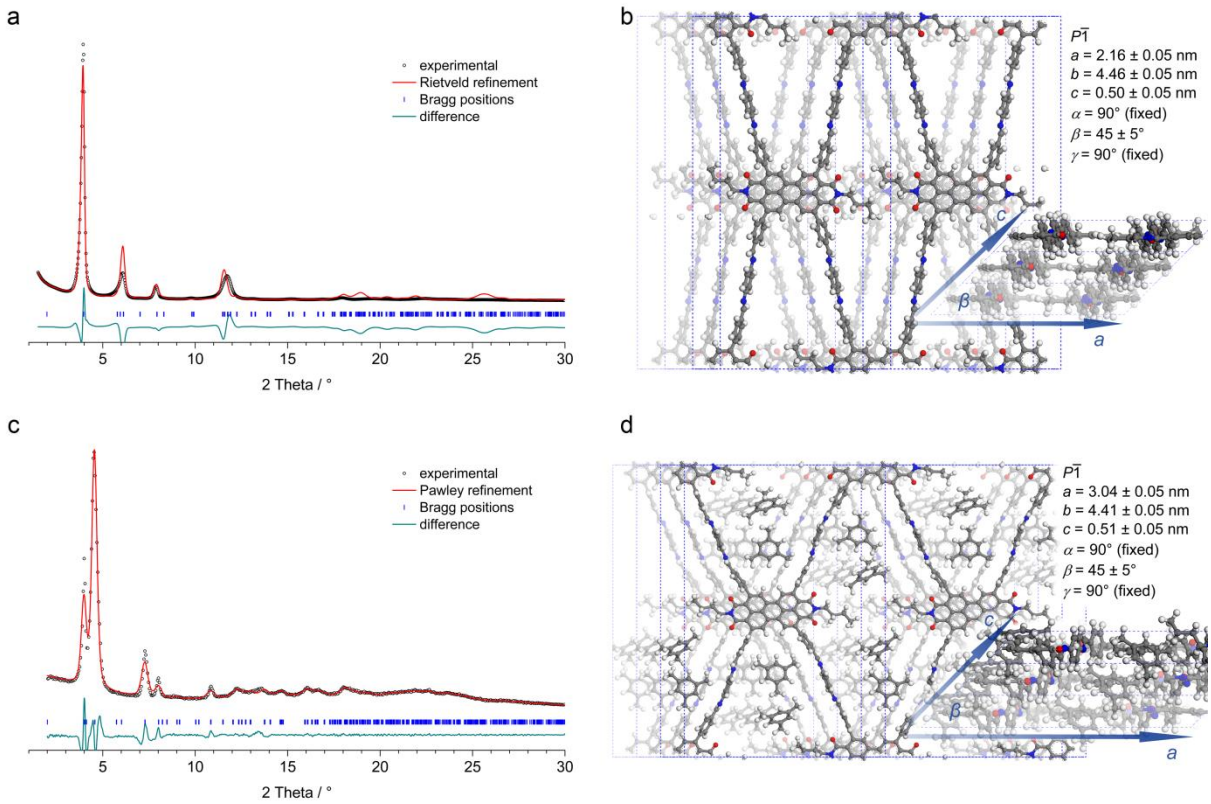

Figure 6.6 Structure of the PDI_{Bu}-1P COF (**a + c**) Experimental PXRD patterns (black dots) of the **PDI_{Bu}-1P** COF powder in the dry (**a**) and solvent-saturated (**c**) state. Refinements (red lines) using the structure models displayed in (**b + d**) provide a very good fit to the experimental data with only minimal differences between the experimental and the refined patterns (green lines).

PDI_{Pro}-1P COF structure analysis

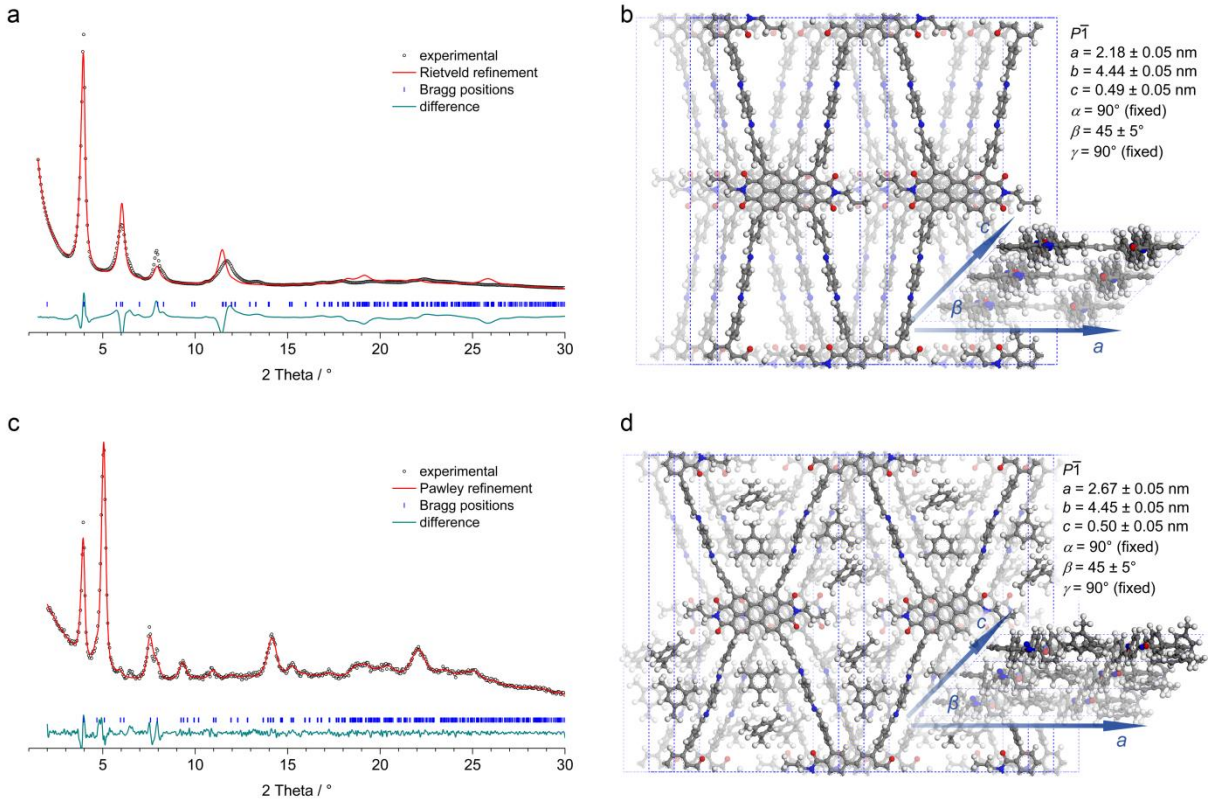

Figure 6.7 Structure of the PDI_{Pro}-1P COF (a + c) Experimental PXRD patterns (black dots) of the **PDI_{Pro}-1P** COF powder in the dry (**a**) and solvent-saturated (**c**) state. Refinements (red lines) using the structure models displayed in (**b + d**) provide a very good fit to the experimental data with only minimal differences between the experimental and the refined patterns (green lines).

Additional breathing studies

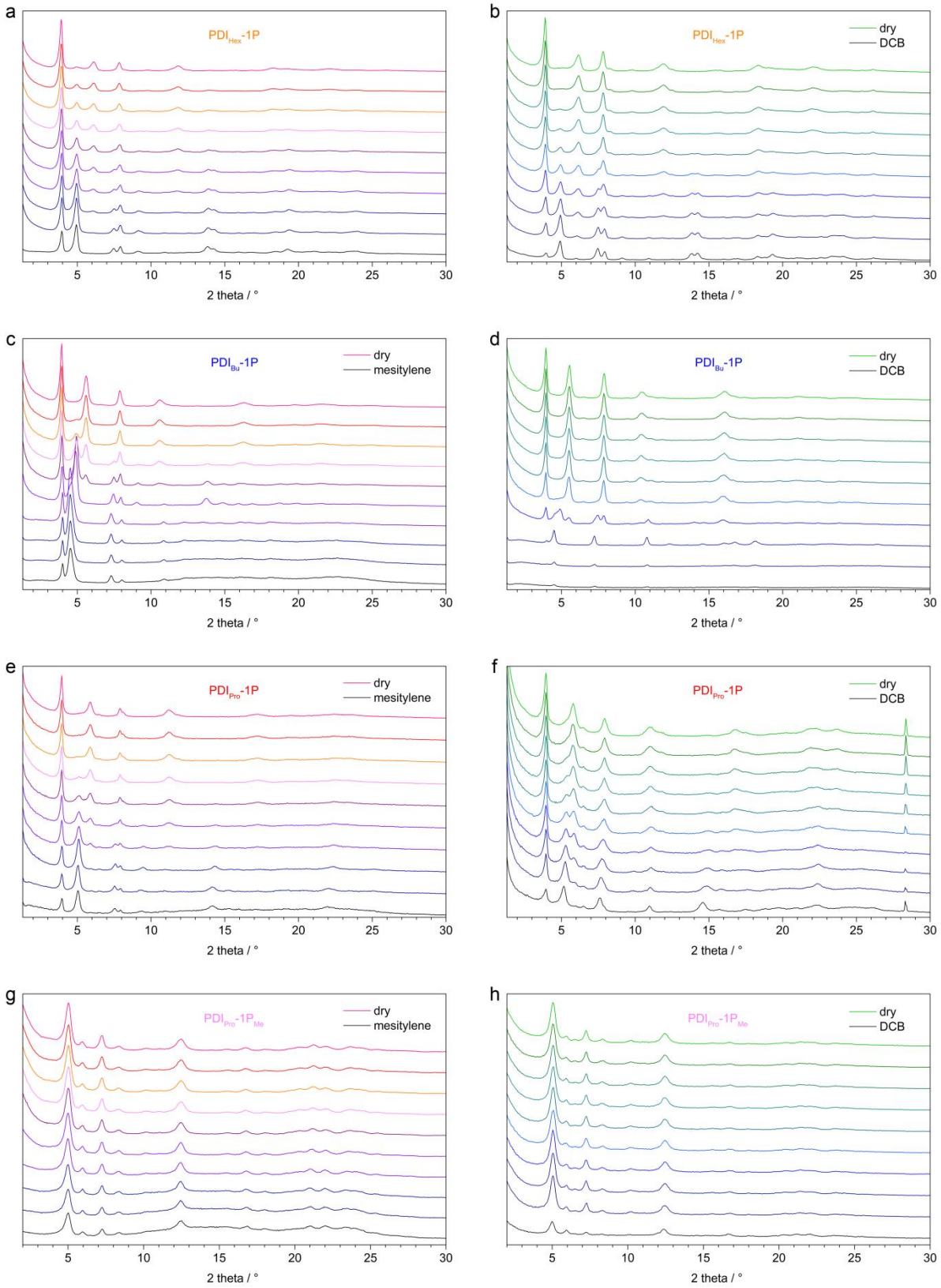

Figure 6.8 In-situ breathing studies of the four PDI-COFs regarding mesitylene and 1,4-dichlorobenzene (DCB). The reflex at 28.2° in (f) stems from the substrate.

The breathing studies were conducted via moistening the COFs with the respective solvent. Upon evaporation of the solvent at ambient conditions, PXRD spectra were recorded.

Toluene sorption analysis

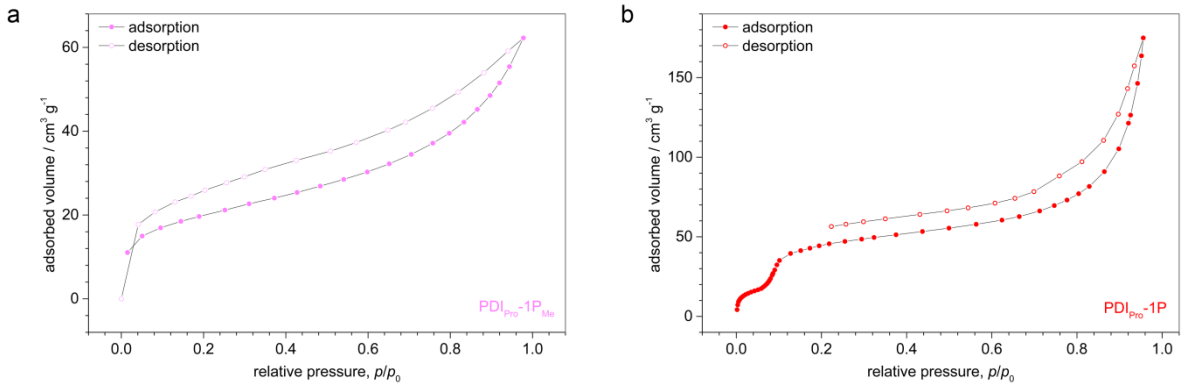

Figure 6.9 Toluene sorption analysis of the flexible PDI_{Pro}-1P COF (b) and the rigid PDI_{Pro}-$1P_{Me}$ COF (a).

Comparing the sorption isotherms of the two COFs reveals differences in the uptake of toluene. Whereas the isotherm of the rigid **PDI_{Pro}-$1P_{Me}$** COF appears smooth (a), the flexible **PDI_{Pro}-1P** COF exhibits a distinctive kink in the adsorption branch. These data are reminiscent of classic sorption studies in flexible MOFs, where steps in the isotherm are attributed to gate-opening transitions induced by the guest molecule.[36]

Additional photoluminescence (PL) spectroscopy

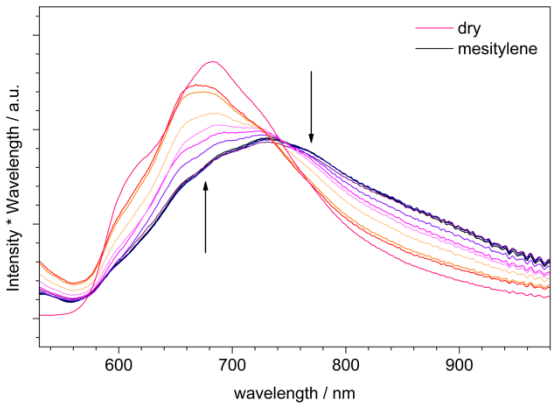

Figure 6.10 Photoluminescence of the PDI_{Pro}-1P COF upon the evaporation of mesitylene.

When in the solvent-saturated state, the photoluminescence (PL) of the flexible **PDI_{Pro}-1P** COF appears a broad bump at 730 nm. Upon evaporation of mesitylene, the maximum of the PL intensity shifts towards shorter wavelengths (680 nm) when completely dry.

Infrared (IR) spectroscopy

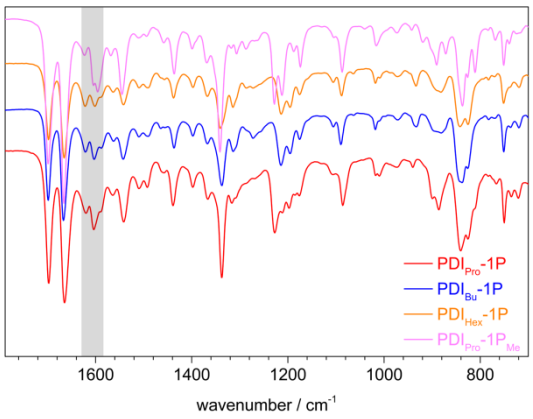

Figure 6.11 ATR-IR spectra of the PDI based COFs.

The ATR-IR spectra of the breathing **PDI_{Pro}-1P**, **PDI_{Bu}-1P** and **PDI_{Hex}-1P** COFs appear nearly identical, owing to the same linkage and types of building blocks in the framework. The **PDI_{Pro}-$1P_{Me}$** COF however exhibits a slightly different fingerprint region, which becomes particularly apparent around 1600 cm^{-1}, frequencies at which characteristic imine C=N stretching vibrations occur (marked in grey).

Additional UV-Vis spectroscopy

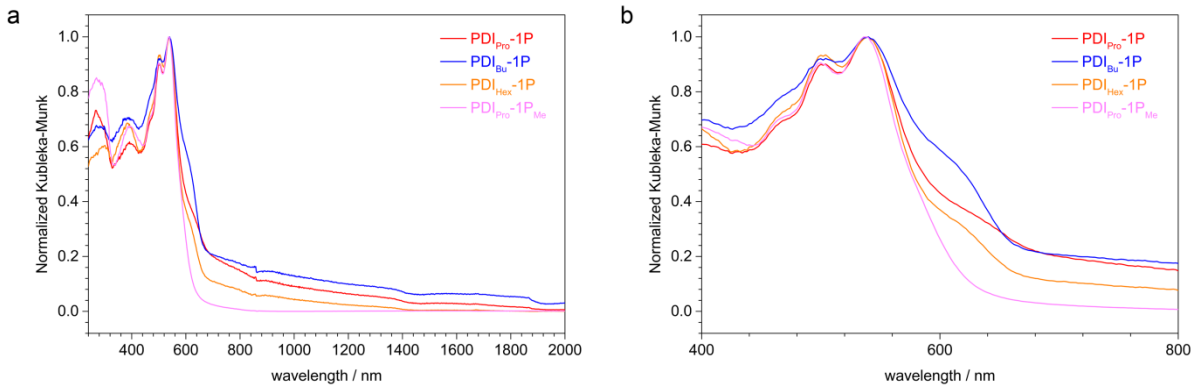

Figure 6.12 Diffuse reflectance spectra of the PDI based COFs.

Diffuse reflectance spectroscopy of the COF powders reveals trident absorption features at 400 – 600 nm which are typical for PDIs. The occurrence of defined, sharp absorption edges further signifies a large lateral offset between the COF layers and confirms our structure models of the frameworks. Taking a closer look at the onset region of the individual spectra, we notice a difference in the electronic structure between the breathing and the non-breathing COFs. Whereas the **PDI_{Pro}-1P**, **PDI_{Bu}-1P** and **PDI_{Hex}-1P COFs** exhibit an additional shoulder at around 620 – 630 nm, the **PDI_{Pro}-$1P_{Me}$** COF is lacking this distinct feature.

Themogravimetric analysis

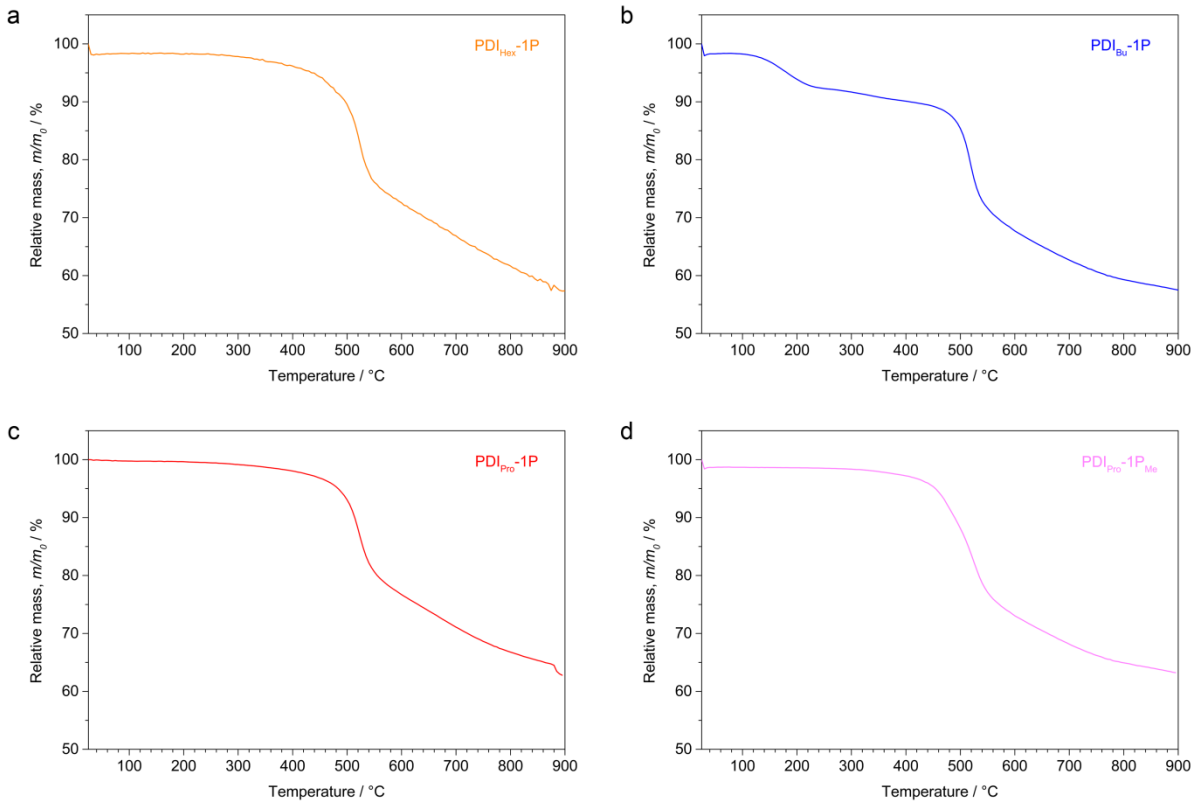

Figure 6.13 Thermogravimetric analysis of the four PDI-based COFs measured under an N_2 atmosphere at a heating rate of 1 K min^{-1}.

Thermal decomposition starts only at 500 °C, placing the four PDI-based COFs among the most stable COFs to date. The initial mass loss of the **PDI$_{Hex}$-1P** COF between 50 and 200 °C can be attributed to the desorption of water and residual MeCN from washing the COF after synthesis.

6.6 References

[1] R. Kitaura, K. Seki, G. Akiyama, S. Kitagawa, *Angew. Chem. Int. Ed.* **2003**, *42*, 428-431.

[2] S. Henke, A. Schneemann, A. Wütscher, R. A. Fischer, *J. Am. Chem. Soc.* **2012**, *134*, 9464-9474.

[3] A. Knebel, B. Geppert, K. Volgmann, D. I. Kolokolov, A. G. Stepanov, J. Twiefel, P. Heitjans, D. Volkmer, J. Caro, *Science* **2017**, *358*, 347-351.

[4] A. Ghoufi, K. Benhamed, L. Boukli-Hacene, G. Maurin, *ACS Cent Sci.* **2017**, *3*, 394-398.

[5] C. A. Fernandez, P. K. Thallapally, B. P. McGrail, *ChemPhysChem* **2012**, *13*, 3275-3281.

[6] A. L. Goodwin, M. Calleja, M. J. Conterio, M. T. Dove, J. S. O. Evans, D. A. Keen, L. Peters, M. G. Tucker, *Science* **2008**, *319*, 794-797.

[7] K. J. Gagnon, C. M. Beavers, A. Clearfield, *J. Am. Chem. Soc.* **2013**, *135*, 1252-1255.

[8] A. U. Ortiz, A. Boutin, K. J. Gagnon, A. Clearfield, F.-X. Coudert, *J. Am. Chem. Soc.* **2014**, *136*, 11540-11545.

[9] L. L. Gong, X. F. Feng, F. Luo, *Inorg. Chem.* **2015**, *54*, 11587-11589.

[10] F. Luo, C. B. Fan, M. B. Luo, X. L. Wu, Y. Zhu, S. Z. Pu, W.-Y. Xu, G.-C. Guo, *Angew. Chem. Int. Ed.* **2014**, *53*, 9298-9301.

[11] C. R. Murdock, B. C. Hughes, Z. Lu, D. M. Jenkins, *Coord. Chem. Rev.* **2014**, *258*, 119-136.

[12] E. J. Carrington, C. A. McAnally, A. J. Fletcher, S. P. Thompson, M. Warren, L. Brammer, *Nature Chem.* **2017**, *9*, 882-889.

[13] J. A. Mason, J. Oktawiec, M. K. Taylor, M. R. Hudson, J. Rodriguez, J. E. Bachman, M. I. Gonzalez, A. Cervellino, A. Guagliardi, C. M. Brown, P. L. Llewellyn, N. Masciocchi, J. R. Long, *Nature* **2015**, *527*, 357-361.

[14] N. Yanai, K. Kitayama, Y. Hijikata, H. Sato, R. Matsuda, Y. Kubota, M. Takata, M. Mizuno, T. Uemura, S. Kitagawa, *Nature Materials* **2011**, *10*, 787-793.

[15] P. Horcajada, T. Chalati, C. Serre, B. Gillet, C. Sebrie, T. Baati, J. F. Eubank, D. Heurtaux, P. Clayette, C. Kreuz, J.-S. Chang, Y. K. Hwang, V. Marsaud, P.-N. Bories, L. Cynober, S. Gil, G. Férey, P. Couvreur, R. Gref, *Nature Materials* **2009**, *9*, 172-178.

[16] S. Ling, B. Slater, *J. Phys. Chem. C* **2015**, *119*, 16667-16677.

[17] C. A. Fernandez, P. C. Martin, T. Schaef, M. E. Bowden, P. K. Thallapally, L. Dang, W. Xu, X. Chen, B. P. McGrail, *Sci Rep.* **2014**, *4*, 6114.

[18] G. J. Halder, C. J. Kepert, B. Moubaraki, K. S. Murray, J. D. Cashion, *Science* **2002**, *298*, 1762-1765.

[19] C. Huang, S. Barlow, S. R. Marder, *J. Org. Chem.* **2011**, *76*, 2386-2407.

[20] M. Sadrai, G. R. Bird, *Opt. Commun* **1984**, *51*, 62-64.

[21] X. Zhan, A. Facchetti, S. Barlow, T. J. Marks, M. A. Ratner, M. R. Wasielewski, S. R. Marder, *Adv. Mater.* **2011**, *23*, 268-284.

[22] R. Gvishi, R. Reisfeld, Z. Burshtein, *Chem. Phys. Lett.* **1993**, *213*, 338-344.

[23] M. J. Ahrens, M. J. Fuller, M. R. Wasielewski, *Chem. Mater.* **2003**, *15*, 2684-2686.

[24] F. Auras, L. Ascherl, A. H. Hakimioun, J. T. Margraf, F. C. Hanusch, S. Reuter, D. Bessinger, M. Döblinger, C. Hettstedt, K. Karaghiosoff, S. Herbert, P. Knochel, T. Clark, T. Bein, *J. Am. Chem. Soc.* **2016**, *138*, 16703-16710.

[25] N. Keller, D. Bessinger, S. Reuter, M. Calik, L. Ascherl, F. C. Hanusch, F. Auras, T. Bein, *J. Am. Chem. Soc.* **2017**, *139*, 8194-8199.

[26] D. Bessinger, L. Ascherl, F. Auras, T. Bein, *J. Am. Chem. Soc.* **2017**, *139*, 12035-12042.

[27] S. W. Eaton, L. E. Shoer, S. D. Karlen, S. M. Dyar, E. A. Margulies, B. S. Veldkamp, C. Ramanan, D. A. Hartzler, S. Savikhin, T. J. Marks, M. R. Wasielewski, *J. Am. Chem. Soc.* **2013**, *135*, 14701-14712.

[28] A. L. Briseno, S. C. B. Mannsfeld, C. Reese, J. M. Hancock, Y. Xiong, S. A. Jenekhe, Z. Bao, Y. Xia, *Nano Lett.* **2007**, *7*, 2847-2853.

[29] P. E. Hartnett, A. Timalsina, H. S. S. R. Matte, N. Zhou, X. Guo, W. Zhao, A. Facchetti, R. P. H. Chang, M. C. Hersam, M. R. Wasielewski, T. J. Marks, *J. Am. Chem. Soc.* **2014**, *136*, 16345-16356.

[30] F. Würthner, A. Sautter, J. Schilling, *J. Org. Chem.* **2002**, *67*, 3037-3044.

[31] S. Nakazono, S. Easwaramoorthi, D. Kim, H. Shinokubo, A. Osuka, *Org. Lett.* **2009**, *11*, 5426-5429.

[32] A. B. Cairns, A. L. Thompson, M. G. Tucker, J. Haines, A. L. Goodwin, *J. Am. Chem. Soc.* **2012**, *134*, 4454-4456.

[33] J. C. de Mello, H. F. Wittmann, R. H. Friend, *Adv. Mater.* **1997**, *9*, 230-232.

[34] J. Mooney, P. Kambhampati, *J Phys Chem Lett* **2013**, *4*, 3316-3318.

[35] T. E. Kaiser, H. Wang, V. Stepanenko, F. Würthner, *Angew. Chem. Int. Ed.* **2007**, *46*, 5541-5544.

[36] G. Ferey, C. Serre, *Chem. Soc. Rev.* **2009**, *38*, 1380-1399.

7 Longer, better, harder, stronger

7.1 Introduction

Covalent organic frameworks (COFs) are gradually conquering more advanced fields beyond the classic and straight forward gas storage and gas separation purposes that are investigated for any new porous material. Benefiting from the principles of reticular chemistry, stable COFs can be tailored regarding their pore size, pore shape and potential anchoring groups for post-modification, further diversifying the scope of potential applications. COFs as vapour sensors or as switchable photodetectors are just two examples that prove that these materials offer potential for applications beyond classical fields such as gas sorption or catalysis.

Beside these rather physical fields of research recent progress has been made in establishing COFs as versatile platforms for drug delivery, focusing on different pore geometries,[1] [2] distinctive approaches for fixing the respective drug molecule in the COF[3] or installing recognition groups for targeted delivery.[4]

For instance, Banerjee et al. applied a post-modification approach based on subsequential chemical functionalization of preinstalled anchoring groups to attach a cellular targeting ligand before loading the COF with the respective drug. 5-FU, an antimetabolite based anticancer drug, was hereby chosen because of its small diameter, however, the loading efficiencies were rather low.[4]

The approach of Lotsch et al. addressed this loading issue by using free electron pairs of imine-linked COFs as anchors for non-covalently fixing the model drug molecule quercetin in the porous system. Although they succeeded in drastically raising the loading capacities, quercetin, a flavonoid known for its anticancer activities, again is very small owing to the rather small pore size of the respective COF.[3]

If COFs, however, are to be used for practical drug delivery without adjusting to the demands of small pore sizes, COFs with bigger apertures that are capable of incorporating established drugs that exceed the size of these model drugs would be highly desirable. The biggest reported COF pore so far is 5.3 nm in diameter[5], which would already be sufficient for taking up larger commonly used anticancer drugs such as doxorubicin or pemetrexed. In this HHTP-based COF, the building blocks are linked via boronic esters, making the network prone to easily getting destroyed by traces of humidity. To address this stability issue, there is

a need to develop stable, large-pore COFs systems that can act as vehicles for targeted drug-delivery. This chapter is thus focusing on different approaches for extending the pore sizes of COFs via building block elongation.

7.2 Results and Discussion

We chose the 1,1,2,2-tetrakis(4-aminophenyl)ethene (**4PE**) building block as a basis for designing our large-pore networks, as tetraethylene-based COFs have proven to yield highly crystalline and stable frameworks.[6] In order to increase the pore size for the incorporation of larger guest molecules, two approaches can be considered: The first, straight forward method is to simply elongate the bridge in-between the multidentate building blocks. Starting from our already existing structures of **4PE**-based COFs, we simulated a network comprising a potential pentaphenyl-dicarboxaldehyde linker (**5P**) with the same dual-pore geometry, revealing a wall-to-wall distance of 5.9 nm (Figure 7.1) and exceeding the present largest pore aperture by 0.6 nm.

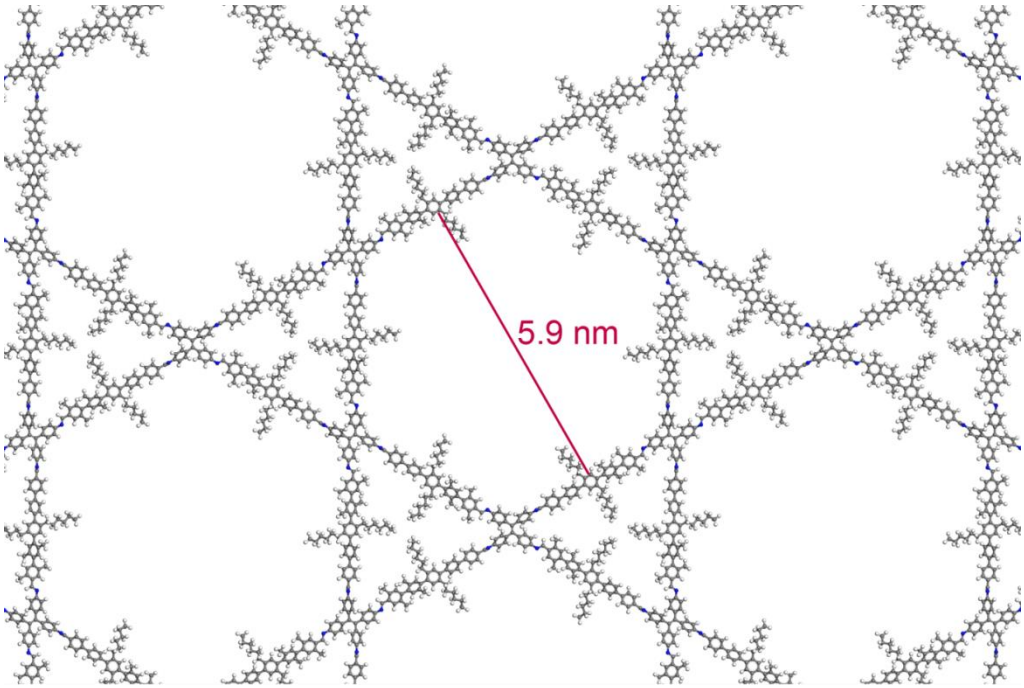

Figure 7.1 Simulation of a 4PE-based COF with a 5P linker.

We reasoned that introducing alkyl chains to the linker was crucial for a successful COF synthesis, as the shorter homologue terphenyl-dicarboxaldehyde had already turned out to be hardly soluble in the respective reaction mixture in our previous studies. To further fulfil the geometric requirement of exhibiting a C_2 rotational axis (see Chapter 3 and following

discussion), we chose the ortho-positions of the central phenyl ring for the installation of the solubility-enhancing groups (Figure 7.2).[6]

Starting from 1,4-dibromobenzene, we introduced two *n*-hexyl-chains via a Grignard reaction with hexylmagnesiumbromide. Bromination and subsequent borylation with bis(pinacolato)diboron yielded an intermediate that was subjected to a twofold Suzuki cross coupling reaction to give the desired **5P** building block (see Supporting Information for the reaction scheme). We used the **5P** linker together with **4PE** in solvothermal syntheses, drawing on well-established reaction conditions regarding solvent mixture, catalyst concentration and temperature. Despite various attempts, only amorphous bulk material could be obtained.

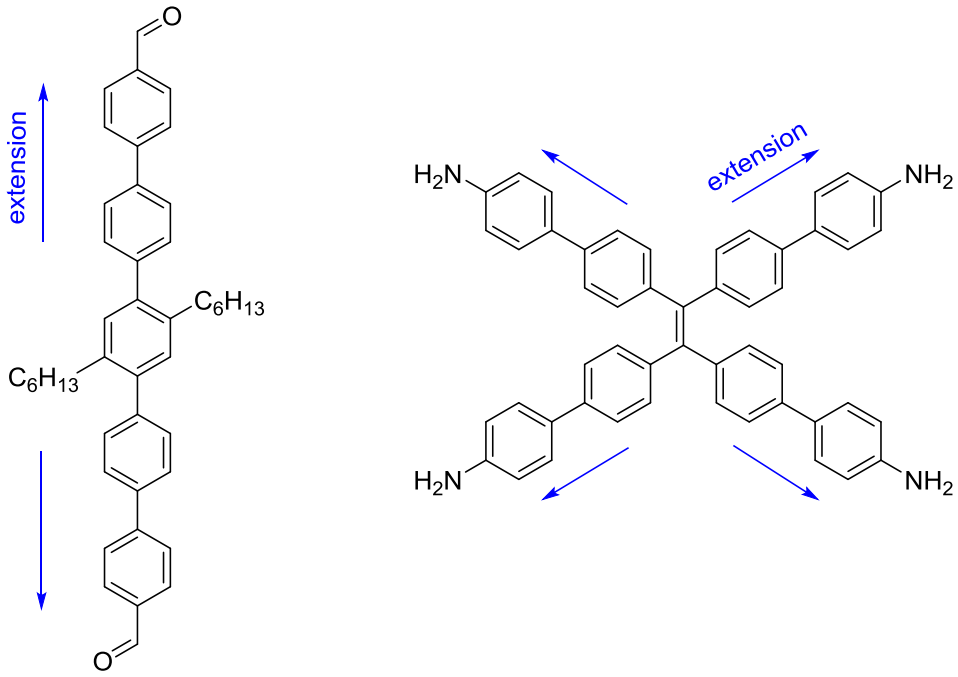

Figure 7.2 Linker design strategies towards large-pore COF systems.

Considering that a pentaphenyl linker might already be too floppy to yield stable COFs, our second approach towards bigger pore sizes was the elongation of the central multidentate building block (Figure 7.2). This way, shorter bridging molecules could be incorporated without compromising on the pore aperture. We started with the bromination of tetraphenylethene, followed by Suzuki or Sonogashira cross coupling reactions to yield the respective propeller-shaped building blocks as amines or aldehydes (see Supporting

Information for the reaction scheme). However, applying the building blocks together with linear dicarboxaldehydes in solvothermal syntheses did not provide any COF material either.

We decided to investigate these findings from a geometrical point of view in order to gain a more profound understanding of the correlation of linker geometry and successful COF synthesis, aiming for a more targeted building block design in the future. Therefore, we took a closer look at the molecular conformation of each building block regarding the incorporation into a potential COF structure.

For a better understanding of the following discussion, the peculiarities of **4PE** based COFs are briefly recapitulated. As **4PE** is a chiral molecule with both right- and left-turning enantiomers possible, a geometric mechanism to synchronize all molecules within one 2D sheet is crucial for realising highly crystalline COFs. Bridges with a C_2 rotational axis are able to transmit configurational information from one propeller-shaped tetraphenylene to the other via the twist of phenyl rings or the position of heteroatoms, ensuring that all tetraphenylene molecules within one sheet have the same sense of motion (Figure 7.3).

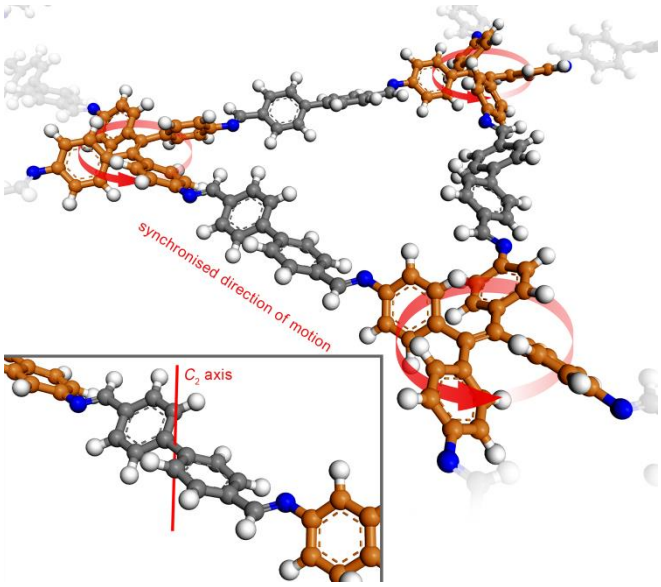

Figure 7.3 Fragment of the 4PE-2P COF structure.

In an ideal **4PE**-based COF structure the angle between the ethylene core and its propellers is roughly 45°, leading to a 90° twist of the complete bridge including the terminal phenyl rings. In a COF with biphenyl-dicarboxaldehyde, this results in a torsion angle of 90° / 3 = 30° between the individual rings. For the terphenyl version, this angle drops to 90° / 4 = 22.5°, which is still in the range of normal twist angles for poly(*p*-phenylenes).[7] For a **5P** based

COF this angle would decrease drastically to only 90° / 6 = 15°. When we model a free **5P** bridge, we note that the array of the phenyl rings deviates drastically from a spiral behaviour with small torsion angles (Figure 7.4). In fact, the bridge twists about 180°, indicating that forcing this linker into a COF structure might impose too much strain to the whole bridge.

The second geometric issue of this linker design might be the position of its alkyl chains. A **4PE**-based COF structure with an odd number of bridging phenyl rings forces the ring in the middle position to be co-planar with the *ab* plane of the whole COF, as the packing of the 2D sheets is perfectly eclipsed. This would constrain the alkyl chains to pack in an eclipsed way as well, however our recent studies indicate that they preferably stack with an offset. That would again enforce its core to tilt or slip, distorting the bridge and precluding the ability to transmit the sense of motion from one propeller to the other.

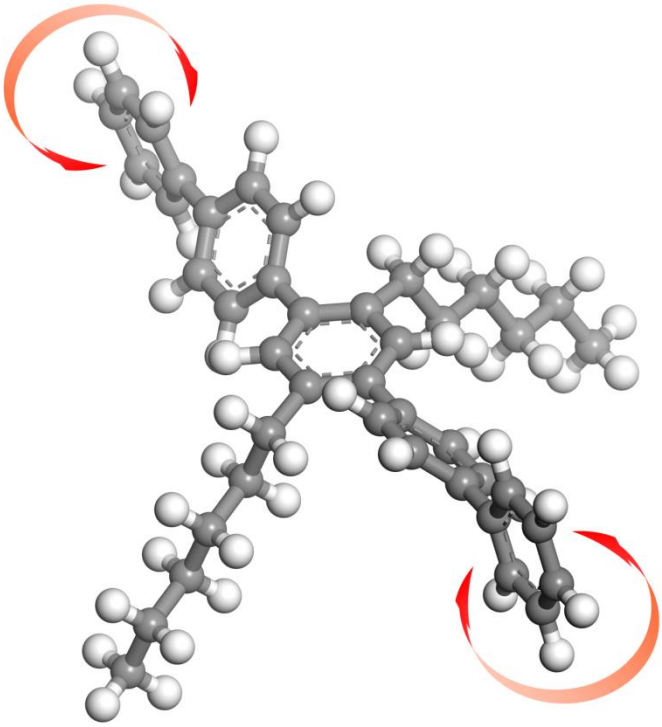

Figure 7.4 Simulation of a free 5P moiety.

Regarding the extended multidentate building blocks, we thoroughly examined the stacking of propeller-shaped tetraphenylenes. In COFs based on large aromatic multidentate building blocks like pyrene, attractive van-der-Waals interactions represent the major driving force that "glue" the 2D sheets together (see Chapter 1). However, our previous theoretical calculations have shown that the lock-and-key mechanism of **4PE**-based COFs is mainly based on

permanent electrostatic interactions between the aromatic rings, preventing any packing mode except the perfectly eclipsed one.[6] In fact, each phenyl ring within one sheet is tightly interlocked with its adjacent ring from the sheet below (Figure 7.5).

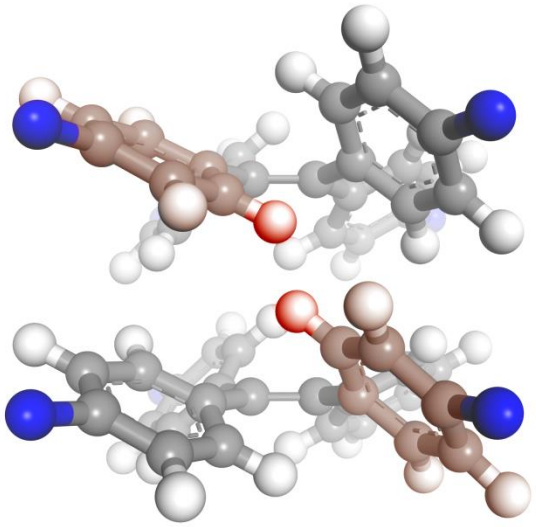

Figure 7.5 Interlocked stacking of 4PE-based COF sheets.

In extended versions of **4PE** (Figure 7.2), the outer set of phenyl rings cannot be fixed via this gearing mechanism as there are no adjacent phenyl rings in the layer underneath. In order to still get some degree of stabilisation, the outer rings are very likely to adopt a typical edge-on-face stacking motif (Figure 7.6), suppressing the synchronisation mechanism between adjacent propeller molecules: For each extended **4PE**, there are now 2^4 possible conformations to arrange the outer set of aromatic rings, obstructing any means to transmit configurational information from one inner propeller to the other.

According to our present knowledge, we would now suggest different approaches for designing new building blocks for large-pore COFs. Our first recommendation would be the reduction of individual segments in order to release torsion strain of long linkers. This could be achieved through coupling larger systems like thienothiophenes or benzodithiazoles. We furthermore suggest to install solubility-enhancing groups only at positions that stack with an offset. In our potential **5P** linker this would be the case for the phenyl rings 1, 2 and 4 and 5. Larger versions of **4PE** should furthermore exhibit propeller blades consisting of one single π-system (naphthalene, anthracene) to maintain stability and synchronisability.

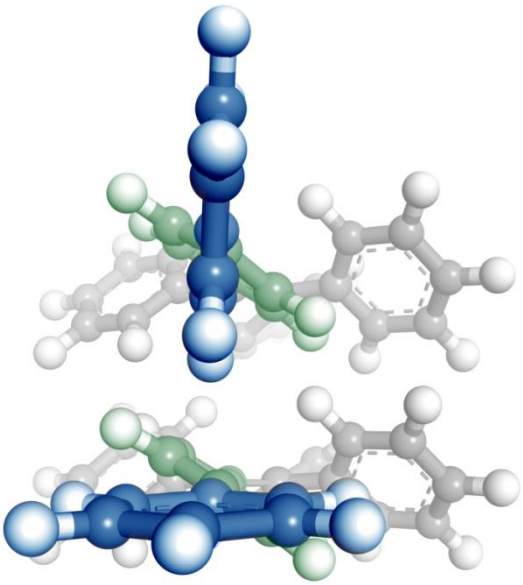

Figure 7.6 Double layer of extended 4PE building block. Whereas the inner set of aromatic rings (green) is parallel to each other, the outer set of phenyl rings (blue) is very likely to adopt an edge-on-face stacking motif.

7.3 Conclusion

We have successfully synthesized building blocks for the creation of COFs with big apertures as potential vehicles for drug delivery. Even though no crystalline material could be prepared so far, this work provides important insights into the design of future large-pore networks, allowing for a better understanding of geometrical principles in COF design. We can conclude that a stable network is only likely to emerge if each of its comprising building units has its own a natural tendency to adopt the same final COF structure. Therefore the two coupling partners have to be matched appropriately, taking into account multiple aspects including offset, alkyl chain packing and tilt angles.

7.4 Supporting information

Nuclear magnetic resonance (NMR) spectra were recorded on Bruker AV 400 and AV 400 TR spectrometers. Proton chemical shifts are expressed in parts per million (δ scale) and are calibrated using residual undeuterated solvent peaks as an internal reference (DMSO-d_6: 2.50). Data for ^{1}H NMR spectra are reported in the following way: chemical shift (δ ppm) (multiplicity, coupling constant, integration). Multiplicities are reported as follows: s = singlet, d = doublet, t = triplet, q = quartet, m = multiplet, or combinations thereof.

The **structure models of the COFs** were constructed using the Accelrys Materials Studio software package.

All reactions were performed in oven-dried glassware under argon atmosphere using standard Schlenk and glovebox techniques. Commercially available reagents were used as received. Solvents were obtained in high-purity grades from commercial suppliers and were, unless shipped under argon, degassed and saturated with argon prior to use.

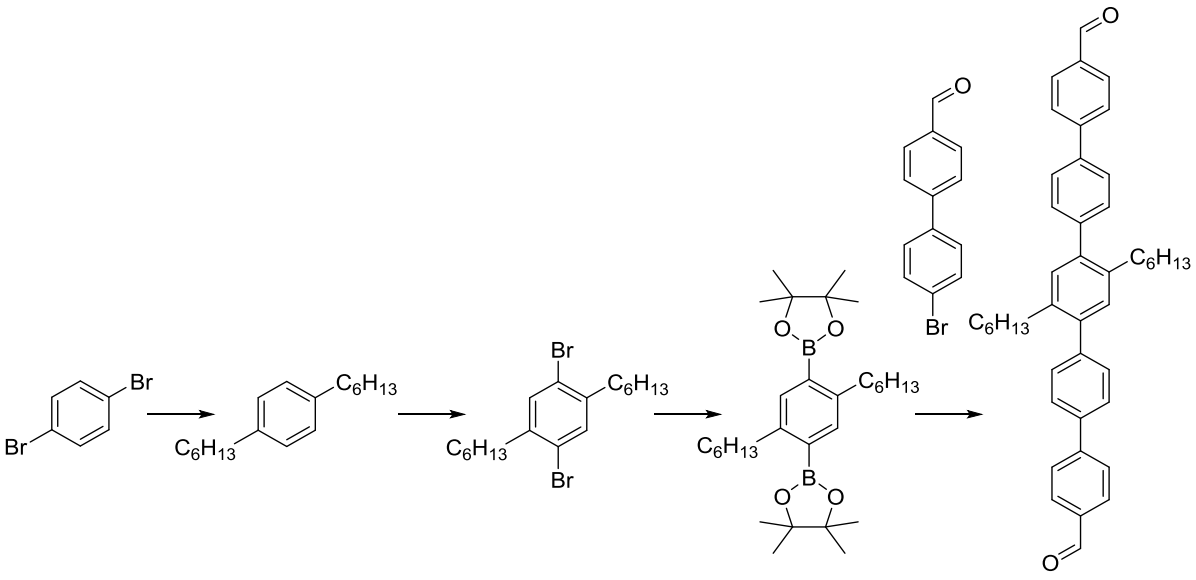

Figure 7.7 Reaction scheme for the synthesis of a 5P linker.

1,4-Dihexylbenzene

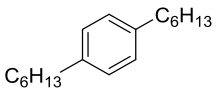

A 2.0 M solution of hexylmagnesiumbromide in ether (25 ml, 50 mmol, 2.5 eq) was slowly added to suspension of 1,4-dibromobenzene (4.7 g, 20 mmol, 1 eq) and $NiCl_2$(dppf) (325 mg, 6 mmol, 0.03 eq) in dry THF (40 ml). The reaction mixture was heated to 50 °C and stirred at this temperature for 24 h. The reaction mixture was allowed to come to room temperature, was quenched with a 0.1 M ammoniumchloride solution and extracted with DCM. The organic phase was further washed with water and brine and dried with $MgSO_4$. After removing the solvent, the crude product was purified via distillation (10^{-3} mbar, 98 °C) to yield the title compound as a colourless oil.

^{1}H NMR (400 MHz, $CDCl_3$): 7.09 (s, 4H), 2.57 (t, *J* = 8.1 Hz, 4H), 1.64 – 1.26 (m, 16H), 0.88 (t, *J* = 7.1 Hz, 6H).

1,4-Dibromo-3,6-dihexylbenzene

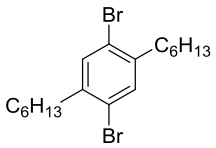

To a solution of 1,4-dihexylbenzene (1 mmol, 246 mg, 1 eq) in 2 ml of DCM was added a catalytic amount of iodine (1 bead). The flask was wrapped in tin-foil and bromine (256 µl, 5 mmol, 5 eq) was added slowly. The mixture was stirred at room temperature for 24 h, before quenching with sodium bisulfite solution. The organic part was washed with $NaHCO_3$ solution and dried over $MgSO_4$. The dried organic phase was purified via silica gel column chromatography (*n*-hexane) to yield 1,4-dibromo-3,6-dihexylbenzene as a white solid in 56 % yield (226 mg, 0.56 mmol).

^{1}H NMR (400 MHz, $CDCl_3$): 7.35 (s, 2H), 2.63 (t, *J* = 7.7 Hz, 4H), 1.56 – 1.27 (m, 16H), 0.89 (t, *J* = 6.6 Hz, 6H).

1,4-Bispincolato-3,6-dihexylbenzene

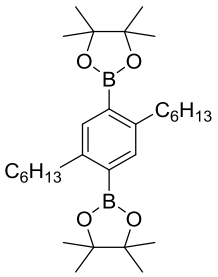

1,4-Dibromo-3,6-dihexylbenzene (101 mg, 0.25 mmol, 1 eq), bis(pinacolato)diboron (190 mg, 3 eq), KOAc (147 mg, 6 eq) and $PdCl_2$(dppf) (18 mg, 0.025 mmol, 0.1 eq) were stirred in 2.5 ml of dioxane at 105 °C for 3 days. The mixture was allowed to cool to room temperature, dried under high vacuum and diluted in water before it was extracted with DCM. The combined organic phases were dried with $MgSO_4$ and purified via silica gel column chromatography (*n*-hexane/DCM, 2:1) to yield 1,4-bispinacolato-3,6-dihexylbenzene as yellowish fluffy crystals (85 mg, 0.22 mmol, 68 %).

^{1}H NMR (400 MHz, $CDCl_3$): 7.53 (s, 2H), 2.82 (t, *J* = 8.1 Hz, 4H), 1.58 – 1.31 (m, 16H), 1.31 (s, 24H), 0.89 (t, *J* = 6.7 Hz, 6H).

2'',5''-Dihexyl-[1,1':4',1'':4'',1''':4''',1'''':quinquephenyl]-4,4''''-dicarbaldehyde (5P)

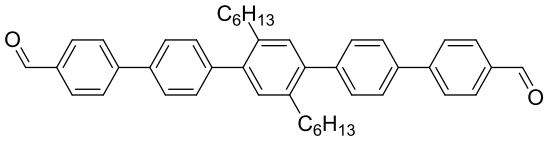

1,4-Bispincolato-3,6-dihexylbenzene (498 mg, 1 mmol, 1 eq), 4'-bromo-[1,1'-biphenyl]-4-carbaldehyde (783 mg, 3 mmol, 3 eq), K_2CO_3 (553 mg, 4 mmol) and $Pd(PPh_3)_4$ (116 mg, 0.1 mmol, 0.1 eq) were dissolved in 5 ml of dioxane and stirred at 95 °C for 4 days. The mixture was diluted with water and extracted with DCM. The combined organic phases were dried over $MgSO_4$ and purified via silica gel column chromatography (EtOAc/cyclohexane, 1:4) to yield the title compound as white crystals (416 mg, 0.67 mmol, 67 %).

^{1}H NMR (400 MHz, $CDCl_3$): 10.09 (s, 2H), 7.99 (d, *J* = 8.1 Hz, 4H), 7.85 (d, *J* = 8.2 Hz, 4H), 7.71 (d, *J* = 8.2 Hz, 4H), 7.50 (d, *J* = 8.2 Hz, 4H), 7.20 (s, 2H), 2.63 (t, *J* = 8.1 Hz, 4H), 1.55 – 1.21 (m, 16H), 0.81 (t, *J* = 7.1 Hz, 6H).

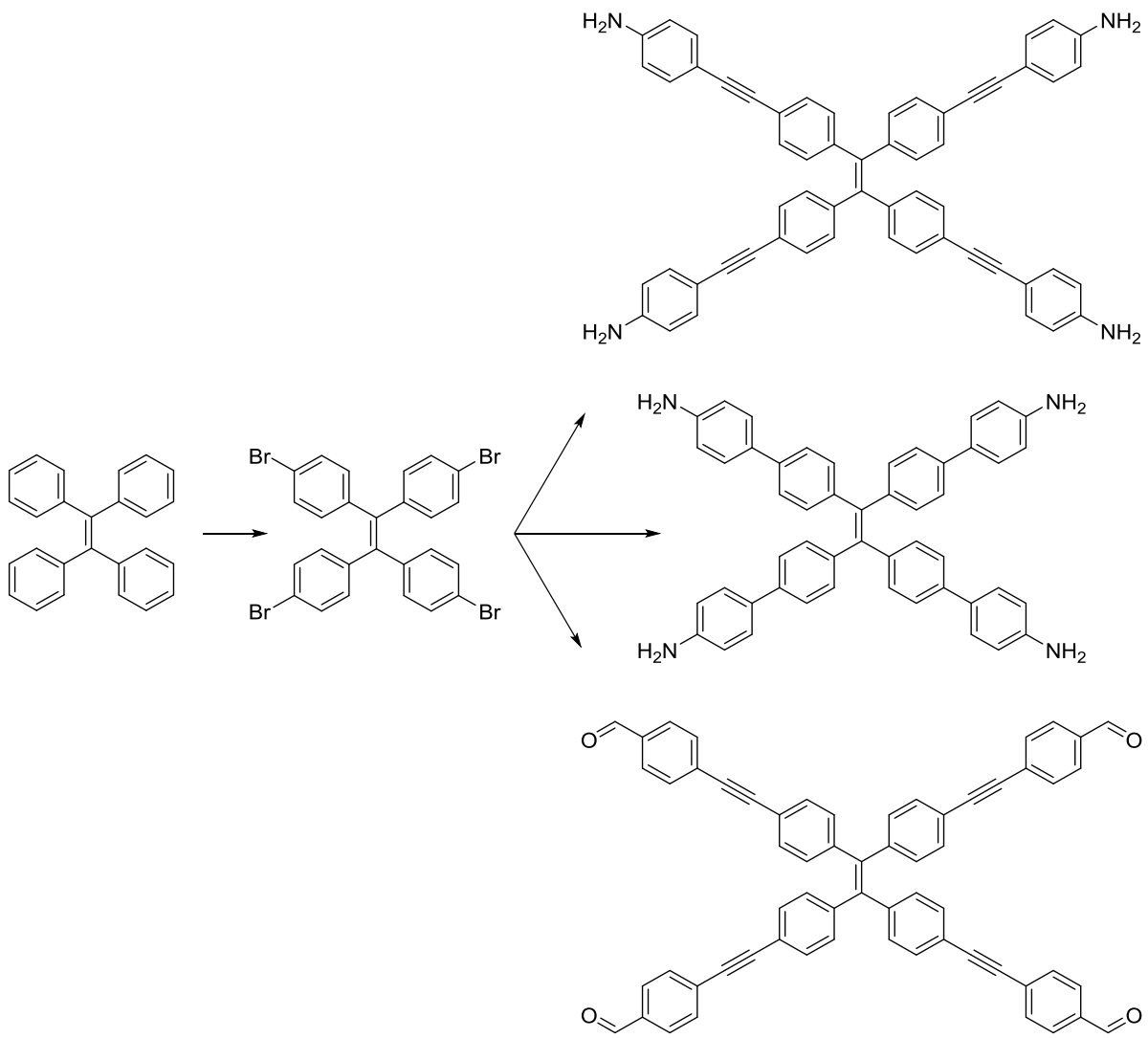

Figure 7.8 Reaction scheme for elongated versions of the multidentate 4PE building blocks.

1,1,2,2-Tetrakis(4-bromophenyl)ethene

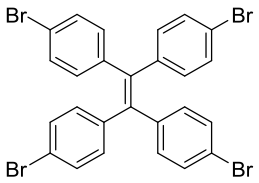

Method a)

Tetraphenylethene (2 g, 6 mmol, 1 eq) was placed in a desiccator and bromine (2.3 ml, 44 mmol, 7 eq) was put in a bath beneath. The desiccator was closed and left at room temperature for four days. The resulting yellow crude product was purified via column chromatography (n-hexane/DCM, 20:1) and the solvent was removed under vacuum. The product was dissolved in hot DCM and layered with isohexane until the first crystallites started to form. The mixture was allowed to cool down overnight and after removing the excess solvent, the title compound was obtained as colourless crystals (1.45 g, 2.2 mmol, 37 %).

Method b)

Bromine (3.74 ml, 73 mmol) was added dropwise to an ice-cooled solution of tetraphenylethene (5.78 g, 17.4 mmol) in DCM (87 ml, 0.2 M). The mixture was allowed to come to room temperature and stirred for 72 h. The reaction mixture was quenched with an aqueous solution of sodium thiosulfate (0.1 M). The aqueous phase was extracted with DCM and the combined organic phases were dried over $MgSO_4$. Evaporation of the solvent led to the desired title compound in form of a white powder.

^{1}H NMR (400 MHz, $CDCl_3$): 7.26 (d, *J* = 8.4 Hz, 8H), 6.84 (d, *J* = 8.6 Hz, 8H).

4',4''',4''''',4'''''''-(Ethene-1,1,2,2-tetrayl)tetrakis(([1,1'-biphenyl]-4-amine))

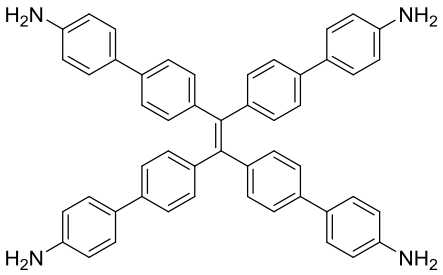

1,1,2,2-tetrakis(4-bromophenyl)ethane (648 mg, 1 mmol, 1 eq) and aminophenylboronic acid pinacol ester (1315 mg, 6 mmol, 6 eq) were dissolved in dry dioxane (30 mL). K_2CO_3 (1106 mg, 8 mmol, 8 eq) and $Pd(PPh_3)_4$ (116 mg, 0.1 mmol, 0.1 eq) were added and the mixture was stirred at 100 °C for 4 days. After coming to room temperature, the mixture was precipitated in water, washed with methanol, dissolved in DCM and washed with water and brine. The organic phases were dried over $MgSO_4$ and the remaining solvent evaporated under reduced pressure. The crude product was purified via silica gel column chromatography (DCM/MeOH, 20:1) yielding the title compound as a yellow compound.

^{1}H NMR (400 MHz, DMSO- d_6): 7.36 (d, J = 9.1 Hz, 8H), 7.54 (s, J = 9.1 Hz, 8H), 7.36 (d, J = 9.1 Hz, 8H), 6.65 (d, J = 9.1 Hz, 8H), 3.58 (s, 8H).

4,4',4'',4'''-((Ethene-1,1,2,2-tetrayltetrakis(benzene-4,1-diyl))tetrakis(ethyne-2,1-diyl))tetraaniline

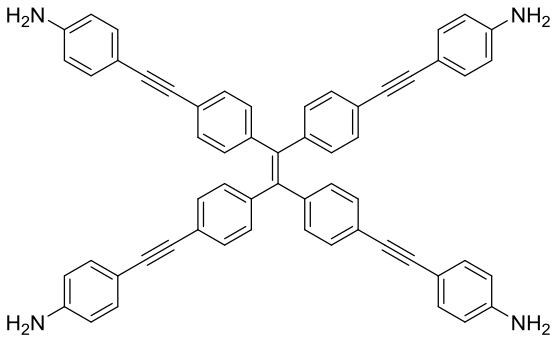

1,1,2,2-tetrakis(4-bromophenyl)ethane (1296 mg, 2 mmol, 1 eq), 4-ethynylaniline (1125 mg, 9.6 mmol, 4.8 eq), $Pd(PPh_3)_4$ (231 mg, 0.2 mmol, 0.1 eq) and CuI (76 mg, 0.4 mmol, 0.2 eq) were dissolved in 20 ml of a 3:1 mixture of THF and diisopropylamine. The mixture was refluxed at 80 °C for 16 h, allowed to come to room temperature and dried under vacuum.

The crude product was purified via silica gel column chromatography (EtOAc) to yield the title compound as yellow crystallites.

^{1}H NMR (400 MHz, DMSO- d_6): 7.25 (d, J = 8.0 Hz, 8H), 7.16 (d, J = 8.2 Hz, 8H), 6.97 (d, J = 8.0 Hz, 8H), 6.54 (d, J = 8.2 Hz, 8H), 5.56 (s, 8H).

4-(Trimethylsilyl)ethynyl-benzaldehyde

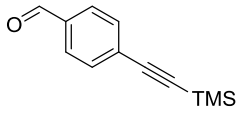

4-Bromobenzaldehyde (3.7 g, 20 mmol, 1.0 eq), ethynyltrimethylsilane (2.36 g, 24 mmol, 1.2 eq), CuI (228 mg, 1.2 mmol, 0.06 eq) and bis-(triphenylphosphine)palladium(II) dichloride (422 mg, 0.6 mmol, 0.03 eq) were dissolved in THF (40 mL). Diisopropylamine (12 ml, 85 mmol, 4.25 eq) was added and the reaction mixture was stirred at 80 °C for 16 h. The mixture allowed to come to room temperature and was filtered. The filtride was washed with ethylacetate and the combined organic phases were dried under vacuum. The crude product was diluted in DCM and washed with water and brine and dried over $MgSO_4$. The excess solvent was removed and the remaining crude product was purified via silica gel column chromatography (n-heptane/EtOAc, 20:1), yielding the desired product, which was used without further analysis.

4-Ethynylbenzaldehyde

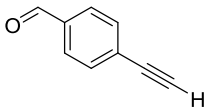

4-(trimethylsilyl)ethynyl-benzaldehyde (3.68 g, 18.2 mmol, 1 eq) and K_2CO_3 (251 mg, 1.82 mmol, 0.1 eq) were diluted in 72 ml methanol. The reaction mixture was stirred at room temperature until the base was dissolved. The organic phase was washed with water and brine and dried over $MgSO_4$. After removing the solvent under vacuum, the title compound was obtained as orange crystals.

^{1}H NMR (400 MHz, $CDCl_3$): 9.95 (s, 1 H), 7.80 – 7.76 (m, 2 H), 7.59 – 7,55 (m, 2 H), 3.23 (s, 1 H).

4,4',4'',4'''-((Ethene-1,1,2,2-tetrayltetrakis(benzene-4,1-diyl))tetrakis(ethyne-2,1-diyl))tetrabenzaldehyde

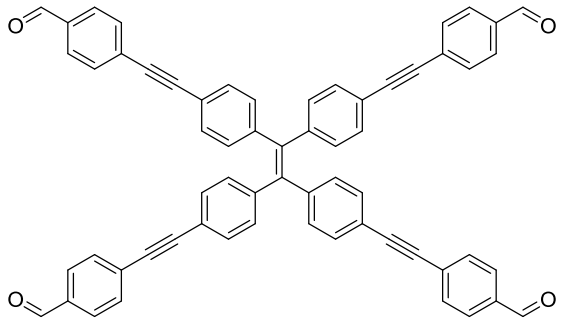

1,1,2,2-tetrakis(4-bromophenyl)ethane (65, 0.1 mmol, 1 eq), 4-ethynylbenzaldehyde (65 mg, 0.5 mmol, 5 eq), $Pd(PPh_3)_4$ (12 mg, 0.01 mmol, 0.1 eq) and CuI (4 mg, 0.02 mmol, 0.2 eq) were dissolved in 1 ml of a 3:1 mixture of THF and diisopropylamine. The mixture was heated under reflux at 80 °C for 16 h, allowed to come to room temperature and dried under vacuum to yield the title compound as a yellow powder.

^{1}H NMR (400 MHz, $CDCl_3$): 10.02 (s, 4H), 7.85 (d, *J* = 8.4 Hz, 8H), 7.64 (d, *J* = 8.3 Hz, 8H), 7.26 (d, *J* = 8.3 Hz, 8H), 6.85 (d, *J* = 8.5 Hz, 2H).

7.5 References

[1] Q. Fang, J. Wang, S. Gu, R. B. Kaspar, Z. Zhuang, J. Zheng, H. Guo, S. Qiu, Y. Yan, *J. Am. Chem. Soc.* **2015**, *137*, 8352-8355.

[2] L. Bai, S. Z. F. Phua, W. Q. Lim, A. Jana, Z. Luo, H. P. Tham, L. Zhao, Q. Gao, Y. Zhao, *Chem. Commun.* **2016**, *52*, 4128-4131.

[3] V. S. Vyas, M. Vishwakarma, I. Moudrakovski, F. Haase, G. Savasci, C. Ochsenfeld, J. P. Spatz, B. V. Lotsch, *Adv. Mater.* **2016**, *28*, 8749-8754.

[4] S. Mitra, H. S. Sasmal, T. Kundu, S. Kandambeth, K. Illath, D. Díaz Díaz, R. Banerjee, *J. Am. Chem. Soc.* **2017**, *139*, 4513-4520.

[5] S. Jin, K. Furukawa, M. Addicoat, L. Chen, S. Takahashi, S. Irle, T. Nakamura, D. Jiang, *Chem. Sci.* **2013**, *4*, 4505-4511.

[6] L. Ascherl, T. Sick, J. T. Margraf, S. H. Lapidus, M. Calik, C. Hettstedt, K. Karaghiosoff, M. Döblinger, T. Clark, K. W. Chapman, F. Auras, T. Bein, *Nature Chem.* **2016**, *8*, 310-316.

[7] S. Sasaki, T. Yamamoto, T. Kanbara, A. Morita, T. Yamamoto, *J. Polym. Sci., Part B: Polym. Phys.* **1992**, *30*, 293-297.

8 Conclusion and Outlook

This thesis was focused on investigating the interplay of linker design and resulting properties of two-dimensional covalent organic frameworks (COFs).

The first project of this thesis (Chapter 3) was based on developing a concept to drastically enhance the crystallinity of COFs by utilizing the molecular conformation of rigid tetraethylene, propeller-shaped building units in synthesis. Whereas conventional COFs were hitherto mainly based on flat multidentate building blocks that stack with random offset direction, our self-repeating docking sites help to guide the attachment of subsequent linkers towards one single, predefined lateral position. Investigating a series of COFs with bridging units that differ in symmetry, we learned that the transmission of configurational information within one COF layer is of key importance for the realisation of an error-free domain. We found that bridges with C_2 symmetry can successfully synchronize adjacent propeller-molecules, allowing for the incorporation of only one propeller enantiomer within one crystallite. The implementation of our concept led to a drastic reduction of stacking faults during synthesis, yielding COFs with an unmatched degree of crystallinity and well-defined crystal facets.

We were able to extend our concept further in the second part of this thesis (Chapter 4), making it applicable to a broader range of bridging units. Bearing in mind the importance of three-dimensional docking sites and applying tetraphenylpyrene-derived building blocks with armchair configuration, we were able to realise highly faceted COF single crystals on the order of half a micrometre. Our COFs owe their unprecedented long-range order to a predefined offset direction between adjacent COF layers, which is directed through the molecular geometry of the pyrene entities. The synchronisation of these armchair-molecules can be accomplished through flat and rigid π-stacked bridges, allowing for electronic communication between all subunits of the framework. The application of linear linkers that vary in their electron densities enabled us to modulate the optoelectronic properties of the respective COFs and prove that it is possible to induce charge-transfer excitations across the imine bonds.

Applying our stacking concept and keeping in mind that charge-transfer transitions are possible across imine bonds, we were able to develop the first solvatochromic COFs (Chapter 5). By combining electron-rich and electron-deficient building blocks we realised COFs that

can act as fully reversible, solid-state supramolecular sensors. When in contact with solvent or water vapours, these materials react with a distinct colour shift dependent on the solvent polarity and the vapour concentration. We found that the solvatochromic effect is of purely electronic origin and can be explained as a facilitated charge-transfer transition, as no structural or chemical changes occur in the framework during the transition. To enhance the accessibility of the porous channel system, we grew the COFs as oriented thin films that reach ultrafast response times below 200 ms. Constructing a simple, fast and extremely stable humidity sensor device by using the COF film as a vapour-sensitive light filter between an LED and a light-dependent resistor, we demonstrated for the first time the viability of COFs for practical applications.

Designing multidentate building blocks based on perylenetetracarboxylic acid diimides (PDIs) enabled us to realise the first flexible 2D COFs (Chapter 6). The molecular design of our central core molecules enforces a large lateral displacement of adjacent COF layers, keeping the linear bridging units at sufficient distance to not obstruct each other. On the other hand, the intermolecular interactions between adjacent PDI molecules are strong enough to preclude delamination, allowing for a "wine-rack" breathing mechanism upon the contact with solvent molecules. During this reversible crystal-to-crystal phase transition, the electronic structure of the COFs was found to be altered as well. The inclusion of solvent molecules separates the individual PDI entities laterally, inhibiting additional in-plane electronic coupling. By introducing sterically demanding groups at the bridge, we were further able to freeze the breathing mechanism and lock the COF in a decoupled-only configuration.

Finally, we were able to deduce guidelines towards the design of successful COF linkers (Chapter 7). We reasoned that stable networks can only be achieved if each of the building blocks tends to adopt the same final COF structure, underlining the necessity to specifically tailor matching coupling partners beforehand.

In conclusion, this thesis illustrates the great potential of a new and emerging class of crystalline and porous materials. The benefits of reticular chemistry combined with the almost infinite possibilities of linker synthesis offered by organic chemistry allow for designing COFs on the drawing board and broaden the scope for practical applications beyond fundamental research.

9 Appendix

List of Abbreviations

2D	two-dimensional
3D	three-dimensional
BET	Brunauer-Emmett-Teller
Bn	benzyl
Bu	butyl
COF	covalent organic framework
DCE	1,2-dichloroethane
DCM	dichloromethane
DFT	density functional theory
DMSO	dimethyl sulfoxide
eq.	equivalents
GIWAXS	grazing-incidence wide angle X-ray scattering
Hex	hexyl
IR	infrared
ITO	indium tin oxide
LED	light-emitting diode
LDR	light-dependent resistor
Me	methyl
MOF	metal organic framework
NMR	nuclear magnetic resonance

PP	polypropylene
ppm	parts per million
Pro	propyl
PTFE	poly(tetrafluoroethylene)
PXRD	powder X-ray diffraction
QSDFT	quenched solid density functional theory
RH	relative humidity
SCLC	space-charge-limited current
SEM	scanning electron microscopy
TEM	transmission electron microscopy
TGA	thermogravimetric analysis
THF	tetrahydrofuran
TMS	trimethylsilyl
UV-Vis	ultraviolet-visible

10 Publications and Presentations

10.1 Publications

1. Solvatochromic Covalent Organic Frameworks

   L. Ascherl, M. Hennemann, D. Di Nuzzo, A. G. Hufnagel, M. Beetz, R. H. Friend, T. Clark, T. Bein and F. Auras, *under review at Nature Communications.*

2. Oligothiophene-Bridged Conjugated Covalent Organic Frameworks

   N. Keller, D. Bessinger, S. Reuter, M. Calik, L. Ascherl, F. C. Hanusch, F. Auras, T. Bein, *J. Am. Chem. Soc.* **2017**, *139*, 8194-8199.

3. Spectrally Switchable Photodetection with Near-Infrared-Absorbing Covalent Organic Frameworks

   D. Bessinger, L. Ascherl, F. Auras, T. Bein, *J. Am. Chem. Soc.* **2017**, *139*, 12035-12042.

4. Synchronized Offset Stacking: A Concept for Growing Large-Domain and Highly Crystalline 2D Covalent Organic Frameworks

   F. Auras, L. Ascherl, A. H. Hakimioun, J. T. Margraf, F. C. Hanusch, S. Reuter, D. Bessinger, M. Döblinger, C. Hettstedt, K. Karaghiosoff, S. Herbert, P. Knochel, T. Clark, T. Bein, *J. Am. Chem. Soc.* **2016**, *138*, 16703-16710.

5. Molecular docking sites designed for the generation of highly crystalline covalent organic frameworks (Cover Picture)

   L. Ascherl, T. Sick, J. T. Margraf, S. H. Lapidus, M. Calik, C. Hettstedt, K. Karaghiosoff, M. Döblinger, T. Clark, K. W. Chapman, F. Auras, T. Bein, *Nature Chem.* **2016**, *8*, 310.

6. New Acyclic Neutral Phosphorus Sulfides and Sulfide Oxides

   S. Schönberger, C. Jagdhuber, L. Ascherl, C. Evangelisti, T. M. Klapötke, K. Karaghiosoff, *Z. Anorg. Allg. Chem.* **2014**, *640*, 68-75.

7. The activation of Woollins' reagent. Isolation of pyridine stabilised $PhPSe_2$

   L. Ascherl, A. Nordheider, K. S. A. Arachchige, D. B. Cordes, K. Karaghiosoff, M. Bühl, A. M. Z. Slawin, J. D. Woollins, *Chem. Commun.* **2014**, *50*, 6214-6216.

8. Chemistry and Structures of Hexakis(halogenomethyl)-, Hexakis(azidomethyl)-, and Hexakis(nitratomethyl)disiloxanes

   L. Ascherl, C. Evangelisti, T. M. Klapötke, B. Krumm, J. Nafe, A. Nieder, S. Rest, C. Schütz, M. Suceska, M. Trunk, *Chem. Eur. J.* **2013**, *19*, 9198-9210.

10.2 Oral presentations

1. Creating highly crystalline covalent organic frameworks through docking interactions

   EuroMOF **2017**, Delft, Netherlands.

2. The realization of highly crystalline covalent organic frameworks

   Federation of European Zeolite Associations (FEZA) **2017**, Sofia, Bulgaria.

3. Let’s play with molecular LEGOs

   Science Rocks! **2017**, Munich, Germany.

4. The art of growing highly crystalline covalent organic frameworks

   Deutsche Zeolith Tagung (DZT) **2017**, Frankfurt, Germany.

5. Molecular docking sites designed for the generation of highly crystalline covalent organic frameworks

   Pitch talk at SolTech Symposium **2016**, Munich, Germany.

10.3 Poster presentations

1. Realising highly crystalline covalent organic frameworks through docking interactions

   Faraday Discussions **2017**, Edinburgh, Scotland.

2. Molecular docking sites designed for the generation of highly crystalline covalent organic frameworks

   MOF **2016**, Long Beach, United States of America.

3. The taming of the screw – Designed molecular docking sites for creating highly crystalline covalent organic

   Deutsche Zeolith Tagung (DZT) **2016**, Gießen, Germany.

4. Molecular docking sites for the creation of highly crystalline covalent organic frameworks

   SolTech Symposium **2016**, Munich, Germany.

5. The taming of the Screw – A concept for realizing covalent organic frameworks with an exceptionally high degree of crystallinity

   EuroMOF **2015**, Potsdam, Germany.

6. Realizing covalent organic frameworks with an exceptionally high degree of crystallinity

   SolTech Symposium **2015**, Kloster Banz, Germany.

7. Covalent Organic Frameworks as Photoconductive Materials

   CeNS Symposium **2014**, Venice, Italy.